DEUTSCHES ELEKTRONEN-SYNCHROTRON

DESY 93–103
July 1993

The H1 Detector at HERA

H1 Collaboration

ISSN 0418-9833

NOTKESTRASSE 85 - 22603 HAMBURG

To be sure that your preprints are promptly included in the
HIGH ENERGY PHYSICS INDEX,
send them to (if possible by air mail):

DESY **Bibliothek** **Notkestraße 85** **22603 Hamburg** **Germany**	**DESY-IfH** **Bibliothek** **Platanenallee 6** **15738 Zeuthen** **Germany**

DESY 93-103
July 1993

ISSN 0418-9833

The H1 detector at HERA

H1 Collaboration

Abstract:

Technical aspects of the H1 detector at the electron-proton storage ring HERA are described. Some performance figures from the first luminosity phase of HERA are given, too.

To be submitted in abbreviated form to Nuclear Instruments and Methods

H1 Collaboration

I. Abt[7], T. Ahmed[3], V. Andreev[24], B. Andrieu[27], R.-D. Appuhn[11], C. Arnault[26], M. Arpagaus[34], A. Babaev[23], H. Bärwolff[33], J. Bán[17], E. Banas[6,11], P. Baranov[24], E. Barrelet[28], W. Bartel[11], U. Bassler[28], D.E. Baynham[5], G.A. Beck[19], H.P. Beck[35], D. Bederede[9], H.-J. Behrend[11], C. Beigbeder[26], A. Belousov[24], Ch. Berger[1], H. Bergstein[1], R. Bernard[9], G. Bernardi[28], R. Bernet[34], R. Bernier[26], U. Berthon[27], G. Bertrand-Coremans[4], M. Besançon[9], J.-C. Biasci[26], P. Biddulph[22], E. Binder[11], J.C. Bizot[26], V. Blobel[13], F. Blouzon[26], H. Blume[26], K. Borras[8], V. Boudry[27], C. Bourdarios[26], F. Brasse[11], W. Braunschweig[1], D. Breton[26], H. Brettel[25], V. Brisson[26], D. Bruncko[17], C. Brune[15], U. Buchner[3], L. Büngener[13], J. Bürger[11], F.W. Büsser[13], A. Buniatian[11,37], S. Burke[19], A. Busata[27], G. Buschhorn[25], A.J. Campbell[10], T. Carli[25], F. Charles[28], R. Chase[26], D. Clarke[5], A.B. Clegg[18], M. Colombo[6], V. Commichau[2], J.F. Connolly[5], J.A. Coughlan[5], A. Courau[26], Ch. Coutures[9], A. Coville[25], G. Cozzika[9], D.A. Cragg[5], L. Criegee[11], H.I. Cronström[21], N.H. Cunliffe[5], J. Cvach[27], S. Dagoret[28], J.B. Dainton[19], M. Danilov[23], A.W.E. Dann[22], D. Darvill[11], W.D. Dau[16], J. David[26], M. David[9], R.J. Day[5], E. Deffur[11], B. Delcourt[26], L. Del Buono[28], F. Descamps[28], M. Devel[26], J. P. Dewulf[4], A. De Roeck[11], P. Dingus[27], K. Djidi[9], C. Dollfus[35], J.D. Dowell[3], H.B. Dreis[2], A. Drescher[8], U. Dretzler[8], M. Drewe[3], J. Duboc[28], A. Ducorps[26], D. Düllmann[13], O. Dünger[13], H. Duhm[12], J. Dupont[26], R. Ebbinghaus[8], M. Eberle[12], J. Ebert[32], T.R. Ebert[19], G. Eckerlin[11], B.W.H. Edwards[5], V. Efremenko[23], S. Egli[35], S. Eichenberger[35], R. Eichler[34], F. Eisele[14], E. Eisenhandler[20], N.N. Ellis[3], R.J. Ellison[22], E. Elsen[11], M. Erdmann[14], G. Ernst[3], E. Evrard[4], G. Falley[11], A. Fedotov[23], D. Feeken[13], R. Felst[11], J. Feltesse[9], Z.Y. Feng[28], I.F. Fensome[3], J. Fent[25], J. Ferencei[11], F. Ferrarotto[31], K. Flamm[11], W. Flauger[11,†], M. Fleischer[11], P.S. Flower[5], G. Flügge[2], A. Fomenko[24], B. Fominykh[23], M. Forbush[7], J. Formánek[30], J.M. Foster[22], G. Franke[11], E. Fretwurst[12], W. Fröchtenicht[25], P. Fuhrmann[1], E. Gabathuler[19], K. Gadow[11], K. Gamerdinger[25], J. Garvey[3], J. Gayler[11], A. Gellrich[13], M. Gennis[11], U. Gensch[33], H. Genzel[1], R. Gerhards[11], K. Geske[13], I. Giesgen[2], D. Gillespie[19], W. Glasgow[5], L. Godfrey[7], J. Godlewski[6], U. Goerlach[11], L. Goerlich[6], M. Goldberg[28], A.M. Goodall[19], I. Gorelov[23], P. Goritchev[23], C. Grab[34], H. Grässler[2], R. Grässler[2], T. Greenshaw[19], C. Gregory[27], H. Greif[25], G. Grindhammer[25], C. Gruber[16], S. Günther[33], J. Haack[33], M. Haguenauer[27], D. Haidt[11], L. Hajduk[6], O. Hamon[28], D. Handschuh[11], K. Hangarter[2], E.M. Hanlon[18], M. Hapke[11], U. Harder[33], J. Harjes[11], P. Hartz[3], P.E. Hatton[5], R. Haydar[26], W.J. Haynes[5], J. Heatherington[20], V. Hedberg[21], C.R. Hedgecock[5], G. Heinzelmann[13], R.C.W. Henderson[18], H. Henschel[33], R. Herma[7], I. Herynek[29], W. Hildesheim[28], P. Hill[11], D.L. Hill[5], C.D. Hilton[22], J. Hladký[29], K.C. Hoeger[22], R.B. Hopes[5], A. Hrisoho[26], J. Huber[25], Ph. Huet[4], H. Hufnagel[14], N. Huot[28], J.-F. Huppert[26], M. Ibbotson[22], D. Imbault[28], H. Itterbeck[1], M.-A. Jabiol[9], A. Jacholkowska[26], C. Jacobsson[21], M. Jaffre[26], J. Janoth[15], T. Jansen[11], P. Jean[26], J. Jeanjean[26], L. Jönsson[21], K. Johannsen[13], D.P. Johnson[4], L. Johnson[18], H. Jung[2], P.I.P. Kalmus[20], G. Kantel[11], S. Kasarian[11], R. Kaschowitz[2], P. Kasselmann[12], U. Kathage[16], H. H.Kaufmann[33], G. Kemmerling[2], I.R. Kenyon[3], S. Kermiche[26], C. Keuker[1], C. Kiesling[25], M. Klein[33], C. Kleinwort[13], G. Knies[11], W. Ko[7], T. Köhler[1], M. Kolander[6], H. Kolanoski[8], F. Kole[7], J. Koll[11], S.D. Kolya[22], B. Koppitz[13], V. Korbel[11], M. Korn[8], P. Kostka[33], S.K. Kotelnikov[24], M.W. Krasny[6,28], H. Krehbiel[11], F. Krivan[17], D. Krücker[2], U. Krüger[11], M. Kubantsev[23], J.P. Kubenka[25], T. Külper[11], H. Küster[2], M. Kuhlen[25], T. Kurča[17], J. Kurzhöfer[8], B. Kuznik[32], F. Lamarche[27], R. Lander[7], M.P.J. Landon[20], W. Lange[33], R. Langkau[12], P. Lanius[25], J.F. Laporte[9], H. Laskus[25], A. Lebedev[24], M. Lemler[6,11], U. Lenhardt[8], A. Leuschner[11], C. Leverenz[11], S. Levonian[11,24], D. Lewin[11], Ch. Ley[2], A. Lindner[8], G. Lindström[12], F. Linsel[11], J. Lipinski[13], P. Loch[11], A.B. Lodge[5], H. Lohmander[21], G.C. Lopez[20], D. Lüers[25,†], B. Lundberg[21], K. Maeshima[7], N. Magnussen[32], E. Malinovski[24], S. Mani[7], P. Marage[4], J. Marks[10], R. Marshall[22], J. Martens[32], F. Martin[28], G. Martin[26], R. Martin[19], H.-U. Martyn[1], J. Martyniak[6], V. Masbender[11], S. Masson[2], A. Mavroidis[20], S.J. Maxfield[19], S.J. McMahon[19],

A. Mehta[22], K. Meier[15], J. Meissner[33], D. Mercer[22], T. Merz[11], C.A. Meyer[35], H. Meyer[32], J. Meyer[11], S. Mikocki[6,26], J.L. Mills[5], V. Milone[31], E. Monnier[28], B. Montés[27], F. Moreau[27], J. Moreels[4], J.V. Morris[5], J.M. Morton[19], K. Müller[35], P. Murín[17], S.A. Murray[22], V. Nagovizin[23], B. Naroska[13], Th. Naumann[33], P. Nayman[28], A. Nepeipivo[23], D. Newton[18], D. Neyret[28], H.K. Nguyen[28], F. Niebergall[13], C. Niebuhr[11], R. Nisius[1], T. Novak[29], H. Novakova[29], G. Nowak[6], G.W. Noyes[5], M. Nyberg[21], H. Oberlack[25], U. Obrock[8], J.E. Olsson[11], J. Olszowska[6,11], S. Orenstein[27], F. Ould-Saada[13], P. Pailler[9], J.-Y. Parey[27], C. Pascaud[26], G.D. Patel[19], E. Peppel[11], P. Perrodo[27], A. Perus[26], S. Peters[25], J.-P. Pharabod[27], H.T. Phillips[3], J.P. Phillips[22], Ch. Pichler[12], W. Pimpl[25], D. Pitzl[34], S. Prell[11], R. Prosi[11], H. Quehl[11], G. Rädel[11], F. Raupach[1], K. Rauschnabel[8], A. Reboux[26], P. Reimer[29], G. Reinmuth[26], P. Ribarics[25], V. Riech[12], J. Riedlberger[34], H. Riege[13], S. Riess[13], M. Rietz[2], S.M. Robertson[3], P. Robmann[36], R. Roosen[4], A. Rostovtsev[23], C. Royon[9], A. Rudge[7], M. Rudowicz[25], M. Ruffer[12], S. Rusakov[24], V. Rusinov[23], K. Rybicki[6], N. Sahlmann[2], E. Sanchez[25], D.P.C. Sankey[5], M. Savitsky[11], P. Schacht[25], P. Schleper[14], W. von Schlippe[20], C. Schmidt[11], D. Schmidt[32], W. Schmitz[2], H. Schmücker[25], V. Schröder[11], J. Schütt[13], M. Schulz[11], A. Schwind[33], W. Scobel[12], U. Seehausen[13], R. Sell[11], M. Seman[17], A. Semenov[23], V. Shekelyan[23], I. Sheviakov[24], H. Shooshtari[31], L.N. Shtarkov[24], G. Siegmon[16], U. Siewert[16], Y. Sirois[27], A. Sirous[11], I.O. Skillicorn[10], P. Skvaril[29], P. Smirnov[24], J.R. Smith[7], L. Smolik[11], D. Sole[5], Y. Soloviev[24], J. Špalek[17], H. Spitzer[13], R. von Staa[13], J. Staeck[2], P. Staroba[29], J. Stastny[29], M. Steenbock[13], P. Štefan[17], P. Steffen[11], R. Steinberg[2], H. Steiner[28], B. Stella[31], K. Stephens[22], J. Stier[11], J. Stiewe[15], U. Stösslein[33], J. Strachota[11], U. Straumann[35], A. Strowbridge[5], W. Struczinski[2], J.P. Sutton[3], G. Tappern[5], S. Tapprogge[15], R.E. Taylor[36,26], V. Tchernyshov[23], C. Thiebaux[27], K. Thiele[11], G. Thompson[20], R.J. Thompson[22], I. Tichomirov[23], C. Trenkel[16], W. Tribanek[25], P. Truöl[35], M. Turiot[28], J. Turnau[6], J. Tutas[14], L. Urban[26], M. Urban[27], A. Usik[24], S. Valkar[30], A. Valkarova[30], C. Vallée[28], G. Van Beek[4], M. Vanderkelen[4], L. Van Lancker[4], A. Vartapetian[11,37], Y. Vazdik[24], M. Vecko[29], P. Verrecchia[9], R. Vick[13], G. Villet[9], E. Vogel[1], K. Wacker[8], I.W. Walker[18], A. Walther[8], G. Weber[13], D. Wegener[8], A. Wegner[11], P. Weissbach[25], H. P.Wellisch[25], D. White[5], S. Willard[7], M. Winde[33], G.-G. Winter[11], Th. Wolff[34], L.A. Womersley[19], A.E. Wright[22], N. Wulff[11], B.E. Wyborn[5], T.P. Yiou[28], J. Žáček[30], P. Závada[29], C. Zeitnitz[12], H. Ziaeepour[26], M. Zimmer[11], W. Zimmermann[11], F. Zomer[26] and K. Zuber[15]

[1] *I. Physikalisches Institut der RWTH, Aachen, Germany*[a]
[2] *III. Physikalisches Institut der RWTH, Aachen, Germany*[a]
[3] *School of Physics and Space Research, University of Birmingham, Birmingham, UK*[b]
[4] *Inter-University Institute for High Energies ULB-VUB, Brussels, Belgium*[c]
[5] *Rutherford Appleton Laboratory, Chilton, Didcot, UK*[b]
[6] *Institute for Nuclear Physics, Cracow, Poland*[d]
[7] *Physics Department and IIRPA, University of California, Davis, California, USA*[e]
[8] *Institut für Physik, Universität Dortmund, Dortmund, Germany*[a]
[9] *DAPNIA, Centre d'Etudes de Saclay, Gif-sur-Yvette, France*
[10] *Department of Physics and Astronomy, University of Glasgow, Glasgow, UK*[b]
[11] *DESY, Hamburg, Germany*[a]
[12] *I. Institut für Experimentalphysik, Universität Hamburg, Hamburg, Germany*[a]
[13] *II. Institut für Experimentalphysik, Universität Hamburg, Hamburg, Germany*[a]
[14] *Physikalisches Institut, Universität Heidelberg, Heidelberg, Germany*[a]
[15] *Institut für Hochenergiephysik, Universität Heidelberg, Heidelberg, Germany*[a]
[16] *Institut für Reine und Angewandte Kernphysik, Universität Kiel, Kiel, Germany*[a]
[17] *Institute of Experimental Physics, Slovak Academy of Sciences, Košice, Slovak Republik*
[18] *School of Physics and Materials, University of Lancaster, Lancaster, UK*[b]
[19] *Department of Physics, University of Liverpool, Liverpool, UK*[b]
[20] *Queen Mary and Westfield College, London, UK*[b]

[21] *Physics Department, University of Lund, Lund, Sweden*[f]
[22] *Physics Department, University of Manchester, Manchester, UK*[b]
[23] *Institute for Theoretical and Experimental Physics, Moscow, Russia*
[24] *Lebedev Physical Institute, Moscow, Russia*
[25] *Max-Planck-Institut für Physik, München, Germany*[a]
[26] *LAL, Université de Paris-Sud, IN2P3-CNRS, Orsay, France*
[27] *LPNHE, Ecole Polytechnique, IN2P3-CNRS, Palaiseau, France*
[28] *LPNHE, Universités Paris VI and VII, IN2P3-CNRS, Paris, France*
[29] *Institute of Physics, Czech Academy of Sciences, Praha, Czech Republik*
[30] *Nuclear Center, Charles University, Praha, Czech Republik*
[31] *INFN Roma and Dipartimento di Fisica, Universita "La Sapienzia", Roma, Italy*
[32] *Fachbereich Physik, Bergische Universität Gesamthochschule Wuppertal, Wuppertal, Germany*[a]
[33] *DESY, Institut für Hochenergiephysik, Zeuthen, Germany*[a]
[34] *Institut für Mittelenergiephysik, ETH, Zürich, Switzerland*[g]
[35] *Physik-Institut der Universität Zürich, Zürich, Switzerland*[g]
[36] *Stanford Linear Accelerator Center, Stanford California, USA*
[37] *Visitor from Yerevan Phys.Inst., Armenia*
[†] *Deceased*

[a] *Supported by the Bundesministerium für Forschung und Technologie, FRG under contract numbers 6AC17P, 6AC47P, 6DO57I, 6HH37P, 6HH27I, 6HD17I, 6HD27I, 6KI17P, 6MP17I, and 6WT87P*
[b] *Supported by the UK Science and Engineering Research Council*
[c] *Supported by IISN-IIKW, NATO CRG-890478*
[d] *Supported by the Polish State Committee for Scientific Research, grant No. 204209101*
[e] *Supported in part by USDOE grant DE F603 91ER40674*
[f] *Supported by the Swedish Natural Science Research Council*
[g] *Supported by the Swiss National Science Foundation*

Contents

List of Figures

List of Tables

1 Introduction

1.1 The physics case

The H1 detector described in this paper is one of the two detectors built around the interaction regions of the first ever constructed electron-proton storage ring – HERA at the DESY laboratory in Hamburg, Germany. In this accelerator, which was recently successfully commissioned, 30 GeV electrons collide with 820 GeV protons at a center of mass energy of 314 GeV.

Deep inelastic lepton scattering experiments have played a crucial role in understanding the fundamental forces of nature and in providing first ever evidence for the pointlike constituents of the nucleons [1]. Compared to previous fixed target experiments [2], HERA provides an increase by one order of magnitude in resolving power. The values of Q^2 can reach 4×10^4 GeV^2, at least two orders of magnitude more than ever before.

The proton structure functions and hence the valence quark, sea quark and gluon densities within the proton can be measured over a wider kinematical range, not only in Q^2, but also in x, the momentum fraction carried by the struck parton. Over the whole Q^2 range, the strong coupling constant $\alpha_s(Q^2)$ decreases by a factor of two, and it is possible to test quantum chromodynamics in a region where non-perturbative effects become negligible. At moderate Q^2 and low x the transition into the non-perturbative regime occurs, where parton wavefunctions may overlap and shadowing and saturation effects could manifest themselves [3]. In contrast to previous experiments the unique kinematics at HERA makes it easy to observe the hadronic recoil. HERA also makes it possible to study the weak charged current at high momentum transfer.

Momentum distributions for s and c quarks as well as b quarks can be measured via the γ–gluon fusion process. The high cross section for producing charmed quark-antiquark pairs makes HERA a prolific source of $D-$mesons with much cleaner background conditions than obtained with hadron beams and this makes the study of rare and forbidden decays feasible. Photoproduction also benefits from the extension to higher energies and larger transverse momenta, where remnants of the hadronic components of the photon may be directly observable as jets leading to a measurement of the photon structure function.

As well as these previous studies of neutrino, muon and photon interactions the HERA physics program also covers the search for new physics at the Fermi scale of ≈ 300 GeV.

If quarks and electrons are not pointlike, but have structure, it is possible that effects could be observed in the inclusive scattering cross sections and polarisation asymmetries, provided the mass scale does not exceed 5 TeV. The observation of excited leptons or the formation of leptoquarks would also provide evidence for structure. In particular leptoquarks could be easily identified by their decay into leptons and quarks. New gauge bosons with masses up to 0.5 TeV would also lead to modifications of the inclusive cross section at high Q^2. HERA's polarized beams of electrons and positrons should be a particularly useful tool for these studies.

The catalogue of possible reactions given above illustrates the need for a detector to have good identification for leptons (especially electrons), high granularity and resolution for jets and good hermiticity to recognize missing transverse energy. These requirements follow from the fact that the final states will contain several leptons accompanied by quark and gluon jets. The inclusive measurements of neutral and charge current interactions also demand the best possible hadron calorimeter. In addition charmed hadron spectroscopy, charmed quark tagging, electron identification and charged particle reconstruction within jets require a high-resolution, large solid angle tracking system. The efficient use of all these tools must rely on a sophisticated trigger system to overcome the adverse background conditions met at a proton-electron collider.

A detailed account of all aspects of HERA physics can be found in the proceedings of the three workshops held before the experimental program started [4, 5, 6].

1.2 Some design considerations

The differential cross section measurement at an electron-quark collider such as HERA requires the reconstruction of kinematical variables as close as possible to the parton level. The most relevant kinematical quantities in the deep inelastic electron scattering process are the square of the four momentum transfer Q^2, the fraction of the protons momentum carried by the struck quark x (Bjorken scaling variable) and the fractional energy loss of the electron y (measured in the rest frame of the proton). These are given in terms of the energies of the incoming electron E_e, the scattered electron E'_e, the incoming proton E_p, the hadronic recoil jet E_h and the corresponding polar angles θ_e and θ_h (both measured relative to the proton direction $\theta = 0$, positive $z-$direction) as:

$$Q^2 = 4E_eE'_e\cos^2\frac{\theta_e}{2} \qquad x = \frac{Q^2}{4E_eE_py} = \frac{E_eE'_e(1+\cos\theta_e)}{E_p(2E_e - E'_e(1-\cos\theta_e))}$$

$$y \equiv y_e = 1 - \frac{E'_e}{E_e}\sin^2\frac{\theta_e}{2}$$

$$Q^2 = \frac{E_h^2\sin^2\theta_h}{1-y_h} = \frac{(\sum_{h,i}\vec{p}_{t\,h,i})^2}{1-y_h}$$

$$y \equiv y_h = \sum_{h,i}\frac{E_{h,i} - p_{z\,h,i}}{2E_e}$$

Figure 1.1 shows contour plots of fixed θ_e and E'_e in the x, Q^2 plane for $E_e = 30$ GeV and $E_p = 820$ GeV. For the electron alone the influence of finite angle and energy resolution can be easily shown [7] by taking the partial derivatives of the above expressions giving the uncertainties Δ for x and Q^2 to:

$$\frac{\Delta Q^2}{Q^2} = \frac{\Delta E'_e}{E'_e} \qquad \frac{\Delta Q^2}{Q^2} = -\tan\frac{\theta_e}{2}\Delta\theta_e$$

$$\frac{\Delta x}{x} = \frac{1}{y}\frac{\Delta E'_e}{E'_e} \qquad \frac{\Delta x}{x} = \tan\frac{\theta_e}{2}(x\frac{E_p}{E_e} - 1)\Delta\theta_e$$

The resolution in Q^2 is determined by the electron energy resolution except for very small scattering angles, where the angular resolution becomes the dominant term. The latter term only influences the x resolution for large x and small Q^2. At low y the x resolution is quite poor, because of the term y^{-1} in the corresponding derivative. It could be hard to measure x in this region with an electromagnetic sampling calorimeter. These results are illustrated in Figure 1.1 using the actual design values of the H1 detector. Before one can translate such results into a contour plot in the x, Q^2 plane indicating where a reliable structure function measurement is possible (as shown in Figure 1.2), one must consider also the effects of migration and the systematic errors. Migration is the effect where a fraction of events move from one bin in x, Q^2 into a neighbouring bin as a result of measurement errors. This can be dealt with by computing a smeared acceptance factor $A(x, Q^2)$ where the observed number of events in a given bin is corrected to get the true number. It depends on the experimental resolution and also on the cross section and hence the basic Q^{-4} dependence. For the HERA conditions and the H1 detector one finds $0.9 < A(x, Q^2) < 1.1$ holds for essentially the whole region with $y > 0.1$. The systematic errors are of particular importance, as demonstrated by the somewhat controversial history of structure function measurements, where a wrong energy calibration, or instability of the energy calibration has an effect. Since event rates at high Q^2 are quite low, long term stability is clearly required. Systematic shifts of the outgoing electron energy can generate large shifts in the differential cross section because there is an amplification factor roughly proportional to y^{-1}, e. g. for $y \approx 0.1, x < 0.5$ an energy shift of 1 % results in 10 % cross section change. Since

angles are measured both by the calorimeter and the tracker, alignment errors influencing angle measurements are less important.

On the hadron side, which we will not discuss here in detail, the above formulas implicitly make use of the Jacquet–Blondel method [8]. It is possible to measure x and Q^2 by using only the outgoing hadronic flow, without even using any jet identification or hypothesis on the proton structure. Furthermore, for HERA kinematics y and Q^2 are more suitably expressed in terms of laboratory variables using the energy-momentum balance between the leptonic and the hadronic system (as done above) and then deducing x. Because hadrons emitted in the forward direction contribute little to y_h or Q^2, the unavoidable dead areas along the beam pipe have only a minor influence. It is the total hadron flow, that enters in the above expressions and so no assumption about the internal structure of the proton needs to be made either. Reconstruction errors depend on the size of the beam hole, the errors on the angles and the energies of the outgoing hadrons. Use of the hadron information alone or in combination with the electron information, e. g. by using θ_e and θ_h without any energy information as in the so-called double angle method [9], extends the measurable regions to considerably lower values of y as indicated in Figure 1.2.

To give an example from low Q^2 photoproduction and to illustrate the need for high quality tracking, we discuss briefly $D^{*\pm}$ tagging of charmed events [10]. The tagging exploits the fact, that in the decay chain $D^{*+} \to D^0\pi^+$ with e. g. $D^0 \to K^-\pi^+$ the π^+ from D^{*+} decay is nearly at rest in the D^* center of mass system (the mass excess is only 6 MeV). Hence the K^- and π^+ candidate tracks with an invariant mass M_D^{in*} near $M(D^0)$ can be combined with a usually low momentum π^+ candidate to form a D^* candidate. Due to the special kinematic conditions one achieves a higher mass resolution in the variable

$$\Delta M = M_{D^*}^{in*}((K^-\pi^+)\pi^+) - M_D^{in*}(K^-\pi^+)$$

than in the mass $M_{D^*}^{in*}$ itself. This is illustrated in Figure 1.3, where the expected signal is superimposed on a combinatorial background from light quark photoproduction. With the tracking system of H1 one actually obtains a mass resolution of 20 MeV at the D^0 mass. Since the D meson momentum is sufficiently well correlated with the charmed quark produced in γ gluon fusion, the gluon momentum can be reconstructed knowing y_h and the gluon density within the proton be measured. If forbidden decays such as $D^0 \to \mu^+\mu^-$ or e^+e^- are to be studied it is important to have good muon identification, and good electron identification at momenta near 1 GeV/c, because the D meson spectrum peaks at rather low energies in particular in the midrapidity region, where these low multiplicity events can be reconstructed.

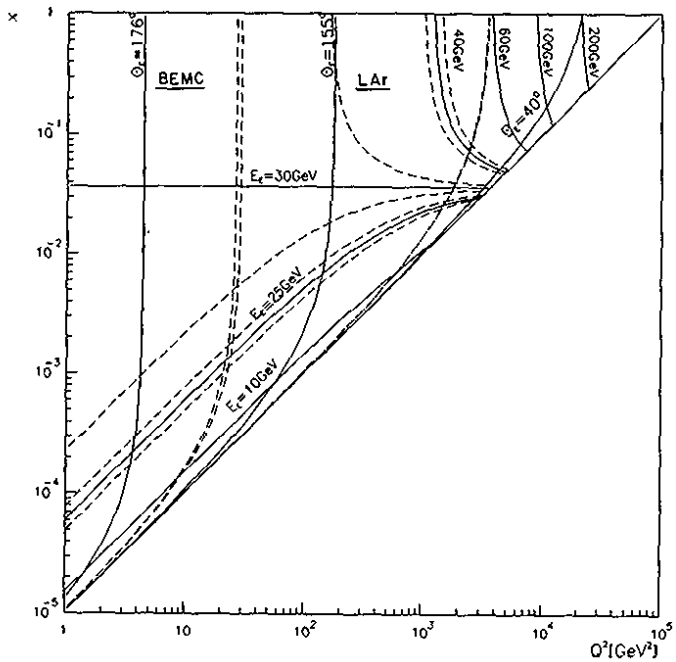

Figure 1.1: Contour plots of fixed θ_e and E'_e in the x, Q^2 plane for $E_e = 30$ GeV and $E_p = 820$ GeV. The dashed lines bracketing the isoenergy lines at $E'_e = 30$ and $E'_e = 25$ GeV show the energy resolution of the backward electromagnetic calorimeter (BEMC, $151° < \theta_e < 177°$) at these energies, the dashed lines bracketing the isoenergy line at $E'_e = 40$ GeV the resolution of the liquid argon calorimeter (LAr, $4° < \theta_e < 153°$). Similarly the dashed isoangle lines indicate the angular resolution at $\theta_e = 165°$ and $\theta_e = 90°$, respectively.

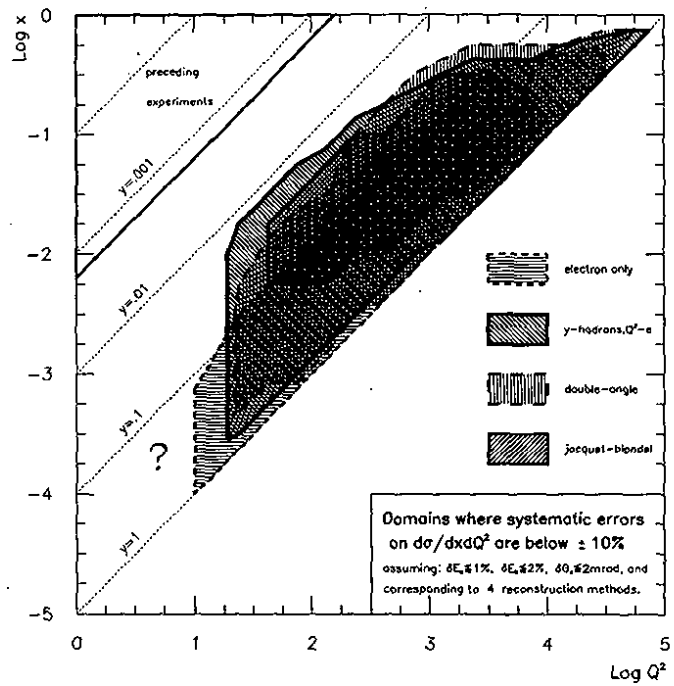

Figure 1.2: Domains in the x, Q^2 plane, where the systematic errors on $d^2\sigma/(dxdQ^2)$ are below 10%. The dotted lines correspond to constant y. The different shadings indicate the method of kinematical reconstruction used (from reference [11]). The area in the upper left corner corresponds to the range accessible to previous experiments.

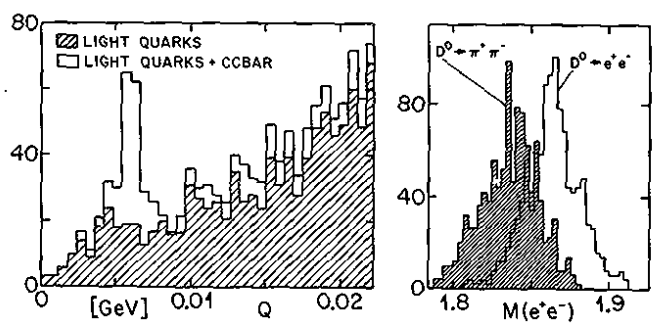

Figure 1.3: Left: D^* tagging signal in the distribution of mass excess $\Delta M \equiv Q$ (see text for definition) for $c\bar{c}$ events produced in γg fusion superimposed on combinatorial background from light quark production. Right: D^0 mass resolution for the decay into e^+e^- (similar for $K^-\pi^+$, $\mu^+\mu^-$ and $\pi^-\pi^+$), the shaded histogram gives the result if the e mass is assumed for the $\pi^+\pi^-$ channel. Results from a reconstruction of Monte Carlo simulated data.

2 General description of the H1-detector

In order to carry out the physics program which was outlined in the previous section prime attention has to be given to the clean identification of electrons and to their energy measurement. To facilitate this we opted for a large coil, which contains the electromagnetic and the hadronic calorimeter. With this choice the amount of dead material in front of the calorimeter and its total weight are minimized. Choosing a liquid Argon calorimeter we further benefit from the proven stability of this technique, the ease of its calibration and the fine granularity, which allows to separate electrons from pions to a high degree. Lastly the homogeneity of the response and overall hermiticity are helpful for energy flow measurements as well as neutrino detection for charged current events. Supplementing the calorimeter by high resolution tracking on the inside and an instrumented iron yoke on the outside is crucial for the identification of high-density particle jets characterizing the hadronic final states in deep inelastic scattering events as well as for muon detection. Identifying muons is particularly important for some exotic channels and for photoproduced low multiplicity heavy flavour events. In these design aspects the H1-detector does not differ strongly from the detectors at e^+e^- colliders, or $p\bar{p}$ colliders built in the past. Different at HERA is however the imbalance in the energy of the two colliding beams, which requires an asymmetric detector. Different also is the microstructure of the two beams, which leads to short intervals (≈ 100 ns) between two subsequent bunch crossings, and also the high background level, as proton induced background arises from beam line vacuum conditions, usually met with electron accelerators and which are worse than for pure proton accelerators.

Since the centre of mass for HERA collisions is boosted along the proton direction with $\gamma_{cm} = 2.86$ the H1-detector is considerably more massive and higher instrumented in this direction. This is apparent from Figure 2.1, which shows a perspective view and cut along the beam axis. The cut perpendicular to the axis in Figure 2.2 shows that the different shells of the H1-detector are at least symmetric in azimuth. In the following we often refer to the direction of the exiting electron (incoming proton) as the backward direction (negative z–values relative to the center of the interaction region and $\theta = \pi$), and vice versa to that of the exiting proton as the forward direction (positive z and $\theta = 0$).

Starting the description from the center of the interaction region the detector consists of a central and a forward tracking system, each containing different layers of drift chambers and trigger proportional chambers. The liquid argon cryostat surrounds the trackers. It houses the lead absorber plates and readout gaps of the electromagnetic section, which are followed by the steel plates of the hadronic section with their readout gaps. A superconducting and cylindrical coil with a diameter of 6 m and a length of 5.75 m provides the analysing field of 1.15 T. The iron return yoke of the magnet is laminated and filled with limited streamer tubes. The small fraction of hadronic energy leaking out of the back of the calorimeter is registered here and muon tracks are found. Muon identification further benefits from additional chambers inside and outside of the iron. The very stiff muon tracks in forward direction are analysed in a supplementary toroidal magnet sandwiched between drift chambers. The remaining holes in the liquid argon calorimeter are closed with warm calorimeters, a Si-Cu plug at very forward angles, a Pb-scintillator calorimeter backed by a tail catcher (part of the muon system) in backward direction and lastly an electron tagger at $z = -33$ m from the interaction point not shown in Figure 2.1. The tagger marks the energy of an electron with very small scattering angle inducing a photoproduction event and, taken in coincidence with a corresponding photon detector at $z = -103$ m upstream from the interaction point, monitors the luminosity by the bremsstrahlung process. Two scintillator walls in backward direction are installed to recognize background produced by the proton beam upstream of the H1-detector. A survey of detector parameters is given in Table 2.1.

Calorimetry		
Main calorimeter: liquid Ar	Electromagnetic part	Hadronic part
Granularity	10 to 100 cm^2	50 to 2000 cm^2
Depth (number of channels)	20 to 30 X_0 (30784)	4.7 to 7 λ_{abs} (13568)
Resolution $\sigma(E_{e,h})/E_{e,h}$	$12\%/\sqrt{E_e} \oplus 1\%$	$\approx 50\%/\sqrt{E_h} \oplus 2\%$
LAr purity (stability of el. calibration)	$\leq 0.2\%$ over one year (one month)	
Noise per channel	10 to 30 MeV	
Angular coverage – dead channels	$4° < \theta < 153°$	$< 0.3\%$
Backward calorimeter: Pb–scintillator		
Angular coverage – granularity	$151° < \theta < 177°$	16×16 cm^2
Depth – resolution $\sigma(E_e)/E_e$	22.5 X_0 (1 λ_{abs})	$10\%/\sqrt{E_e} \oplus 2$ [1]%
Tail catcher: iron–streamer tubes		
Angular coverage	$4° < \theta < 177°$	
Depth – resolution $\sigma(E_h)/E_h$	4.5 λ_{abs}	$100\%/\sqrt{E_h}$
Plug calorimeter: Cu–Si		
Angular coverage – granularity	$0.7° < \theta < 3.3°$	5×5 cm^2
Depth – resolution $\sigma(E_h)/E_h$	4.25 λ (44.6 X_0)	$\approx 150\%/\sqrt{E_h}$
Electron tagger: Tl(Cl/Br)		
Angular coverage – granularity	$\theta > 179.7°$	2.2×2.2 cm^2
Depth – resolution $\sigma(E_e)/E_e$	21 X_0	$\approx 10\%/\sqrt{E_e} \oplus 1\%$
Tracking		
Coil: radius – field	3 m – $B = 1.15$ T, $\Delta B/B \leq 2\%$	
Central tracking		
Angular – radial coverage	$25° < \theta < 155°$	$150 < r < 850$ mm
Jet chamber: spatial resolution	$\sigma_{r\phi} = 170\,\mu$m	$\sigma_z = 22.0$ mm
z-chambers: spatial resolution	$\sigma_{r\phi} = 25$ and 58 mm	$\sigma_z \approx 350\,\mu$m
Momentum – dE/dx resolution	$\sigma_p/p^2 < 0.01$ [0.003] GeV^{-1}	$\sigma(dE)/dE = 10$ [6]%
Forward/backward tracking		
Angular – radial coverage (f)	$7° < \theta < 25°$	$120 < r < 800$ mm
Spatial resolution (f)	$\sigma_{r\phi} = 170\,\mu$m ($\sigma_r = 29$ mm)	$\sigma_{x,y} = 210\,\mu$m
Angular coverage – resolution (b)	$155° < \theta < 175°$	$\sigma_{x,y} = 1$ mm
Trigger proportional chambers		
Angular coverage – channels	$7° < \theta < 175°$	3936
Muon detection		
Instrumented iron		
Angular coverage – total area	$4° < \theta < 171°$	4000 m^2
Number of channels	wires: 103700, strips: 28700, pads: 4000	
Spatial resolution	$\sigma_{wire} = 3 - 4$ mm	$\sigma_{strip} = 10 - 15$ mm
Angular – momentum resolution barrel	$\sigma_\theta(\sigma_\phi) = 15(10)$ mr	$[\sigma_p/p \approx 0.35]$
Forward muon toroid		
Angular coverage – resolution	$3° < \theta < 17°$	$[0.25 < \sigma_p/p < 0.32]$
Overall size (x, y, z) – weight	$12 \times 15 \times 10$ m^3	2800 t

Table 2.1: Summary of H1-detector parameters.
The actual status after the first running phase of HERA in 1992 has been given. Alternatively design and test beam figures have been given in brackets []. Energies are given in GeV.

2.1 Electron detection

Neutral current events at HERA will provide a large fraction of the data, in a wide range of (x,Q^2). The inclusive measurement of these events can be based either on the electron data or on the hadronic energy flow.

The detection of electrons is done in the backward electromagnetic calorimeter (BEMC) for $Q^2 \leq 100$ GeV^2 and in the liquid argon calorimeter for larger values of Q^2. In the case of photoproduction events, an electron tagger which is part of the luminosity measuring device, is used.

The BEMC is a conventional electromagnetic lead-scintillator sandwich calorimeter with photodiode readout, providing an energy resolution sampling term of $10\%/\sqrt{E}$. The backward proportional chamber (BPC) located just in front of the BEMC provides the angular measurement of the electron together with track and vertex data given by the central tracker. The presence of a kinematical peak in the energy spectrum of the scattered electron at the electron beam energy allows a precise overall calibration (present uncertainty $\leq \pm$ 2 %)

The liquid argon calorimeter covers the polar angular range $4° \leq \theta \leq 153°$ in a single cryostat. The fine granularity electromagnetic calorimeter with lead absorber plates of total depth of 20 to 30 radiation lengths provides an energy resolution $\sigma/\mathrm{E} \approx 12\ \%/\sqrt{E}$. Electron identification is based on fine transverse and longitudinal shower shape measurement and a cross-check of the absolute energy calibration of the calorimeters is provided by comparing the calorimetric energy measurement of electrons to the corresponding momentum measurement in the central tracking chambers.

2.2 Hadron and jet detection

The fine granularity hadronic calorimeter with stainless steel absorber is located within the same cryostat as the electromagnetic calorimeter and supports the latter. Both calorimeters together provide the energy measurements of hadrons. Its depth ranges between 5 and 7 absorption lengths, depending on the polar angle θ. Events with large energy leaking out of the liquid argon calorimeter are efficiently tagged by the tail catcher consisting of the analog readout of the pads of the limited streamer tube system in the iron instrumentation. Measurements in a test beam show that the expected resolution $\sigma/\mathrm{E} = 50\ \%/\sqrt{E}$ has been achieved, with an energy independent term of 2%. Here too combining the calorimetric information with the momentum information from the central tracking chambers provides a cross-check of the absolute energy calibration. Further intercalibration between calorimeters is possible by checking the balance in transverse momentum between the calorimetric energy of scattered electrons in the BEMC or the liquid argon calorimeter and the hadronic energy measurement for low or high Q^2 events. Intercalibration of the hadron energy flow and the electron energy inclusive measurements in NC events is very important for CC scattering where only the jet measurement can be used.

2.3 Muon detection

The dominant source of muons at HERA are semileptonic decays of charm- and bottom mesons, therefore the muon system was designed to identify muons within jets. In the large coil solution the calorimeter serves to absorb the hadronic activity, allows to detect penetrating singly ionizing tracks and the high field provides sufficient bending power for a momentum measurement. The spatial resolution of the chambers was matched to the multiple scattering in the material in front of the instrumented iron.

The necessary resolution of a few mm is reached with a total of sixteen streamer tube layers with a basic cell size of 10 × 10 mm^2, a triple layer each in front and after the iron, a double layer after four iron sheets of 75 mm thickness, and eight single layers in the remaining gaps in between the ten iron sheets. The multiple layers are also equipped with cathode strips for the measurement of the coordinate perpendicular to the wires.

In the barrel part muons with energies below 1.2 GeV do not reach the first layer, muons with energies below 2.0 GeV stop within the iron. In forward direction the effective threshold is 2.5 GeV, but here normally the muon energy is sufficiently large, that the muons traverse usually all 16 layers of chambers. An independent track segment can then be measured which can be linked to extrapolated forward tracker segments. This is of course also possible for the few high momentum muons in the barrel part. The comparison between momentum measurement in the tracker and through the muon system further reduces misidentification probabilities and also allows to discriminate against muons from π and K-decay.

In the central part the muons from heavy flavour decays have typically momenta of a few GeV/c or less, hence usually only a few hits are seen. However a muon range measurement is often possible. Ten of the sixteen layers are equipped with cathode pads (40 × 50 cm^2 in the barrel and 28 × 28 cm^2 in the endcap region), which are used for a measurement of the deposited charge and for crude $z-$ or $x,y-$ information respectively, helpful for identification of muon tracks. These layers are also used to measure the hadronic leakage, i. e. provide the tail catcher feature needed to improve the calorimeter energy resolution.

In the extreme forward direction the central tracker and the chamber system in the flux return iron are not adequate for measuring muon momenta with sufficient accuracy. This is why a toroidal magnet with an average field of 1.6 T was added. The driftchambers are constructed in such a way, that correlated angle and position measurements are possible. This is needed because the hadronic activity from secondary interactions of the target jet is quite high. The spectrometer is useful in the momentum range between 5 and 200 GeV/c. The lower limit is determined by the amount of material traversed, while beyond the upper limit the muon charge can no longer be measured unambiguously.

2.4 HERA beam features

The electron-proton colliding beam facility HERA consists of two independent accelerators designed to store respectively 820 GeV protons and 30 GeV electrons and to collide the two counterrotating beams head on in four interaction points spaced uniformly around its 6.3 km circumference. The main HERA parameters are given in Table 2.2. We have listed the design values and the values actually achieved during the first data taking period in 1992.

Between the last two beam focussing quadrupoles 11.3 m of free space are available for the detector. The beams pass the detector at a height of 5.9 m above floor level ($\approx$ 20 m below ground) at an inclination of 5.88 mr. Presently a 190 mm inner diameter beam pipe is installed, with a wall of 150 μ Al on the inside backed by 2 mm carbon fibre reinforced plastic comprising 1 % radiation length. Details of the beam line are shown in Figure 2.4. The beam pipe is cooled with nitrogen gas, which also circulates on the outside of the central tracker to avoid buildup of larger amounts of inflammable gases leaking from the chambers. Incorporated into the beam pipe are a capacitively coupled proton position monitor [12], synchrotron radiation shielding masks (see below), getter pump connections and a flexible bellow to absorb temperature dependent variations of the beam pipe. For the future upgrade of the tracking near the beam pipe [13, 14] a smaller beam pipe with an inner diameter of 90 mm (80 μm Al backed by 1 mm carbon fibre) will be installed.

While the radial extension of the beams is small (see Table 2.2), the finite time spread of the bunches and the zero degree crossing leads to total length of the interaction zone of $\approx \pm 50$ cm. The zero degree crossing was chosen to reduce $e - p$ beam coupling, which could result in beam blow up. The width of the interaction zone is apparent from Figure 2.5, which shows the projection of central drift chambers tracks onto the beam axis for a background free sample of photoproduction data. Typical vacuum conditions in the beam pipe during the initial running phase lead to a residual gas pressure of $\approx 1 - 2 \times 10^{-9}$ mbar, primarily consisting of atomic hydrogen and carbonmonoxyde. Assuming nitrogen as an average representation of the residual gas and and a reaction cross section for protons at 820 GeV ($\sqrt{s} = 39$ GeV) of ≈ 200 mb [15] one expects one proton nitrogen interaction in 10^4 bunch crossings at design luminosity along the interaction region (1 m) compared to one genuine $e - p$ event every 10^5 bunch crossings. The physics rate is dominated by photoproduction giving a visible event rate of about 200 Hz at design luminosity, the beam gas rate given above corresponds to ≈ 1 kHz. Of course beam gas background is not restricted to the interaction zone proper, but can originate from the whole proton path through the detector. Furthermore beam halo protons hitting apertures contribute, too. Monte Carlo simulations and measurements from the first data taking period indicate roughly a factor 50 higher rate for the latter process than for beam gas events from the interaction zone. These contributions are however more easily removed in the different trigger and filter levels.

The actual tuning of the luminosity optics for the two beams is relying partly on the H1-luminosity system. It makes use of the $ep \rightarrow ep\gamma$ bremsstrahlung process and hence is sensitive to electron interactions with the residual gas. By filling both electron and proton bunch sequences in such a way, that there is always at least one bunch of each type with no partner for a collision (pilot bunches) background subtraction can be made. During the filling phase the trigger scintillators of the time-of-flight wall can be remotely removed from the beam pipe. The integrated rate in these counters provides an efficient means for monitoring the quality of the beam tune. Only when a lower threshold for this rate has been reached the counters are moved back in, and the high voltage on all drift and proportional chambers is raised. Figure 2.6 shows a typical sequence of storage fills. While proton fill lifetimes well exceeding 24 h have been reached, the lifetime of the electron ring fills during the HERA startup phase was limited to about 6 hours.

2.4.1 Synchrotron radiation shielding

The HERA e^- beam is accompanied by a strong flux of synchrotron radiation photons which are produced in the last bending magnet before the interaction point and the interaction quadrupoles. Synchrotron radiation from the arcs is absorbed before the H1-detector and need not be considered.

At a beam energy of 30 GeV and a stored current of 60 mA we expect a flux of 10^{18} photons per second with an energy above 5 keV into the interaction region. This flux represents a radiated power of 3.6 kW. The critical energy is 42.4 keV. In order to protect the detector elements a system of masks inside the beam pipe is installed.

The design criteria for the synchrotron radiation absorbers were such that only photons which have undergone at least two scatters can reach the central detector region. In order to reduce the photon flux the aperture of the collimators should be as small as possible. The width is thus determined by the requirement for sufficient aperture at injection. Masks which are hit by synchrotron radiation are sources of secondary photons. Therefore the albedo of all surfaces has been reduced by coating the tungsten absorbers with 0.5 mm silver and 0.2 mm copper. For 100 keV photons the albedo is reduced from 10% for pure tungsten to 1% with the appropriate coating.

	Design		Autumn 1992		unit
	p–ring	e–ring	p–ring	e–ring	
Energy	820	30	820	26.7	GeV
Luminosity	1.5×10^{31}		3.0×10^{29}		$cm^{-2}s^{-1}$
Integrated luminosity	10^5		32		nb^{-1}/y
Interaction points	4		2		
Magnetic field	4.68	0.165	4.68	0.149	T
Number of particles	210	80	2.6	3.7	10^{11}
Current per bunch	760	290	200	280	μA
Number of bunches	210	210	10	10	
Bunch separation	96	96	96	96	ns
Injection energy	40	14	40	12	GeV
Filling time	20	15	120	30	min
σ_x/σ_y at interaction point	0.29/0.07	0.26/0.02	0.36/0.10	0.30/0.07	mm
σ_z at interaction point	110	8	≈ 200	≈ 10	mm
Energy loss per turn	6.2×10^{-6}	127			MeV
RF-frequency	52.03/208.1	499.8	52.03	499.8	MHz

Table 2.2: Summary of HERA parameters (taken from references [16, 17]).

The geometry of the absorbers is shown in Figure 2.7. The collimators C_1, C_2 and C_3 are hit by direct synchrotron light and have to stand a radiated power of about 1 kW each. These collimators are movable and water cooled. The synchrotron radiation, missing C_3, is passed through the detector area and hits an absorber 24 m behind the interaction point. The collimators C_4, and C_5 have a fixed horizontal aperture of +30 mm -25 mm and $\pm$ 50 mm, respectively. They protect the detector elements against secondary photons originating from edge scattering at the collimators C_1 - C_3 and backscattered photons from the absorber at 24 m. The collimator C_6 is movable and provides an additional shield against photons from 24 m downstream. The aperture can be set between 65 mm and 25 mm with respect to the beam.

The present arrangement of synchrotron radiation masks cuts down the number of photons which enter the central part of the detctor to a level of 10^6 photons per second with an energy above 20 keV. Thus at nominal beam conditions we expect about 10^{-1} spurious synchrotron hits in the central tracking chamber per bunch crossing. The observations during the first runs in 1992 are consistent with the above estimates. Due to the low currents and the reduced electron energy of 27 GeV we did not observe synchrotron radiation hits in the tracking chambers.

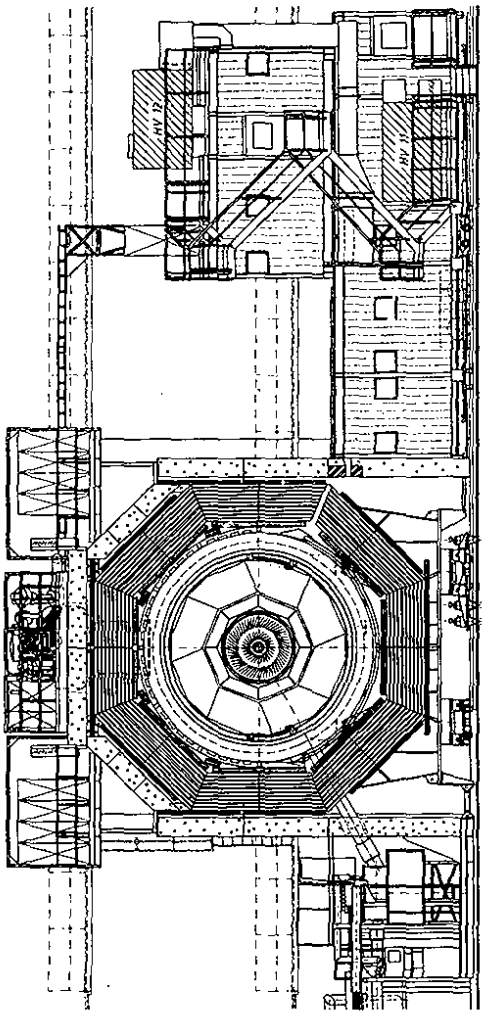

Figure 2.2: Transverse cut through the H1-detector at the center of the interaction region.

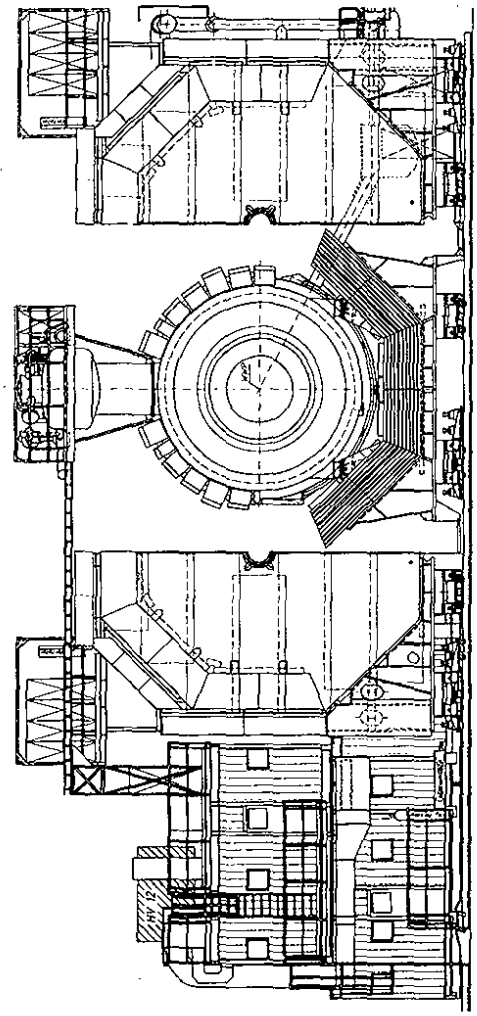

Figure 2.3: Front view of the H1-detector with the southern and the northern shells of the iron yoke opened.

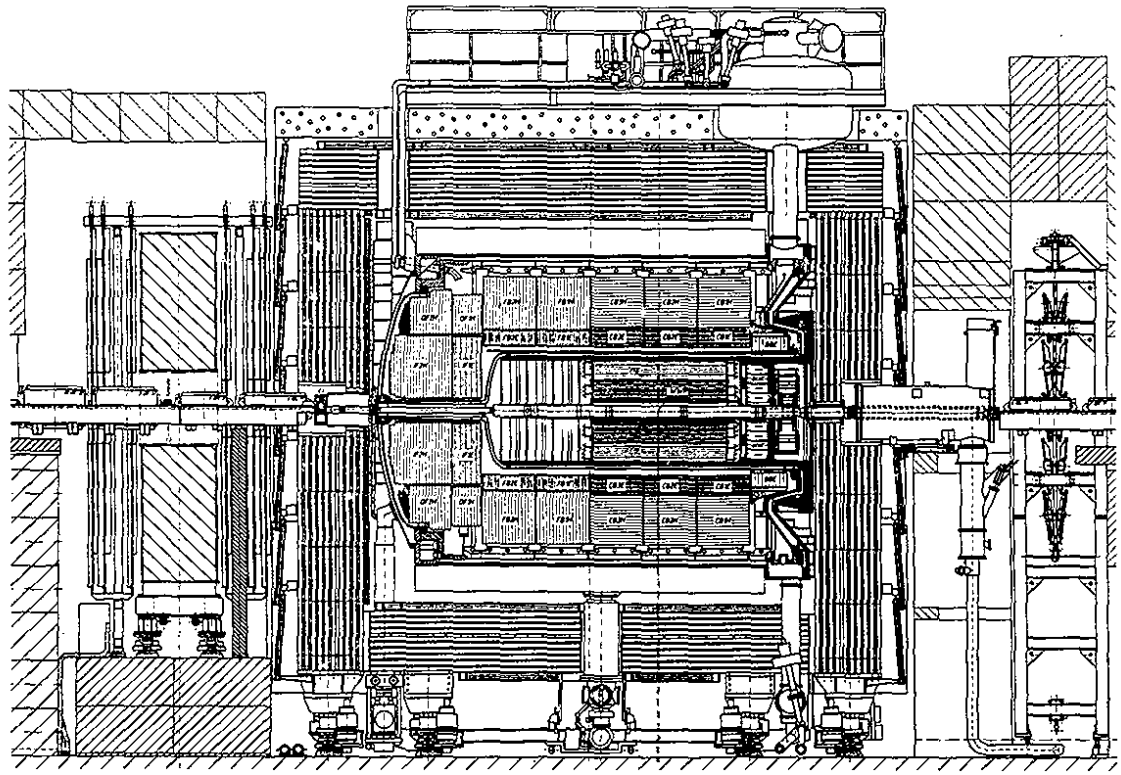

Figure 2.1: Longitudinal cut through the H1-detector along the beam line.

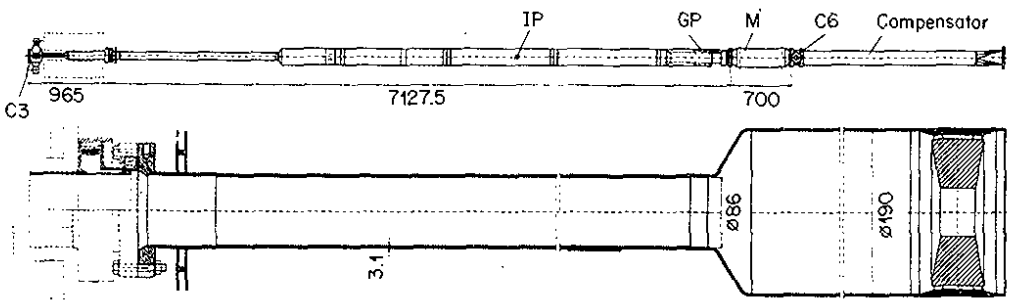

Figure 2.4: Cross section of the beam pipe in the H1-detector. IP: interaction point, GP: getter pump, M: beam profile monitor, C6: synchrotron radiation mask (see also Figure 2.7). The lower part shows an enlarged view of the forward part with the flexible bellow connections and synchrotron radiation mask C4 (right).

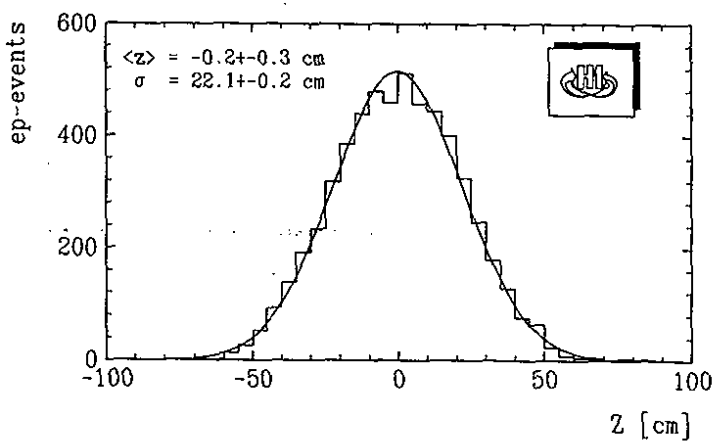

Figure 2.5: Width of the interaction zone in beam direction extracted from the projection of central drift chamber tracks onto the beam axis after cuts for rejection of beam gas background.

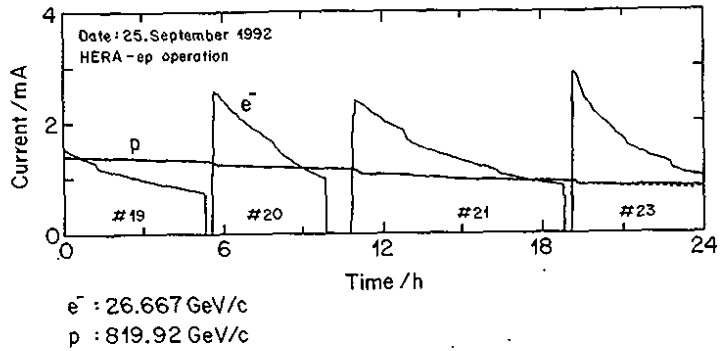

Figure 2.6: Sequence of electron ring fills with one proton fill in September 1992. The total integrated luminosity during that day was 3 nb^{-1}.

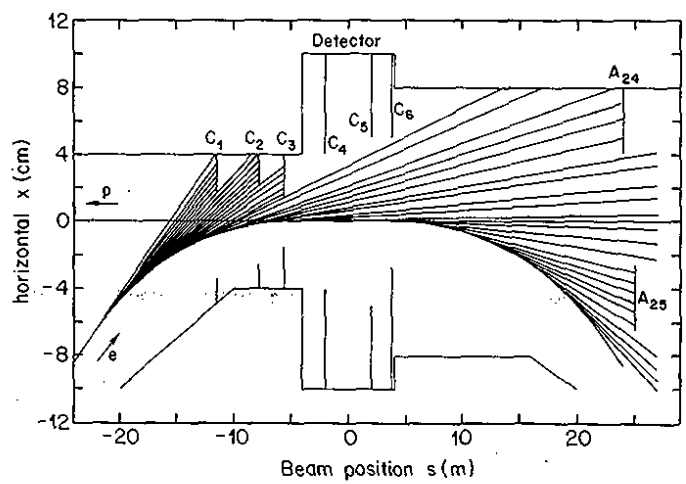

Figure 2.7: Arrangement of synchrotron masks shielding the H1-detector from direct synchrotron radiation (from reference [18]).

3 Magnet

The magnet consists of a superconducting solenoid and an iron yoke producing an almost uniform field parallel to the HERA beams. The field has only a few percent variation over the region of the tracking chambers. Within that region, 3600 mm in length and 1600 mm in diameter, the field has an average value 1.15 T.

3.1 The iron yoke

When closed the iron yoke consists of an octagonal barrel with axis that of the HERA beams and also that of the solenoid which it encloses, plus flat end caps. In overall size it is similar to the ALEPH [19] and DELPHI [20] magnets at CERN but the requirements on uniformity of field are less stringent than for those experiments, which have chambers very sensitive to radial field components. Thus reentrant end caps are not needed for the H1 magnet and a much simpler opening mechanism is possible.

The iron yoke of the H1 magnet has three parts, the northern and southern shells and the base structure (see Figure 2.3). The base structure consists of the three lower faces of the octagonal barrel, and supports the superconducting coil. The northern and southern shells are mirror images of each other, symmetric about a vertical plane through the beam. Together they form all the rest of the octagonal barrel and the two end caps. Thus each shell is a rigid structure consisting of half of the western endcap and half of the eastern endcap, connected by 2.5 of the 8 faces of the octagonal barrel. Each of the three parts of the iron yoke moves independently on rails.

The iron of the octagonal barrel is made up of 10 laminations each 75 mm thick, separated by air gaps of 25 mm except for one air gap of 50 mm. The iron of the end caps is made up of 10 laminations each of 75 mm, separated by air gaps of 35 mm except for one air gap of 50 mm.

3.2 The superconducting coil

The main solenoid consists of four separate coaxial coils powered in series. This set of four coils is symmetrically placed about the median plane, as shown in Figure 3.1. The two coils nearest to the median plane are single layers, each of 201 turns, extending from 400 mm to 1420 mm from the median plane. The two coils farthest from the median plane are double layers, each of 418 turns, extending from 1520 mm to 2580 mm from the median plane. All four of these windings are housed in one cryogenic envelope with an overall length 5750 mm, inner diameter 5180 mm, outer diameter 6080 mm, and total weight 74.5 tons. The parameters of this superconducting coil assembly are given in Table 3.1.

The superconductor, bonded into its aluminium substrate, was manufactured in industry [21]. The coils were fabricated from this conductor in modular form of length up to 1.5 m for both double and single layers on a custom built machine using the inside winding technique [22].

3.3 The magnetic field measurements

The general similarity in size and shape of the H1 magnetic volume to those of the Aleph and Delphi magnets [19, 20] made it possible to use the same apparatus for the field measurements, by kind permission of CERN.

Seven NMR probes and 96 Hall plates were carried on the two measuring arms of the apparatus. These arms were 180° apart in azimuthal angle ϕ. The NMR probes and Hall plates were

at accurately known positions along the arms. The arms and supporting collar could move in axial position z by sliding along a large rigid beam which extended from one end of the magnet to the other. This large beam was mounted in bearings at each end, and could rotate in phi through 360° so that any given probe could sweep over the whole azimuth.

The Hall plates were mounted in groups of six on the surfaces of accurately machined rectangular boxes, two to measure the axial field component B_z, two to measure the radial field component B_r, and two to measure any azimuthal field component B_ϕ. All of the Hall plates were calibrated at CERN. Those measuring B_z could be checked against the readings of the NMR probes and were found to agree to an accuracy of 0.1%. The measuring arms were temperature controlled and protected by styrofoam covers from thermal changes.

Magnetic measurements were made with this apparatus throughout a cylindrical volume of radius 1775 mm and length 5200 mm. The volume occupied by the tracking chambers for H1, where the field needs to be known to approximately 0.3% accuracy, is the much smaller cylindrical volume of radius 800 mm and length 3600 mm (from 2200 mm on one side of the median plane to 1400 mm on the other side). Over this tracking volume the value of the axial component B_z is shown in Figure 3.2 as a function of radius at r = 0, 200, 400, 600, 800 mm and as a function of axial position z from the magnet median plane. The average value over this volume is 1.15 T at a magnet current of 5514 A, and the maximum departure from this value is 4.5% at the extreme backward end of the central tracker.

Detailed magnetic measurements were made at currents of 4500 A and 5514 A. Measurements at a restricted set of space points were made at currents of 1000, 2000, 3000, 4000, 4500, 5514 A in order to study the effects of iron saturation on the internal field. It was found that from zero current to 4500 A the field on the median plane at radius 550 mm was 0.20866 T per kA, but at 5514 A it fell to 0.20794 T per kA at the same space point, a fall of 3.5 parts per thousand.

The longitudinal field integral $\int B_z dz$ for the H1 magnet was evaluated to be 8.32 Tm at the operational current of 5514 A. This longitudinal field integral is cancelled by the external compensating coil (see below).

3.4 The forward muon toroid

The toroidal magnet for the forward muon detector consists of 8 solid iron modules built into two mobile halftoroids for access reasons. The inner radius of the toroid is 0.65 m, the outer radius 2.90 m, and the length between the flat ends 1.20 m. The weight is 250 tons.

There are 12 coils wound on the toroid, each consisting of 15 turns of watercooled copper, carrying a current of 150 A. The copper windings are square in cross section with side 11.5 mm, with a 8.5 mm diameter hole for water cooling.

The magnetic field within the iron toroid has been measured by the change in flux, as the magnet is turned on or off, through loops of wire threaded through small holes in the iron. The field varies with radius, from 1.75 T at radius 0.65 m to 1.5 T at radius 2.90 m.

3.5 Compensating magnet

The compensating coil is located at the proton entrance side of the H1-magnet with its center at 4.4 m from the interaction point. Its purpose is to provide a longitudinal field integral $\int B_z dz$ equal and opposite to that of the main H1 magnet. This is required if longitudinal polarisation of the electron beam is to be achieved, avoids horizintal-vertical coupling and minimizes closed orbit shifts in HERA due to any slight misalignment of the H1 magnet [23]. Its downstream

end extend into the endcap of the main magnet. This 1.8 m long superconducting coil was manufactured in industry [24] from NbTi cable embedded into a copper matrix insulated by glasfiber epoxy. The magnetic field is shielded by an iron yoke, with both iron and coil mounted inside a pressure vessel, which is cooled by liquid He from the main DESY transfer line. The relevant parameters are also given in Table 3.1. The field integral and the magnetic field axis have been determined by means of a rotable Hall probe described in detail in ref. [25].

Solenoid parameters	Main H1-magnet	Compensating magnet
Superconductor		
Dimensions	26 × 4.5 mm²	3.1 × 2.1 mm²
Type	Rutherford cable	ABB-Zürich cable
Material	Nb-Ti (44%) Cu (56 %)	inner/outer layers
	on high purity Al (RRR 500)	Nb(47%)-Ti(53%) [0.88/0.55]
	substrate bonded by extrusion	Cu [4.35/4.67] [mm²]
Critical current (B, T)	11000 A (3 T, 4.5 K)	2023/1264 A (5 T, 4.2 K)
Maximum field	2.4 T	4.85/3.2 T
Length (weight)	22.5 km (7.7 t)	4.5/4.5 km (0.49 t)
Winding geometry		
Length	central/peripheral	$\|z\| < 902$ mm
	$400 < \|z\| < 1420$	
	$/1520 < \|z\| < 2580$ mm	
# of coils	2 / 2	1
# of layers (turns)	1 (201)/2 (209)	14 (534)
# of turns: total	1238	7576
Inner radius	2750/2750 mm	320 mm
Outer radius	2800/2850 mm	429 mm
Cooling	support cylinder	cryostat
Type	forced flow	bath cooled
Inner diameter	5600/5700 mm	308 mm
Outer diameter	5670/5830 mm	772 mm
Length/material	5160 mm/AL 5083	2050 mm/stainless steel
Vacuum chamber		
Inner/outer diameter	5200/6080 mm	238/870 mm
Length/thickness	5750/10 mm	2270/6 mm
Material	stainless steel	stainless steel
Radiation shield (80 K)		
Inner/outer diameter	5330/5950 mm	268/800 mm
Length/thickness/material	5370 mm/5 mm/Al	2135 mm/1.2 mm/Cu
Cold yoke length/material		1982 mm/ ASTM A105 steel
Inner/outer diameter		444/696 mm
Overall weight (rad. length)	74.5 t (1.2 X_0)	6.8 t
Operational performance		
Power supply voltage	15 V	7 V
Current nominal (max.)	5514 (6000)	870 (1000) A
Run up (down) time	60 (120) min	40 (40) min
Cooling time	168 h	168 h
He flow (4.5/80 K)	4/3 gs^{-1}	1.3/1.3 gs^{-1}
Cryogenic losses (4.5/80 K)	40/420 W	12.2/34.6 W
Total stored energy	120 MJ	1.87 MJ
Fast discharge time constant	60 s	40 ms
Fast discharge voltage	750 V	860 V
Inductance	7.84 H	2.8 H
Quench detection level		0.15 V (400 mm conductor)
Field on axis (integral)	1.15 T (8.32 Tm)	4.83 T (8.74 Tm)

Table 3.1: Parameters of the superconducting magnets.

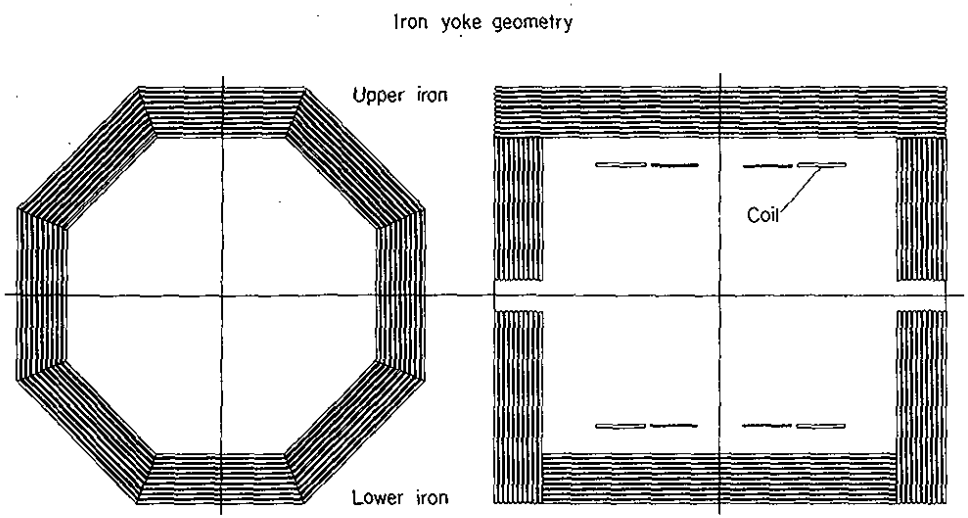

Figure 3.1: Iron yoke geometry.

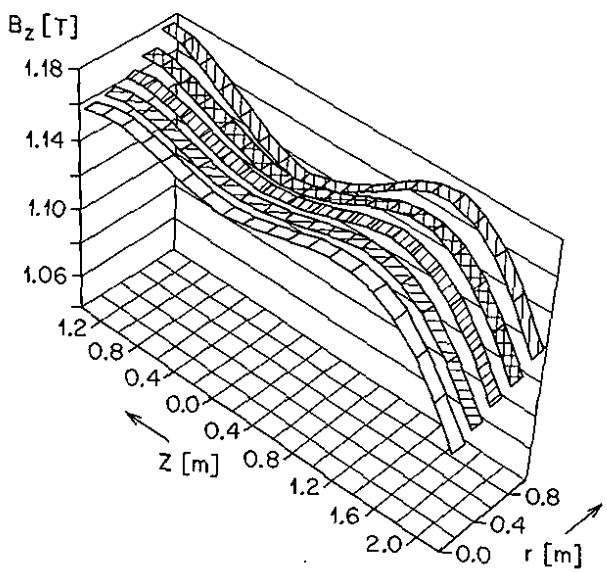

Figure 3.2: Main coil field map over the tracking volume.

4 Tracking

The tracking system of H1 provides simultaneous track triggering, reconstruction and particle identification for the event topology particular to HERA electron proton collisions. It has been designed to reconstruct jets with high particle densities and to measure the momentum and angles of scattered isolated charged particles to a precision of $\sigma_p/p^2 \approx 3 \times 10^{-3}$ GeV^{-1} and $\sigma_\theta \approx 1$ mr.

Because of the asymmetry between the electron and proton beam energies many charged particles are produced at small angles θ to the incident proton (forward) direction. To maintain good efficiency for triggering and reconstruction over the whole solid angle, we divide the tracking system between the central and forward regions (see Figure 4.1). Two mechanically distinct tracking detectors have been constructed, the central (CTD) and forward (FTD) trackers, respectively. Each is optimised for tracking and triggering in its angular region.

Track reconstruction in the central region (see Figure 4.2) is based on two large concentric drift chambers, CJC1 and CJC2. The chambers have wires strung parallel to the beam axes (z-direction) with the drift cells inclined with respect to the radial direction. We have measured a space point resolution of 170 μm in the drift coordinate ($r\phi$ plane) and can, by comparing signals read out at both wire ends, achieve a resolution of one percent of the wire length in z. From the signals recorded in these chambers the transverse track momentum is determined and in addition the specific energy loss dE/dx is used to improve particle identification.

Two thin drift chambers, the central inner (CIZ) and central outer (COZ) z-chambers complement the measurement of charged track momenta in the central chambers. The CIZ chamber fits inside CJC1, and the COZ chamber fits in between CJC1 and CJC2. These two chambers deliver track elements with typically 300 μm resolution in z and 1 to 2% of 2π in ϕ. This requires a drift direction parallel to, and sense wires perpendicular to the beam axis.

Triggering over the full solid angle is based on multiwire proportional chambers with pad readout in the central and forward region and wire readout in the backward direction. They provide a fast first level (L1) trigger decision which can be used to distinguish between successive beam crossings. In addition, in the central and forward region, combinations of pads hit in the central inner proportional chamber (CIP), the central outer proportional chamber (COP) and the forward proportional chambers (FWPC) are used to trigger on tracks coming from a nominal interaction vertex.

Each of the central chambers has an independent gas volume and separate electrostatic shielding. They were built and tested separately, and then assembled and locked to one mechanical unit. The detector walls are thin to reduce photon conversion, and in particular its effect on identification of primary electrons. Neighbouring volumes share a thin (1.5 mm) cylinder of carbon fibre reinforced epoxy with a 50 μm aluminium coating on each side. The complete system of central tracking detectors is housed in a single aluminium cylinder of 4 mm wall thickness. The assembly also provides a precise alignment of the chambers relative to the outside support.

Charged tracks produced at polar angles θ close to the beam axis (forward $\theta < 30°$, backward $\theta > 150°$) no longer traverse the full bending ($r\phi$) plane radius of the solenoid magnetic field. Consequently in the CTD both track pattern recognition and track accuracy of reconstruction deteriorate as the measured track length and the number of precision space points decrease. A way of rectifying this loss is to compensate for the reductions in track length and the number of points in the central region by means of a higher radial density of accurate space points obtained using wires strung in the bending plane closely spaced in z. This is provided by the forward tracking detector which consists of an integrated assembly of three

nearly identical supermodules as also illustrated in Figures 4.13 and 4.14. Each supermodule includes, in increasing z: three different orientations of planar wire drift chambers designed to provide accurate θ measurements, a multiwire proportional chamber (FWPC) for fast triggering, a passive transition radiator and a radial wire drift chamber which provides accurate $r\phi$ (drift coordinate) information, moderate radius measurement by charge division and limited particle identification by measuring the transition radiation produced immediately upstream.

The FTD and CTD are linked together, aligned and surveyed prior to installation into the calorimeter cryostat.

4.1 Central jet chambers: CJC1 and CJC2

4.1.1 Design criteria

The design of CJC1 and CJC2 [26, 27] follows that of the jet chamber used in the JADE experiment at PETRA [28]. The wire pattern characteristic for a jet chamber is a plane of anode sense wires parallel to the beam line with two adjacent (cathode) planes shaping the drift field. In the CJC's the cathode planes are also built up by wires.

A jet chamber cell extends azimuthally from the sense wire plane to both adjacent cathode wire planes, and radially over the full radial span of CJC1 or CJC2 each with no further subdivision, as shown in Fig. 4.2. This minimizes the disturbing influence of field shaping wires at the inner and outer radii.

The jet cells are tilted by about 30° such that in the presence of the magnetic field the ionization electrons drift approximately perpendicular to stiff, high momentum tracks from the center. This gives optimum track resolution. The 30° tilt provides additional advantages:

- The usual drift chamber ambiguity is easily resolved by connecting track segments of different cells. The wrong mirror track segments do not match, as demonstrated in Figure 4.3. It can also be seen that they do not point to the event vertex and therefore obstruct only small parts of a real track in the opposite half cell.
- Each stiff track crosses the sense wire plane at least once in CJC1 and in CJC2. From the fine match at the crossing, the passing time of a particle can be determined to an accuracy of $\sim$ 0.5 ns. This allows an easy separation of tracks coming from a different bunch crossing.
- The drifting electrons from stiff tracks arrive at neighbouring sense wires with a time shift of about 100 ns, and therefore produce only negligible disturbance by cross-talk.
- Every track traverses several good regions of uniform driftfield inside the cells. Systematic errors of drift time measurement, which are known to arise in the nonuniform fields near the cathode and sense wire planes, reverse sign at the crossing, and therefore cancel in good approximation.

Adjacent sense wires are separated by two potential wires (see Figures 4.2 and 4.4). This reduces both the surface field and the cross-talk by nearly a factor of two as compared to a single potential wire. Most important, it allows to adjust drift field and gas amplification nearly independently. The actual positions of the sense wires are staggered off the nominal sense wire plane by ± 150 μm, such that adjacent wires are pulled by the electric field to definite positions on opposite sides of the plane.

A cell is azimuthally limited by two cathode wire planes, and at the inner and outer radius by the field wires. The cathode wires are set to a voltage proportional to the distance from the sense wire plane in order to create an uniform drift field and hence a constant drift velocity over almost all the cell. The voltages for the cathode wires are supplied by a resistor network (cathode chain) on the adapter cards connected to the cathode wires. The field wires shape the field at the inner and outer end of the cell such that the deviations from a uniform drift field are minimal. The sense wires are connected to a positive voltage and are AC coupled to the amplifiers. The potential wires are set to ground. To prevent aging of the chambers due to high electric surface fields, the diameters of the potential, cathode and field wires were chosen conservatively large : 127, 180 and 500 μm. This limits the surface field to $\leq$ 2KV/mm. The anodes are 20 μm (25 μm at the cell ends) gold plated tungsten wires with 3 % rhenium.

The electrostatics of the cells have been studied in detail by computer simulations. Figure 4.4 shows drift lines and isochrones in CJC1 for a Lorentz angle of 30°. In most of the drift region the electric field is constant to better than 1 %. At the first and the last sense wires the wire geometry produces local distortions of the field which, however, do not exceed 2 %. This introduces only negligible variations of the drift velocity, in particular around the maximum of the drift velocity.

The parameters of the jet chamber are listed in Table 4.1. All sense wires ($\sim$ 2200 mm long) are read out at both ends and yield via charge division a $z-$measurement. About 56 space points are measured on a track over a length of $\sim$ 620 mm.

4.1.2 Mechanics

The volume of each jet chamber is defined by two endwalls perpendicular to the beam line and an inner and outer cylinder concentric to the beamline. The volume has to be gas tight and to support small overpressure with respect to the atmosphere. The design of the mechanics of the tracking detectors was guided by the requirement to keep the detectors thin in terms of radiation length.

The bulk material of the endwalls was chosen to be an insulator (10 mm glass fibre reinforced epoxy [29]). This material combines excellent insulation with good mechanical properties. The fact that there are two jet chambers allowed for relatively thin endwalls, because the support lengths between inner and outer cylinders are small and thus the bending under the summed wire tension could be kept below 1 mm.

To facilitate installation, insulation and high voltage testing of all connections, the signal- and HV leads are integrated into the endwall structure by means of multilayer printed circuit (PC) boards. One board (2 mm thick) covers one drift cell. Of its four layers, one provides a nearly complete electric shield of the chamber, while the others make the contacts between the wire feedthroughs and the (signal and HV) connector sockets. A second PC board inside the chamber, 0.8 mm thick, carries strips for shaping the end fields.

Optimum precision of the wire positions is achieved by first glueing 3 mm thick massive brass pins into pre-bored holes in the endwalls, and then drilling precision holes into the brass. The precision of the sense wire positions, ± 15 μm within one cell, is determined by a small excentric holes in the brass. Details of the wire supports are shown in Figure 4.5.

The endwalls are kept apart by cylinders. To minimize material the cylinders are used commonly by adjacent drift chambers: e.g. the outer cylinder of CJC1 serves also as inner cylinder of the COZ. There are four cylinders to build the two jet chambers. The two inner and the outer cylinder of CJC1 are made of 1.5 mm thick carbon fibre reinforced epoxy [29]. Carbon fibre reinforced epoxy has been chosen because of its excellent mechanical stability (Young's

modulus $\epsilon = 80$ kN/mm^2) at a very long radiation length ($X_0 = 230$ mm). The chamber volume forms a Faraday cage in order to be screened against external electromagnetic noise. Since the conductivity of the carbon fibres is not sufficient in all directions, an aluminum coating of the inner and outer surface was mandatory. The thickness of 50 μm of the Al surface liner was a compromise between electromagnetic screening down to low frequencies (skin depth at 20 MHz in Al is $\approx$ 20 μm) and minimum material. The surface liner is made of 100 mm wide Al foil wrapped helically and overlapping by about 5 mm around the tube, carefully avoiding insulation between the turns.

The outer cylinder of CJC2 is made of aluminum and is the main support vessel for all tracking detectors. It has feet which glide on rails positioned on the inner warm wall of the liquid argon cryostat and which are the mechanical link to the rest of the H1-detector. The Al cylinder has a wall thickness of 4 mm. At both ends the Al cylinder has thicker flanges ($\Delta r = 12$ mm), which are machined to 0.1 mm tolerances in order to house the endwalls precisely. The body is made from a single sheet of Al, welded to a cylinder. At final assembly the stability and shape of the Al cylinder is guaranteed by the insertion of the endwalls.

	unit	CJC1	CJC2
active length Δz	mm	2200	
active zone starts at z	mm	-1125	
total length Δz	mm	2500	
inner radius R_i	mm	203	530
outer radius R_o	mm	451	844
active radial length	mm	224	296
number of cells		30	60
number of sense wires per cell		24	32
number of potential wires per cell		50	66
number of field wires per cell		10	10
number of cathode wires per cell		49	65
sense wire distance	mm	10.16	
maximum drift distance at R_i	mm	22.9	28.5
maximum drift distance at R_o	mm	44.5	43.1
sense wire material		W-Rh(3%)	
sense wire resistance	kΩ/m	0.3	
sense wire diameter	μm	20	
potential wire material		Cu-Be(2%)	
potential wire diameter	μm	127	
sense wire tension	N	0.65	
gas mixture: $Ar/CO_2/CH_4$	%	89.5/9.5/1.0	
sense voltage	V	1170	
field gradient	V/mm	120	
drift velocity	mm/μs	$\approx$ 50	
$\sigma_{r\phi}$ (σ_ϕ)	μm (°)	170 (0.1)	
σ_z (σ_θ)	cm (°)	2.2 (1.2)	
σ_κ	cm^{-1}	3×10^{-5}	
σ_{DCA}	μm	420	
$\sigma_{dE/dx}$	%	10	
double hit resolution	mm	2	

Table 4.1: Central jet chamber parameters

4.1.3 Track reconstruction

4.1.3.1 Track parametrization Tracks of charged particles are characterized by the five helix parameters. We use the signed curvature ($\kappa = \pm r^{-1}$, positive if the direction ϕ coincides with a counter-clockwise propagation along the circle), the signed closest distance from the z–axis in the (x,y)–plane (d_{ca}, positive if the vector to the point of closest approach and the trajectory direction form a right-handed system), azimuth and polar angle (ϕ and θ), and the z–position (z_0) at the point of closest approach. The first three parameters are determined by a circle fit to the data in the xy-projection using the non-iterative algorithm of Karimäki [30]. The circle equation is expressed in polar coordinates (r,φ) as

$$\frac{1}{2}\kappa\left(r^2 + d_{ca}^2\right) + (1 - \kappa d_{ca})\, r \sin(\phi - \varphi) - d_{ca} = 0$$

For a track traversing both rings of the CJC a single parametrization for both rings is usually sufficiently accurate. Due to multiple scattering in material especially between the two rings (there is material equivalent to 2 % of a radiation length between the two rings) for some tracks two separate sets of parameters are determined; the two sets are constrained to join in a point at a radius between the two rings under a scattering angle compatible with the mean angle expected form multiple scattering.

The other two parameters are determined by a linear least-squares fit of $z_i = z_0 + S_i^{xy}(dz/dS)$, where S_i^{xy} is the track length for the point z_i in the xy-projection, with $S^{xy} = 0$ at d_{ca}. The slope parameter (dz/dS) determined by the fit is converted to the angle θ by $\theta = \arctan(1/(dz/dS))$.

The track finding is followed by further modules to determine the xy-vertex for a given run, and to perform track fits to the primary and secondary vertices. The track parameters in this stage are κ, ϕ and θ, together with the xyz-coordinates of the vertex.

4.1.3.2 Track finding Two versions are used for the track finding and fitting. A fast version, efficient for tracks originating from the primary vertex with a momentum > 100 MeV/c, is used on the fourth trigger level filter farm (see Section 8.5) for background rejection and fast classification of events. The fast version is roughly a factor ten faster than the standard version, which is efficient for all kinds of tracks and is used within the normal reconstruction.

The algorithms used for track finding are determined by the basic properties of the CJC. The two rings of the CJC are treated separately to a large extent. The first phase of track finding, the search for short track elements (curvature negligible), is done independently in the angular cells with 24 (CJC1) and 32 (CJC2) radial wires. Data within angular cells have very simple geometrical properties and track-element finding does not depend on parameters like the Lorentz angle α_L or the drift velocity v_d. However accurate values of these parameters are necessary when hits from more than one angular cells are combined.

Track finding is based almost exclusively on drift time data in the xy-plane (the spatial precision in this plane is about two orders of magnitude better than for z, which is measured in the CJC by charge division). Track finding includes removal of outliers, which would distort the circle fit. Only in a later stage of the track reconstruction the measured z-values are used; here it is necessary to remove again outliers before the data are fitted.

4.1.3.2.1 Fast track finding

Determination of the bunch crossing time t_0: An approximation to the time reference value t_0 for an event is determined from the threshold in the drift time histogram. The value is sufficient for the fast track finding.

Hit triples: The first phase of track finding is the search for track elements defined by three hits within angular cells, with the three hits on three wires with a wire distance of two. Due to the simple geometry the search for hit triples is done with integer arithmetic using only the values of measured drift distances d_j^n (unsigned) (n = wire index, j = hit index).

In order to reduce the large possible number of triples to be checked the algorithm starts with hit pairs. Trying all pairs of hits at the wires $n \pm 2$ possible values of drift distances $\tilde{d}^n$ at the wire n are calculated by

$$(d_i^{n-2} + d_k^{n+2})/2 \qquad \text{and/or} \qquad |d_i^{n-2} - d_k^{n+2}|/2$$

and stored in a list, if the direction of the pair does not deviate too much from the radial direction. Very dense regions with many hits are not analysed. The list of possible values $\tilde{d}^n$ is sorted and then compared with the (also sorted) measured values d_j^n; in case of a small difference $|d_j^n - \tilde{d}^n|$ the indices $[i, j, k]$ of the hits at the wires $n-2, n, n+2$ are stored as a possible track element.

The length and accuracy of a track element defined by a hit triple from wires $n-2, n, n+2$ is already high enough to determine the track parameters curvature κ and angle ϕ_m with sufficient accuracy, assuming a track from the origin ($d_{ca} \equiv 0$). The parameter ϕ_m is the track angle at a mean radius r_m of the CJC1 and the CJC2, respectively.

No attempt is made at this stage to resolve the drift sign ambiguity; triples with a large value of $|\kappa|$ (very low momentum) are rejected, otherwise both solutions are kept. A z-value and a value for dE/dz is assigned to the triples from the median of the three single-hit values and later used to determine the z-slope and -intercept z_0 and the mean dE/dz-value of the track.

Track finding and definition: Tracks from the origin show up as narrow clusters in the plane of the two parameters κ and ϕ_m of the triples, with a width of typicaly only one degree for ϕ_m. After sorting all triples according to the ϕ_m-values, narrow clusters in ϕ_m are searched for, and then, within each cluster found in ϕ_m, a search is made for clusters in κ, again by sorting. A sufficient separation of clusters, i. e. definition of tracks, is achieved. The coordinates of triples within clusters are then used to determine the standard track parameters by a circle fit, now allowing $d_{ca} \neq 0$, and by a z-fit. Track candidates with large $|d_{ca}|$ or very low momentum are rejected.

The track candidates are then checked in the order of decreasing number of triples (decreasing significance) rejecting tracks with several triples already used before for an accepted track. Drift sign ambiguities are normally resolved at this stage, since most tracks traverse several cells and the correct solution has a much larger number of triples than the wrong one.

The fast track finding is in general efficient enough to allow sensitive recognition of background or classification of physics events.

4.1.3.2.2 Standard track finding

Determination of t_0: The standard track finding starts from the results of the fast track finding on the time reference value t_0 and the tracks. The time reference value t_0 for an event is improved for the standard track finding by special fits to the drift length values of long tracks. This improvement of the t_0 value is the first step in the standard track finding and is done as follows.

For a given track, found by the fast track finding module, the values of the circle parameters in the xy-plane are used to calculate the expected drift length values on all possible wires.

Then hits with their measured drift length values compatible with the expected values are collected, and the drift length differences are calculated, taking into account the sign of the drift length. To these differences an expression is fitted, which in addition to a parabolic dependence on the track length (to allow for a small inaccuracy in the track parameters) parametrizes the effect of a t_0 difference (which depends on the sign of the drift length) and also a small difference of the drift velocity. This fit yields an accurate value of the time reference value t_0 and allows in addition to detect changes of the drift velocity.

The method gives at the same time an improvement of the definition of tracks; often the range of the found hits is extended and additional hits are assigned to the track. Another circle fit is performed to all long tracks traversing more than one cell (drift sign ambiguity resolved). If the χ^2 value of the track fit (after removing single bad hits eventually) is acceptable the complete set of track parameters is stored already at this stage, the hits assigned to the track are flagged and not used in the following standard track finding.

Hit triples: The first phase of standard track finding is again the search for track elements defined by three hits. The algorithm used here is similar to the one used in the fast track finding module, but looks for triples at the wires $n-1, n, n+1$, i. e. at adjacent wires. All possible wires are considered, except for very dense regions. Triples with common hits are connected by pointers and when all hits of an angular cell are analysed, chains of hits are extracted. These chains of hits are then checked by a fit to the drift times for effects like kinks; eventually long chains of hits are split into two shorter chains. For long chains the staggering of wires sometimes allows already to resolve the drift sign ambiguity; otherwise both solutions are kept. Chains accepted at this stage are stored as track elements together with their parameters determined by a circle fit.

Merging of track elements to track candidates: The merging of short track elements to larger ones is done on different levels, first using track elements in the same or the neighbouring angular cell, then using track elements within one ring (CJC1 or CJC2), finally merging track elements from CJC1 and CJC2. Almost the same algorithm is used in all levels of merging. Simple and clear cases of pairs of track elements are merged earlier in this algorithm.

The algorithm starts with a comparison of pairs of tracks elements, with simple and loose cuts. For pairs of track elements with similar helix parameters and not a too large distance between them, which could belong to the same track, a χ^2-fit is performed, using all available information in the xy-plane. A list of all acceptable (χ^2 not too high) pairs is formed and sorted in the order of an increasing "distance", assigned to each pair. The distance is constructed from the χ^2-value and other parameters (for example the length of the track element - long elements will get a smaller distance assigned). The list of pairs is then checked sequentially, starting with the "close" pairs. Two elements from a pair are combined to a new (longer) track element, if acceptable. If in this sequence one element of a pair has already been used in the construction of a new element, the fit to the modified element(s) is repeated and rejected eventually. By this process longer and more accurate track elements are formed, starting with the simple and clear cases, thus avoiding with high probability a wrong combination of short track elements.

Track definition: Although the track elements defined so far are already of good quality, another step is performed to increase the track finding efficiency and precision. In the order of decreasing track length (number of hits) the values of the circle parameters in the xy-plane are used to calculate the expected drift length values on all possible wires. Then hits at the expected wires are collected (hits flagged as used already by another track are rejected) and analysed in a series of simple fits to the differences of measured and expected drift length values. Depending on this analysis hits not compatible with a track are rejected. Found tracks are allowed to have a rather large gap of several wires, since parts of tracks may be

invisible, especially within jets, due to the limited double track resolution of about 2 mm. The fits for a determination of the track parameters are repeated using all acceptable hits.

Finally, before storing the result of the track reconstruction in the output bank, very short track candidates are rejected, unless they start with the first few wires of a ring. As last track parameter a mean value of dE/dx is determined from the single-hit values. Because of the asymmetric Landau distribution of the single values $k_i = (dE/dx)_i$ the mean value is determined from the transformed values $1/\sqrt{k_i}$, which have an almost symmetric distribution. Hits which are close to another track are not used for the calculation of the mean value.

4.1.3.3 Vertex determination The ep−interaction vertex region in the xy-plane has a size of a few hundred μm in x and in y; the mean position of the region is rather stable for a sequence of runs. For a determination of the mean vertex coordinates (x_v, y_v), long high momentum tracks with a small value of d_{ca} from many events are used in a fit of the parameters x_v and y_v, minimizing the sum of squares of the distance b of the tracks (track parameters ϕ and d_{ca}, assuming $\kappa = 0$) to the vertex:

$$b = x_v \sin\phi - y_v \cos\phi - d_{ca} \,.$$

With a few hundred tracks a sufficient accuracy is obtained. The fitted values of the vertex coordinates are stored in the data base.

The known position of the (x_v, y_v) run vertex can be used to improve the parameters of track originating from the primary interaction vertex. The circle equation

$$\frac{1}{2}\kappa\left(x_v^2 + y_v^2 + d_{ca}^2\right) + \left(1 - \kappa d_{ca}\right)\left(x_v \sin\phi - y_v \cos\phi\right) - d_{ca} = 0$$

is used as a constraint in a fit, where the effect of multiple scattering in the beam pipe and the CJC wall for low-momentum tracks and the vertex precision is taken into account. Since the standard deviation of the curvature value is roughly inversely proportional to the track length squared, the track precision is significantly improved by this vertex fit in the xy-plane. A z-value of the primary interaction vertex in an event is determined from all tracks fitting to the xy-vertex. The polar angle θ for these tracks is changed accordingly.

Within the standard reconstruction program a search is made for neutral particles decaying into a pair of oppositely charged particles with tracks in the CJC; in addition to K_S^0, Λ and $\bar{\Lambda}$ particles also e^+e^--pairs from conversion are found by this module. Candidate pairs are determined using simple geometrical cuts. For each candidate pair a fit is performed applying geometrical (common secondary vertex of the charged particles) and kinematical constraints. Use is made of the known position of the primary vertex. Momentum balance perpendicular to the direction of the neutral particle is used as kinematical constraint, but no masses are assumed. For very small opening angle of the pair the transverse momenta in the xy-plane are both constrained to zero, to improve the stability of the fit for e^+e^--pairs. Pairs with an acceptable χ^2-probability are stored.

At later stages of the analysis alternative methods for reconstructing secondary vertices are also employed (see references [31, 32] and Figure 12.5). Kalman filtering techniques have also been shown to be useful [33].

4.1.4 Calibration and performance

The main task of the CJC is the accurate measurement of the parameters of charged tracks in the $x-y$−plane. These are obtained from up to 56 points on a track, which are derived from the drift time measurements on different sense wires. The measurement of the z−coordinate (along the wire) from charge division serves essentially the linking of jet chamber tracks with the z−chamber hits, which give a much higher accuracy of the z−coordinate. In addition the measurement of dE/dx helps to identify electrons and to reject beam-gas events by identifying protons.

Good knowledge of all variables and constants involved is needed in order to obtain the best accuracy. It is limited by the intrinsic resolutions:

- $\sigma_{r\phi} \approx 150$ μm for drift time measurements with a gas mixture of Ar-CO_2-CH_4 (89.5 : 9.5 : 1.0) at atmospheric pressure;
- $\sigma_z \approx 1\%$ of the wirelength (2.2 cm) for the charge division measurements with the given electronics and gas amplification (limited by pulseheight and noise);
- $\sigma_{dE/dx} \approx 6\%$ for this gas mixture at atmospheric pressure.

A large variety of constants is involved to determine the coordinates of a hit from the timing and pulse-integral of a drift chamber signal. We distinguish:

Overall constants, i. e. event timing, average drift velocity and average Lorentz angle: The overall constants are sufficient to determine the track parameters with moderate accuracy: The use of event timing, average drift velocity, and average Lorentz angle gives a resolution of e.g. $\sigma_{r\phi} \approx 350$ μm. They are determined and continuously monitored by fitting them as additional parameters to long tracks at high momentum. The use of the average effective wire length and gain gives resolutions of $\sigma_z \approx 5$ cm and $\sigma_{dE/dx} \approx 17\%$.

Wire dependent constants, i. e. timing, signal propagation, relative gain (both wire ends), absolute gain, position at both wire ends: These individual calibration constants have been determined in two steps. The first step consists of the evaluation of testpulse data. It is possible to pulse simultaneously the 4 odd/even wires of an 8-channel amplifier card on both chamber ends separately. This allows the exact determination of the relative timing of the 4-wire groups, the timing difference, and the relative gain at the two wire ends. The start values for effective wire length are determined, apart from an overall factor. In the second step reconstructed and fitted tracks are used. The hits are fitted to a circle in the $x-y$−plane and a straight line in the $r-z$−plane. The residua of the hits are evaluated to obtain the absolute values of the wire constants. The use of individual wire constants improves the resolution to $\sigma_{r\phi} \approx 170$ μm, $\sigma_z \approx 2.2(3.3)$ cm for protons (pions) and $\sigma_{dE/dx} = 10\%$ (see Figures 4.6 and 4.7).

The performance of the CJC is represented by the accuracy of the track parameters. It has been determined from cosmic ray tracks by comparison of the track parameters obtained for the two track branches individually [34]. The resolutions obtained presently are shown in Table 4.1. The resolutions achieved at this early stage of calibration are already comfortably close to the expected ones. Improvements are expected by better controls of timings and gas parameters like composition, pressure and temperature.

The resolution achieved in the z−coordinate [35] depends on the deposited ionization and is shown in Figure 4.6. The ionization measurement is also used to perform particle identification via dE/dx. Data from HERA electron-proton collision runs were analysed [35]. The dependence of the specific ionization on the particle momentum is show in Figure 4.7. There are clearly visible bands of pions, proton and deuterons , where the latter two particle species are mainly produced by protons colliding with the residual rest gas.

4.2 Central $z-$ chambers

Two thin driftchambers, the central inner and outer $z-$chambers (CIZ, COZ) surround the inner half of the jet chamber and complement the measurement of charged track momenta in the latter chamber. These two chambers deliver track elements with typically 300 μm resolution in z and 1 to 2 % of 2π in ϕ. This requires a drift direction parallel to the beam axis and sense wires running perpendicular to the beam axis on the surface of two cylinders with 180 and 460 mm average radii. Linking these track element to those obtained from the jet chamber with accurate $r\phi$ and moderate $z-$information gives the final accuracy on both the longitudinal as well as the transverse momentum components. A double track resolution of a few mm, high efficiency and low chamber mass were further design criteria for CIZ and COZ. A first level, background rejecting trigger is beeing developed [36] which combines CIZ and COZ hits to trigger on straight tracks pointing to the interaction region. The CIZ uses the inner carbon fibre wall of the CJC for closing its gas volume, while the COZ uses the outer carbon fibre cylinder for its basic structural element. The polar angles covered by CIZ and COZ are $16° < \theta < 169°$ and $25° < \theta < 156°$, respectively. The properties of both chambers are summarized in Table 4.2, more details on their construction and performance can be found in the following paragraphs and in references [37, 38, 39, 40, 41].

4.2.1 CIZ

For CIZ a laminar construction technique quite similar to that described below for CIP was used, starting from a steel mandril with an inner diameter of 347 mm. Successive layers include 25 μm Kapton with a 2.5 μm Al coating for electrical shielding, a 6 mm thick Rohacell [43] cylinder with its outer surface machined and polished to produce 16 flat surfaces forming a regular polygon in cross section (see Figure 4.8), and a 25 μm Kapton foil with 10 μm Cu field forming strips on both sides. All Cu strips are coated with 0.1 μm of Au to avoid oxidation. Each layer is glued to the previous one using epoxy glue. The 15 independent cells are separated by printed circuit boards, 1.6 mm thick with 5 μm Cu on each side serving as the cathode plane. These walls as well as the axial dividers extending from the corners of the polygon are also glued to the chamber body. This is indicated in Figure 4.8, where the geometry of the cells is exposed. Details on the types of feedthroughs used for the potential and the sense wires can be found in ref. [37, 38, 41]. The cells are closed electrically with another Kapton foil identical to that on the bottom of the cell, here backed by 1 mm of Rohacell. The end flanges of the CIZ (see Figure 4.18 in Section 4.5.2) are sealed against the CJC end plates with O-rings.

The sense wire planes are tilted by 45° from the normal to the chamber axis, with the first nine cells in backward direction tilted backward and the last six in forward direction tilted forward, i. e. following the direction of the tracks crossing the respective cells. As explained in ref. [37] this tilt produces a distortion of the equipotential lines resulting in a non-uniform distribution of the charge collected on the four wires and an equivalent tilt of the isochrones. In the orientation shown in Figure 4.8 wire # 0 collects charge only when a track crosses to the left of the sense wire plane and wire # 3 collects charge only if a track crosses to the right. Both collect roughly 60 % of the total charge, while wires # 1 and # 2 collect about 20 % for both sides. This unusual wire arrangement hence solves the left-right ambiguity automatically without a need for wire staggering and furthermore dampens the dependence of the resolution on the crossing angle in particular for low crossing angles. The wires are soldered to both side walls of a 23 mm wide cable channel at $\phi = 0°$. Here the signal wires are connected to line drivers and the potential wires to high voltage cables. The line drivers are amplifiers which allow a proper matching of the impedances to the 50 Ω coaxial cabels, which performs the connection from the different $z-$positions of the rings to the chamber end plate. There the lines are terminated

	unit	CIZ	COZ
active length Δz	mm	1800	2160
active zone starts at z	mm	-1080	-1105
mechanical length Δz	mm	2254	2230
total length Δz[1]	mm	2467	2590
thickness Δr[2]	mm	20	24
chamber starts at z[1]	mm	-1373	-1140
inner diameter	mm	347	920
outer diameter	mm	400	970
number of driftcells (rings) in z		15	24
number of $\phi-$sectors		16	24
number of sense wires per ring		4	4
number of potential wires per ring		3	6
mean wire length	mm	1120	2970
drift cell length Δz	mm	120	90
maximum drift distance Δz	mm	61.25	45
sense wire material		Elgiloy[3]	Stablohm[3]
sense wire resistance	kΩ/m	3.0	0.6
sense wire diameter	μm	20	48
potential wire material		Au	CuBe
potential wire diameter	μm	120	127
wire tension	N	0.2	0.9
dead zone in ϕ (readout channel)	° (%)	7.5 (2.1)	7.5 (2.1)
dead zone in ϕ (wire support)	° (%)	14.4 (4.0)	5.4 (1.5)
dead zone in z (cell walls in active zone)	%	1.6	1.7
radiation length in active zones	% X_0	0.6	0.8
radiation length averaged	% X_0	1.2	1.5
gas mixture	%	Ar(80)	Ar(50)
	%	CH_4(20)	C_2H_6(50)
cathode voltage	V	4500	3000
potential wire voltage	V	2250	2250
field gradient	V/mm	52.7	82
drift velocity	mm/μs	52	48.5
resolution for single tracks σ_z [4]	μm	260	200
double track resolution Δz [4]	mm	4.6	3.5
charge division resolution $\sigma_\phi(\sigma_{(r\phi)})$ [4]	° (mm)	8.6 (28)	7.2 (58)

Table 4.2: $z-$ driftchamber parameters.
[1] Incl. preamplifiers; [2] gas volume;
[3] alloys from ref. [42];
[4] performance data at HERA using extrapolated and linked CJC-tracks (see text).

and fed in to the standard H1 driftchamber electronics. The input impedance of the current-amplifiers is 430 Ω and the risetime is better than 10 ns. We selected a high resistance alloy for the sense wire material to improve the measurement of the ϕ coordinate along the wire by charge division. To save space the high voltage cables to the electrodes and cathodes are buried in the Rohacell chamber body and the miniaturized 10 MΩ resistors (1.25 mm × 2 mm × 0.5 mm), which supply the field forming strips are embedded in the printed circuit board chamber partitions. As indicated in Figure 4.8 each fieldshaping electrode is 1.75 mm wide and separated from the next by 0.25 mm. To limit field distortion near these gaps, the electrode pattern is repeated on the back side of the foil, offset by 1 mm and contacted through the foil at a few points. The voltage step between two electrodes is 106 V with the voltage settings given in Table 4.2.

Since the CIZ is the drift chamber closest to the interaction point, a dedicated current monitoring system (see ref. [44] for details) was included into each potential wire supply line. It allows to measure the precise currents in the nA range. These wires control the gas amplification in the chamber. In this way the activity introduced by interaction products or stray beam can be monitored quite sensitively. Typically we found 10 nA current increase per ring for a luminosity of 20 $mb^{-1}s^{-1}$. This corresponds to an accumulated charge of 10 Cb/m per wire for the expected luminosity of 100 pb^{-1} per year, if design intensities for the beam currents can be reached. Furthermore the potential wire HV-lines are protected by a 64 MΩ series resistor and the cathode HV-lines by a 1 MΩ series resistor at the chamber input. Presently we run the chamber with an $ArCH_4$ gas mixture, to which a small amount of water (0.4 %) for radiation damage protection is added.

The inefficiencies near the cell walls were discussed in detail in ref. [38]. Table 4.2 contains a summary of the different contributions, which add up to 7.7 %. Away from these boundaries the efficiency was measured to 98 % in test beams at PSI [38]. At HERA in the initial phase often unstable beams with occasional complete losses near the detector were encountered, which is why the CIZ high voltage was kept 100 V below its plateau, where the efficiency is only 91 %. The (Q,t) analysis, i. e. the way the total charge and arrival time of a pulse are determined from the FADC data is described in Section 4.4.7 below, because it is similar for all drift chambers. A small modification is necessary to eliminate 10 MHz (HERA frequency) noise pulses, which occur at a rate of a few %, but are usually shorter than the real track induced pulses. Therefore at the scanner level a pulse is required to exceed the threshold for at least five consecutive ADC channels (50 ns). Double pulses can be resolved, if their separation exceeds 90 ns, which converts into 4.6 mm spatial separation in z (see ref.[38]).

Figure 4.9 shows the test beam results for the measured resolution as function of drift distance and crossing angle of the track. These results were obtained with a prototype [38], however could be confirmed with cosmics test data, and with central jet chamber tracks extrapolated into the z-chambers and there linked to the corresponding track elements. The average deviation from a straight line fit (in the $z-r$ plane) is $\sigma_z = 260$ μm for CIZ internal track elements and 400 μm for linked tracks. For the $\phi-$projection a resolution of 2.4 % of the wire length was measured. The correlation of the ϕ measurements of CIZ and COZ with that of CJC are shown in Figure 4.10. For some angular regions ($16° < \theta < 25°$, $156° < \theta < 169°$) the CIZ track segment is the only accurate information for a polar angle measurement. If a vertex has been found otherwise, a precise $z-$point suffices of course, but the internal resolution of the CIZ to determine the slope $dz/dr = z'$ with $\sigma_{z'} = 83$ mr greatly helps eliminating parasitic tracks not coming from the vertex.

4.2.2 COZ

This chamber was also erected on a Rohacell [29] body with the cross section of a regular 24-edge polygon, but resting on a cylinder of carbon fibre reinforced plastics. The Kapton foils with field

shaping copper strips were glued to the Rohacell surfaces. Guided by a mechanical positioning device the wire supporting rods (G10 with Cu strips, double sided) were placed and soldered to the Kapton foil. Between these rods planar cathodes were introduced made of G10/Cu with holes to enable the gas flow through the chamber. The top cover of the drift cell structure consists of a Kapton-Rohacell sandwich which is fixed at the cathodes. The whole chamber has a cylindrical shape due to its G10-Cu gas cover held by the endflanges. The chamber represents on average a material thickness of 1.5 % X_0 for perpendicularly crossing tracks.

Figure 4.11 shows a schematic view of the COZ. The dead zones for the wire readout are distributed in azimuth which allows a corresponding distribution of the preamplifiers at the end flanges. Readout zones, wire supporting rods and cathodes limit the active chamber area to 94.7 %. The anode signals are transmitted by flexible lines from the wire ends to the preamplifiers. The input resistor of the preamplifier (see below) is 200 Ω which is comparable to the impedance of the wire arrangement in the chamber. This led us to use twin readout lines (signal-ground-signal) with an impedance matched to this value. The signals are transmitted to both chamber ends, the length of the readout lines ranging from 0.2 to 1.2 m. The electronics chain (preamplifier at the flanges and FADC after 30 m cable) is common to all H1 tracking drift chambers and described below. Each drift cell is 24 mm high, the maximum drift length is 46 mm which limits the drift time to about 1 μs. Electrons can drift to the anode wires from both sides. There is no wire stagger implemented because mirror tracks can be removed by software as they do not point to the vertex. Each cell has four sense wires as indicated in Figure 4.12 and three pairs of potential wires. The wire feedthroughs in the supporting rods are in their nominal position to about 30 μm (σ). Before closing the chamber it was extensively surveyed with a precision of 100 μm.

The electric field distribution can be influenced by four different voltages: U_{SW}, U_{CS}, U_{FS} and U_{CA} applied to the sense wires, the central field shaping strip, the first strip and the cathode, respectively. The cathode is connected to the last strip. The potential wires are grounded. These four voltages fulfill different functions: U_{SW}, mainly, defines the gas amplification, U_{CS} the field homogeneity, and the divider voltages U_{FS} and U_{CA} determine the field gradient. Due to the rectangular geometry, the field of the COZ looks simple, its optimization, however, is non-trivial as gas amplification (signal height), field uniformity and gradient have to be carefully defined for a given gas. Typical values we were using are U_{SW}=2.25 kV, U_{CS}=0.25 kV, U_{FS}=0.2 kV, U_{CA}=-3.0 kV, which gave a measured drift velocity of 48.5 mm/μsec at a field gradient of 82.0 V/mm. The driftvelocity is determined from the chamber itself based on tracks crossing the sense wire plane and the cathode plane, respectively.

As for the CIZ inefficiencies along the cell walls and other performance parameters were extensively studied in test beams (3 GeV electrons at DESY and low energy pions and electrons at PSI, see references [39, 40]). Apart from a small region near the sense wire feedthroughs the efficiency was determined to be 98 % over the full drift cell. Work is going on to reduce the noise level and stabilize the chamber operation under beam conditions in order to reach that value with the full chamber. Figures 4.9 and 4.10 show the resolution versus drift distance and crossing angle for a sample of data taken at HERA. For 90° crossing angle the resolution is about 200 μm which deteriorates to 500 μm for low crossing angles. The azimuthal angle is determined by charge division to an averaged accuracy of 7.2 °, i. e. 2 % of the wire length. Double pulses can be resolved if their separation is larger than 70 ns which corresponds to 3.5 mm distance. For a discussion of the optimum method to resolve double tracks and a comparison of different algorithms for (Q,t) analysis we refer to references [39, 40, 45].

4.3 Forward tracking detector

The basic design aims for the forward tracking system can be summarised as follows. It should provide an accurate measurement of charge particles in the forward direction (momentum reso-

lution $\sigma_p/p < 0.003\,p$ and track angular resolution $\sigma_{\theta,\phi} < 1$ mr), track information on individual particles within jets, electron identification by means of transition radiation detection and a fast forward ray track trigger.

The layout of the FTD is illustrated in Figures 4.13 and 4.14. Key parameters are listed in Table 4.3. The drift chambers have different wire geometries - the planars contain parallel wires whereas the radial wires radiate outwards from the beam pipe – all have wires strung perpendicular to the beam direction. The planar module consists of three drift chambers, each four wires deep in x and rotated at 60° to each other in azimuth, is situated at the front of each supermodule, since its homogeneous spatial precision in x and y is most suitable for linking to tracks in the central detector. For practical reasons the FWPC is mounted directly behind the planar drift chambers in order to share the same gas mixture and maximise the geometrical trigger efficiency of the FTD. The FWPC's contain two planes of pad readout, a coincidence of which provides a fast ($\Delta t < 96$ ns) signal for bunch crossing timing and triggering purposes. After the FWPC the particles traverse a transition radiator consisting of 400 polypropylene foils contained in its own gas volume. The transition radiation photons after passing through a thin mylar window are detected in the radial chamber which produces up to 12 accurate space track points from ionisation drift timing and charge division. To improve double track resolution the second and third radial modules are rotated by 3.75° and 2.5° (1/2 and 1/3 of a wedge) relative to the first. The interleaving of planar and radial chambers provides the optimum lever arm for momentum measurement.

The individual chambers (Figures 4.13 and 4.14) were assembled and tested separately. The components for a single supermodule were installed into a three section tank consisting of aluminium outer cylinders ($\varnothing_{max} = 1700$ mm) and glass free carbon fibre inner cylinders ($\varnothing_{min} = 243$ mm, 4 mm thick, lined with Al foil), each tank section forming an independent gas volume and electrically isolated environment. Each chamber is bolted to the rigid central U-shaped outer cylinder using a set of precision dowels for alignment. Assembly was carried out on high quality surface tables with dimensional tolerances kept to $< 30\,\mu$m throughout the build sequence. After commissioning each supermodule on a cosmic ray test facility the three supermodules were then bolted together, separated by thin gas tight kapton windows, and the end faces closed with stiff plates made from a sandwich of 1.2 mm thick Al alloy and 17.6 mm thick Nomex honeycomb [46]. The final alignment of the whole FTD was measured using cosmic rays after installation into the H1 experiment. Water at constant temperature (±1 °C) is circulated around each tank section through copper pipes in order to maintain dimensional stability and provide cooling for the preamplifiers. Temperatures are monitored at the tank, the inlet and outlet water manifolds, preamplifiers and within the detector volumes. As well as maintaining the relative alignment of the tracker elements and support for the various services – water, gas, cables, preamplifiers, position monitors etc., the tank provides an electromagnetically sealed environment and serves as the common ground for the chambers. The HV and signal cables access the tracker volume via the outer cylinder using hermetically sealed feedthroughs where they are grounded. The HV cables are also filtered before entering the tank. The tracker is electrically isolated from the central tracker and the cryostat.

Three different gas mixtures are used, two working gases for the chambers and one purge gas for the transition radiation (TR) volumes. Gas is fed into each supermodule volume via the U-shaped channels in the outer cylinder, two feed pipes and one pipe for local pressure sensing, a total of nine pipes per supermodule. Gas tightness is maintained by rubber O-ring seals at the outer and inner flanges. The gas is supplied at atmospheric pressure from three computer controlled closed loop gas circuits (see Section 4.6) which maintain gas purity and provide the accurate pressure control, $\pm 10\,\mu$bar required in order to prevent damage to the fragile TR windows. During HERA operation the oxygen level in all volumes has been kept to < 50 ppm.

The whole tracker is kinematically mounted on four insulated feet and rests on the cryostat rails in stress-free condition.

Parameter	unit	Radials	Planars
number of cells per supermodule		48	32
inner active radius R_i	mm	150	≈150
outer active radius R_o	mm	750	≈750
number of sense wires per cell		12	4
total number of sense wires		1728	1152
sense wire diameter	μm	50	40
sense wire material		Stablohm[1]	W (Au plated)
sense wire resistance	Ω	450	
sense wire spacing Δz	mm	10	6
sense wire stagger	μm	280	300
sense wire tension	N	1.75[2]	1.20[2]
doubled ended readout		yes	no
number of grid wires per cell		11	10
total number of grid wires		1584	2880
grid wire material		Cu-Be(2%)	Cu-Be(2%)
grid wire diameter	μm	125	125
grid wire tension	N	2.80[2]	4.00[2]
sense wire suface field	kV/cm	170	135
sense voltage	V	+2228	+1575
bulk field gradient	kV/cm	1.2	1.0
grid field	kV/cm	−6.9	−5.0
maximum drift distance ($B = 0$ T)	mm	50	28
drift velocity ($B = 0$ T)	mm/μs	$\sqrt{3} \times 37$	43.5
drift velocity ($B = 1.14$ T)	mm/μs	37	42
Lorentz angle ($B = 1.14$ T)	°	45	41.8
gas mixture (1992)		Ar/C_2H_6	$Ar/C_3H_8/C_2H_5OH$
	%	50/50	89/10/1
design gas mixture		$He/C_2H_6/Xe$	$Ar/C_3H_8/C_2H_5OH$
	%	40/40/20	89/10/1
typical FTD tank temperature	K	293	
typical preamplifier temperature	K	307	
$\sigma_{r\phi}$ from track segments	μm	180 – 200	
σ_r from track segments	cm	3	
$\sigma_{z,y}$	μm		150 – 170
double track resolution	mm	2	2

Table 4.3: Forward tracker drift chamber parameters.
[1] alloy from ref. [42]; [2] 60 % of the limit of proportionality.

4.3.1 Planar drift chambers

Each chamber is constructed as a self-supporting module containing 32 drift cells of identical rectangular cross section with wire lengths between 460 mm and 1410 mm as shown in Figure 4.14. The chamber walls are formed from two circular discs with an outer diameter of 1.57 m and a central aperture of 280 mm diameter. These are composed of a low mass composite of fibredux skinned Nomex honeycomb 3.4 mm thick, manufactured to be parallel and flat to within 100 μm. A 0.8 mm thick double sided printed circuit board carrying the drift field forming strips and voltage bus on opposite faces is bonded onto one side of the honeycomb laminate. the drift cells are defined by parallel sets of copper clad PCB's, 0.8 mm thick by 32 mm high, mounted perpendicularly and bonded at 57 mm intervals into precisely machined slots in the honeycomb panels, resulting in a multiple box section structure of high mechanical strength and rigidity. The vertical PCB's constitute the cathode planes and define the maximum drift distance as 28.1 mm (for $B = 0$). Each cell contains four sense wires of 40 μm diameter gold plated tungsten uniformly spaced by 6 mm in z and staggered alternately 300 μm each side of the median plane of the cell. Each sense wire is surrounded by four grid wires of 125 μm diameter Cu-Be arranged on a 6 mm square matrix. Significant benefits arise from the double grid design including reduced cross talk, lower wire tensions, improved cell isochronicity, and reduced grid wire surface fields. All wires are crimped under tension (T_{sense} = 120 g, T_{grid} = 400 g) in pins which are held in position by means of high precision extruded Noryl templates at each end of the cell. The principal source of error in the wire position ($\approx$ 20 μm) arises from the inherent inaccuracies in the crimping technique. The cell ends are closed by PCB's containing electrodes which cleanly terminate the electrostatic field of the cell. Aluminium foils covering the outer surfaces and connected to the tank provide electromagnetic isolation between the individual planes. A set of precision dowels fix the relative orientation of each plane (to $<$ 0.06 mr), the orientation of the planar supermodule with respect to the FWPC and the planar chamber/FWPC combination with respect to the tank.

The cell electric field distibution is controlled by seven different voltages: the sense voltage defines the gas amplification, the central strip voltage affects the sense field homogeneity, four drift strips and the cathode voltages determine the field gradient. The grid wires are grounded. All voltages are supplied directly from the HV supplies, after suitable fan out, without the use of resistor chains at the chamber. Field optimisation and chamber operation are considerably aided by the fact that the double grid geometry produces a strong decoupling between the sense field (gas amplification) and the drift field. The chambers are operated at atmospheric pressure in a mixture of 90% argon, 10% propane with an admixture of alcohol obtained by passing the gas over a bath of ethanol maintained at 0° C. Throughout HERA operation all of the planar chambers have been operated with a bulk drift field of 1 kV/cm and gas amplification of $1 - 2 \times 10^4$ (V_{sense} = 1550 V, E_{sense} = 135 kV/cm, E_{grid} = -5 kV/cm, $V_{cathode}$ = -2400 V). At these settings the drift velocity and Lorentz angle at B = 1.14 Tesla are 42 μm/ns and 41.8°, respectively.

The outer end of each sense wire is AC coupled into a current sensitive preamplifier (two drift cells per preamplifier) and the signals transmitted via 40 m of 50 Ω coaxial cable to the FADC's. Pulse profile (Q, t) analysis in the front end data aquisition system yields one drift time coordinate measurement perpendicular to the sense wire and one pulse integral measurement. Resolutions achieved on ep data are typically 150 – 170 μm for the single point spatial resolution and $<$ 2 mm for the double track resolution.

4.3.2 Radial chambers

Each of the three identical modules in the FTD contains a radial wire drift chamber as its most forward (positive z) component. Each of these chambers covers 360° of the azimuthal angle ϕ,

which it does as 48 separate sectors of 7.5°. Each sector is a drift cell having 12 sense wires (50 μm diameter Stablohm [42]) staggered alternately 287 μm each side of a plane which bisects the sector. The sense wires, which are all parallel within one of these cells, are separated by 10 mm. Between adjacent sense wires, and positioned on the plane which bisects the the sector, are field wires parallel to the sense wires and half way between them. All these wires are supported by crimp pins. At the small radius end (r = 152 mm), the crimp pins are mounted in a cylindrical Noryl hub, and at the large radius end (r = 760 mm), in Noryl templates precision bonded into the cylindrical wall of the composite structure which contains the whole 48 cells of the radial chamber as one rigid unit. The structure of these radial drift chambers has been described in references [47, 48, 49].

The wedge-shaped drift cells are separated from each other by cathode planes which consist of voltage graded copper strips on each side of thin paper-epoxy material (PCB technology). The electrostatic field cage for each drift cell is completed by voltage graded shaped conducting strips bonded onto the plane inner surface of the composite structure (for the high z end of the wedge), and onto a rather complex window assembly, described below, which is affixed as a lid to the composite structure (for the low z end of the wedge).

Detailed design of this window, forming the plane surface of the radial chamber towards low z was determined by the requirement to detect the transition radiation (TR) entering the radial drift chamber. The X-ray component of TR produced by an ultra relativistic charged particle contributes to an enhanced track ionisation, hence to enhanced charge collected on one or more of the sense wires, provided that all ionisation deposited anywhere in the cell is collected onto the sense wires and not onto field wires. The window of the radial chamber is thus designed to be as X-ray transparent as possible, and to ensure maximum X-ray detection efficiency as close as possible to it inside the drift cell. Because of the imperfect nature of the field grading close to the V shaped strips, ionisation deposited within about 2 mm of the window cannot be collected onto the first sense wire. Such a loss of X-ray sensitivity is significant at the TR entry (low z) side of the radial chamber, where most of the X-ray photons photo-ionise the chamber gas. For this reason the V shaped strips to create the drift field are of aluminium on mylar and are supported on Rohacell [43] spacers which position them 5 mm from the thin mylar window which isolates the chamber gas volume. The effect of this window assembly on the electrostatics is to move the drift field inhomogeneities out of the sensitive gas volume. Then at the mylar wall closing the gas volume the drift field is uniform and parallel to the surface, except directly opposite the sense wire. Charging effects on the mylar window are then minimal, and the ionisation collection efficiency on the first sense wire is optimal right to the edge of the gas volume.

Because all the sense wires are in the radial direction, a coarse determination of the radial position of a track may be made from charge division if a wire is read out at both ends. However it is not physically possible to have preamplifier cards at the small radius end. For this reason the sense wires of one 7.5° sector drift cell are connected at the inner hub to the sense wires of another 7.5° sector drift cell, actually 105° away in azimuth, so that when sense wires are read out at the outer radius charge division is possible along this double length of radial wire. Current sensitive preamplifiers are at each end of these sense wire pairs, each channel of which drives approximately 40 m of cable to the FADC system. Pulse profile (Q, t) analysis gives the drift coordinate perpendicular to the sense wire plane, and two pulse integral measurements Q_L and Q_R from the two ends give the radial position by charge division.

The spacing in the z direction between the sense wires of the radial chambers, and between the three modules, may be seen from Table 4.4. The spacing between the sets of planar drift chambers and the radial drift chambers may also be seen in this Table. Concerning the azimuthal position of the radial chambers, the plane which bisects a 7.5° sector cell (and about which the sense wires are staggered) is at ϕ = 3.75° in the first module, at ϕ = 7.5° in the second module

and at $\phi = 6.25°$ in the third module. The resolution achieved with the 50 % argon, 50 % ethane gas mixture used so far is $150 - 200$ μm. The gas mixture which is intended to use for optimal detection of transition radiation is given in the following section.

4.3.3 Transition radiators

A passive array of polypropylene layers provides a sufficient number of dielectric interfaces for useful transition radiation (TR) X-ray emission. The dielectric constant, the layer thickness and the mark to space ratio of the polypropylene sheets determine the X-ray yield and the energy spectrum. For the values chosen the spectrum peaks around 6 keV for 20 GeV electrons. The interface between the TR and the radial wire drift chambers has been optimised for transmission of these X-rays. As described in the previous section the radial wire drift chambers are designed and operated both for optimal track point measurement and efficient X-ray detection. The combination of TR and radial wire drift chamber is designed for electron-pion discrimination, at the level of 90% electron acceptance with less than 10% pion contamination, up to 80 GeV for tracks passing through all three modules of the FTD. To achieve this, it is planned to operate the radial wire chambers with a gas containing xenon which has a high photoionisation cross section at 6 keV. A 20 % xenon, 40 % helium, 40 % ethane mixture satisfies the requirements of TR detection, and acceptable charged track dE/dz ionisation density, and also suitable drift velocity for the requirements of the drift chamber. Data taken with a radial drift chamber in a test beam at CERN have shown that the design discrimination between electrons and pions can be achieved with this gas [50, 51].

The assembly of polypropylene sheets is self supporting but is enclosed in its own gas envelope in order to isolate it from the gases used in the rest of the FTD. The helium-ethane mixture surrounding the polypropylene sheets is chosen to give the same partial pressure of helium as in the radial drift chamber. This is important because the interface is the thin mylar TR window of the radial drift chamber section which could be damaged by pressure differences in excess of about 100 μbar.

parameter	unit	module 0	module 1	module 2
$z-$position first planar wire ($z-$plane)	mm	1324.4	1746.4	2168.4
$z-$position first planar wire ($u-$plane)	mm	1367.0	1789.0	2211.0
$z-$position first planar wire ($v-$plane)	mm	1409.6	1831.6	2253.6
$z-$position first radial	mm	1539.0	2015.0	2437.0
rotation of radial chambers with respect to $\phi = 0°$	°	3.75	7.5	6.25

Table 4.4: Forward tracker drift chamber positions.

4.4 Drift chamber electronics, readout, and front end data processing

4.4.1 Introduction

All drift chambers in H1 are connected to one of the three independent branches of central data acquisition system (CDAQ). Each branch provides an independent readout of part of the apparatus with a dedicated connection to the central trigger (subtrigger controller crate, STC) and central event builder (VMEtaxi optical link, see Section 10.1.2). The drift chamber branches are organised as a microcosm of the whole H1 readout. There are a number of front end crates where the analog signals are digitised and processed. There is a trigger connection based on the

H1 standard STC crate and STC interface cards (see Section 8.3.5 and reference [52]), and local logic to produce and distribute control signals to the front end crates. Finally there is a master crate where the complete data from the branch is collected and sent to the CDAQ. It is possible to add monitoring crate(s), where local data monitoring can be performed. Figure 4.15 shows the general layout of each drift chamber branch.

The drift chambers are distributed between the branches according to position in the detector. The inner and outer jet chambers and the inner and outer z chambers form branch 4 (CTD). The forward radial and planar chambers form branch 5 (FTD). The $\theta-$ and $\phi-$ chambers of the forward muon spectrometer form branch 6 (FMu). Table 4.5 shows the sizes of the various components, and the typical size of the zero suppressed digitisations (raw data) and processed summary data ((Q,t) data).

4.4.2 Operation of the readout

The analog signals from the preampflifiers mounted on the detector are received by 104 MHz FADC cards which continually digitise and store the data - at this point we are recording data at a rate of over 600 Gbyte/s over all drift chambers. On receipt of a first trigger level (L1) signal the digitisation is stopped so that the data recorded in the FADC card memory includes, for each detector, all digitisations which could have occured between the time of the event and the maximum possible drift time for that chamber.

At a second trigger level signal the data is copied by the scanner controller cards, which simultaneously build a list of significant transitions above and below a predefined detector dependant threshold. The full 2.5 Mbyte of raw data for an event is copied into the second level buffer at a speed of 3.3 Gbyte/s. At a third trigger level signal, the processor card in the FADC crate reads the data from the scanner, and writes an off-line format data bank into an intermediate buffer which contains blocks of significant data, i. e. zero suppressed data. The zero suppressed event size is approximately 100 Kbyte. An asynchronous background task of the processor then analyses this data to produce summary charge and time information only. Considered crate by crate this corresponds to 50 Kbyte of raw digitsations, $4 - 5$ Kbyte of zero suppressed digitisations, and 1 Kbyte of summary information. The output of the processing is written into triple ported buffer memory on the VIC8251 intercrate connection [53]. When a complete event is available from all front end crates the master processor collects the data from this buffer memory and writes the complete event to the multi-event buffer of the optical fibre VMEtaxi link (see Section 10.1.2).

Chamber	Branch #	# of crates	# of channels	Raw data [Kbyte]	(Q,t) data [Kbyte]
Radial	5	9	1728	20.5	2.4
Planar	5	6	1152	28.5	4.1
CJC1 and CJC2	4	23	2640	33.2	5.4
COZ	4	1	96	3.41	0.5
CIZ	4	1	60	5.14	0.9
Forward muons θ	6	4	1024		

Table 4.5: Summary of drift chamber readout data.

4.4.3 Amplifier

The sense wires of the tracking drift chambers are connected to amplifiers either at one or at both wire ends, depending on whether charge division is to be used to calculate a position along the wire. The eight-channel amplifier cards are mounted directly on the chamber vessel so that they are as close as possible to the ends of the sense wires. The sense wire and the grounded potential wires serve as differential input. The sense wire is at positive high voltage and therefore it is coupled to the amplifier via a capacitor (1.5 nF). The sense wires (in some chambers) and amplifier are protected by a spark gap, and a pair of crossed diodes to ground. Each amplifier channel consists of two stages of video amplifiers. The amplification is large enough that no further amplification is needed on the readout card. This gives optimum noise rejection and minimises the influence of pick-up on the cable to the readout card. The amplifier card has two test inputs which allow the application of test pulse signals to the inputs of odd or even amplifier channels.

4.4.4 FADC

The 9520 signals from the drift chamber are digitised by F1001-FADC's (flash-analog-to-digital-converter) [54]. The sampling frequency is 104 MHz, generated by an oscillator phase locked to the bunch crossing clock of the HERA storage ring of 10.4 MHz. The differential outputs of the amplifiers are connected to the FADC cards with multi-coaxial cable of about 28 m length. This cable also carries the power and test lines to the preamplifiers. The FADC-chips used have a resolution of eight bits [54]. The combined signal is fed to the FADC chip through a transformer eliminating DC offsets and via a resistor network that includes feedback of the input signal to the voltage reference, providing a non linear response with 8 bit accuracy for small signal amplitudes and a 10 bit dynamic range. Each FADC-chip is connected to one 256 byte deep memory which serves as circular buffer. During the active sampling phase of the FADC system signals are continuously digitised and stored in the memories. This recording process is stopped by a trigger signal that freezes the history of 2.5 μs in the memory. Sixteen FADC-channels are housed on one F1001-card, serving for the two amplifier cards i. e. 16 signal wires for the planar chambers of the FTD, or eight signal wires for other chambers which use double ended readout (both ends of the signal wire are connected to amplifiers). Up to 16 F1001 cards are housed in a F1000 crate. It has a VME backplane used for fast 32-bit wide readout of the digitised signals from the FADC-memories. The signal risetime at the sense wire is a few ns. It is deliberately degraded by the amplifier band width, cables, and coupling transformer to 18 ns (20 % to 80 % of pulse amplitude) at the input of the digitising FADC. This is the optimum for a time measurement with a FADC sampling at 100 MHz.

4.4.5 The *scanner*

In each F1000 front end crate there is an M1070 scanner card that acts as a sample controller for the FADCs, and provides fast readout and zero suppression of the FADC data. The scanner supplies the 104 MHz clock to the FADC cards, and at a level 1 trigger gates this clock such that the circular buffers of the F1001 cards contain the required time segment. At a second level trigger signal it copies the data from the FADCs into a local buffer in a series of synchronous bursts over the VME bus, in this way a transfer speed of 80 Mbyte/s is achieved, and the data for a full crate can be copied within the 800 ms requirement of H1. During the copy the data is compared with programmable thresholds and any significant transition (presently two subsequent time bins above or below threshold) is recorded in the hit table.

4.4.6 The front end processor (FEP)

At a third trigger level signal the scanner interrupts the front end processor (24 MHz FIC 8231 [55]) present in each F1000 crate. The interrupt handler reads the hit table from the scanner, calculates the required blocks of raw data, and copies these blocks into a mulitevent raw data buffer in an off-line format data bank. Each block includes four pre-samples before the hit starts to allow dynamic calculation of the pedestal, and blocks are merged in cases where a block would influence a subsequent block on the same wire. The background task of the FEP operating asynchronously to the events reads data from this multievent buffer and processes it where possible to produce summary information as described below. An output bank is written into a multievent output buffer in the memory of the VIC 8251 interconnect card, using the VSB bus connecting the processor and the interconnect (The VME bus may be occupied by the scanner reading a subsequent event). The input raw buffer and output buffer both typically hold 30–40 events, and this allows derandomisation over many events of the large range in processing times caused by localised high rack density.

4.4.7 Determination of charge and time (Q, t)

The relevant parameters of a signal pulse from a drift chamber wire are signal timing (t) and the pulse integral (Q). They allow the calculation of the distance of a crossing particle, from the sense wire (using the drift time), the position along the sense wire (using the pulse integral from both wire ends), and the energy loss dE/dx (using the sum of the pulse integrals). The determination of these signal parameters is done in a program which runs on the front end processors (FEP). In this way the amount of raw data is reduced by a factor of about five. In the following the (Q, t)–algorithm will be described. The input data are digitised signals with suppressed digitisations of the base line (zero suppression, as provided by the scanner hardware). The data are treated in several steps. For the CJC, CIZ, COZ and the radial chambers the first three steps consider the data of both wire ends separately,while the further steps use the combined information.

Linearisation: The FADC has a nonlinear characteristic. For the (Q, t)–analysis the measured digitisations are first linearised.

Hit search: One or more signal pulses may show up within the train of digitisations above the hit detector threshold. The leading edge of a new pulse shows the most prominent feature because of its steep rise. Therefore, the search for a maximum in the DOS (difference of successive samples) is used to identify a pulse.

Pedestal determination: The signal pulses are digitised by FADCs with an offset of approximately 10 counts due to the base line. This pedestal has to be taken care of in the determination of both charge Q and time t. At present the six pre-sample digitisations (before the pulse start) are used to evaluate the median and use it as pedestal for the whole pulse.

Combination of pulses from either wire end: Hits are detected by the above described algorithm on both wire ends independently. Hits from the two ends are combined if the leading edges differ by less than or equal to two clock bins.

4.4.7.1 Determination of drift time (t) The essential information for the drift time determination originates from those ionisation electrons which arrive earliest and rather simultaneously at the sense wire. This is best explained by Figure 4.4 showing the drift region of a CJC sense wire with drift lines and isochrones (lines of constant drift time). Ionisation electrons are produced along the indicated track. They drift along the drift lines towards the sense wire. Neglecting diffusion effects, those electrons arrive first at the sense wire, which are produced along the track in the region tangential to the isochrones. These electrons result in a sharp rise of the pulse at the wire, which is, however, smeared out by diffusion, chamber capacity, and amplifying electronics. Fluctuations of ionisation density can effect this behaviour only in the extreme case of a big ionisation gap in the tangential region. The remaining off-tangential electrons arrive at later times.

The trailing edge of the pulse is produced by the differentiating amplifying electronics. In addition, the trailing edge is influenced by fluctuations of ionisation density in the off-tangential region of the track. The resulting late arriving electrons produce big variations of the trailing edge of the pulse. The drift time is determined by chamber specific algorithms. For the CJC we describe it briefly here. Initially the time at 50 % of the full amplitude is determined by linear interpolation. The average $t_{50\%}$ of both wire ends and the average risetime are used for extrapolation to the arrival time of the first electrons, which is estimated to be at about 10 % of the pulse amplitude.

4.4.7.2 Determination of the pulse integrals (Q) The average pulse consists of about 20 digitisations. The pulse integral is determined by summing some fraction of these digitisations. Most important for the CJC (and radial drift chambers) is the relative error of the integral for the $z(r)$ determination. It is minimised by choosing a rather short integration interval of eight time bins. The timings of the pulses from the two wire ends differ because of different cable length and signal propagation along the wire. Therefore the phase of the integration interval has to be properly adjusted in order to guarantee the integration over the same part of the pulse on both wire ends.

4.4.7.3 Pulse subtraction for analysis of subsequent pulses If a pulse is recognised on the tail of a previous one it is analysed after effects from the previous pulse has been subtracted. After this procedure there is no special treatment of secondary pulses needed. For subtraction a standard pulse shape is used which has been determined by averaging a large number of pulses. This standard pulse has to be matched in phase and normalised in height in order to agree with the proceeding pulse. The pulse subtraction is done for the signals of the two wire ends independently.

4.4.8 STC crate

The STC provides a standard interface to the central trigger electronics. Two cards described below provide the special functions required in the drift chamber readout. A FIC and VIC provide readout of scalers etc. and event by event steering of the trigger interface logic. The processor can broadcast 12 byte of data to the scanner during the scanning time via a serial link - this allows e. g. event processing to be dynamically altered on the basis of trigger bits.

The 104 MHz phase locked loop (PLL) card generates a clock of ten times the frequency of the HERA clock via a phase locked loop circuit accurate to about 1 ns determined by the jitter on the input clock.

A logic card acts as sequence controller. Although responses from the scanner could by simple combination be used directly to respond to the central trigger, inclusion of the logic card

in the path allows better overall performance by overlapping some stages of processing with refill and other delays of subsequent events. This places much of the response time of the DC systems in second or even third order dead time, and allows the DC systems to be run at almost full throughput with little or no actual dead time (see description of central trigger operation in Section 8.3.5)

4.4.9 The master crate

The master crate contains interfaces to the CDAQ (VMEtaxi link) and to other crates in that branch (VIC8251). On startup, the master processor loads all other processors with code and data stored in non volatile ram. Once the other processors are running, all communication is made through the buffer memory of the VIC boards connected to each of the remote processors. During a run the master processor operates asynchronously, waiting for an event to be signalled by the trigger processor, and then polling the FEP's until the complete event is ready to be built. The events are not buffered or processed by the master processor.

4.4.10 The monitoring crate

The monitoring provides access to the readout branch for chamber specific control and monitoring systems. A small fraction of the event data can be passed to the monitoring crate for local specialist monitoring, especially that which requires raw data that might be unavailable in the CDAQ monitoring systems. Data is collected from a dedicated memory in the master crate using a differential VSB extension [56] – the VIC8251 connection is not used for technical reasons. Data may also be fed back from the monitoring system into the data stream, to allow important slow control information (e. g. HV, currents) to be recorded together with the event.

4.4.11 Implementation

The drift chamber readout uses processors of the Motorola 68000 family throughout. These CISC processors are relatively easily programmed at the native instruction level, and all the readout code was written in assembler. For the (Q, t) processing, where software had to be developed with high level languages in an offline environment, the software was incorporated by simulating the environment of a development host (Apple Macintosh). By splitting the workload between many processors each fulfilling a specific task it has been possible to avoid the use of an operating system on any of the readout processors. This has minimised response times and maximised performance. All software run by the processors (including system software) was written by members of the H1 collaboration.

4.5 Proportional chambers

Between 5° and 175° the solid angle seen from the interaction region is completely covered by multiwire proportional chambers. Six independent planes in forward direction, four in central and as well in backward direction serve three different functions: they deliver a fast timing signal with a time resolution better than the separation of two succeeding HERA bunch crossings, they provide moderately accurate space points for charged particle track reconstruction at the first level trigger and lastly add an accurate track element in the backward direction, where the drift chambers fail.

The planar forward chambers (FWPC) are interspaced between different driftchambers and are exposed to high particle rates increasing towards the beam pipe. Hence minimum overall

thickness and minimal amount of material traversed, sufficient ageing prospects, and cathode pad size adapted to increasing rates near the beam pipe became the primary design criteria. These points do also apply for the two cylindrical chambers in the central region. The inner one (CIP) is closest to the interaction region and covers the largest solid angle. In order not to degrade the track reconstruction of the surrounding drift chambers, the CIP and its outer partner (COP), were fabricated with low mass materials and a narrow active gap. To get the necessary stability for this light stucture a sandwich type construction is used . Since the main purpose of the FWPC, COP and CIP is to provide space points for the first level trigger, a pad segmented cathode readout was chosen with graphited surfaces as in other chambers built for high rates [57, 58]. From the reconstructed tracks the event vertex can be deduced and other detector data like calorimeter and muon information can be validated. Since the trigger logic requests three space points per track, spurious background hits from uncorrelated noise and synchroton radiation are removed.

In backward direction the reconstruction of the scattered electron in low momentum transfer events calls for an accurate track segment. This is given by the signals from the four differently oriented anode wire planes of the backward chamber (BWPC). Several wires can be combined for triggering purposes. Standard planar chamber construction techniques sufficed here, since more than one radiation length of electronics and cables from the central tracker separate the BWPC from the interaction region. The BWPC covers the front surface of the backward electromagnetic calorimeter (BEMC) and hence also serves to discriminate electrons and photons.

The properties of all four chamber types are summarized in Table 4.6, more details on their construction and performance can be found in the following paragraphs. The front end electronics and readout system is identical for all chambers and is therefore discussed in common below.

4.5.1 Forward proportional chambers (FWPC)

Each of the three chambers in the forward tracker volume consists of two wire planes interleaved with three cathode planes. The gap between the two adjacent cathode planes is 4 mm wide, as indicated in Figure 4.16. All chamber frames are fabricated from glasfiber epoxy. To reduce the mass in the active area a laminated structure consisting of the following layers is used: 100 μm graphited mylar foil serving as cathode plane, 250 μm printed circuit board carrying 10 μm Cu readout pads, 3.3 mm Nomex [46] mesh, another 250 μm printed circuit board covered with 10 μm Cu for the strips leading from each pad to the preamplifiers on the chamber ends, a further 100 μm of graphited mylar foil in the central plane or aluminized mylar foil on the external planes for electromagnetic shielding. The graphite layers are produced by spraying a mixture of DAG 5466/DAG 213 [59] at 5 bars giving an initial surface resistivity of 1 M$\Omega/\Box$, which was reduced to 300 k$\Omega/\Box$ by polishing. Each chamber is strengthened by a backplane, 12 mm thick, with two layers of 250 μm fibreglas epoxy sandwiching 11.5 mm Nomex. The mechanical tensions of the wires and the foils are supported by 24 and 8 axial rods on the external and internal frames, respectively. The anode planes contain gold plated tungsten wires spaced by 2.5 mm. They are crimped on pins fixed on the frames. Each wire is connected to the following one through 1 MΩ resistors and to ground through 330 nF capacitors. Groups of 15 wires are connected to separate high voltage lines, which allows degradation of malfunctioning sectors. The cathode pads are ring shaped and cover an azimuthal angle of $\pi/8$ each, except for the four outermost of the 20 rings where the they cover $\pi/16$. The radial pad width increases with radius in geometrical progression between 18 and 37 mm. Two consecutive cathode planes are offset by one half of a ring, such that the effective polar angle resolution is halved: $r_{min,i+1} = r_{min,i} \times 1.0382$ with $167.5 \leq r \leq 750$ mm. The Pluto-gas mixture (see Table 4.6) was chosen, because the FWPC share their gas volume with the forward drift chambers and transition radiation detectors.

	unit	CIP inner/outer	COP inner/outer	FWPC # 1/# 2/# 3	BWPC
active length $\Delta z/\Delta r$[3]	mm	2190	2172	583	515
active zone starts at z/r[3]	mm	-1125	-1107	167	135
mechanical length $\Delta z/\Delta r$[3]	mm	2254	2262	665	597
total length $\Delta z/\Delta r$[1,3]	mm	2467	2360	665	708
thickness $\Delta r/\Delta z$[3,7]	mm	21.5 (25)	30 (34)	40	52 (60)
chamber starts at z/r[1,3]	mm	-1376	-1270	135	110
position of first anode r/z[3]	mm	157/166	501/514	1451/1874/2297	-1423
number of anode planes		1	1	2	4[6]
number of wires		480	1574/1615	724	2496
wire separation	mm	2.1/2.2	2.0	2.5	2.5
gap width	mm	3.0	4.0	4.0	4.0
capacity of chamber	pF/m	7.1/7.3	5.8		6.5
number of cathode pads		480	288	384	
cathode resistivity	k$\Omega/\Box$	$\approx$ 400	$\approx$ 200	$\approx$ 300	$\approx$400
length of pad $\Delta z/\Delta r$[3]	mm	36.6	120	13 to 54[4]	
thickness of pad	μm	Al 0.5	Cu 1	Cu 10	
width of pad $\Delta\phi$	°	45	22.5	45 (22.5)[2]	
readout wire diameter	μm	Al, 150	Cu, 50	PCB	
total thickness [6]	% X_0	0.0014	0.0018	0.017	0.063
anode wire tension	N	0.63	0.60	1.5	0.98
critical anode wire tension	N	0.33	0.32	$\leq$ 0.35	$\leq$ 0.83
anode wire ØW-Re(Au)	μm	25	20	25	30
plateau length	V	200/250	200	300	200
plateau starts at	V	2425/2375	2900	1900	2800
gas mixture	%	49.9–Ar		89.4–Ar	49.9–Ar
	%	49.9–C_2H_6		9.9–C_3H_8	49.9–C_2H_6
	%	0.2–Freon (R12)		0.7–C_2H_5OH	0.2–R12

Table 4.6: Proportional chamber parameters. The separate columns for CIP and COP refer to the two planes, for the FWPC to the whole module containing two planes.
[1] Inclusive preamplifiers.
[2] Only for the four outermost of the 20 radial pads.
[3] First coordinate for CIP and COP, second for FWPC and BWPC.
[4] Width increases with radius, $\Delta r_i = 0.0782 r_i$, where r_i is the inner radius of the pad.
[5] The anode wire of each successive plane are rotated by 45°.
[6] Incident particle trajectory perpendicular to the anode wires in the sensitive zone.
[7] In active zone (and at end flanges).

A track crossing all three or at least two modules of the FWPC has to fall into the polar angle range $6.6° \leq \theta \leq 18.0°$ or $5.1° \leq \theta \leq 21.6°$, respectively. For such tracks an effective timing resolution of 20 ns (FWHM) and 47 ns (base width at 10 % of the maximum) was measured in the first H1-data, well below the required separation of two bunches (see Figure 4.17).

4.5.2 Central proportional chambers

4.5.2.1 CIP The laminar structure of the CIP called for special construction techniques, which are summarized below and are described in detail in [60]. Figure 4.18 shows a cut through the two chambers and the end flanges with the connections to the preamplifiers.

The double layer of chambers consists of three concentric cylinders. During construction each chamber cylinder was formed on a steel mandril. The latter was manufactured from a steel tube, milled to a precision of 25 μm over the full length, closed by end caps and equipped with small holes in its walls. These holes were used to stretch the different foils on the mandril by evacuating the inner volume. With a smaller overpressure on the inner volume the finished chamber could also be easily removed from the mandril.

The innermost layer of the first cylinder, a 25 μm thick Al-foil provides the electromagnetic shielding. The next layer, 2 mm thick Rohacell foam [43] gives the chambers the necessary rigidity. Prior to cutting, the Rohacell was heated for 48 h at 160 °C and again heated at 180 °C for 24 h while held on the cylinder by Teflon bandages. This way it lost all internal stress and could be glued onto the Al-foil with 20 g/m^2 epoxy-glue [61]. The Rohacell surface was polished, and a second 25 μm Al-foil glued to it which serves as the inner cathode. After cutting the cylinder to the right length the Al-foils were connected to Cu-foils,at the ends and the glasfiber epoxy [29] end flanges were added. These carry the printed circuit boards for the anode wires, which are supported further by glasfiber epoxy rings at 1/3 and 2/3 of the chamber length. The active gap is 6 mm wide. The anode wires (gold plated tungsten) were transfered to the axially prestressed cylinder from planar frames. The latter were needed for the transport of the wires from a weaving machine operating with a tension of 0.7 N. During the transfer the wire tension was monitored electronically by measuring the resonating frequency, the axial stress was continuously released with each wire which was soldered to the chamber and glued to the inner support rings.

The middle cylinder forms the outer cathode of the inner chamber and the inner cathode of the outer chamber. Here the innermost layer, a 20 μm Kapton foil is coated with highly resistive graphite (400 k$\Omega/\Box$) on one side and 0.5 μm Al on the other side. The Al layer is segmented into pads on which the induced charge on the cathode is collected. The graphite layer in front guarantees a fast disappearance of the accumulated ion charge. This has the advantage, that the readout wires of the pads can be mounted outside the gas volume. The pads are edged from the Al with a felt pen saturated with 50 % NaOH solution. Comparing signal sizes in CIP, COP and FWPC, which have all different pad thicknesses indicates, that in CIP part of the induced signal is lost due to the skin effect. After several tests on prototypes [60] the graphite layer in the final chamber was produced by spraying a mixture of DAG213, DAG305 [59] and isobutylmethylketon (IBMK) in a ratio of 20 : 1 : 7 onto the Kapton foil with 3 bar. To improve the stability of the graphite layer and to evaporate the IMBK, the layer was heated to 110 °C. The cathode foils are again backed by 2 mm Rohacell. The readout wires (150 μm Al) are embedded into 250 μm deep grooves in the Rohacell running along the $z-$axis from the chamber end ($-z$ side) to hole centered over the pads. The wires were contacted onto the pads with silver paint, fixed mechanically into the holes with a "plug" and soldered at the flange end. Another 20 μm thick Kapton foil with Al-coating is glued on the Rohacell, which forms together with the wires a wave guide of $\sim 70\ \Omega$ impedance. The Kapton foil again backed by 1 mm Rohacell with a polished surface covered by another 25 μm Al foil serving as the cathode for the outer

chamber. End flanges and connections are made similar as for the first cylinder and the sequence of layers for the third cylinder is identical to that of the second.

The three sections were assembled together by sliding the outer over the inner cylinder which was fixed in z on a special tool. The same tool can be used to reopen the chamber. Gas sealing is provided by two O-rings at the end flanges (2 mm Ø). The overpressure in the chambers has to be kept small and needs to be monitored carefully in order not to distort the gap. The two chambers have independent gas distributions and are rotated by $\pi/16$ in ϕ with respect to each other. In this way the eightfold segmentation of each chamber can be halved at the trigger level by requiring coincidence of two planes. In z there are 60 pads in each ϕ sector of 36 mm width.

The chamber is normally operated with an argon–ethane–freon mixture (see Table 4.6, gas gain $\approx 10^5$). The single pad efficiency was measured in a test beam to 99 %, while at HERA 94 ± 2 % was measured with extrapolated jet chamber tracks. From the measured pulse height distributions the gap variations for this light chamber were deduced to be less than 0.2 mm. The measured test beam time resolution (FWHM 21 ns) compares well with the results at HERA (see Figure 4.17). This results converts into a 2 % probability to register a given pad with the wrong (neighbouring) bunch crossing. The probability for crosstalk, i. e. the probability to register signals also in neighbouring pads in z and ϕ and the inefficiencies across the pad boundaries are discussed in detail in reference [60]. The average number of active pads for crossing angles larger than $\theta = 40°$ in a test beam (1.4) compares well with what is observed at HERA.

We investigated the ageing of the anode wires, as well as of the aluminum and graphite cathode with a test chamber. A total charge of 0.2 C/cm per wire was accumulated using a ^{90}Sr source. A gain reduction of less than 10 % was observed for the standard gas mixture. The Al-cathode had a whitish deposit and on the graphite cathode dark lines parallel to the anode wires were seen. No ageing was observed for an additive of 0.2 % water after an irradiation of 2 C/cm. These results corroborate the more extensive tests using the same gas mixture summarized by Kadyk [62].

4.5.2.2 COP The construction of the COP follows closely that of CIP in those aspects concerning the sandwich structure (see Figure 4.19). Steel mandrils appropiate to the larger chamber radii were used. These mandrils were made of 2 cm thick steel plates reinforced on the inside by 1.5 cm thick flanges. The mandrils are machined to a precision of 60 μm. To improve the stability of the sandwich structure, the thickness of the core material (Rohacell) was increased to 4 mm. The graphite cathodes (7 m^2 area per chamber) are produced with a screenprinting technique using a resistor ink solution, rather than spraying . The ink [63] has a resistivity of 170 K$\Omega/\Box$ for a 15 μm layer and was diluted with a solvent monobutylic ether of ethylene glycol in a ratio of 1 : 3. A surface resistivity of 200 K$\Omega/\Box$ was obtained after polymerisation at 120 °C during 1 hour. The cathode pad structure is provided by glueing patches of 25 μm Kapton coated with 1 μm of Cu to the back side of the graphite cathodes, giving an 18–fold segmentation in z and 16–fold segmentation in ϕ. The cathode layer is backed by 3 mm Rohacell, in which 50 μm diameter Cu wires are imbedded. A 25 μm Kapton foil coated with 1 μm Cu put on top of the previous layer constitutes with the copper wires the transmission line that transports the chamber signals to the $-z$ end of the chamber. This layer is then backed by 2 mm Rohacell. The Vetronite (G10) end flanges of the chamber support the printed circuit boards to which the anode wires ($\approx$ 1600 per chamber) are soldered and assure the 8 mm chamber gap size. They form the only rigid structure to which the gas distribution and preamplifiers are connected. The three cylinder sandwiches are assembled in vertical position. Pulse height measurements showed that the gapsize variation is of the order of 0.3 mm [64, 65].

Despite its three times larger radius the COP is only moderately thicker than CIP (0.18 % radiation length instead of 0.14 %). The efficiency plateau is reached at 500 V higher tension

with the same gas mixture, a consequence of the larger gap. While in test beams CIP and COP behaved similar, at HERA noise level in COP is slightly higher due to more difficult grounding. This requires a higher threshold setting and leads to a typical efficiency of 92 ± 2 %, determined as above. The timing resolution is as required and shown in Figure 4.17.

4.5.3 Backward proportional chamber (BWPC)

The BWPC is equipped with five graphited cathode planes (50 μm Mylar foil) and four anode wire planes. It is the only chamber of the H1 set, in which the cathodes are not segmented and the anodes are read out. The graphite coating was fabricated with the same technique as described for CIP above. The wires and the foils are stretched between a 23 mm wide inner and a 67 mm wide outer ring of glasfibre epoxy (G10). These rings are 4 mm thick and sustain the active gap of 8 mm per chamber, as indicated in Figure 4.16. The wires are strung every 2.5 mm, but signals from two wires each are fed to one preamplifier. The wire orientations are vertical, horizontal and $\pm 45°$ for the four layers. Gas sealing and structural support for the whole assembly is given by a G10 front and back plane of 10 mm thickness milled down to 6 mm in the active zone. The latter starts at an inner radius of 135 mm and ends at 650 mm, while the whole chambers occupies the region betwenn $r = 110$ mm and $r = 818$ mm. The BWPC therefore covers polar angles of $174.5 \geq \theta \geq 155.5°$. The space points given by the BWPC contribute 0.5 mr to the angular resolution, of the same order as the multiple scattering in the material in front of it. For high energy electrons an efficiency of 87 % per plane was measured again from extrapolated jet chamber tracks. Normally three out of four planes are required in coincidence with the BEMC and additional hits due to preshowering are encountered, which leads to an efficiency of 98 %. The timing resolution is shown in Figure 4.17.

4.5.4 Proportional chamber electronics and readout

Preamplifier		Amplifier–Shaper	
Differential gain	65 nV/e	Max. differential gain	400
Rise time (10–90)%	2 ns	Rise time	9 ns
Fall time (10–90)%	20 ns	Pulse width (FWHM)	16 ns
Input impedance	64 Ω	Max. output voltage	3.2 V
Output load	$2 \times 50\ \Omega$	Overload recovery:	
Dynamic range	$\pm$ 300 mV ($\approx 10^7\ e$)	$V_{in} < 5 \times V_{in,sat}$	70 ns
Power supply	$\pm$ 3.5 V (22 mW)	$V_{in} = 10 \times V_{in,sat}$	100 ns
Size	$25 \times 10 \times 2$ mm^3	$V_{in} = 20 \times V_{in,sat}$	120 ns
		$V_{in} = 30 \times V_{in,sat}$	170 ns
		Power supply	+5, -5.2 V (320 mW)
		Size	$36 \times 3 \times 6$ mm^3

Table 4.7: Characteristics of the MWPC preamplifier and amplifier–shaper.

A schematic picture of the frontend electronics is shown in Figure 4.20. The cathode pad signals (CIP, COP, FWPC) and anode wires (BWPC), respectively are preamplified directly on the chambers. A differential signal is then transmitted through a 35 m long cable to the electronic trailer. Each cable contains 16 signal pairs and is connected to a receiver card. The latter contains shaping amplifiers, followed by discriminators with computer controllable thresholds. The characteristics of the preamplifier-shaper chain are listed in Table 4.7. The overall gain can be adjusted to chamber pulse height between 1.3 μV/e and 26 μV/e by means

of a resistor on the receiver card. A typical equivalent noise charge is about 3800 e, assuming a chamber capacity of 60 pF.

The digitized signals are synchronized with the HERA clock and stored in a pipeline constructed from the same gate arrays as used in the muon system (see Figure 6.5). Upon a positive first level trigger decision (L1-Keep), the pipeline clock is stopped. A positive second level trigger decision then initiates the data readout. The synchronized pad signals are furthermore made directly accessible to the z–vertex and forward ray trigger (see Section 8.3.1). Test registers allow controlling the readout and trigger chains.

The MWPC readout system, an independent branch of the H1 data acquisition system (see Figure 10.3), is responsible for reading 3936 channels, originating from 270 receiver cards in 15 crates, and some decision data from the two first level triggers. Besides the frontend crates, the system consists of two standard VME crates and one STC crate [52]. The latter is primarily responsible for distributing the clock and L1-Keep signals to the receiver cards and for notifying the readout processor, located in one of the VME crates, of central trigger decisions through a VMIC module [66].

The readout processor, a 24 MHz FIC 8232 [55], coordinates the data collection and zero suppression, and makes the event data available to the central data acquisition system (CDAQ) through a 512 Kbyte multi event buffer (MEB). The connection to CDAQ is maintained through a VMEtaxi module (Section 10.1.2), which accesses the MEB through the VSB bus, thus freeing the VME bus for frontend processes.

The second VME crate is dedicated to monitoring purposes. Processors therein can request a subset of events from the readout processor and perform any sort of monitoring tasks without slowing down the data acquisition. A VICbus interface is used as a link to the master crate [53].

Both the master and monitoring VME crates are connected to a supervising MacIntosh via a MICRON-MacVEE interface [67]. Although the DAQ program and a default configuration data base reside on a 512k EEPROM memory board in the master VME crate, which guarantees an automatic start-up without any operator intervention after a power interruption, a control program running on the Mac can overrule these default settings. Furthermore, the Mac serves as a user interface to the monitoring processes and as a debugging tool.

The frontend crates are equipped with a customized 'EasyBUS', which is essentially a simplified 16 bit wide VME bus with a 64 kWord address space lacking any interrupt capabilities but with added analog and ECL signal lines. The latter are used to distribute the clock and L1-Keep signals. The analog lines allow measuring the digitization thresholds loaded to the discriminators through an ADC located on a crate controller (CC) card. The primary task of the CC's is however to connect the crate to a branch driver card (BDC) residing in the master VME crate. The BDC-CC combination map the EasyBUS address space into the VME frame [68].

Each BDC is directly connected to the STC and contains a DMA (direct memory access) controller and a 4 Kbyte deep FIFO (first in, first out) buffer. An L2-Keep signal can thus initiate a frontend data transfer to the master crate without processor intervention. The maximum speed is 4.5 Mbyte/s. Each of the six BDC's installed in the MWPC area can theoretically control as many as eight frontend crates. The latter are grouped into pairs to make use of the 32 bit wide data path of the VME bus. To optimize readout speed, we have connected between two and six crates to one BDC.

The DAQ program [69] is written on top of a purpose built interrupt driven multi-tasking system. Tasks are scheduled every 100 ms on a software priority basis. DAQ related interrupts invoke the scheduler ensuring a fast real time response.

Upon an L2-Keep interrupt, the processor first reads STC related data. About 200 μs later, the first BDC has collected all data and generates an interrupt. The DAQ program keeps track of it and reinitialises the DMA for the next event transfer. The last BDC-generated interrupt is responsible for checking whether all BDC FIFOs have enough free space to store an additional event. If so, a front end ready (FER) signal is sent to the trigger independently of an L3 decision. The time needed until FER can be sent depends on the number of bunch crossings one wants to read out before and after the triggered event. With typically 10 events read, it occurs about 650 μs after the trigger. The FER signal is further delayed, if one of the BDC's does not contain enough empty space.

As soon as the first BDC generates its interrupt, the readout processor starts the treatment of the event data. It is zero suppressed by means of a lookup table, which translates each fired pad to a channel number, and stores the data to the MEB. An interrupt caused by a rejection of the event at the third trigger level may prematurely abort this process, scratch any data already stored in the MEB and stop ongoing BDC transfers. The status of the DMA's is used to determine how much data to flush from the FIFO's and the transfers are reinitialised for the next event. A L3-Keep interrupt causes the DAQ program to notify CDAQ upon completion of the data transfer to the MEB.

Each time a new event is started, the DAQ program checks whether a monitoring task posted a request for data. If so, an additional copy of the data in the MEB is written in the internal buffer of the VIC board. These data are complemented with the non zero-suppressed bit patterns and some status information. Events for which monitoring data are requested, increase for up to 50% the time spent for that event depending on the amount of non-zero data. A new event is only supplied when all the BDC FIFO's are empty. This is done on purpose in order to avoid a dead-time increase at very high rates due to the monitoring.

The first order dead time is only determined by the front-end transfer to the BDC as long as the BDC FIFO are not saturated. The saturation rate is given by the average time spent by the DAQ processor per event. During the 1992 run an average time of 4.2 ms per event was needed. This corresponds to an average of 237 hits in 10 bunch crossings.

4.6 Gas systems

As discussed above nine different types of tracking detectors are contained in the H1 detector. Since each detector has a different cell geometry for optimal track recognition, it naturally follows that each detector uses also a different gas for its optimal performance. Therefore nine separate gas circuits are necessary, in which the gas mixtures can be analysed, and where the gas flow and especially the pressure of the fragile detectors needs to be carefully controlled.

In addition, the requirements on the gas quality differ for the various detectors, e. g. the forward chambers and CJC need high purity gas because of long drift distances. Their relatively large volumes require also relatively large gas flows. Therefore in order to minimize gas costs and fulfill the condition of high purity and constant gas mixtures over long time periods, closed loop circuits were built for these chambers.

The central and backward proportional and the z–chambers are flushed with premixed gases. Also for these chambers pressure, gas flow and composition is controlled automatically in open circuits.

For simplicity three independent but otherwise almost identical units denoted in the following as systems I, II and III were built.

The main parameters concerning gas mixtures, flow rates and operational pressures of the detectors and the gas systems are given in Table 4.8.

Detector	Gas volume	Gas mixture + additives: volume ratio	Pressure relative to atmosphere		Flow rate		System
			typ.	max.	typ.	max.	circuit
	[l]	[%]	[μbar]	[mbar]	[l/min]		type
Planars+ FWPC	~900	$Ar/C_3H_8+C_2H_5OH$ (90/10)+1	150±100	1	1.3	3	I closed
Radials	~700	Phase I:Ar/C_2H_6 (48/52) Phase II: $Xe/C_2H_6/He$ $+C_3H_7OH$ (20/40/40)+1	150±100	1	1.0	2	I closed
Radiators	~500	He/C_2H_6 (60/40)	250±100	1	0.1	1.5	I open
CJC 1	~1140	Phase I: $Ar/CO_2/CH_4$ (89.5/9.5/1)	1500±500	5	1.5	3	II closed
CJC 2	~3080	Phase II: $Ar/C_2H_6+H_2O$ (50/50)+0.5	1500±500	5	4.5	9	II closed
CIZ	~55	Ar/CH_4+H_2O (80/20)+0.2	150±100	1	0.1	0.6	III open
COZ	~240	$Ar/C_2H_6+C_3H_7OH$ (48/52)+1	150±100	1	0.2	0.8	III open
CIP	~30	Ar/C_2H_6/Freon12 + H_2O (49.9/49.9/0.2)+0.2	150±100	1	0.07	0.6	III open
COP	~150	Ar/C_2H_6/Freon12 (49.9/49.9/0.2)	150±100	1	0.1	0.6	III open
BWPC	~120	Ar/C_2H_6/Freon12 (49.9/49.9/0.2)	150±100	1	0.1	0.6	III open

Table 4.8: The different circuits of the gas systems.

4.6.1 Gas supply and pipe-installation

Outside of the H1-hall two large dewars serve as liquid supply storages for argon and nitrogen gas. All bottles with inflammable, pure and premixed gases are housed in two rooms on the same level equipped with the necessary safety installations. From here stainless steel pipes are installed to the three gas systems, located in a well ventilated room on the first underground floor. All mixing of gases, purification and automatic analysis, flow and pressure control of the detectors takes place in this gas control room. It is connected via a 25 m deep chimney with the experimental hall. For each circuit a gas inlet and outlet stainless steel pipe runs through this chimney and is from there connected to a stainless steel hose, which ends on a gas distribution system at the top of the electronic trailer, at the same height as the tracking detectors. The use of flexible pipes with typical inner diameter of 10 mm saved costs and considerably facilitated the installation through the hall, especially for the detector in- and out-beam position and from the gas distribution rack to the detectors inside the iron.

The gas distribution rack itself serves two purposes: Firstly, the gas inlet flow for each detector is split corresponding to the number of independent chambers supplied and is adjusted by mechanical flowmeters to assure correct flow in each chamber. Secondly, the static pressure of chambers relative to atmosphere is measured at this position with highly sensitive pressure sensors in the μbar range in order to avoid too high hydrostatic pressure differences between chambers and sensors.

4.6.2 Gas circuits

A simplified diagram of the gas circuit of the planar chambers, which is typical for all gas circuits used in our systems is shown in Figure 4.21. From an inlet manifold either pure or premixed gases can be fed into the circuit which together with the barrel has a volume of about 100 l. As in most of the chambers inflammable gases are used during running conditions, it is essential to purge them beforehand. This is done by gently filling helium or argon via the two flowmeters FL1-1 and FL1-2 into the chambers, while the chamber gas at the same time is sucked out by the membrane pump CP1-1 and vented to the atmosphere. To hold the chamber pressure during this operation within adjustable tolerances of about ± 100 μbar, the solenoid valves SV1-2 and SV1-3 will be either opened or closed depending on the actual pressure conditions inside the detector. As seen from Figure 4.21, the inflow and outflow of the chamber gas is split into two paths, one of them containing instruments for continous gas analysis like infrared meters, a hygrometer and a gas chromatograph in combination with an oxygen trace analyzer.

After the purging the chambers have to be filled with the real chamber gases. This is done either by using premixed gas in a similar way as in the purging procedure, or by introducing approximately the right proportions of first the non-inflammable and later the inflammable gases into the chambers. Then, inlet valve and vent valve are closed and the circuit switched from the open to the closed mode. The gas circulates through the barrel, the purification units, if needed, through a temperature controlled alcohol or water bath, and through the chambers.

To some extent the purification units absorb part of the gas components particularly hydrocarbons. Therefore a readjustment of the mixture is necessary after typically one day of circulation. To maintain the correct mixture gas can be added to the barrel manually. Repeated circulation for several days, especially when additives like water or alcohol are used, leads then to a homogenous gas mixture constant in time.

4.6.3 Gas additives

As can be seen from Table 4.8 for each detector a small amount of vapour is admixed to the chamber gas to prevent ageing. Freon 12 is directly admixed into the premixed bottle. Alcohol or water are added by passing the chamber gas over a bath of the corresponding cooled or frozen liquid. This is achieved by installing into a conventional refrigerator six different reservoirs, which can be temperature controlled within a certain range, thereby allowing the adjustment of the amount of additives by varying the bath temperature.

4.6.4 Purifiers

The closed loop circuits are supplied with purification units for removing oxygen, water and low concentrations of higher organic compounds. For oxygen removal 2 kg BTS-catalyst R3-11 [70] in the reduced state is used as an absorption agent and oxygen levels as low as 20 to 40 ppm have been reached over long time periods. Optimal oxygen removal is obtained with catalyst temperatures of 100 °C to 150 °C. However in the case of ethanol admixture, as is foreseen for the planar chambers, the alcohol will be cracked [71, 72]. Working near room temperature up to 80 °C at maximum circumvents this problem at the cost of a lower oxygen capacity for the purifier of only about 6 to 15 l [O_2/kg (catalyst)]. A similar problem arises when isopropanol is added to the chamber gas, which is recommended for Stablohm wires and the radial chambers [62, 47]. Since the isopropanol molecule is more fragile than the ethanol molecule, it is cracked even at room temperature into hydrogen and acetone by the catalyst [73]. Use of other O_2-purifiers working at low temperature like Oxisorb [74] and palladium-catalyst [75] give similar problems with alcohol-additives, especially with isopropanol, so that up to now isopropanol could not be added into the closed circuit of the radial chambers.

At room temperature water and higher organic compounds are removed by a mixture of 1.5 kg 3 Å and 0.5 kg 5 Å molecular sieve. In case of water or ethanol additives in the gas, the molecular sieve eventually saturates, but it is still capable of removing other impurities. Both, molecular sieve and BTS-catalyst are regenerated twice per year, which seems to be sufficient until now.

4.6.5 Gas analysis

Continuous control of gas compositon and inspection of new gas bottles connected to the systems are necessary for constant operation. Infrared meters, dedicated to a certain gas type, but with some sensitivity left for the gas additives give permanent information on changes in the quencher gas. Hygrometers in the ppm-range and an O_2-trace analyser allow an early indication of leaks in the systems. Complete analysis of the gas compositions are performed by an automatic gas chromatograph station, routinely switched into the different circuits. Independent of the use of calibration gases this instrument gives the different gas portions to an accuracy of ± 2 % of the measured value with an overall sensitivity of about 300 ppm [76, 77].

4.6.6 Electronic control

Based on the good experiences with the electronic controls of the L3 gas system at LEP for the time expansion chamber, the concept of the H1 gas system control follows this solution [78, 79].

A Motorola 68000 CPU serves as a crate master, integrated in a VME-system with the necessary resources for monitoring, logging and control equipment. The instantaneous values of all analog outputs of the measuring devices, especially those for pressure and temperature, but

also those for supply voltages are controlled with a set of suitable parameters allowing variations only within certain limits. Warnings or alarms are generated if one of the relevant parameters is exceeded and in the case of an alarm the whole system is stopped and the high voltage supplies of the detectors concerned are switched off. A computer independent hard wired logic with a more generous alarm setting protects the chambers against destruction in case of malfunctioning of the program or other unforeseen accidents. In this case also an alarm is generated and the powerless open solenoid valves in the distribution rack on top of the electronic trailer connect the chambers with an argon flushed reservoir at atmospheric pressure as indicated in Figure 4.21. A set of four independent serial links per gas system allows in addition the regular monitoring of all gas parameters. It provides information on the current situation for other users like the slow control system (Section 9) or the central data acquisition.

4.6.7 Safety

Since inflammable gas mixtures are used in all tracking detectors safety is an important aspect. For primary protection against explosion hazards all rooms in which inflammable gases are handled are installed with a good ventilation directly to the atmosphere. In the gas control room each gas system is surrounded by a tub-like fence 30 cm high with additional ventilation. All plumbing of the gas systems is made from copper or stainless steel tubes and fittings are Swagelok or Gyrolok types as recommended by the DESY-safety-group. Up to thirty gas sensors dedicated to different inflammable gases are distributed in the rooms, tubs and in places where pipe connections are made. These gas sensors generate two different alarm levels at 20 % and 40 % of lower explosion limit where the lower one initiates a power cut in the gas room and therefore a stop of the gas systems. At the same time all inflammable gases are disconnected from their supply bottles and the alarm information is distributed to the main control room and the technical support group.

Gas sensors are also distributed in the H1-detector region, on the electronic trailer with the distribution rack and in the volume occupied by the trackers. In addition this volume is flushed with $\simeq 6$ m^3 of nitrogen gas per hour to prevent accumulation of inflammable gases in case of a leak.

Since the operational pressure of most chambers is as low as 150 μbar relative to atmosphere and only 1.5 mbar in case of CJC, the amount of gas which may escape through a sudden leak in the chamber region is at maximum only a few liters, which are flushed away by the nitrogen. Small continuous leaks can be best controlled in the closed loop circuits by measuring the pressure drop in the barrel over several days. The maximum working pressure in these circuits is limited to 1.6 bar absolute. A typical leakage of about 4 l/day corresponds to a pressure drop of ~40 mbar/day. In the open circuits additional electronic flow controls, in series with FL1-1 and FL1-2, restrict the input flow. In case of a major leak the operational chamber pressure cannot be reached with the low flux adjusted by these controls. In addition daily control of the gas consumption by reading the pressure drop of all supply bottles ensures that there is no abnormal gas loss in one of the circuits.

4.7 Scintillators

Both the scintillator arrays discussed in this section are located in the backward region (see Figure 4.22) and have been installed to reject proton beam associated background at the first trigger level. The present life time of the stored proton beam in HERA varies between 10 and 48 h. The stored proton current design value is 160 mA with 2×10^{13} circulating protons in total. These protons are lost by beam gas and beam wall interactions producing background showers of energetic penetrating hadrons and halo muons. With showers ranging up to 30 m and a beam life time of 10 h the H1 sensitive detector volume is hit by such background with a frequency of 2.6 MHz, if losses are equally occuring everywhere around HERA.

4.7.1 Time-of-flight counters

The time of flight device (ToF) is located upstream of the interaction region at $z \approx -2$ m. This choice of position represents a compromise between good coverage of the detector and time resolution. The mean separation of particles from proton background and those from ep collisions at this point is ~ 13 ns. The electron bunches have negligible size whereas the proton bunches have a spread of 2 to 3 ns FWHM.

ToF is a hodoscope consisting of two planes of 3 cm NE102A plastic scintillator mounted perpendicular to the beam pipe. The plane nearest the interaction point (ToF1) lies at $z = -1.95$ m and has 16 butted counters, measuring 317×317 mm^2 thus matching the size of four BEMC stacks. The outer plane lies at $z = -2.25$ m and has eight larger counters (317×634 mm^2).

In order to function inside the 1.14 T field, ToF utilises 24 Hamamatsu R2490-01 high field photomultiplier tubes (PM). It is necessary to mount these perpendicular to the planes of ToF, requiring a light collection countersink to be machined into one of the large faces. A corresponding perspex truncated cone is glued to the other side to match the PM sensitive area. The PM's themselves are housed in non-magnetic holders and held in contact with the small light guide by springs.

Each wall of ToF is made up of a sandwich of scintillator and lead (Figure 4.23), mounted on a backing plate of non-magnetic steel to minimize stresses from the large magnetic field. The lead is 6.5 mm (1.1 X_0) thick to absorb synchrotron radiation, both to protect the counters from damage and to limit the number of triggers from this source. Eddy currents, produced during a magnet quench must be minimised, so steel is used rather than aluminium.

The six inner counters (four on ToF1, two on ToF0) can be moved horizontally up to 20 cm from the beam pipe using computer controlled pneumatic rams. This removes them from the high radiation fluxes around the beam pipe during injection which can damage the scintillator. With the counters in the open position, ToF can be split in half about the horizontal axis, allowing removal without breaking the vacuum in the beam pipe.

Signals produced by the PM's (24 in all) are amplified (×40), up to ~ 1 V before travelling down 29 m of cable to NIM logic located in the electronics trailer. Here the signals are discriminated and strobed in three time windows: background, interaction and global. A logical OR of the signals from each of the two walls is made for the three time windows and any coincidence causes a corresponding trigger signal to be sent to the central trigger logic (CTL) for use in the first level trigger. Most important is the background trigger which is used to suppress triggers from other subdetectors, leading to a 99 % decrease in the overall trigger rate,and subsequent reduction in dead-time. The interaction and global ToF signals are used in conjunction with other trigger elements to form physics and cosmic ray subtriggers.

A total of five trigger signals are sent to the CTL: the three coincidence triggers and two which require a hit in ToF1 only. The first of these provides a trigger for any hit in ToF1 in the global window, the second is a similar trigger for the background window. This last trigger was added after it was shown that the background singles rate from ToF1 was only 2.5 times the background coincidence rate,and the majority of the singles were from a source which did not give a background coincidence, but still caused triggers in the rest of H1. The getter pump for the vacuum system in the beam pipe, located just beneath ToF0 ($z = -2.25$ m) is the most likely source of this background. This signal will be installed into the first level trigger when luminosity is high enough to make the rate significant.

After the light transit time across the scintillator, the PM transit time and the 190 ns delay from the readout cable, the trigger decision is made within 60 ns after the signals reach the NIM

logic giving a total decision time of 250 ns. The device as a whole has a resolution of 4 ns, while individual counters have a resolution of the order of 2 ns.

Signals from each counter in each time window, plus the three coincidence triggers (75 total) are also sent to readout for later detailed analysis. Excess capacity in the MWPC cards allow these to be utilised for the readout of these few signals.

The setting and width of the time windows greatly affects the performance of ToF, and they have been continually updated as offline analysis proceeds. The background window currently starts 18 ns before the centre of the background distribution, and is 25 ns long. The interaction window starts 1 ns after the background window ends and is 13.1 ns long (Figure 4.24). A constant background of cosmic ray hits is present, about 200 entries per bin. Triggers in the interaction window are in fact much dominated by synchrotron radiation.

4.7.2 The veto wall

In addition to the ToF device two double scintillator veto walls were installed at a distance of 6.5 and 8.1 m, respectively upstream from the interaction point (Figure 4.22).

The smaller inner veto wall covers the near beam area down to a radius of 11 cm. The total area covered is 100×90 cm^2. A view perpendicular to the beam is given in Figure 4.25. The four scintillator pairs (NE 114, thickness 6 mm) are read via two photomultipliers (56 AVP, VALVO) each. The pairs are shielded against electromagnetic showers by lead walls of 4 cm thickness. Hard penetrating background particles are than identified in coincidences between two scintillators with a time resolution of $\pm$ 3 ns.

The large outer veto wall with an area of ca. 5×4 m^2 overlaps the inner veto and nearly all of the liquid argon calorimeter and the instrumented iron end caps (Figure 4.22). More details on the whole veto wall system can be found in references [80, 81, 82].

An additional 3 m concrete wall is installed between the outer veto wall and the experiment to protect the H1 detector against low energetic shower particles from upstream. The sketch in Figure 4.25 shows an array of 10 large scintillation counter pairs of up to 2.1×0.90 m^2 each, grouped around the last upstream HERA quadrupole with a 0.8×0.8 m^2 sized hole. The scintillator material used is NE 110, 1 cm thick. The large area scintillators are coupled to 20 large 5" phototubes of type VALVO XP 2041. These tubes are shielded with thick iron tubes and μ - metal cylinders against the strong magnetic fringe field ($\approx$ 10 mT) of the main and compensating coils. A large iron wall of 5 cm thickness separates all scintillator pairs of the outer wall. The coincidence resolution of such pairs is $\pm$ 8 ns. It is dominated by the light path differences over the large area. The light attenuation length is measured to be larger than 1.5 m and leads to inefficiencies for the detection of minimum ionizing particles of $< 10^{-5}$. The time resolution achieved allows a clear time separation between the background of the passing proton beam and event correlated hits during e-bunch passing.

Amplitudes, signal arrival times, rates and efficiencies of all counters are monitored online via a separated CAMAC-Macintosh readout system with ADC's, TDC's and scalers. This information is used to study the background condition after each filling and during runs. The time of flight information is also used to measure the real *ep* interaction point online with a precision of ca. 30 cm. In addition each of the two veto walls sends two trigger signals with HERA clock timing to the trigger logic. These trigger signals can be used to trigger on real or veto on background events. More information is delivered for each individual HERA bunch cossing via the central data aquisition system: 3×14 individual counter coincidences within the time gate of the event or $e-$bunch crossing, the $p-$beam background passage and the global HERA clock gate. Extrapolating from the 1992 low luminosity running of HERA the dead time induced by proton background in the veto wall can be estimated for the design luminosity. For 1.5×10^{30} cm^{-2}s^{-1} and for the 1992 HERA beam settings and losses the dead time is expected to be 10 to 30 %.

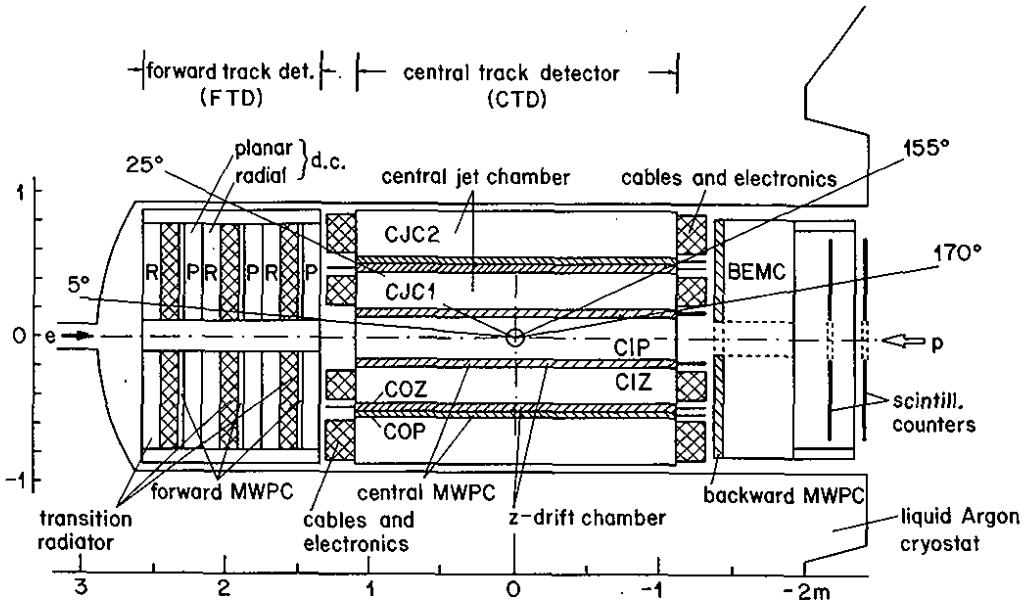

Figure 4.1: The H1 tracking system ($r - z$ view)

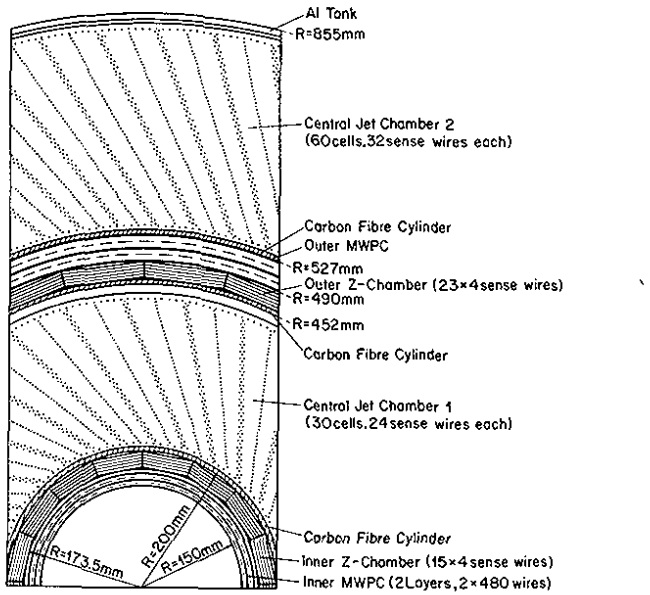

Figure 4.2: Central tracking system, section perpendicular to the beam

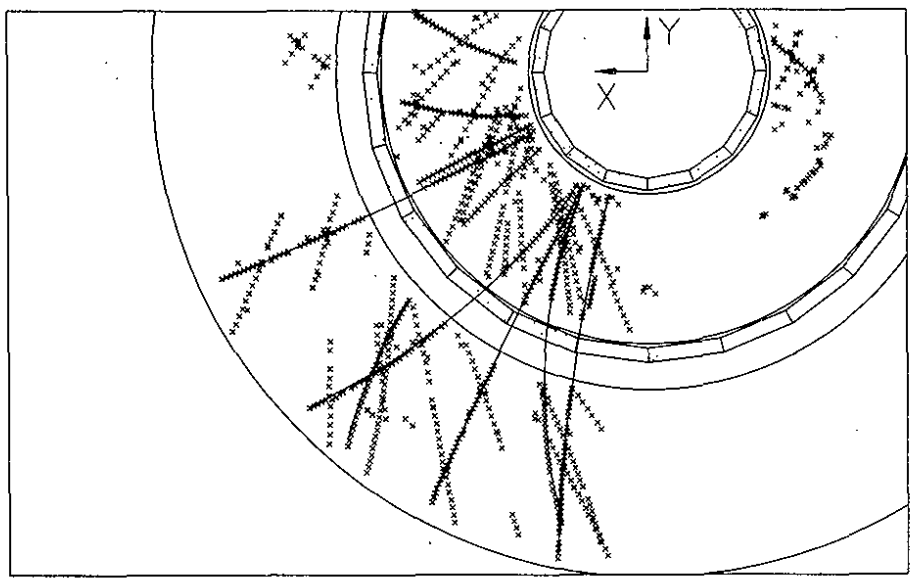

Figure 4.3: Electron-proton scattering event as seen in the CJC showing tracks found by the pattern recognition program and mirror tracks.

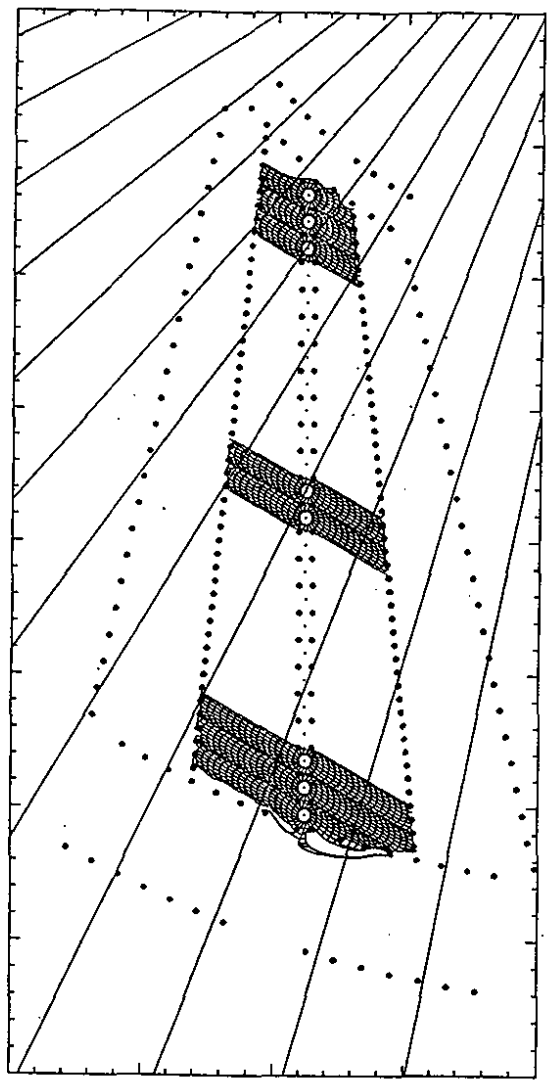

Figure 4.4: Simulation of a CJC cell indicating the drift regions of the senses wires, drift lines and isochrones. The straight lines represent infinite momentum tracks from the beam axis.

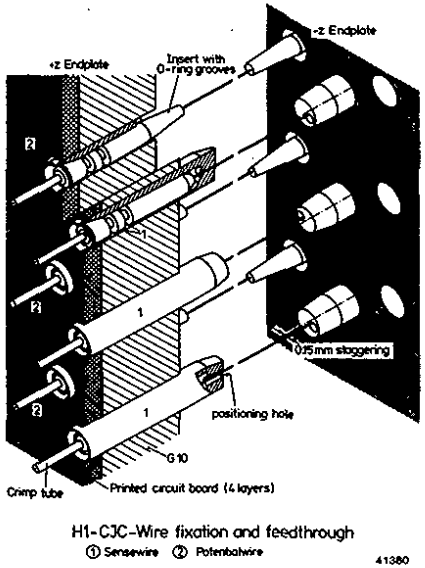

Figure 4.5: Details of the CJC endwalls.

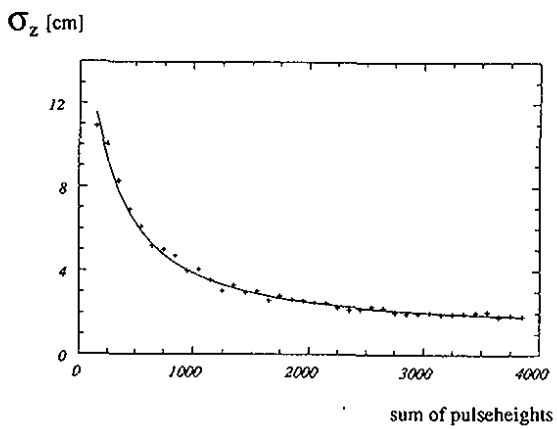

Figure 4.6: Dependence of the CJC z−resolution on the amount of ionization. A minimum ionizing particle deposits typically 1000 counts.

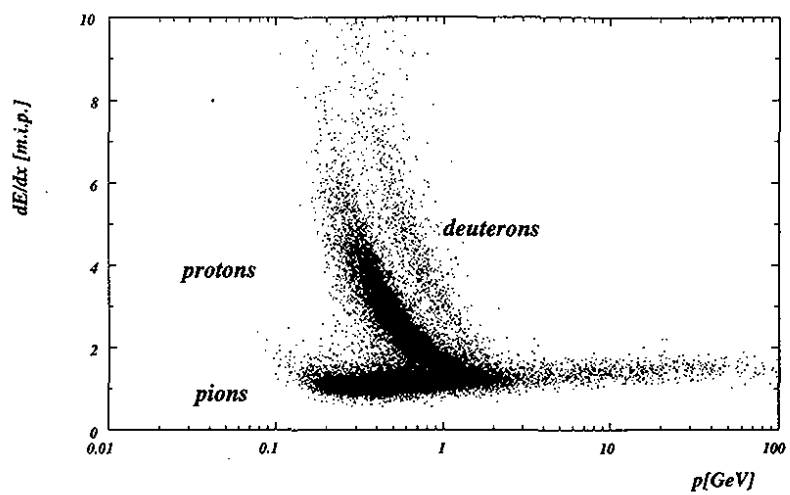

Figure 4.7: Specific ionization versus particle momentum measured in the CJC in HERA runs.

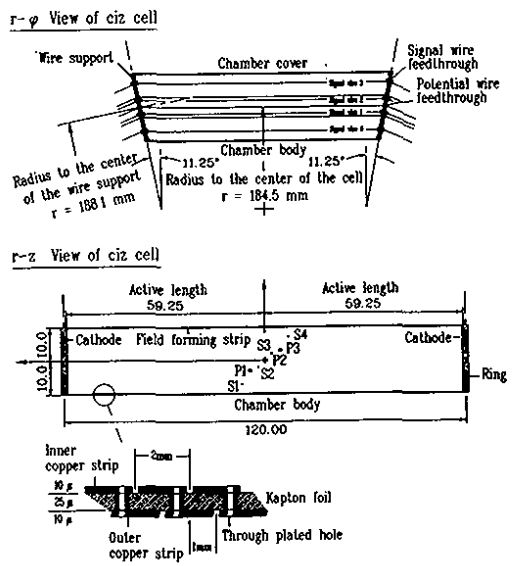

Figure 4.8: Longitudinal and transverse cross section through a cell of the CIZ. S: signal wires, P: potential wires, the z−coordinates are given relative to the center of the cell [mm].

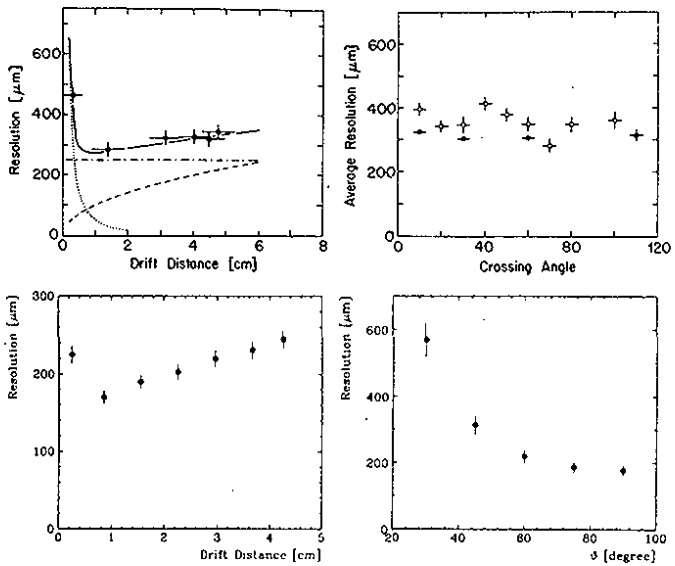

Figure 4.9: Left: Resolution as a function of drift distance for an $ArCH_4$ gas mixture (CIZ, top) and an ArC_3H_8 gas mixture (COZ, bottom). Right: Resolution as a function of crossing angle ($ArCH_4$, CIZ, top; ArC_3H_8, COZ, bottom).

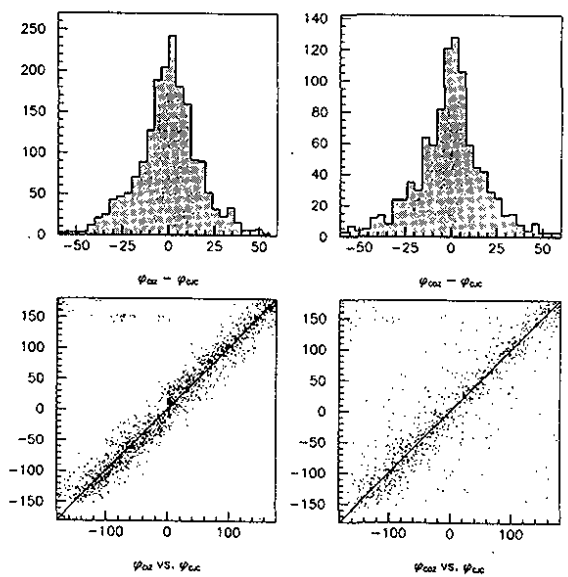

Figure 4.10: Bottom: ϕ coordinate measured with the jet chamber (track extrapolated into CIZ and COZ) versus the ϕ coordinate measured in the CIZ (left) and COZ (right) by charge division. Top: Projection of the twodimensional scatterplot along its diagonal.

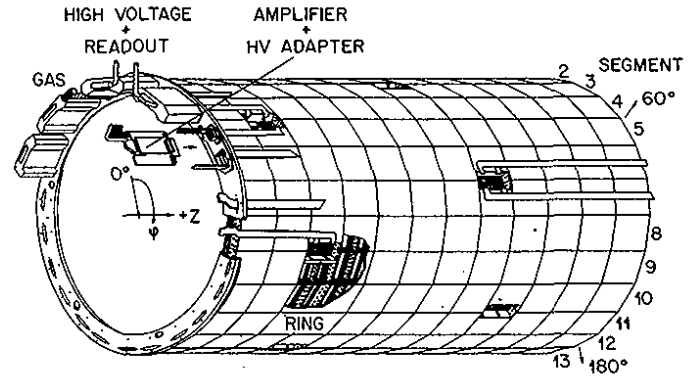

Figure 4.11: Schematic view of the COZ.

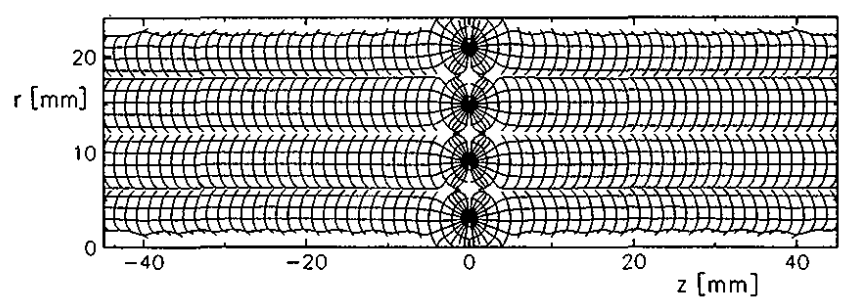

Figure 4.12: Cross section through the drift cell of the COZ indicating sense wire positions, drift lines and isochrones.

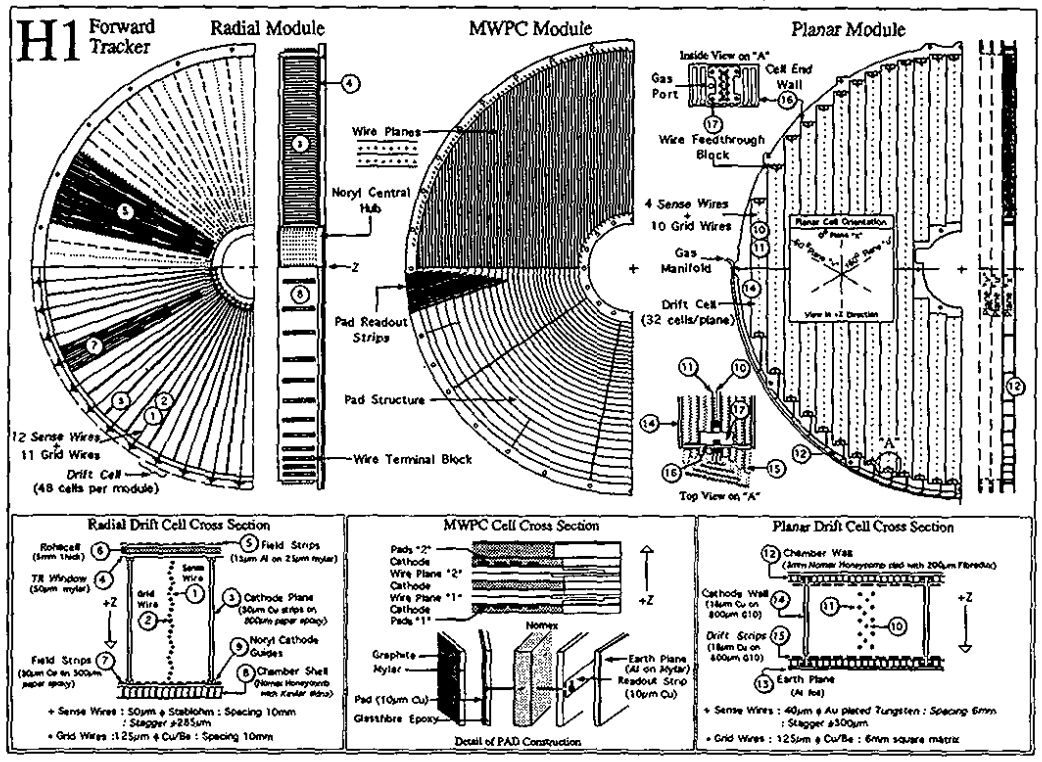

Figure 4.14: Details of the forward tracker construction. Top: cross section in the $r,z-$plane and in the $r,\phi-$plane showing the overall orientation of cells, wires and pads for each supermodule component. Bottom: details of cell construction.

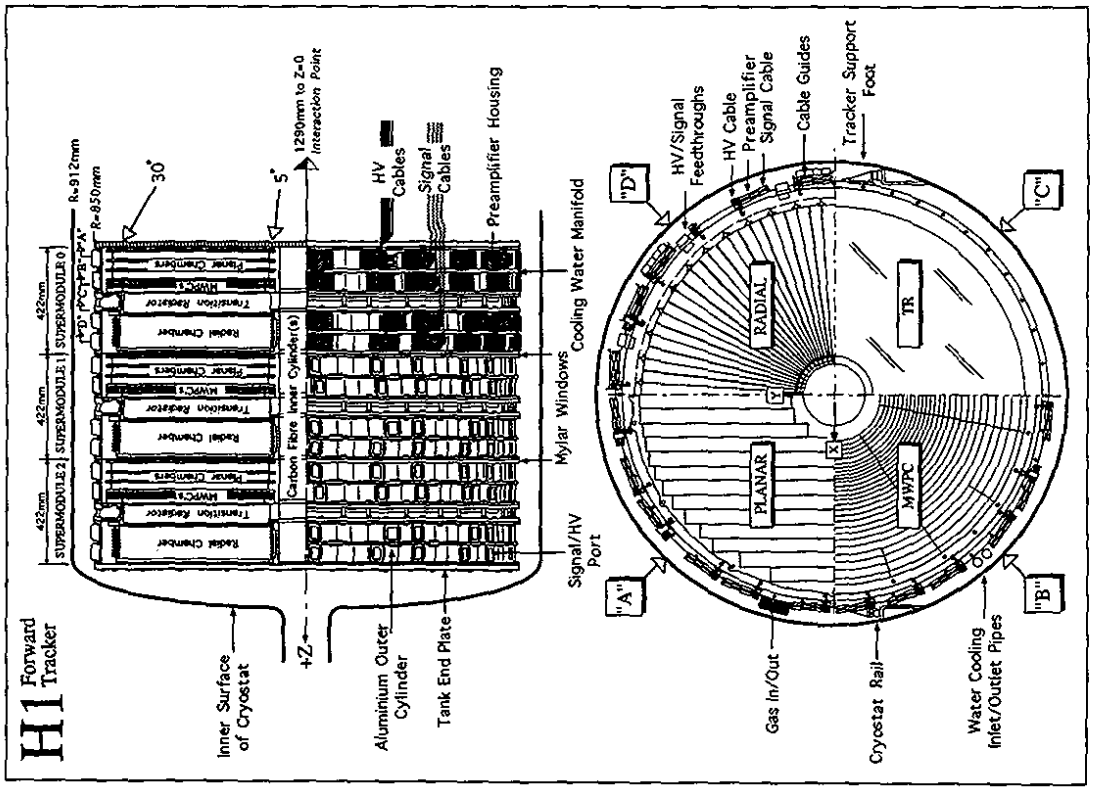

Figure 4.13: Forward tracker overview. Top: cross section in the $r,z-$plane showing the three supermodules. Bottom: cross section in the $r,\phi-$plane showing the basic cell structure of each supermodule component in one quadrant (A: planar chamber, B: FWPC, C: TR, D: radial chamber).

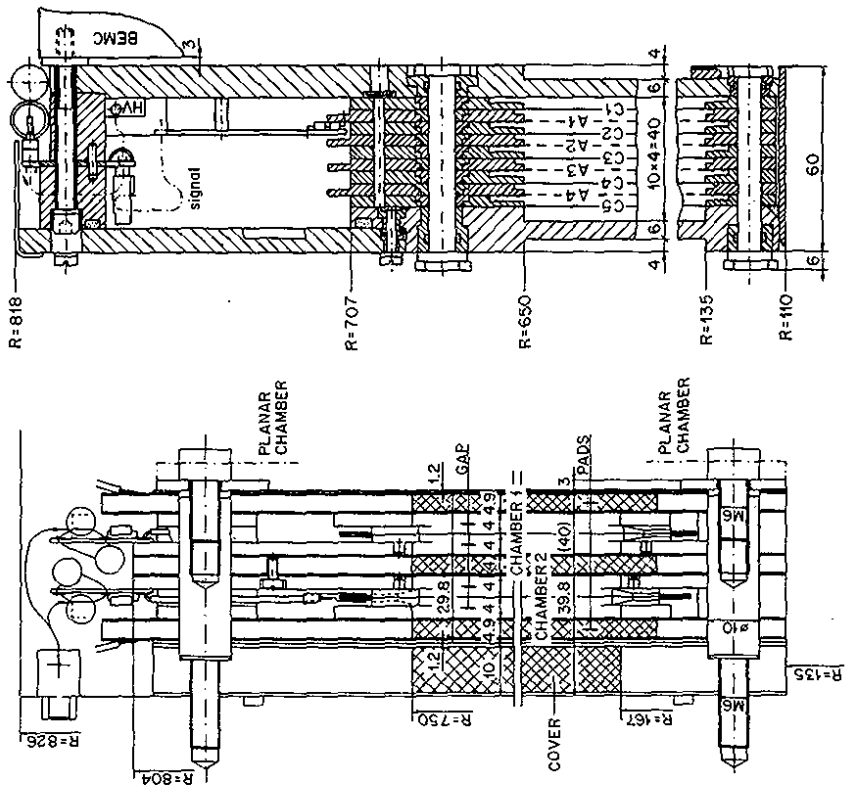

Figure 4.16: Cross section through the forward (left) and backward proportional chamber (right).

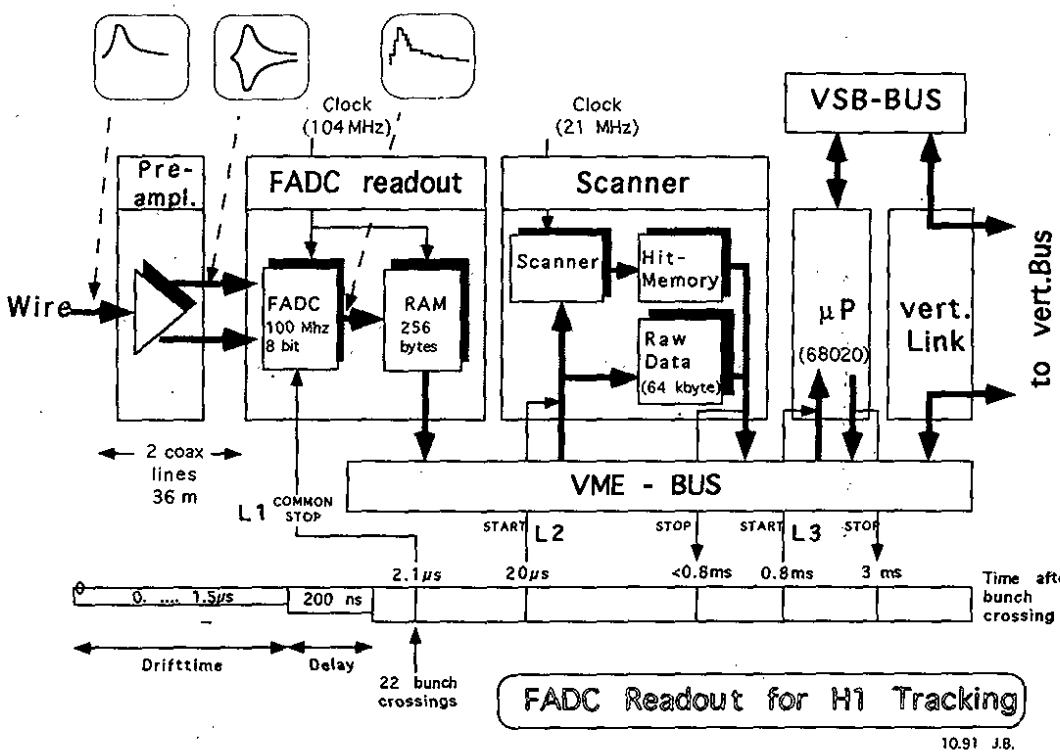

Figure 4.15: FADC readout system for drift chambers

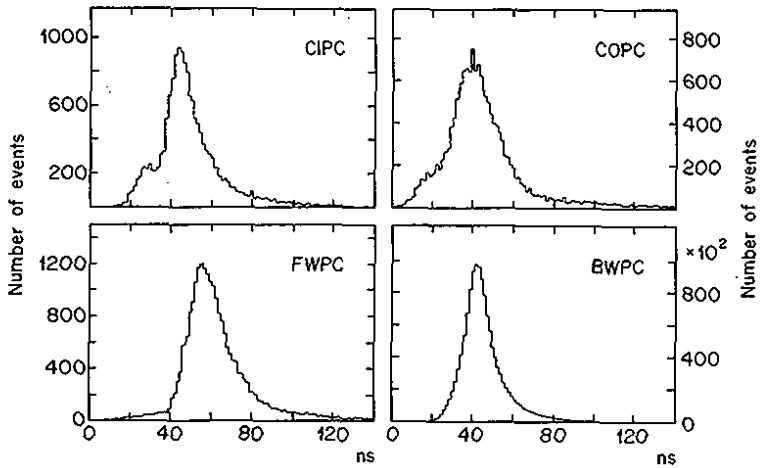

Figure 4.17: Timing resolution of the four proportional chambers with HERA beam. The reference signal is taken from the scintillators of the time-of-flight wall located behind the backward electromagnetic calorimeter.

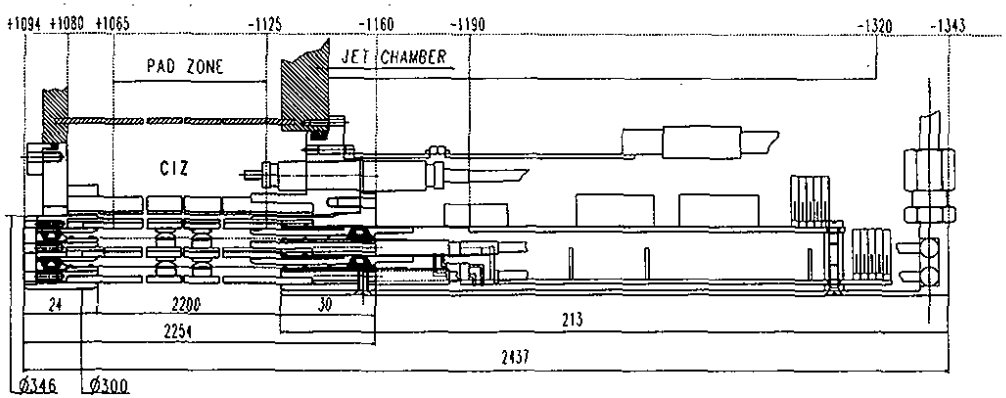

Figure 4.18: Longitudinal cross section through the CIP including the end structure showing the gas sealing and preamplifier connections.

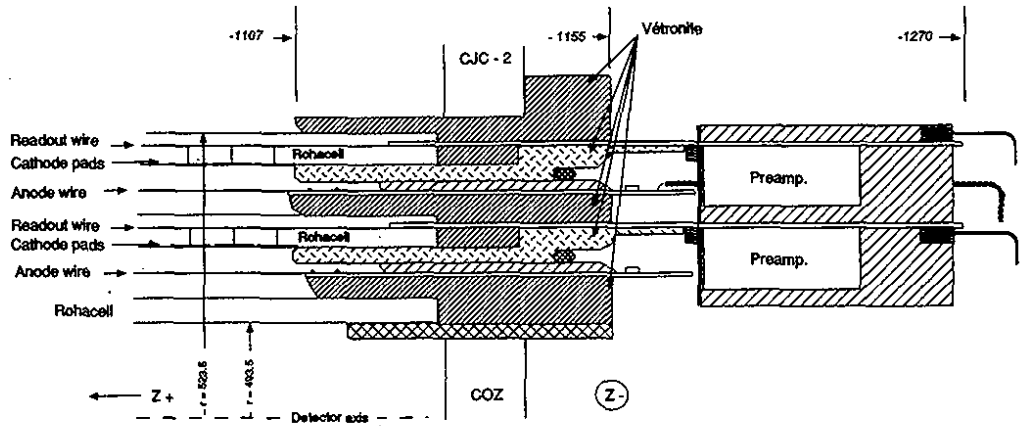

Figure 4.19: Longitudinal cross section and details of the COP.

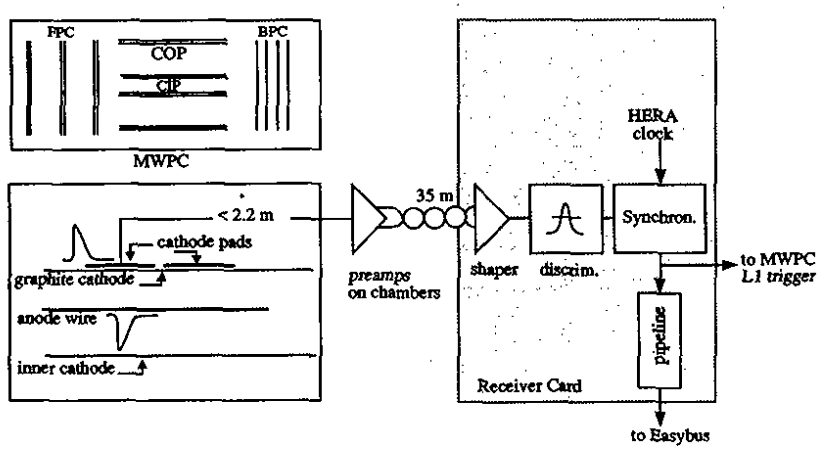

Figure 4.20: MWPC front end electronics and read-out system.

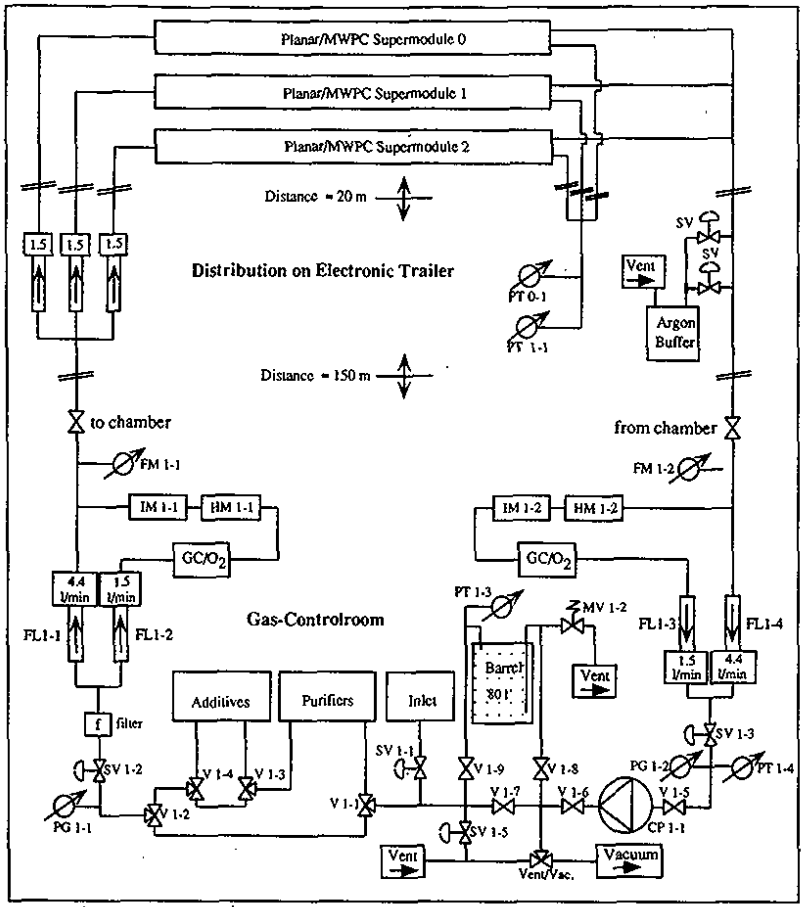

Figure 4.21: Layout of the closed circuit gas system for the planar drift chambers. CP: circuit membrane pump, FL: mechanical flow meter, FM: electronic flow meter, GC: gas chromatograph, HM: hygrometer, IM: infrared meter, MV: mechanical safety valve, O_2: O_2-meter, PG: mechanical pressure gauge, PT: electronic prssure transucer, SV: solenoid valve, V: mechanical two- or three-way valve.

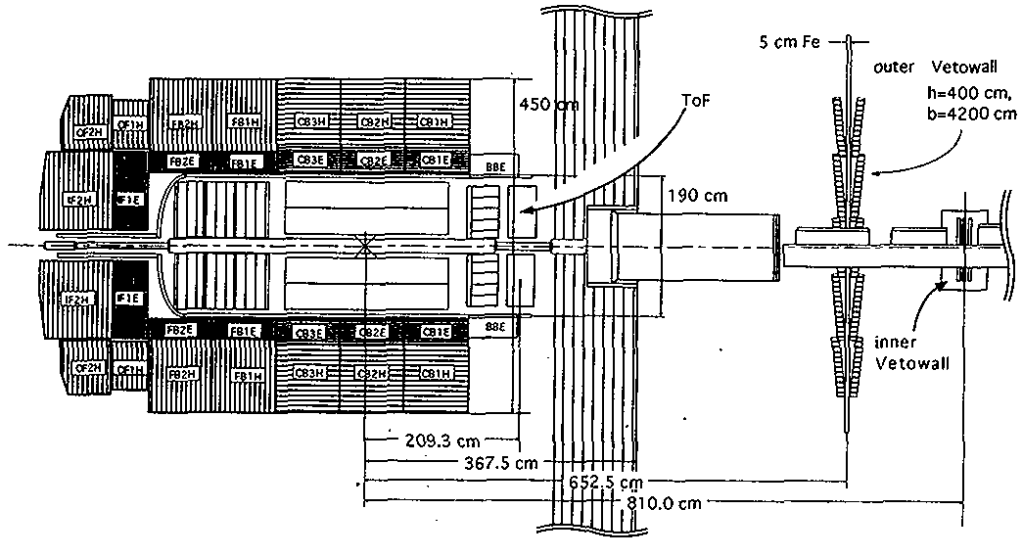

Figure 4.22: Background identification: relative position of veto- and ToF counters with respect to the main detector.

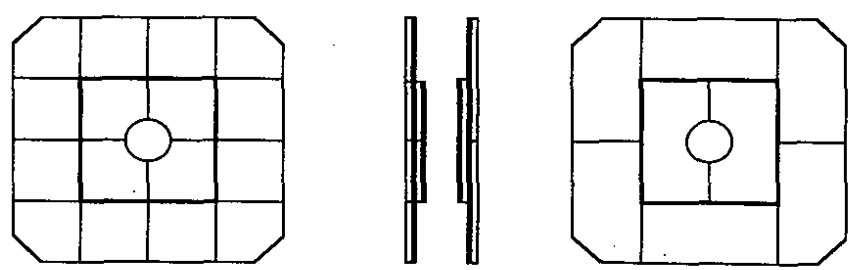

Figure 4.23: Diagram of the time-of-flight system: ToF.

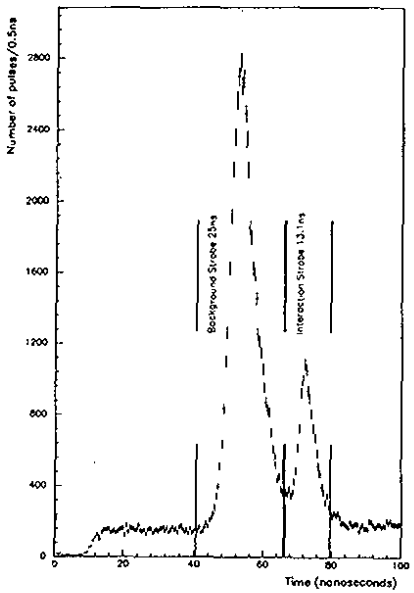

Figure 4.24: Time distribution of hits in a ToF counter.

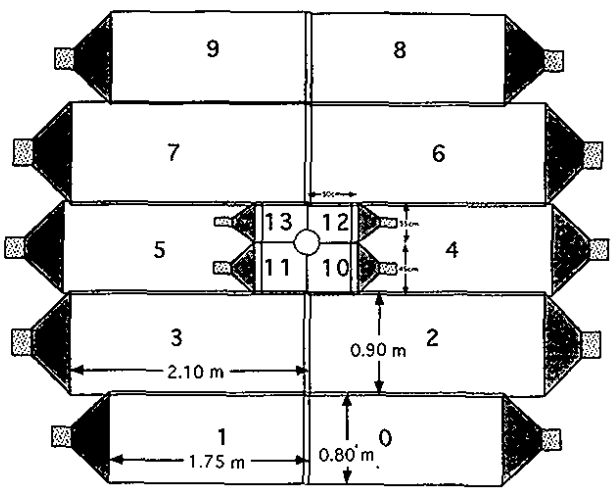

Figure 4.25: Schematic cross section of the inner and outer veto wall.

5 Calorimetry

The H1 detector was designed to provide clear identification and precise measurement of electrons, muons and penetrating neutral particles together with very good performance in the measurement of jets with high particle densities. These requirements were best met by a calorimeter inside a large coil to minimize both the amount of dead material in front of the electromagnetic calorimeter and the overall size and weight of the calorimeter [83].

The main reasons for choosing the liquid argon technique were good stability and ease of calibration, fine granularity for e/π separation and energy flow measurements as well as homogeneity of response.

Figure 5.1a shows the longitudinal view of the calorimeters along the beam axis and Figure 5.1b shows a transverse view of the liquid argon calorimeter (LAC) showing the wheel structure that is described below. The LAC covers the polar angular range between $\theta = 4°$ and $\theta \approx 153°$. The calorimetric coverage is completed with a small calorimeter in the proton direction (PLUG) with copper absorber and silicon pad readout, covering the region between the beam-pipe and the liquid argon cryostat ($\theta \leq 4°$) and a lead scintillator backward electromagnetic calorimeter (BEMC) located in the electron direction after the tracker and covering $151° \leq \theta \leq 177°$ and by the tail-catcher system (TC). The latter is used to provide a rough calorimetric measurement of hadronic particles leaking out of the LAC and is based on the analog readout of the pads of the limited streamer tubes that instrument the iron yoke.

In the next section the LAC is described; descriptions of the BEMC, the PLUG and the TC can be found in *sections 5.2, 5.3 and 5.4 respectively. Further details on the instrumentation of* the iron yoke are given in the section on the muon detector (see Section 6). For a more detailed description of the LAC system we refer to reference [84].

5.1 The liquid argon calorimeter (LAC)

5.1.1 Cryostat and cryogenic system

To minimize the wall thickness in front of the electromagnetic calorimeter while being able to withstand a maximum pressure of 3 bars and to support the weight of the calorimeter modules (600 t) and the liquid argon (53 m^3), all walls are made of stainless steel except for the inner walls of the warm and cold vessels around the beam pipe and the tracker which are made of aluminum alloy. The flat PTFE signal cables for the 45000 channels are brought out of the cryostat through 24 tubular ports distributed at both ends around the top half of the vessel. These feed-throughs have operated continuously without any problem since early January 1991 when the calorimeter was first cooled down.

The main design criteria for the cryogenic system were a maximum cool-down and warm-up time of less than 30 days, a transfer time of the liquid argon into the already cold cryostat within 12 hours, a pumping out time of the liquid argon into the storage tank in about two hours and the ability to keep the temperature and pressure within the cold vessel very stable over several months. Cooling down to liquid argon temperature is achieved by circulation of helium gas cooled in an external heat exchanger; the latter, no longer needed once liquid argon temperature was reached, has been removed. The liquid argon load is transferred from the 70 m^3 storage tank located at ground level (some 20 m above the detector) into the cryostat through the bottom of the cold vessel. Stable temperature and pressure (1.35 bar) are achieved by a regulated flow of liquid nitrogen through sets of coils located within the cold and the expansion vessels. An argon purification system is built in but not used presently because of the low level of

pollution. Complete control of all processes, including cool-down/warm-up and filling/emptying is done by a system of VME automates. Since operations started in early 1991 the calorimeter has remained at liquid argon temperature and most of the time full of liquid argon except for the few days needed to move the detector in or out of the beam. The average liquid nitrogen consumption was 600 l/h during the cool-down and $\simeq$ 95 l/h during stable operation. 250 m^3 of helium gas and 190 m^3 liquid nitrogen were needed for the 25 days cool-down process.

5.1.2 Liquid argon purity

A liquid argon purity monitoring system has been integrated into the LAC to check the stability of the ratio of energy loss to collected charge to the required level of $< 1\%$. The basic sensor is a liquid argon ionisation chamber to which the nominal electric field (1 kV/mm) is applied. Its cathode is coated with a ^{207}Bi source of 10^4 Bq activity. The energy spectrum of the radioactive decays is accumulated and an on-line shape analysis yields the average pulse height corresponding either to the 481 keV conversion-electron peak, or to the edge of the spectrum, around 1005 keV. The latter method is more precise ($\approx$ 0.3 %) because it does not suffer from Compton background. There are 11 such probes distributed around the cryostat. Figure 5.2 shows the relative variation of the charge collected for three of the probes since the cryostat was first filled. Since this date the same load of liquid argon has been used and the purity measurements show that the signal attenuation is less than 0.5 % per year. Furthermore a small movable cryostat is used to measure the quality of liquid argon at delivery or after a filling or to cross-check with the H1 test setup in a test beam at the CERN SPS.

5.1.3 Stack design and construction

The segmentation of the calorimeter followed the basic two-fold requirement of minimizing the dead volumes and of dealing with objects practical to build and to handle. The segmentation along the beam axis is done in eight self supporting 'wheels' as shown in Figure 5.1. Each of the six barrel wheels is segmented in ϕ into eight identical stacks or octants. Cracks between stacks of the LAC can be classified as ϕ-cracks - between octants in a wheel, z-cracks - between different wheels, and r-cracks - between electromagnetic and hadronic sections of a wheel. The ϕ-cracks in the electromagnetic calorimeter (EMC) are pointing to the interaction point (IP). All z-cracks are perpendicular to the beam axis, the one between the CB2 and CB3 wheels being almost pointing to the IP. A great effort was made to minimize all cracks. The two forward wheels are somewhat similar in the principle but mechanically assembled as two half rings.

Common features for all active cells are pad readout on the ground side and a high resistive coated high voltage plane (except for the CBH stacks) with integrated decoupling capacitance as described below.

The hadronic stacks are made of welded stainless steel absorber plates with independent readout cells inserted between the plates. They define the rigid structure on to which the corresponding electromagnetic stacks are mounted. The orientation of the absorber plates is such that particles are incident on the calorimeter with angles not smaller than 45°. The structure of each electromagnetic stack consists in a pile of G10(epoxy+fiberglass)-Pb-G10 sandwiches separated by spacers defining the liquid argon gaps. The basic sampling cell is shown in Figure 5.3a. It consists of 2.4 mm Pb as absorber and 2.35 mm liquid argon as active material with, per gap, one readout plane with pads and one high voltage plane coated with high resistive paint (HRC). The latter is a mixture of carbon and glue with a surface resistance of 1-30 MΩ / □, sieveprinted on a Kapton foil. The high resistivity of the coating provides the HV protection while the Kapton foil serves as a distributed decoupling capacity to keep negative cross-talk small. The

hadronic sampling cells, as shown in Figure 5.3b, consist of a total of 19 mm stainless steel, (16 mm absorber from the welded structure and twice 1.5 mm from the plates of the readout cells defining the active liquid argon gap) and of a double gap of 2.4 mm liquid argon. It has, in the middle of the active gap, a G10 board with pads on both sides to collect the charges deposited in the gaps. A Kapton foil coated by a layer of HRC (IF2H, FBH, OF stacks) or with copper (CBH) is glued to the inner side of the stainless steel plates, with the same functions as for the electromagnetic modules. The HV is applied to the HRC (or copper for CBH, in which case neon spark gaps mounted close to the gaps act as active protection). For more details see references [83, 84]).

The total thickness of the electromagnetic calorimeter varies between 20 and 30 radiation lengths (X_0). The reconstruction method used (see Section 5.1.7) requires each tower segment to have a depth of about 1 interaction length (λ_{abs}). The lines of constant λ and X_0 as well as the amount of material in front of the calorimeter in terms of X_0 are shown in Figure 5.4. The granularity of the read-out cells stems from the requirements of a good separation of electromagnetic and of hadronic showers. Longitudinal segmentation is 3 to 4-fold for the EMC and 4 to 6-fold for the hadronic calorimeter (HAC). The overall capacities per channel are below 14 nF so that the electronic noise is kept at a reasonable level. A further constraint to the tower size is directly related to the calorimeter trigger, for which the collected energies must belong to a unique bunch crossing t_0 of the accelerator [84]

The high voltage distribution is done by 1504 independent lines. Each line feeds a group of non consecutive planes in a stack, interleaved with planes linked to another HV line to reduce the chances that a complete tower segment be dead in case of a high voltage problem in one line. The present operating voltage of the whole calorimeter is 1.5 kV which corresponds to an electric field of 625 V/mm. The very good purity observed allows to reach high charge collection efficiency (about 94% [84, 85]) at this low value. This has the consequence that HV problems are minimal. Presently 3% of the high voltage lines do not reach the full voltage.

5.1.4 Electronic system

A major constraint in the design of the system, is that large energies may be deposited at short time intervals (96 ns at HERA) into detectors with large capacitances and long collection times, and the information has to be stored until the arrival of the trigger signal ($\approx$ 2.9 μs). The required dynamic range, defined as the ratio of maximal signal to noise, corresponds to 14 bits for 25 % of the channels, 12 bits being enough for the remaining 75 %. The basic layout of the electronic chain is described in more detail elsewhere [83, 84]. The preamplifiers are located just outside of the cryostat and feed on one hand the analog readout system via two multiplexers giving an overall multiplexing factor of 128, and on the other hand the trigger system which is described in Section 8.3.2.1. To extend the dynamic range to 14 bits while using a 12-bit ADC, a double transmission with two different gains is used where necessary, thus increasing the number of channels to be read-out to about 65000 (electronic channels). The signals are sent twice via $\approx$ 30 m twisted pair lines to differential line receivers located in the analog receiving unit (ANRU) which performs analog baseline subtraction [86]. Each such unit serves 512 calorimeter channels and is connected to an ADC board serving 1024 electronic channels, corresponding to either 512 double gain or to 1024 single gain calorimeter channels. Each ADC board is controlled and read out by a digital signal processor (DSP) module performing basic operations on the data such as pedestal subtraction, zero-suppression and gain correction. This read-out system is described below (section 5.1.6). The total amount of channels where no signal reaches the preamplifier because of bad contacts within the cryostat is 0.15 % and has remained stable for more than two and a half years after closing the cold vessel.

5.1.5 Electronic calibration system

The main goal of this system is to ensure that the calibration of the electronic chain is known and stable to within a few 10^{-3}. Calibration capacitors of 47 pF that have been selected to within ±1 % are charged with voltage pulses of very precisely ($\approx 10^{-3}$) known amplitude.

Two systems have been built into the calorimeter: the first one (cold calibration) with the calibration capacitors in the liquid argon, as close as possible ($\approx$ 1 m) to the stacks, pulses individual channels (one out of 16) allowing detailed cross talk studies to be done. The second system, with calibration capacitors at the preamplifier level (warm calibration), is used mainly as a backup for calibrating those channels for which some problem has occured in the calibration line within the cryostat. This is done by using a warm to cold calibration extrapolation technique from neighbouring channels and yields, for the calorimeter channels involved, a precision of the order of 1 % in the determination of the calibration constants. This method was developed during the runs in test beams at CERN and is presently applied to less than 1 % of the 45000 calorimeter channels.

The hardware consists of 992 pulse generators for the cold calibration and 768 for the warm one, steered by four command modules, each generator pulsing simultaneously up to 64 calorimeter channels. The command module activates selected groups of generators and sets the pulse voltage level by a 16-bit DAC.

The calibration procedure is twofold once the timing of the calibration with respect to the beam particles has been properly set. A high precision determination of the calibration curves (ADC response versus injected charge) is done each time the current calibration constants are no longer valid because of changes in the hardware or of pedestal drifts. A third order fit to this curve is then performed for each channel [84] from which are determined the constants to be downloaded into the DSP's. At H1 such operations are done once every few weeks at present as the stability of the calibration constants over one month is quite good as seen in Figure 5.5.

The calibration constants need no correction for diagonal cross-talk as they are determined by pulsing the cells individually using the high granularity cold calibration system. Non diagonal cross-talk has been determined from the test beam data and was found to be very small ($\leq$ 0.5%), mainly affecting the CBH modules.

5.1.6 Calorimeter data acquisition

The calorimeter data acquisition system reads out data from the LAC, the BEMC, the PLUG calorimeter and the analog part of the instrumented iron (TC). These detectors have the same readout electronics starting from the ANRU. The LAC yields most of the data and is described here as it has strongly influenced the structure of the system. The readout of the LAC data is split into two paths at the preamplifier level: a data path where the signals of the slow shapers are read out (see Section 5.1.4) and a trigger path where the outputs of the fast shaper are processed (see Section 8.3.2.1). In the data path the first level trigger decision samples the slow shaper pulse at its maximum. This shaper acts as a delay line. The encoding of the 65000 electronic channels is started by the level 2 trigger (L2) which arrives 20 μs after the collision. The total encoding time is 1.2 ms. The ADC counts of all electronic channels are then converted into calibrated charges by 69 digital signal processors (DSP) working in parallel.

In the trigger path, the pipelined trigger chain produces digital sums for each of the 22 bunch crossings following the collision. A first level trigger decision (L1) based on total and transversal energies is derived within 2.4 μs. Ten dedicated DSP's read the data of the fast shapers (see Section 8.3.2.1) and verify the signal shape of the trigger towers. They store the signal history

of a total of 474 trigger towers over 256 bunch crossings around the trigger time (t_0). From these data, every second sample in the interval ranging from -25 to +25 bunch crossings is read out for pileup studies.

The formatted data for both paths within independent VME branches, are collected by two event builders based on the RISC processor AM29000 running the real time kernel VRTX. A third processor of the same type runs a fast trigger level L3 algorithm tuned to reject backgound events (see Section 8.4). A processor based on the Motorola 68030 chip and operating under an OS9 system is used for run control and as a stand alone facility.

The DSP boards [87] used in the calorimetric data path for the readout of the analog signals are based on the Motorola DSP56001. They each read one ADC board thus processing 1024 channels. The DSP boards in the trigger path, based on the same DSP chip, are of a different design as a special interface to the trigger data had to be developped. The DSP56001 is a 24bit chip with three instruction fields. Each instruction takes 100 ns. It has a Multiply-Accumulator in one instruction and is interruptible in 100 ns.

All DSP's start working on a trigger level L2 decision. The DSPs in the data path perform an order three polynomial correction on zero suppressed data. On-board memories are downloaded with the current set of calibration constants (for each channel four parameters and the 1σ noise value are needed) whenever necessary. These DSPs yield calibrated charges formatted with the offline numbering of the calorimeter cells. A noise suppression (set to ±2σ for the 1992 data) is done for each cell in parallel to the encoding and does not lengthen the first order dead time. The code contains less than 200 instructions. It is written in assembler language and had to be optimised to fit within timing specifications and the available program memory space in the DSP chip.

DSP's in the trigger data path verify the timing and the signal shape integrity. They calculate pileup estimators based on charge and time analysis, and report any malfunctionings [88].

When the trigger level L3 rejects the current event, the encoding has to be reset. The DSP program can be interrupted and is ready again in 8 μs. If no rejection occurs, the trigger DSP's put the event in a FIFO. The calorimetric DSPs have a double output buffer, enabling each DSP board to buffer two L2 triggered events.

The AM29000 event builders, one for the analog data and the other for the trigger data, run on top of the real time kernel VRTX. Real time mechanisms synchronise the event building tasks with minimal system overhead. The data are passed to the event logging task through a circular buffer. The event is then formatted and sent to the central data acquisition through an optical fiber link (see Section 10.1.2). With the real time mechanism of VRTX and the buffering capability of the DSPs the acquisition sequence is strongly derandomised. Presently with an event size for the calorimeter branch of about 20 Kbyte and a first order dead time of 1.2ms the maximum data taking rate has been measured to be 200 Hz (100 % dead time). At a rate of 100 Hz the dead-time is 15 %.

The acquisition system has run reliably during the first run period of HERA.

5.1.7 Reconstruction techniques

Input to LAC reconstruction are calibrated charges for each calorimeter cell, as provided by the DSPs. The calorimeter reconstruction program eliminates electronic noise, converts charges to energies in the calorimeter cells for both hadronic and electromagnetic showers, corrected for the effects of dead material, and forms clusters from groups of cells with a close correspondence between clusters and particle showers.

	CB	IF
EMC	30 MeV/0.25 mips	10 MeV/.10 mips
HAC	30 MeV/0.15 mips	18 MeV/.11 mips

Table 5.1: Approximate energies and minimum ionizing particle equivalents (mips) corresponding to 1σ noise in the electromagnetic and hadronic sections of the central barrel and inner forward modules respectively.

5.1.7.1 Cell level reconstruction and noise suppression On the level of individual cells the program provides energies at the electromagnetic scale (see Section 5.1.8) and suppresses noise cells. The scaling from charge to energy involves a charge to energy calibration factor, which was determined for each stack geometry in the calibration runs at CERN (see Section 5.1.8), a correction for the charge collection efficiency of the calorimeter operating high voltage of 1500 V, which is derived from HV curves obtained with cosmic muons [84], and correction factors for local variations of gap and absorber thicknesses measured during stack construction.

The noise is measured for each channel during electronic calibration. It varies between 10 and 30 MeV equivalent energy depending on the calorimeter region (see Table 5.1). In events recorded with a random trigger 1100 cells out of a total of 45000 cells pass a $+2\sigma$ noise threshold on average. Adding up this energy for the full calorimeter yields an average value of 48 GeV with a standard deviation of 3 GeV (Figure 5.6a). To suppress the noise further we make use of the negative noise, present in the gaussian distributed noise signals after pedestal subtraction, to provide an automatic compensation for the positive noise contribution to the measured signal. We keep cells above $+4\sigma$ (signal seed), but to keep small signals at the fringe of showers, all neighbours in a $3 \times 3 \times 3$ cube around a seed cell ($> +4\sigma$) are kept, too. In order to compensate automatically for noise picked up in the previous step also cells below -2σ around a signal seed are kept. Cells below -4σ are kept in order to compensate for $+4\sigma$ seed cells from noise. No neighbours are collected around -4σ cells which are purely noise. After this procedure, the residual noise contribution is 0.1 GeV with a $\sigma = 0.5$ GeV (Figure 5.6b).

In order to include the noise in a realistic way in simulated data, noise is added using events recorded with random triggers in special runs where the online noise suppression was not activated. Thus the noise contribution is known for each cell. The effect of noise suppression described above is shown in Figure 5.7 for simulated low Q^2 ($10\ \text{GeV}^2 < Q^2 < 100\ \text{GeV}^2$) deep inelastic scattering events. It shows the distribution of energy in terms of σ_{noise}. A clear structure is visible. Region III (-2σ to $+2\sigma$) contains noise on top of signal in cells containing true energy deposition. Region II and IV (-4σ to -2σ and $+2\sigma$ to $+4\sigma$) contain noise picked up around a $+4\sigma$ signal seed. A good compensation of positive and negative noise is evident. Region V ($> +4\sigma$) arises from noise cells passing the 4σ seed threshold. They are compensated by Region I (-4σ).

The signal loss introduced by the above noise suppression procedure has been studied with simulated low Q^2 deep inelastic scattering events. In these events the hadronic energies are low. In the barrel region of the calorimeter the average deposited energy is 4.5 GeV, the average hadron and photon energies are 800 MeV and 400 MeV, respectively. In this (most difficult) case 17 % of the energy is lost due to noise supression. For high Q^2 events ($< Q^2 > \approx 500\ \text{GeV}^2$) the loss is smaller (5 %). These losses are corrected for in the reconstruction of hadronic energy (see Section 5.1.7.5).

5.1.7.2 Clustering All cells passing the cell level reconstruction are subject to clustering. Its aim is the formation of clusters from groups of cells with a close correspondence between clusters and particle showers. This introduces a conflicting requirement for electromagnetic and hadronic clusters. In order to avoid merging of electromagnetic clusters into hadrons in a

dense environment and to optimize the separation between two nearby showers small clusters are desirable. On the other hand, hadronic showers with their large spatial fluctuations of energy deposition ask for large clusters. Due to these fluctuations, however, the separation of hadronic energy deposition from different initial hadrons is not possible in general. We put emphasis on the identification and separation of electrons and photons. No attempt is made to guarantee the correspondence between clusters and hadron showers. They are, in general, split into several clusters.

The clustering is done in two steps. In the two-dimensional (2D) part the energy distribution in longitudinal sections of individual calorimeter modules is scanned for connected regions. Within a connected region, a search is performed for several separated maxima. In this case the region is split in order to optimize shower separation.

In the three-dimensional (3D) part the 2D clusters are merged into 3D clusters. First 3D objects are built inside the calorimeter modules, then these objects are merged across module boundaries into the final 3D clusters. The 3D merging is based on proximity and cluster dispersion in polar and azimuthal angle space seen from the interaction point.

Before linking over the boundary between the electromagnetic (EMC) and the hadronic (HAC) calorimeter sections, the cluster in the EMC is checked if it is a candidate for an electromagnetic shower, based on the fraction of cluster energy deposited in the first layer (early shower development) and on the four most energetic cells of a cluster (compactness). Such clusters are not joined further in order not to merge them into hadronic energy deposition behind.

5.1.7.3 Further noise suppression An additional information coming from the clustering helps in further reducing the noise in the hadronic part of the calorimeter. A hadron penetrating deeply inside the calorimeter usually deposits enough energy to form at least one cluster with a signal well above the noise level. Other small isolated energy depositions which are not distinguishable from noise are correlated in space with this prominent cluster.

Small signals are suppressed if they are in the last layer of EMC or in HAC and far away (> 50 cm) from the direction given by the center of gravity of any prominent cluster and the nominal interaction point. A cluster is called prominent if its significance, $\sqrt{\sum(E_i/\sigma_{noise})^2}$, is above 8.

The shadowed areas in Figure 5.7 correspond to noise suppressed by this procedure in simulated low Q^2 deep inelastic scattering events. The suppression does not touch region III, where the cells contain true energy deposit, and it does not increase the signal loss mentioned in Section 5.1.7.b. The energy distribution of noise remaining in empty events after the suppression has a peak at zero and sigma of 0.25 GeV, as can be seen in Figure 5.6b.

5.1.7.4 Correction for energy loss in dead material The energy loss in dead material in front of the calorimeter (the beam pipe, the central tracker and the inner cryostat wall) and in cracks between the calorimeter stacks are quite substantial. In low Q^2 deep inelastic scattering events they amount to $\approx 10\%$ of the energy deposited in the calorimeter. About 90% of the losses are due to dead materials in front of the calorimeter.

Corrections for the energy loss were derived using Monte Carlo simulations. The event by event corrections are based on the measured calorimetric energies. To reduce the influence of noise on the correction, only cells with energy above $3\sigma_{noise}$ for cells in prominent clusters (see Section 5.1.7.1) and above $5\sigma_{noise}$, otherwise, are considered. The losses are added to the energy of the cells used for the estimation of these losses.

Energy losses in front of the LAC are corrected by using the first (inner) layer of cells in the LAC. For each cell in the first layer with a signal above the threshold mentioned above, an energy is added according to:

$$E^i_{loss} = \alpha_{f_r} f^i_{dead}$$

Here f^i_{dead} is the thickness of materials (in energy losses by minimum inozining particles) in front of a cell i in projective geometry with respect to the nominal interaction point, taking into account local inhomogeneities of materials. A global factor α_{f_r} was determined for each half wheel along the beam direction by simulation. For the above energy estimate we are using only the fact of the appearance of an energetic cell, but not its energy. This approach allows a common correction procedure for losses caused by electrons and hadrons. Therefore no separation of electromagnetic and hadronic components of the energy flow is needed here.

The energy correction per cell, E^i_{loss}, varies with the position of a cell between 60 and *100 MeV with peaks up to 180 MeV in the FB and BBE regions. The correlation between* the estimate of the energy losses in the reconstruction and the true energy lost in front of the calorimeter for simulated low Q^2 deep inelastic scattering events is given in Figure 5.8. An *example of the effect of the dead material correction for experimental data is shown in Figure* 5.9, where the π^0 peak in the effective mass of two photons (e.m. clusters) is moved by the correction into region of π^0 mass. The average photon energy in the π^0 peak is 1.2 GeV.

The correction procedure for energy losses in cracks uses cells in the layers nearest to a crack at both sides of a crack. Cells at one side of a crack are coupled with cells on the other side and for each such pair an energy loss between them is estimated by

$$E^j_{loss} = \beta f^j_{dead} E^j_l E^j_r / (E^j_l + E^j_r)$$

It is distributed afterwards between the two cells of a pair in proportion to the cell energy. Here E^j_l and E^j_r are energies in a pair j deposited at left and right sides of the crack. f^j_{dead} is a dead material function which takes into account local inhomogeneities of materials. A global factor β was determined for each type of a crack. These factors differ considerably for pions and electrons. For the moment, only corrections of hadronic type are used in the reconstruction because of difficulties in the separation of hadronic and electromagnetic components in ϕ and z crack regions where an electromagnetic shower can penetrate deeply into the calorimeter through the crack.

Figure 5.10 shows the performance of the dead material correction as function of θ and ϕ for simulated pions at 20 GeV. The crack structure which is clearly seen before the correction nearly vanishes after the correction. The CB2/CB3 z-crack almost pointing to the interaction *point was scanned by a pion test beam of 30 GeV at CERN. Results are given in Figure* 5.11. The response across the crack is well described in simulation and the correction works in the same way for both measured and simulated data.

5.1.7.5 The hadronic energy scale The LAC is non compensating. The response for hadrons is about 30 % less than that for electrons. Therefore an additional correction has to be applied to the signal obtained on the electromagnetic scale.

*The fine segmentation of the LAC allows to distinguish the primary electromagnetic compo-*nent of a jet which is already on the correct (electromagnetic) energy scale, and it further allows to reach a high level of compensation within hadronic showers applying a weight to signals in individual calorimeter cells.

The primary electromagnetic clusters are filtered using such characteristics as the fraction of cluster energy deposited in EMC (containment in EMC), in the first layer of EMC (early shower

development), and in the four most energetic cells of a cluster (compactness) (see reference [89]). The filtering is done for clusters with an energy above 1 GeV.

The hadronic objects in the reconstruction are formed by cells which are not included into an electromagnetic cluster and located ($<$ 50 cm in HAC and $<$ 25 cm in EMC) around a direction given by the center of gravity of a hadronic cluster and the nominal interaction point. Here, a cluster is called hadronic if it is prominent (see Section 5.1.7.3) and if it is not recognized in the filtering as an electromagnetic one or, at lower energies, if it is developing deeply inside the calorimeter.

To get the proper hadronic scale for hadronic objects, a software weighting technique is applied, which was initially proposed by the CCFR Collaboration and used in the CDHS experiment [90]. This method was further developed by H1 in the CERN test runs [91, 92, 93, 94, 95]. The aim is to equalize the response to the electromagnetic and hadronic components of a hadronic shower and, therefore, to suppress the influence of the large fluctuations in the hadronic shower composition on the reconstructed energy. The technique exploits the fact that local energy deposits of high density are mainly of electromagnetic origin while the hadronic component is much more spread out. Thus, in a well segmented calorimeter the amount of energy deposited in the cells can be used for statistical separation of electromagnetic and hadronic energy depositions for which different correction factors are needed.

In the reconstruction the weighted energy in a cell i, E^i_{rec}, is calculated from the cell energy on the electromagnetic energy scale, E^i_0, by:

$$E^i_{rec} = \{a_0 + a_1 exp(-\alpha E^i_0 / V^i)\} E^i_0$$

where, a_0, a_1, and α are the parameters of the weighting function (different for EMC and for HAC) and V^i is the volume of the cell. These parameters were determined in function of the reconstructed jet energy (calculated inside cones of 10°) using a Monte Carlo simulation of jets. For hadronic objects with energy below 7 GeV this ansatz is replaced by simple multiplicative factors corresponding to effective e/π ratios in EMC and HAC. In the region 7 to 10 GeV both methods contribute to the correction in order to get a smooth transition from the simple correction factors to the weighting.

The remaining cells not included into electromagnetic clusters or hadronic objects are due to low energy particles depositing energy in the first two (three in the forward region) inner layers of the calorimeter. These leftovers are affected by noise, and the energy correction to be applied depends on particle composition and energy spectra. The corresponding correction factors were defined using simulated low Q^2 deep inelastic scattering events and are applied only if the total signal is above the noise level.

5.1.8 Calibration and performance

The most important part of the testing of the calorimeter modules is the energy calibration. This was done by putting calorimeter modules in a test beam at CERN. Because of the homogeneous readout medium and thanks to the strict manufacturing tolerances it is sufficient to calibrate module geometries with only one module of each type. Checks of the calibration quality were done once the detector was fully operational by using various techniques as described below, such as determining the response of the electromagnetic calorimeter to electrons generated by cosmic muons crossing the detector or verifying the P_t balance between the electromagnetic and the hadronic energy in deep inelastic events at HERA.

5.1.8.1 Overview of the test runs at CERN An extensive calibration program with $e-$, $\pi-$ and $\mu-$ beams was performed in the H6 test beam at the CERN SPS [91, 92, 96, 97, 98]. These beam tests supplied the basic calibration constants of the calorimeter.

Great care was taken during these runs to ensure that the calibration constants obtained could be transferred reliably to the final H1 modules. Only one of each type of the calorimeter stacks was tested as the very strict mechanical constraints (see references [83, 84]) needed to reach a homogeneity at the 1 % level were achieved during the construction phase.

Eight characteristic stack configurations, using in most cases the same modules as those later installed in the H1 cryostat, were tested in separate runs using the same beam setup, calorimeter readout and calibration electronics. These configurations include a full coverage of θ and all important crack configurations. The test cryostat could house two complete stacks so that beam scan data across the dead area (crack) between these two modules in realistic geometry conditions could be collected. It was thus possible to intercalibrate octants from different wheels and to study the influence of the crack on the stack response. This was achieved by moving the cryostat horizontally across the beam in small steps so as to get the behaviour of the calorimeter response starting from the case where the beam particles are fully contained in one stack and ending with the case where the beam particles were fully contained in the neighbouring module. These data could then be compared to Monte-Carlo simulations. Special modules consisting of half stacks assembled to reproduce a ϕ crack were built and put into the test beam in 1992.

The purity of the liquid argon was constantly monitored by probes identical to those used in the detector described in this paper. The decrease of the signal with time was much faster than in the H1 detector because of polluting agents brought by the stacks. It was not possible to use the same flushing and cool down procedures for the test set-up as in the final detector. Big variations in the pollution rate from one configuration to the next were attributed to the different cleaning agents used during the construction of the stacks which were built at various institutes.

The same front end electronics scheme and calibration system as at HERA was used as much as possible. Data were taken with beam energies in the range 3.7 to 80 GeV for electrons and 3.7 to 205 GeV pions.

In some of the data taking periods a tail catcher module was added behind the hadronic calorimeter allowing combined analyses to be performed [92, 96]. These tail catcher modules were also calibrated in standalone tests [99]. Table 5.2 summarizes the various configurations tested during the data taking periods between 1988 and 1992.

5.1.8.2 Test beam results For the electromagnetic energy scale two calibration constants (c^{exp}_{EMC}, c^{exp}_{HAC}) were determined for each wheel, which transform the measured electric charge Q_i per tower into energy deposited by electron showers. Corresponding constants (c^{MC}_{EMC}, c^{MC}_{HAC}), transforming visible energy into deposited energy are obtained for Monte Carlo simulations (MC) by putting electrons (of 30 GeV) directly into the stacks. These constants are defined to be independent of effects of dead materials in front of the calorimeter, any leakage and analysis cuts. The corresponding experimental constant c^{exp}_{EMC} is obtained by comparison (see Figure 5.12) of experimental data with detailed simulation of the test setup and requiring the reconstructed energies to agree:

$$E^{exp}_{rec} = c^{exp}_{EMC} \sum_{i}^{EMC} Q_i = E^{MC}_{rec} = c^{MC}_{EMC} \sum_{j}^{EMC} E^{vis}_j \qquad (1)$$

Year	Wheel	Remarks	Reference
1988	CB3		HAC [100]
1988	TC	stand-alone	[99]
1989	FB1/FB2	z crack	EMC [101]
1989	CB3/FB1	z crack	HAC [100]
1989	CB2/CB3	z crack	EMC [102]; HAC [100]
1989-90	IFE/IFH		[95]
1990	CB1/BBE	z crack	EMC [102], [103]
1990	FB2/OF	z crack	[104], [105]
1992	CB	ϕ crack	
1992	FB	ϕ crack	
1992	TC	stand-alone	

Table 5.2: Stack configurations calibrated in CERN test beams; EMC (HAC) means emphasis put onto electromagnetic (hadronic) calorimeter in reference given.

For the calibration constant a value of $c^{exp}_{EMC} = 3.55$ GeV/pC is obtained on average. For the hadronic stacks no electron data are available yet and $c^{exp}_{HAC} = 7.1$ GeV/pC results from scaling the value of the EMC by MC.

The resolutions σ/E obtained for various stacks are in the range 10 % to 13 %/$\sqrt{E}$ with constant terms below 1 %. Figure 5.13 shows the results for four different stacks and the parametriziation for FB2 according

$$\sigma/E = \sqrt{A^2/E + B^2/E^2 + C^2} \qquad (2)$$

with $A = 11\%\sqrt{E}$, $B = 154$ MeV and $C = 0.6\%$. The measured resolutions differ at low energies due to different handling and influence of electronic noise for the various stacks. The observed non linearities are below 1 % after corrections for effects of dead material and noise by Monte Carlo.

The variation of the calibration constants of the various stacks was found to be about 2.5 % larger than expected from the known mechanical differences of different wheels. The main error source were impurities in the liquid argon during the CERN test. The variation is consistent with the systematic error of the extrapolations of the high voltage plateau curves by which the charge collection efficiency was determined. Further tests of the energy scale are possible at HERA (see below). For further results on the calibration by test beam electrons and simulations we refer to reference [97] and for more details to references [95, 101, 102, 103, 104, 106, 105].

The response to pions has been extensively studied for the various calorimeter wheels and compared to detailed simulations (compare references [96, 95, 104, 107, 108, 109]). An application of the standard H1 reconstruction code (section 5.1.7) is shown in Figure 5.14, where data and GHEISHA simulation [110, 111] for pions at 80 GeV are compared in 3 different wheels on the electromagnetic scale and after reconstruction of hadronic energies. No attempt is made here to correct for leakage. The effect of the inclusion of the streamer tube tail catcher (see Section 5.4 and reference [112]) which adds at the test beam another 4.5 interaction lengths (λ_{abs}) to the 6 of the IF wheel, can be seen in Figure 5.15. It shows the reconstruction at a pion energy of 205 GeV for all events and for those fully contained in liquid argon. The obtained resolutions are about $\sigma/E = 50\ \%/\sqrt{E}$ with an energy independent term of 2 % as shown in Figure 5.16.

5.1.8.3 Performance at HERA The first data taken at HERA, starting in April 1991 with cosmic muons and in summer and fall 1992 with beams allowed for checks of both the overall electromagnetic energy scale and the hadronic energy scale.

The orientation of the three CB wheels is especially favourable for the study of the signals of cosmic muons and allowed to check the charge collection, the overall calibration and the time stability. The charge collection efficiency at the operating voltage of 1.5 kV was determined by high voltage plateau curves to be .944 ± .014. The electromagnetic energy scale as determined at the CERN beam tests (see above) could be verified to ± 8 % ([85]). More precise tests are possible with electrons (see below).

The overall response to muons of the individual electromagnetic and hadronic sections of the three CB wheels varied from October 91 to November 92 by less than ± 3 %. Future high statistics data will allow more precise cross-checks on the hadronic energy reconstruction.

A fraction of the cosmic muons traversing the detector generates electrons. Their momentum p can be measured in the central tracker CJC and can be compared with the energy E measured mainly in the CB wheels. A typical event is shown in Figure 5.17 together with the measured E/p distribution for selected electrons with $p > 1$ GeV/c and angles below 25° with respect to the normal of the calorimeter plates. The mean (0.97 ± 0.02) and width ($\sigma = 0.16$) agree with the simulation. The width corresponds to a resolution of $\sigma/E = 0.20/\sqrt{E}$, but this value is still influenced at these energies ($< p >= 1.6$ GeV/c) by noise and dead material corrections (section 5.1.7) of about 10 %.

With these techniques the forward wheels cannot be reached, but the performance of IF anf FB2 wheels can be checked by two photon mass spectra as demonstrated in Figure 5.9 which shows a clear π^0 mass peak.

Deep inelastic scattering events where the scattered electron and the hadronic jet are detected both in the LAC can be used for a direct comparison of the hadronic and electromagnetic energy measurement exploiting p_t balance. The transverse components p_{te} and p_{th} are calculated by summing vectorially the calorimeter cell energies. Figure 5.18 shows that the measured energy balance is compatible with simulation and $< p_{th}/p_{te} >= 0.95 \pm 0.03$ and 0.99 ± 0.01 for data and simulation, respectively.

5.2 The backward electromagnetic calorimeter (BEMC)

The backward ($-z$) region of the H1 detector is instrumented with a conventional electromagnetic lead-scintillator sandwich calorimeter.

The primary task of this backward electromagnetic calorimeter is to measure energies and directions of electrons scattered under small angles from deep inelastic processes. In addition the BEMC has to contribute to the measurement of hadrons emerging from photoproduction and medium to low-x, high-y hadronic final states.

The kinematics of deep inelastic scattering accessible with this calorimeter is characterised by moderate four-momentum transfers $Q^2 < 100$ GeV^2. Such processes dominate by far the DIS cross section observed in the H1 detector and provide the only access to the low-x part of the proton ($x \approx 10^{-4}$). At the same time the calorimeter has to operate in a very high rate environment caused by the illumination of the rear side with secondary hadrons originating from beam-gas and beam-wall interactions of the 820 GeV proton beam. Due to the location in the within large solenoid the BEMC is exposed to the full magnetic field of 1.15 T.

5.2.1 Mechanical layout

The calorimeter elements (stacks) of the BEMC are mounted in an aluminium barrel with a diameter of 162 cm. Together with the central tracking system the barrel rests on rails

mounted on the inner wall of the liquid argon cryostat. The total weight of the BEMC is 3 t. The calorimeter front face is located at a distance of 144 cm from the nominal interaction point. Scattering angles θ from 151° to 177° are covered with full azimuthal acceptance. This corresponds to $\approx$ 1.5 units of pseudorapidity η ranging from -1.5 to -3. The acceptance of the rear part of the LAC sets in at 153° so that an almost continous transition between the two calorimeter types is achieved.

Support structures, electronics and cabling of the central and forward tracking systems amount to approximately one radiation length of dead material between the central drift chamber and the combined system of backward proportional chamber and BEMC.

Granularity of the calorimeter is provided by segmentation into 88 calorimeter stacks aligned parallel to the beam line. The transverse structure can be seen in Figure 5.19. 56 stacks have a quadratic cross-section. The remaining ones are of trapezoidal and triangular shapes in order to provide an approximation to the circular shape of the support barrel.

The stacks are multilayer lead-scintillator sandwich structures with 50 active sampling layers made of SCSN-38 plastic scintillator [113] of 4 mm thickness. The active layers are interleaved with 49 layers of 2.5 mm lead. The entire structure corresponds to an average density of 5 g/cm^3 giving rise to a total of 22.5 radiation lengths or 0.97 hadronic absorption lengths. The Moliere radius is 3.4 cm. The scintillation light is coupled via an 0.3 mm air gap to Y-7 wavelength shifter bars [113]. Two pairs of 8 cm wide bars cover two opposite sides of a quadratic stack extending over the full active length. The remaining two sides are covered with 16 cm wide bars extending only over the last 15 sampling layers in the stack. These short wavelength shifters see only the last 6.8 radiation lengths of the calorimeter stack thus giving separate access to the tail of energy deposited in electromagnetic showers.

The light emitted in the wavelength shifter bars is detected by PIN photodiodes (S2575 [114]). Each long bar is equipped with one diode. They are read out separately in order to provide a measurement of the shower impact position using the attenuation of light in the scintillator plates. The short bars are connected to a pair of diodes due to their double width. Each pair is connected to one readout channel because no further improvement in space resolution can be expected from the back part of the shower. Special arrangements of wavelength shifters have been made for the non-quadratic stacks. Some of them have a reduced number of readout channels. In total there are 472 read-out channels in the BEMC.

5.2.2 Readout electronics and trigger

The electronics associated with the BEMC must perform two main functions. It processes the analog signals from the PIN photodiodes and converts them into digital form with the required speed, precision and stability. It further provides trigger signals for the physics events of interest

The signals from the PIN photodiodes are fed into charge sensitive pre-amplifiers mounted directly on the back of each calorimeter stack. The preamplifiers produce fast signals of 100 ns rise time and a fall time of 400 μs. A differential pulse is sent from a line driver through 30 m twisted pair cables to a receiver located in an electronics hut mounted on the detector and accessible during data taking. Here the signals are split to provide input for the calorimetric triggers and for the readout.

Two trigger signals are being produced. Firstly the analog signals of the four long wavelength shifter bars within one stack are summed in order to provide input for the high granularity inclusive electron trigger (see Section 8.3.2.2). A second set of stack sums is being formed to feed the overall calorimeter trigger sums with low granularity. The timing and the gain of the backward single electron trigger (BSET) stack sums are individually adjusted in order to assign

events uniquely to one bunch crossing and to compensate for stack-to-stack variations in energy calibraton.

The readout of BEMC energies proceeds through a chain of shapers, sample-and-hold circuits and multiplexing similar to the one of the LAC described previously. Due to the large cross section of calorimeter stacks and the high proton beam related background rates the concept of slow shaping to match the trigger level L1 decision after 25 bunch crosssings cannot be applied for the BEMC. The probability for a distortion of the energy measurement through pile-up would exceed 50 % for a background rate of 100 kHz. To overcome this problem an analog electronics chain consisting of a fast, unipolar shaper and a subsequent analog delay line is used. The shaper has a time constant of 500 ns (FWHM) in order to reduce the pile-up window to about five bunch crossings. To match the trigger decision time the shaped signal is delayed by an analog delay line with a length of 2.5 μs [115]. The fast shaping requires a precise relative adjustment of all 472 delay lines in order to avoid channel-to-channel gain variations of the signal. Equalisation of the delay lines to 60 ns is required to keep the gain variations within 1 %. The result of the equalisation can be seen in Figure 5.20. The channel-to-channel delay variation has a spread of 10 ns (σ).

The subsequent digitisation of the multiplexed signals is performed in the same way as for the LAC.

5.2.3 Calibration

The calibration of the BEMC is based on two contributions. Electronics gain and light collection in the stacks are factorised and monitored independently.

The gain of the electronics chain is determined with the same pulser system used for the LAC. The testpulse is injected at the preamplifier level on the calorimeter stacks. Each stack is connected to an individual pulser channel. This has proven to be a powerful tool for the calibration of the stack oriented high granularity electron trigger. The pulser system measures the response of the entire electronics chain including all cables. It has also been used to transfer the initial absolute calibration from the testbeams to the final experiment. During data taking periods the entire electronics is calibrated once per week. The stability achieved is at the level of a few per thousand. This is far below other sources of calibration uncertainties.

The second contribution to BEMC calibration is light collection and detection in the calorimeter stacks. Here the concept is to obtain the initial absolute energy scale from testbeam measurements and to confirm and improve the scale in situ using electrons scattered under small angles from medium/high x partons, i. e. in the kinematical peak.

The initial absolute calibration of individual quadratic stacks has been obtained in 1990 from measurements with a 5 GeV electron beam at the DESY synchrotron. The individual calibration constants of channels in quadratic stacks differ only slightly with a spread of 5%. This demonstrates the stable and well reproducible construction procedure for the optical part of the calorimeter. Non-quadratic stacks are characterised by higher light collection efficiencies due to their different geometry. Those stacks have been calibrated relative to the majority of quadratic stacks using cosmic muons. A similar procedure has been applied to the back part viewed by short wavelength shifter bars based on measurements carried out with a 120 GeV muon beam at the CERN SPS.

In the environment of HERA ep collisions the BEMC is exposed to a cross-section of 100 nb from deep inelastic scattering. The first year of data taking at HERA has delivered an integrated luminosity of 30 nb^{-1}. Deep inelastic scattering at small angles from medium/high x partons gives rise to a peak in the distribution of scattered electron energies at the value of the

electron beam energy. The distribution observed in the BEMC is shown in Figure 5.21. The data points are compared to a simulation program taking into account energy losses in dead material as well as spatial inhomogenities and channel-to-channel calibration uncertainties. The statistical precision of the kinematic peak method has already reached the 1% level. With increased luminosity the method will be used to track short term calibration uncertainties (like radiation damage) and to remove residual channel-to-channel calibration uncertainties.

5.2.4 Performance

The energy resolution of the BEMC has been determined in test beam studies carried out with electron beams ranging from 1 GeV to 80 GeV. A sampling term of $10\%/\sqrt{E}$ has been found in agreement with expectations from the mechanical design. The average noise per calorimeter stack was measured to be 150 MeV in the real H1 environment. Energy clustering is carried out over stack nonetts giving rise to a contribution of 450 MeV from coherent noise for each cluster. The constant term in energy resolution for a single stack was found to be well below 1%. The response of individual channels has initially been equalised to better than 1 %. During the two year period from the initial calibration to the actual data taking in the H1 detector a dispersion of calibration constants due to various ageing effects has occured. Using the shape of the kinematic peak this channel-to-channel calibration uncertainty has been estimated to be 3%. Although this effect initially enters directly into the effective energy resolution it will eventually be removed using the kinematic peak data themselves.

The inherent mechanical non-uniformities in the stack construction from the wavelength shifters cause an impact point dependend response to electromagnetic showers. Extensive studies carried out with testbeam data and shower simulations exhibit a regular pattern of inhomogenities with losses up to 10% close to the wavelength shifters. A look-up table has been created to correct the impact point dependence to a 2% level. Restricting the measurement of electrons to the central part of quadratic stacks reduces this uncertainty below 1%.

The matching of electron tracks measured in the tracking detectors to the cluster position reconstructed in the BEMC has been determined from DIS events with the electron scattered into the BEMC. Based on the known attenuation properties of light in the scintillator plates a position resolution of 1.3 cm has been achieved. The effective granularity demonstrated with this method is far better than the one to be expected from the large transverse stack dimensions of 16×16 cm^2 (Figure 5.22).

Interacting hadrons deposit typically 30 % of their energy in the BEMC. About 30% of all hadrons do not interact in the calorimeter. Their minimum ionising signal is about 2σ above the level of electronic noise and remains undetected. A satisfactory hadronic resolution of approx. $80\%/\sqrt{E}$ has been achieved in detector simulations by combining the measurements in the BEMC and in the instrumented iron structure behind it with proper weighting. The actual performance of the systems installed will be evaluated from the transverse momentum balance expected between the electron and the hadronic final state in deep inelastic events.

5.3 The plug calorimeter.

The plug calorimeter (PLUG) has been designed to close the gap of acceptance for the energy flow measurements between the beam pipe ($\theta \approx 0.6°$) and the forward part of the LAC ($\theta \approx 3°$). Its main task is to minimize the missing part of the total transverse momentum due to hadrons emitted close to the beam pipe. In addition the energy, emitted into a narrow cone around the beam pipe can be used to separate the proton jet as well as to veto beam gas and beam wall background.

Position	$+476 \leq z \leq +545$ cm
Overall radius	$6 \leq r \leq 32$ cm
Radius of detector planes	$6 \leq r \leq 25$ cm
Polar angular range	$12.5 \leq \theta \leq 58$ mr
Number of detectors	$8 \times 84 = 672$
Number of electronic channels	$4 \times 84 = 336$
Total length	69 cm $\equiv 4.25\lambda_{ab}$, $\equiv 44.6X_0$
Weight	1.48 t

Table 5.3: Global parameters of the plug calorimeter

Owing to the geometrical constraints – the available space inside the return yoke of the H1-magnet was restricted to a cylindrical hole of ≈ 0.7 m length and a diameter of ≈ 0.7 m around the beam axis – only a most compact calorimeter could fit. Facing the physical requirements of good angular resolution, nearly full containment and linearity, the solution was a sampling calorimeter consisting of nine copper absorber plates interleaved by eight sensitive layers of large area silicon detectors [83]. The most important construction parameters are given in Table 5.3.

Figure 5.23 shows a schematic view of one of the two half-cylindrical parts of the PLUG, each mounted in one part of the return yoke. The detector modules are placed within 15 mm wide slots between the absorber plates. These are sealed and easy to replace entities, which contain one half of a detector plane each. Between two 5 mm copper plates a G10 readout board, equipped with 42 silicon detectors of 400 μm thickness, is placed (Figure 5.23, left part). A detailed description of the detector technology can be found in [116]. Typical characteristics of single silicon detectors, as measured in the laboratory, are given in Figure 5.24. Due to a special edge-protection procedure 32 quadratic (5×5 cm^2), six triangular and four rectangular detectors cover one half of the detector plane in a mosaic structure nearly completely, leaving only 4% of the total area inactive (Figure 5.25). By the end of 1992 the first four detector planes with totally 276 detectors have been installed. In the final stage, the PLUG will be equipped with 672 detectors.

The readout electronics of the PLUG represents one branch of the electronic analog chains of all H1 calorimeters and uses the same components (see Section 5.1.6). The 672 detectors in the final stage of instrumentation are read out in pairs in 336 channels. Trigger towers are built by merging the signals from subsequent channels in z–direction.

The calibration of the ADC output in units of visible energy rests on an absolute energy measurement using α-particles. Its conversion into total absorbed energy is based on detailed MC-simulation studies of electromagnetic and hadronic shower developments in silicon instrumented calorimeters in comparison with test measurements [117, 118, 119, 120].

In autumn 1992 the PLUG was operated with four instrumented detector planes. In contrast to long-term laboratory tests, all detector currents showed a slight but steady rise by up to several percent per week. Since radiation damage effects can most likely be excluded [121], atmospheric influences like pollution by ozone, nitro compounds or excessive humidity are assumed.

The energy resolution of the PLUG calorimeter suffers from both the coarse sampling and the lateral and longitudinal leakage. Nevertheless its value of about $150\%/\sqrt{E}$, evaluated from experiment supported MC-calculations [120], turns out to be sufficient for the tasks within the H1-experiment. As an illustration of the PLUG-calorimeter response to selected low-Q^2 events the spectrum of the visible energy is shown in Figure 5.26. It compares remarkably well with H1SIM-MC-simulations, starting with LEPTO 6.1 events ($Q^2 > 6$ GeV^2 and $10^{-4} < x < 1$) [120].

5.4 The tail catcher.

In order to measure the hadronic energy leaking out of the LAC, eleven of the sixteen limited streamer tube (LST) layers of the instrumented iron are equipped with readout electrodes (pads). The details of the LST system are described in chapter 6. Here we describe the features relevant for the energy measurement which is based on the analog readout of the pad signals where the readout segments are two-fold longitudinally (6 resp. 5 pads added). The pad sizes vary from 30×30 cm^2 in the endcaps up to about 50×40 cm^2 in the barrel region. The pad signals from the five inner (six outer) layers are summed up by tower builders (TB) to form the front (back) tower signals. The differential analog signals from the TB's are then relayed in groups of 12 to the cable stations (CS) located at each analog station which reorganise the signals from the towers into groups of 16. From there, the signals are sent to the analog superboards (SB) whose function is to amplify, integrate and store the analog signals in groups of 128 channels each. The geometry of the tower structure is briefly described in Table 5.4.

Region	θ Range	Segmentation	# of Channels
Forward Endcap	$6° \leq \theta \leq 33°$	x and y	552
Central Barrel	$33° \leq \theta \leq 137°$	ϕ and z	2784
Backward Endcap	$137° \leq \theta \leq 172°$	x and y	552

Table 5.4: Layout of the pad readout of the iron instrumentation.

5.4.1 Electronics

The amplifier used on the TB-boards allows for the measurement of single muons as well as hadronic showers without saturation. The signals have a dynamic range of 0.75 mV to 1 V. The upper and lower frequencies for the differential line driver are determined from the rise and fall times of the pad signals (50 ns and 700 ns). Each superboard accepts the input of 128 channels which are individually processed by a line receiver, shaper and sample & hold. The line receiver and shaper are modified versions of the LAC system cards, while the sample & hold cards are identical to those used in the LAC readout system. These signals are multiplexed and held in the output buffer to be read by the analog receiving unit (ANRU). At this point the data is treated as all the data from the calorimeter, it is zero supressed and corrected in the digital signal processor (DSP) and readout (see Section 5.1.6).

The calibration of the superboards is done by sending calibration pulses through the analog readout chain begining at the tower builder board. One hundred pulses are sent through this chain for each voltage level that is to be calibrated. Thirty voltage levels are measured over the dynamic range of the ADC's. These points are then fit to a quadratic curve for each channel and the resulting coefficients are stored in a file. These constants are downloaded into the digital signal processors (DSP) to correct for the channel to channel variations and non-linearities. Channel to channel variations have been found to be less than 2% for 3888 channels (Figure 5.27).

In calibration data taking mode precise DC levels are sent to calibration fanouts at each analog station through the CS's in the opposite direction of normal data collection and into the active elements of the TB's. The resulting analog signals are sent back through the normal data path to the CS's, SB's, and on to the ANRU's. Calibration data are not processed in the normal way by DSP's and emerge uncorrected after conversion in the ADC's.

During data taking and calibration, acquisition is controlled by the LAC OS9 system. However, normal data and calibration results can also be collected in stand-alone mode, in which case the TC OS9 system is used.

5.4.2 Energy calibration

The conversion of the signal charge Q_i as measured in a tower i to the hadronic energy scale $E_{had,i}$ is given by [122]:

$$E_{had,i} = c_1 c_{3,i} \frac{Q_{had,i}}{c_2}$$

The general hadronic energy calibration constant c_1 [GeV] has been determined in test measurements at CERN using pion and muon beams [123]. The parameter c_2 gives the tower charge of an average minimum ionizing particle, i.e. a muon, at an angle of incidence of 0° with respect to the normal of LST chamber. The intercalibration factor for each tower $c_{3,i}$ describes the tower to tower variations of the measured charge with respect to that of an average minimum ionizing particle.

The constant c_1 is derived from the linear relationship between the incident pion energy and the ratio Q_π/Q_μ of the measured charge for pions and muons at zero degree incident angle ($\theta_{\mu,inc} = 0°$). Defined in this way c_1 is essentially given by the sampling fraction of the calorimeter and the gas used in the chambers. It does not depend on the angle of incidence of the hadrons and is also insensitive (in wide limits) to the operation conditions, i.e. voltage, pressure, temperature [123].

The parameter c_2 and of course $Q_{had,i}$ are very sensitive to variations in high voltage, pressure, gas composition, temperature, etc. However, the ratio $Q_{had,i}/c_2$ does not depend on these conditions [123], provided the values of c_2 and $c_{3,i}$ are updated whenever the conditions change. c_2 and $c_{3,i}$ are determined using cosmic muons (see below) requiring special calibration runs which cannot be performed at high repetition frequency. Since atmospheric pressure is the only operation parameter which can change rather quickly and which has a drastic effect on the gain of the streamer tubes, these variations are compensated for by regulating the high voltage using the continuously monitored pressure values. The details are described in Section 6.

The transformation of ADC counts into charge is done online during the readout process. It is sufficient to use a linear conversion:

$$Q_i = p_{1,i}(ADC_i - p_{0,i})$$

. The pedestals $p_{0,i}$ are obtained from random triggers and the gains $p_{1,i}$ are given by the slope of the test pulser response curves of the electronic calibration. Both varied by < 2 % over the whole data taking period. Zero suppression allows to read out only pads above (below) a certain threshold, typically given in terms of multiples of positve (negative) pedestal variations.

The parameters c_2 and $c_{3,i}$ are determined from cosmic muons [124], triggered by opposite pairs of barrel or endcap modules. The analysis starts by requiring a track well reconstructed by the digital wire and strip muon system. Then the analog signals of all towers along the track as well as the neighbours along the wire direction (in order to account for cross talk) are summed up separately for the inner and outer calorimeter cells. The data have to be corrected for non-normal incidence with respect to the chamber plane. Let θ be the angle of a track with respect to the normal measured in the plane spanned by the normal and the wire direction. An inclined particle starts to produce multiple streamers with increasing θ if the projection of the track on the wire exceeds the dead region of the primary streamer. The dependence of the induced pad charge on θ is shown in Figure 5.28a. The corresponding dead zone around the streamer formation amounts to ~ 5.35 mm [123]. The dependence on the orthogonal angle ϕ, measured in the plane perpedicular to the wire direction, accounts for the passage of a track through several streamer tubes and is much weaker (see Figure 5.28b). Both angular dependencies can be well fitted by a second order polynomial:

$$\begin{aligned} Q(\theta) &= Q_0\,(1 + 0.013 \cdot \tan\theta + 0.522 \cdot \tan^2\theta)\,, \\ Q(\phi) &= Q_0\,(1 - 0.105 \cdot \tan\phi + 0.411 \cdot \tan^2\phi)\,. \end{aligned}$$

In order to keep the corrections small, only tracks with $\tan\theta < 0.8$ are considered in the calibration procedure.

The intercalibration constants $c_{3,i}$ vary by $\sim 10\%$ within one module, which can be understood by slight mechanical and geometrical variations between towers, resulting in different local behaviour of the streamer tube chambers. There are, however, larger module to module variations depending on the module location in the iron ioke; these variations are under investigation.

5.4.3 Performance

The performance of the tail catcher has been studied in test measurements at CERN with π and μ beams of 10 to 80 GeV [123]. The energy response is linear up to at least 30 GeV, while the obtained energy resolution is $\sigma/E \simeq 100\%/\sqrt{E}$.

The calibration of the tail catcher at HERA is done using cosmic muons as described above and taking the energy scale from the CERN beam test results as $c_1 = (0.209 \pm 0.002)$ GeV. Figure 5.29 shows representative muon spectra of a complete module for the inner and outer towers. Clean muon signals of a Landau like distribution can be seen with mean and most probable values far beyond the pedestals. The widths relative to the most probable values are ~ 35 %. The ratio of the mean values of inner and outer towers corresponds to the expected value of 0.8.

We do not observe any effect of the magnetic field in the iron yoke on the muon signal.

Most important for energy measurements with the H1 detector is the combination of the tail catcher with the LAC. Test measurements with the LAC have shown that the energy response can be symmetrized (removal of long tails towards low energies) and the energy resolution can be improved by including the information of the tail catcher [92, 112, 96]. One needs, of course, reliable corrections for energy losses in dead materials, which have to be done for each event. Inside the tail catcher dead material appears as cracks between towers, in particular in the transition region between the end cap and barrel yoke. Corrections between adjacent towers are calculated on a geometrical basis as the ratio of the tower areas with and without the crack area. More involved corrections are necessary for the material between the calorimeters, e.g. the cryostat wall and coil between the LAC and the TC. For this purpose a hadronic object in the LAC (i.e. not an e or γ candidate) is geometrically linked with a TC cluster into a generalized cluster. The energy losses are best estimated [112] by a linear interpolation of the energy deposit in the last layer of the LAC, $E_{LAC,last}$, and the first layer of the tail catcher, $E_{TC,first}$:

$$E_{loss} = \alpha(\theta) E_{LAr,last} + \beta(\theta) E_{TC,first}$$

The calculated energy loss is distributed among the cells in proportion to their energy. The functions α and β depend on the polar angle θ of the generalized shower or, more precisely, on the thickness Δt_{dead} of the material between the two calorimeters and are almost independent of the energy over a large range. They have been determined as a function of Δt_{dead} from dedicated test measurements at CERN [112]. At H1 Δt_{dead} varies from 0.5 up to 2.4 interaction lengths depending on the polar angle θ. The corresponding values for α (β) range from 0.2 up to 0.9 (0.1 up to 0.9). The uncertainty of the energy correction was estimated to $\sim 20\%$ [112]. Figure 5.15 shows the effect of the combined LAC and TC measurements with proper energy loss corrections from test beam results [112]. Monte Carlo simulations give consistent results with the energy loss corrections from the test measurements. More checks will be done by a comparison of transverse energy flow in deep inelastic ep scattering events (like for the LAC case).

A similar procedure is applied to the backward region, where non-electromagnetic BEMC clusters are linked to tail catcher clusters. Dead material corrections between the two calorimeters are expected to be smaller. The combined energy is formed by weighting the BEMC and instrumented iron information

$$E_{corr} = \alpha(\theta)E_{BEMC} + \beta(\theta)E_{TC}$$

Since no test measurements exist, the coefficients α and β had to be determined from Monte Carlo simulations of low energy pions (5 – 10 GeV). The expected energy resolution is $\sigma/E \simeq 80\%/\sqrt{E}$.

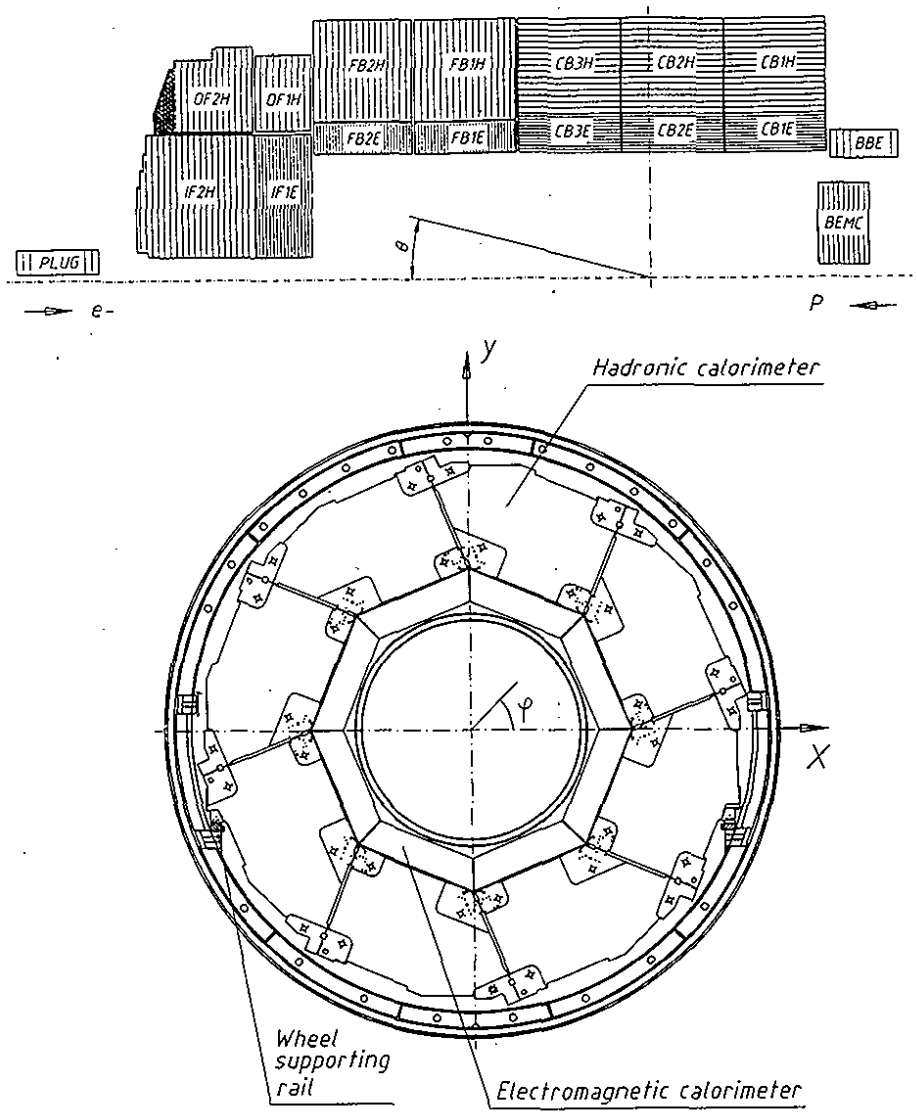

Figure 5.1: a) Longitudinal view of calorimeters. b) Radial view of a calorimeter wheel.

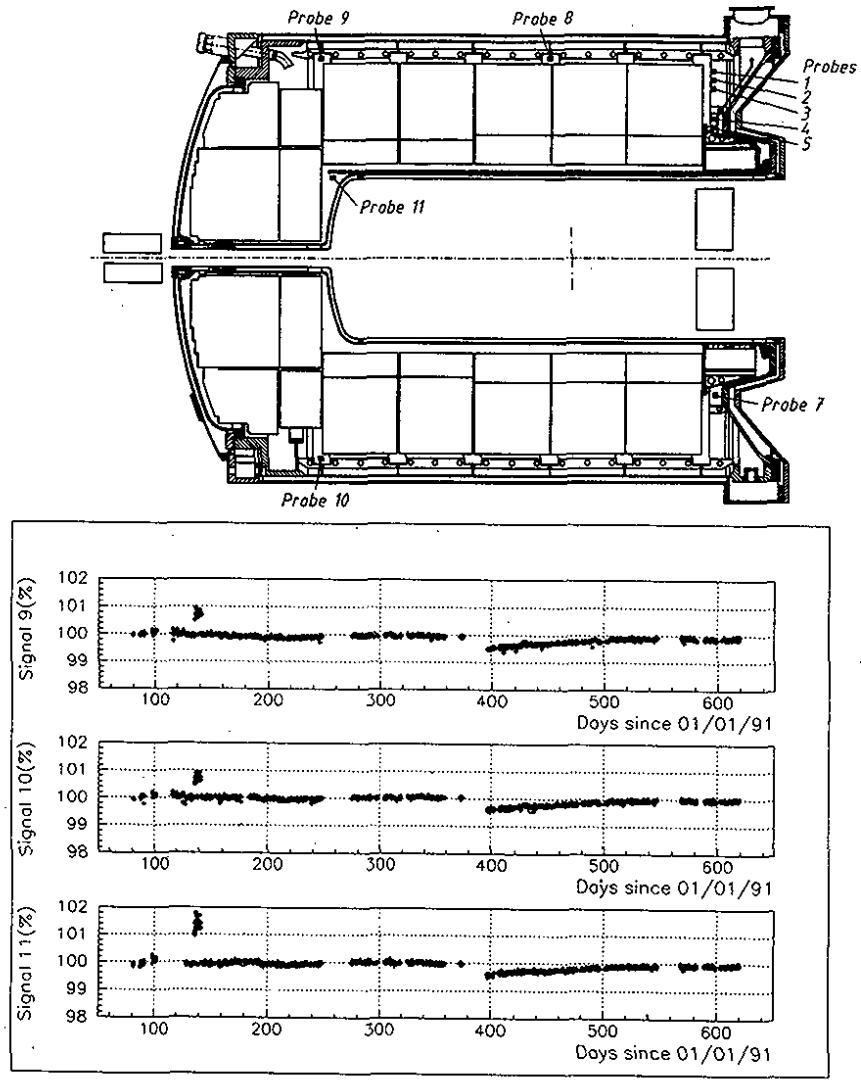

Figure 5.2: Relative variation of the charge collected for three of the liquid argon monitoring probes as a function of time (days since 1/1/1991). The discontinuity corresponds to the time when the cryostat was emptied while moving the detector into the beams. The top view shows the location of the probes within the cryostat.

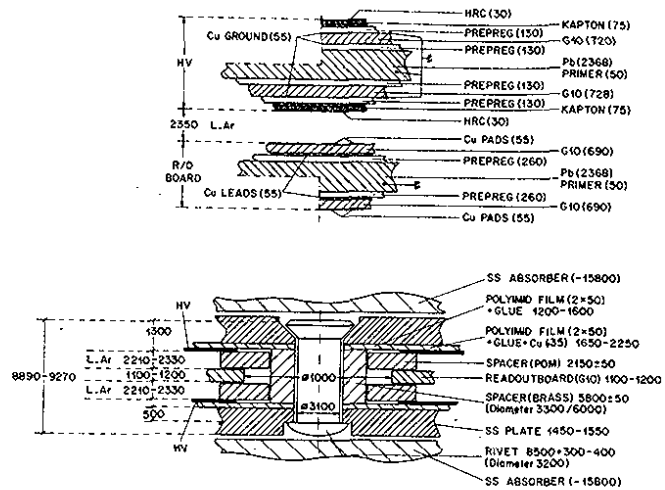

Figure 5.3: Schematic structure of the readout cell: a) e.m. cell, b) hadronic cell. All dimensions given in μm.

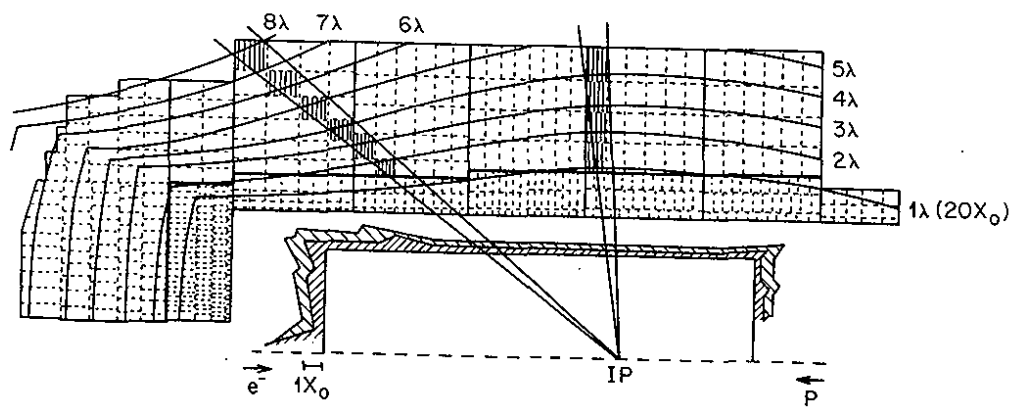

Figure 5.4: Iso-X_0 and iso-λ lines of the liquid argon calorimeter. The hatched areas correspond to the amount of material in front of the calorimeters due to the trackers and to the liquid argon cryostat walls. (Note the different X_0 scale and that all amounts of material are given for particles originating from the interaction point (IP)). The dashed lines show the segmentation.

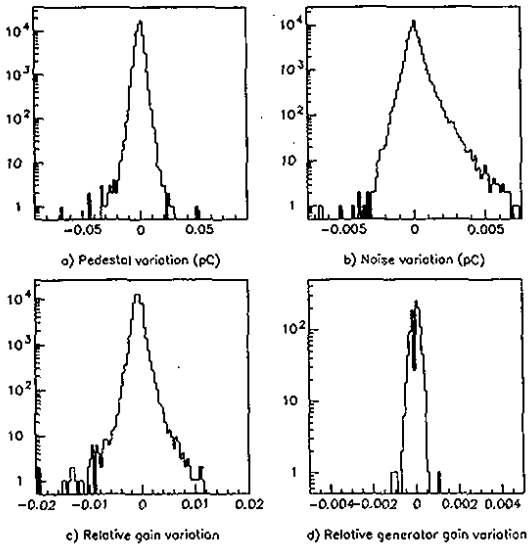

Figure 5.5: Relative stability of the electronic chain over one month.

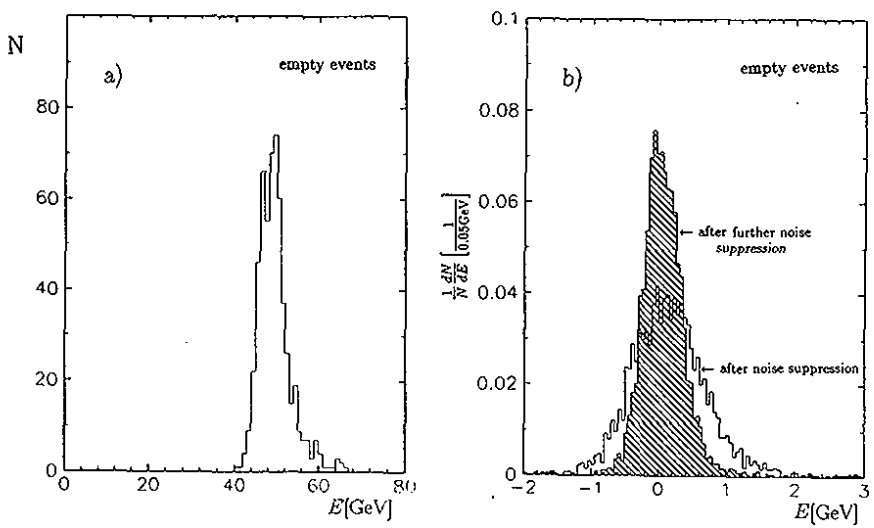

Figure 5.6: Noise contribution summed over all channels of the LAC: a) after applying a $+2\sigma$ noise threshold, b) after noise suppression.

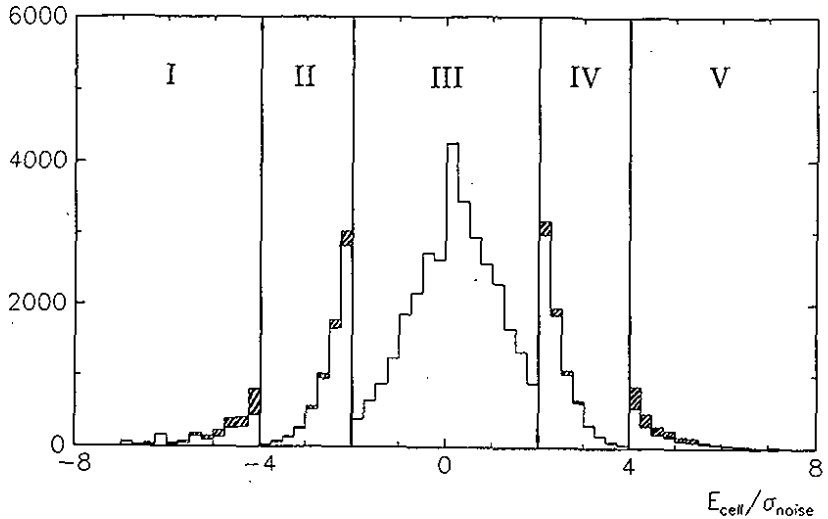

Figure 5.7: Noise (events recorded with a random trigger) on top of true energy deposit (from simulation of low Q^2 ($10\ GeV^2 < Q^2 < 100\ GeV^2$) deep inelastic scattering events) in LAC cells in terms of σ_{noise} after noise suppression.

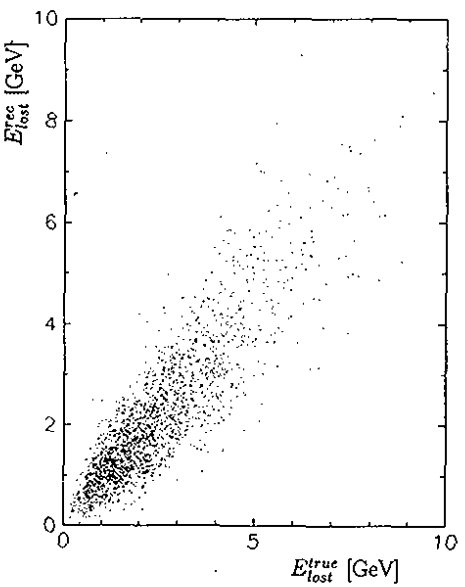

Figure 5.8: Correlation between the true energy lost in front of the calorimeter (E^{true}_{lost}) and its estimation in the reconstruction (E^{rec}_{lost}) for simulated low Q^2 deep inelastic scattering events.

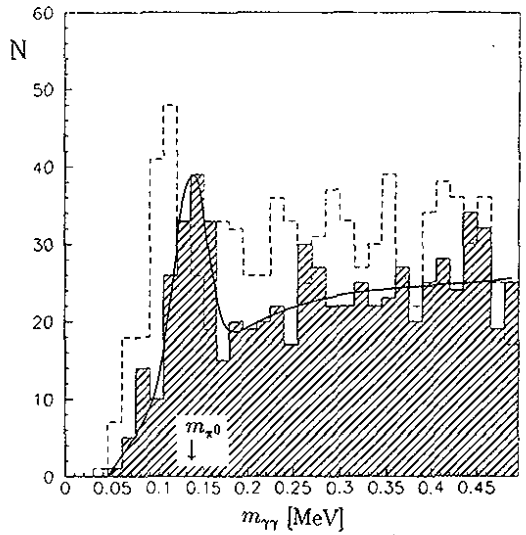

Figure 5.9: The effective mass of two photons before (dashed histogram) and after (hatched one) the dead material correction. The peak in the distribution corresponds to decay $\pi^0 - \gamma\gamma$.

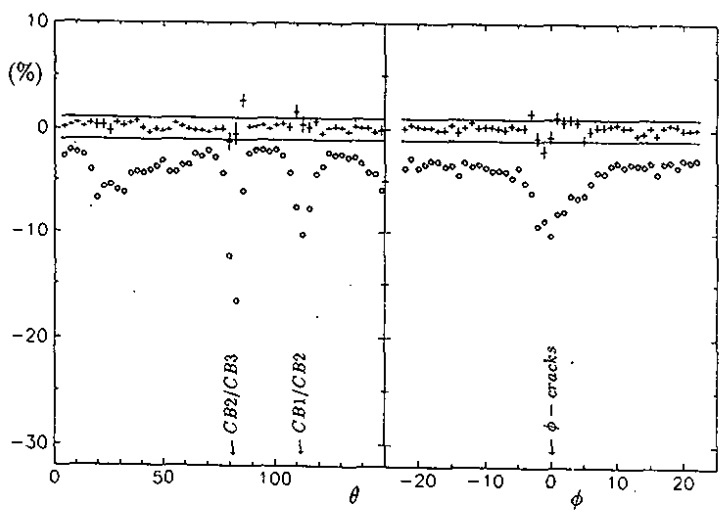

Figure 5.10: Performance of the dead material correction for simulated pions at 20 GeV. Ratios $(-E^{true}_{lost})/E^{true}_{tot}$ (circles) and $(E^{rec}_{lost} - E^{true}_{lost})/E^{true}_{tot}$ (crosses) are shown as function of θ and ϕ (both given in degrees). Before the correction a crack structure is clearly seen. Solid lines correspond to ±1% deviations from the true energy.

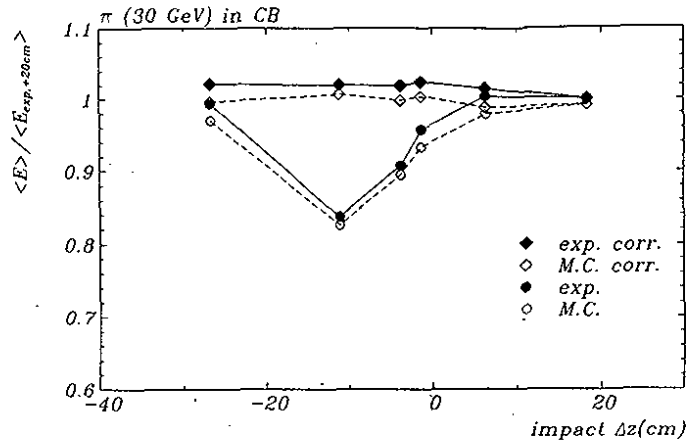

Figure 5.11: Response across the CB2/CB3 z crack in a pion test beam of 30 GeV at CERN.

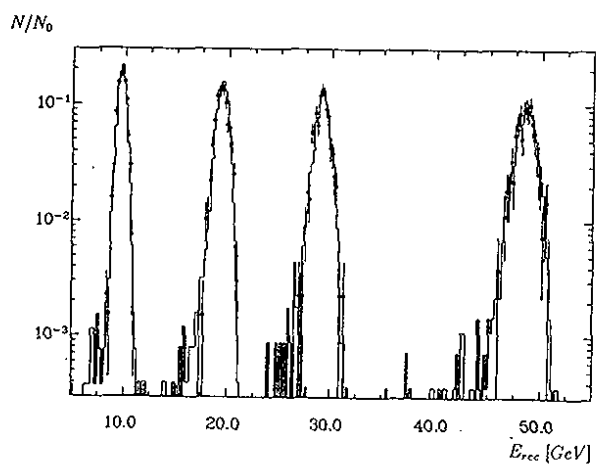

Figure 5.12: Reconstructed energy for data (histogram) and MC (points) for electron energies of 10, 20, 30 and 50 GeV (BBE Wheel).

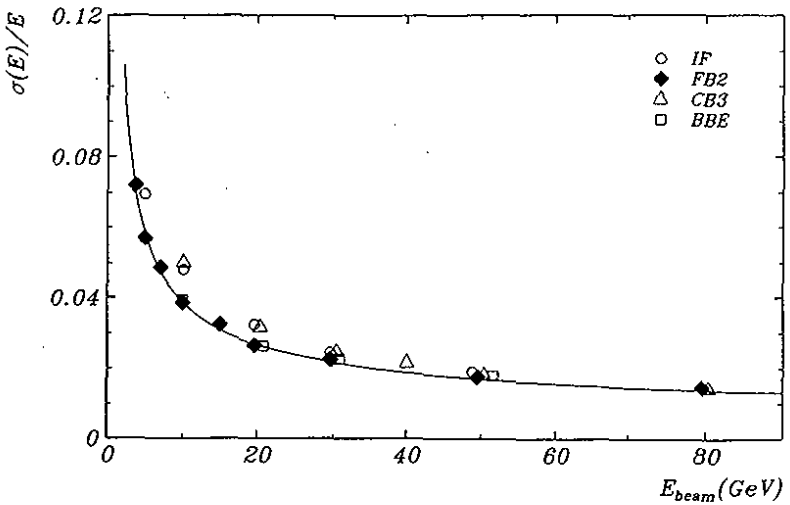

Figure 5.13: Energy resolution as function of electron energy for wheels BBE, CB, FB2 and IF. Solid line: parametrization for FB2.

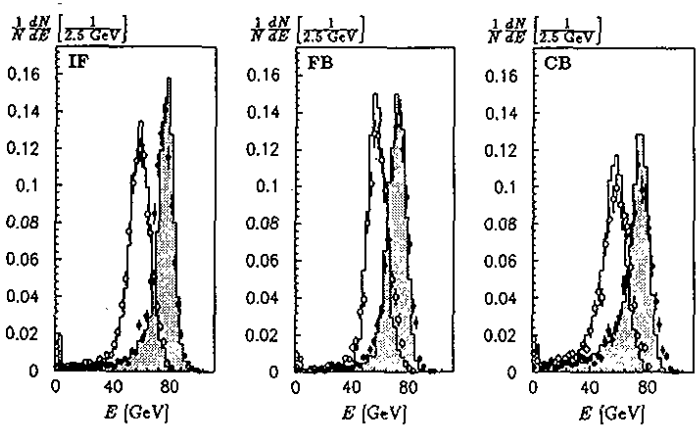

Figure 5.14: Energy reconstruction for pions at 80 GeV for wheels CB, FB and IF on the electromagnetic (open) and hadronic energy scale (closed, shadowed) for data (histogram) and MC (points).

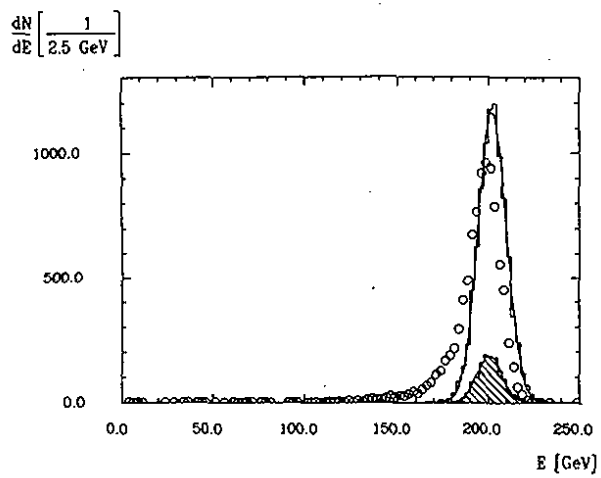

Figure 5.15: *Energy reconstruction for pions at 205 GeV for wheel IF with tail catcher (open* histogram), only IF (circles) and for events fully contained in IF. Solid lines: fitted Gaussian distributions.

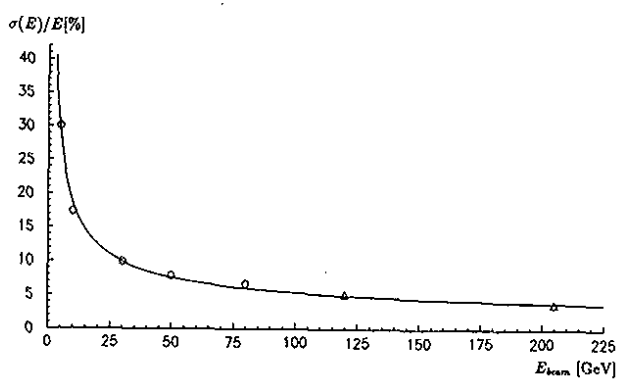

Figure 5.16: Energy resolution as function of pion energy for wheel IF. Circles: IF only , triangles: IF + iron tail catcher. Parametrization according to equation (2) with A = (50.7 ± 0.1)% [$\sqrt{GeV}$], B = 0.9 GeV and C = 1.6 ± 0.1%.

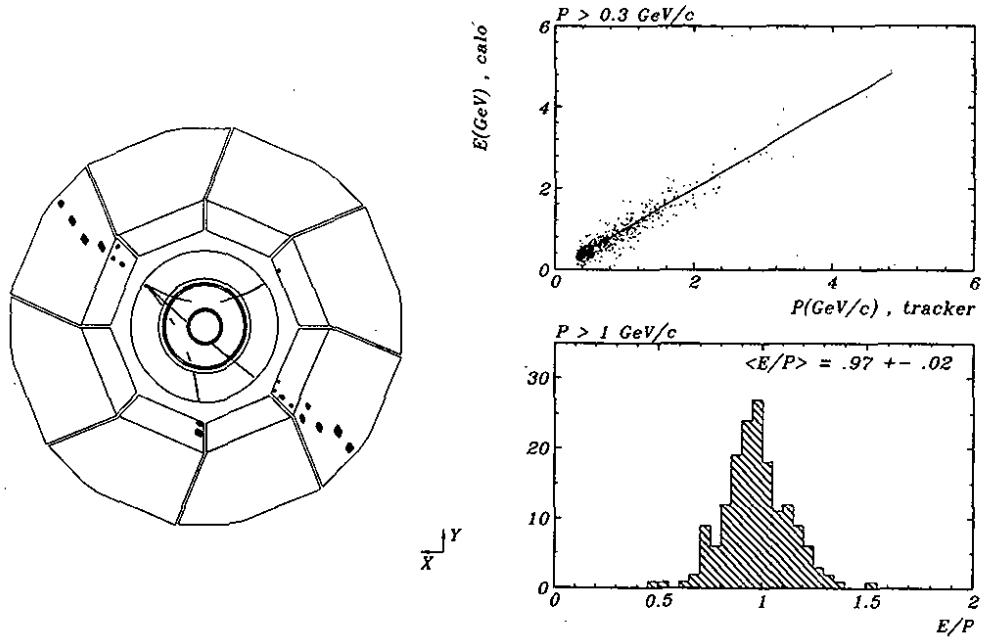

Figure 5.17: Energy/momentum match of electrons generated by cosmic muons measured in the CJC and LAC wheels CB.

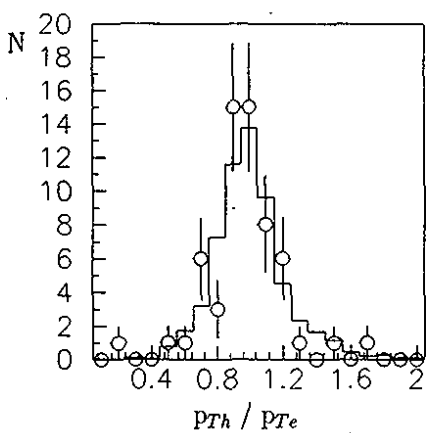

Figure 5.18: Transverse momentum balance p_{th}/p_{te} for both scattered electron and hadronic shower detected in the LAC for data (open symbols) and Monte Carlo (histogram).

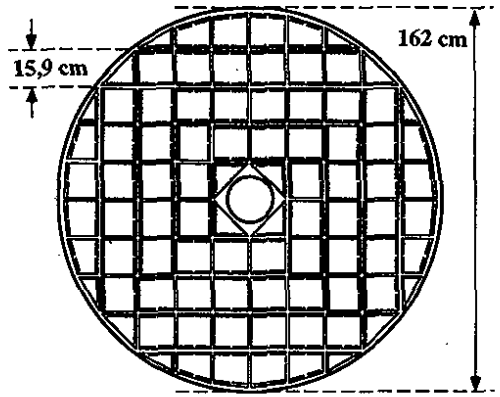

Figure 5.19: Transverse view of the backward electromagnetic calorimeter (BEMC).

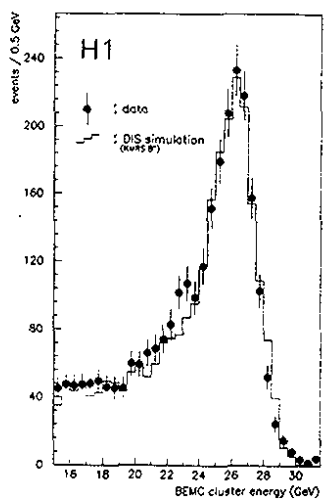

Figure 5.20: Timing precision of the analog delay lines in the BEMC analog electronics in units of HERA bunch crossings (96 ns).

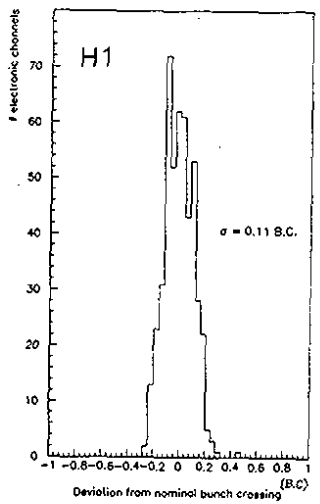

Figure 5.21: Distribution of scattered electrons from deep inelastic scattering observed in the BEMC. The histogram represents a simulation including all known detector effects.

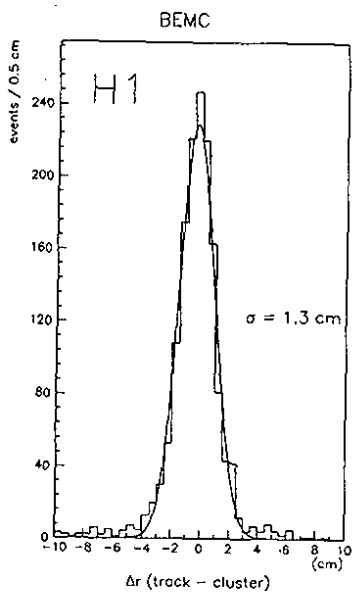

Figure 5.22: Matching precision between electron tracks measured in the central drift chamber and the reconstructed impact point in the BEMC.

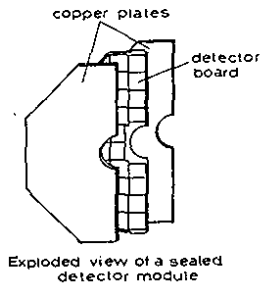

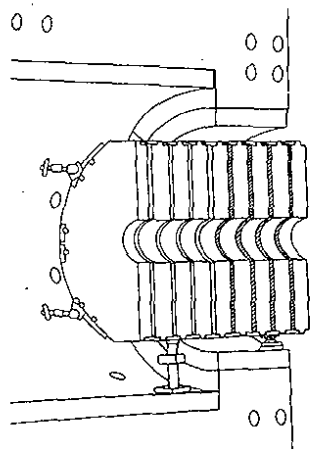

Figure 5.23: Cross sectional view of the plug calorimeter (PLUG).

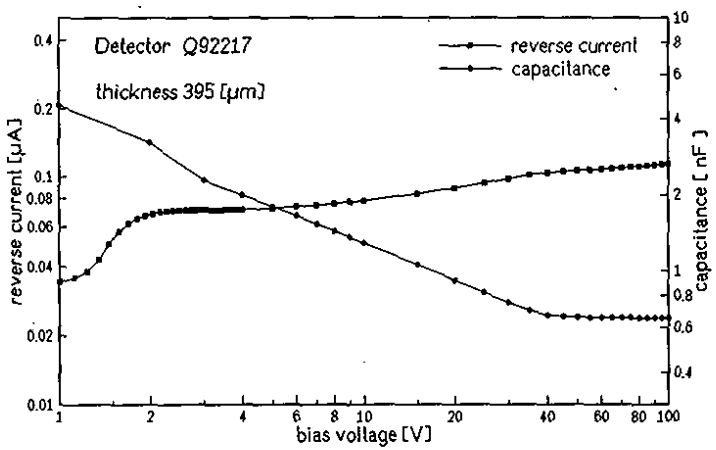

Figure 5.24: Typical $I/V-$ and $C/V-$characteristics of the Si-detectors in PLUG.

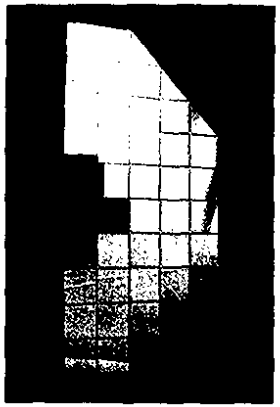

Figure 5.25: Layout of the Si-detectors in one plane.

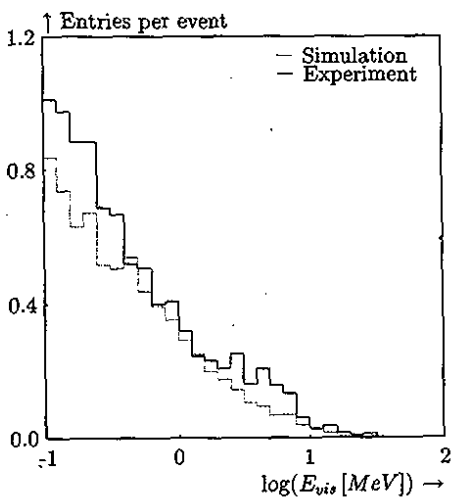

Figure 5.26: PLUG response to ep events compared to MC simulations.

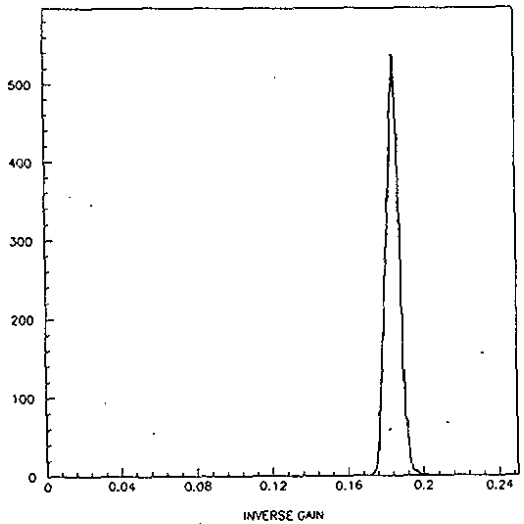

Figure 5.27: Channel to channel variation of the TC electronic calibration constants.

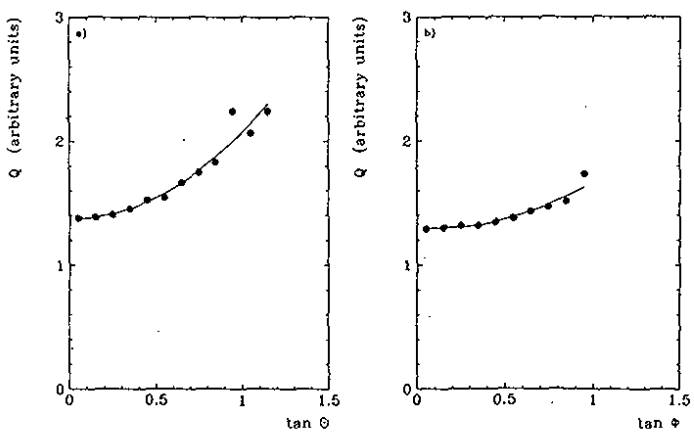

Figure 5.28: Mean muon signal as function of the incident angle with respect to the normal of a chamber plane: a) θ dependence, measured along the wire direction, b) ϕ dependence, measured perpendicular to the wire direction. The curves are fits to a second order polynomial.

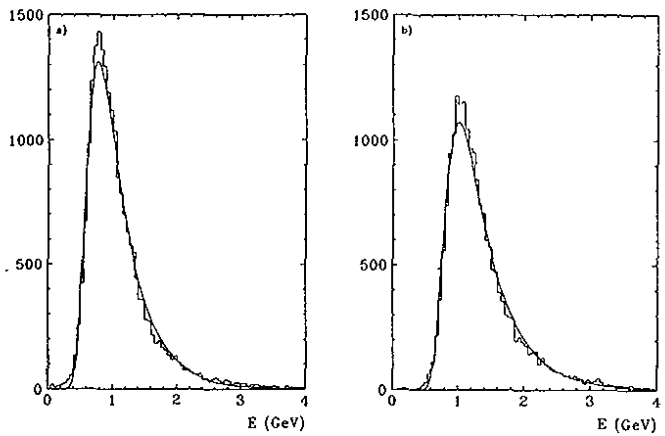

Figure 5.29: Muon spectra summed over a complete module for a) inner towers normalized to 4 planes, and b) outer towers normalized to 5 planes. The curves are fits to a Landau distribution.

6 Muon system

6.1 Iron instrumentation

6.1.1 The limited streamer tubes

As described in Section 3 the iron yoke of the main solenoid magnet surrounds all major detector components of H1. It is interleaved with slits which are equipped with limited streamer tubes (LST) which serve different purposes. Besides the hadronic tail catcher capabilities discussed in Section 5.4 the purpose of the LST system is the detection and survey of tracks of penetrating muons. Considering the large dimensions it is obvious that a reliable detector system is needed which must not be too expensive. The widely used PVC streamer tubes [125] could not be used for safety reasons, since they contain halogen compounds. Instead, after ample investigations, the rather new plastic material Luranyl [126] was found to be suitable for our chambers [127]. Luranyl is a halogen free plastic material which can be extruded with the requested precision, and which also can be painted with the graphite paint needed to obtain the required surface resistivity. Some basic features of Luranyl are listed in Table 6.1. However it is worth mentioning that the required tests delayed the project by approximately two years.

Density	1.06 g cm^{-3}
Thermal expansion (23 - 80 °C)	$0.6 - 0.7 \times 10^{-4}$
Surface resistivity	$10^{14}\,\Omega$
Softening point	100 °C

Table 6.1: Basic properties of Luranyl [126].

The basic elements of our chambers are extruded 8-fold profiles with a cell size of 10×10 mm^2 (including the profile wall thickness). The requested precision was defined to be $\delta = 0.1$ mm and the corresponding straightness of the profiles had to be better than 1 mm per m. The profiles are coated with graphite paint (50 % Electrodag 154 [59] and 50 % butylacetate) to yield a a low surface resitivity of $\approx 10 - 30$ k$\Omega/\Box$. A distribution of the uniformity achieved with this technique is shown in Figure 6.1 [128]. The HV is applied to this surface. The center of each cell is occupied by a silver coated Cu-Be wire of 100 μm diameter at ground potential. This wire is kept in place by spacers every 50 cm. On top of the profiles a Luranyl cover with high resitivity of ≈ 10 M$\Omega/\Box$ is added (25 % Electrodag 154, 25 % Molydag 727A and 50 % butylacetate). Two such profiles are then put into a gas tight box which is also made of Luranyl. All connections to the chamber such as gas, high voltage, and signals are provided on one end of such a box. Several boxes are finally put together to build a complete streamer tube layer. On the high resistivity side either strips or pads are glued onto the planes, depending on their position in the iron. Such a complete plane is then put onto an aluminum plate and finally wrapped into a non conducting foil to guarantee electrical insulation from the iron.

A schematic view of the basic structure is given in Figure 6.2, while Figure 6.3 displays the configuration of the planes within the iron together with an indication where strips and pads are located. As an example, the instrumentation of a barrel octant is shown.

Starting from the interaction point there is first a so called muon-box installed in front of the iron. It consists of three layers (two strip layers with strips perpendicular to the wire direction and a third layer with pads). Pad layers are also installed in the first three iron slits. The fourth slit is twice as wide as the others and houses two chamber layers (one strip and one pad layer). Pad layers are inserted in the remaining five slits. Behind the iron there is again another muon-box. In total there are 16 streamer chamber layers in depth. The pad signals of consecutive

Material	Luranyl
Total size	4000 m^2
Nr. of profiles	13000
Nr. of wires	103000
Nr. of strips	28700
Nr. of analog channels	4000
Angular coverage	$5° \leq \theta \leq 170°$

Table 6.2: The LST detector

pads are added (5 + 6) and are read out via ADCs, providing two-fold energy granularity in depth. All wire- and strip-signals are read out digitally. Three dimensional space-points from tracks can be obtained in the three strip chambers. Table 6.2 lists some parameters of the LST detector.

6.1.2 Gas system

Again due to safety reasons the chambers are operated with a non-inflammable three component gas mixture of CO_2, argon and isobutane with relative volume fractions of 88 %, 2.5 %, 9.5 %. This mixture had to be used during the installation period, and since it provides acceptable performance it is still used. However the gas system is designed such, that the use of the standard gas mixture of only Argon and Isobutane is possible. The total gas volume of all 911 streamer chambers amounts to 36 m^3 with a total surface area of $\approx$ 9000 m^2. Due to the pressure drop within pipes and chambers it is not possible to connect all chambers serially. After a gas distribution system different parallel circuits supply the detector with gas. The flow in each branch can be adjusted with needle valves, and is measurable via computer readable flow meters. 192 branches are used including some spare and test branches. The number of chambers to be connected serially was chosen such that the total gas volume per branch does not exceed $\approx$ 200 l. The main distribution stations are interconnected by stainless steel pipes of 60 mm diameter and located at five places around the detector. The connections from these distributors to the chambers finally are realized with polyurethane pipes with inner diameter of 6 mm. Five such pipes are enclosed in a flame-resistant tube. The gas composition, specially the isobutane content, is monitored. Two units monitor the input gas from the main gas mixer and stop the gas flow if the fraction is outside the range between 8.5 % and 9.9 %. The precision of the system is such that the gas flow of each single component is reproducible within the 1% level.

The gas quality is also monitored exposing monitor LST chambers to an ^{90}Sr source. The pulse height spectra of these chambers are measured independently from the DAQ system in the framework of a slow control concept. At present we use two of these monitor chambers, one in the common incoming gas-flow and one in the outgoing flow of a particular gas module. The chambers allow the monitoring of the gas composition and the HV regulation. In addition the chamber in the gas outlet would indicate the effect of possible leaks.

6.1.3 High voltage system

Five high voltage crates [129] supply the whole LST detector with high voltage. In total 200 independent HV channels are used. Each channel supplies between 20 and 110 profiles depending on the size of such a cluster. The correspondence between HV channels and chambers is realized

such, that it matches with the gas supply. Chambers within one gas circuit are also connected to the same HV channel. But before being fed to the profiles another passive distribution system is implemented. This system allows to disconnect each single profile from HV in case of problems. Moreover the positions of all switches are computer readable, such that the HV configuration of each single 8-fold profile can be stored on a database.

Two different reference voltages can be applied to the detector. One is selected to be well below working conditions at $V1 = 3000$ V. This setting is activated during unstable beam conditions e.g. during beam injection periods and during tuning phases when not yet all collimators and scrapers of HERA are in position. Accidental beam losses have lead to very high activity in the streamer chambers which probably caused the failure of a few profiles in the early phase of HERA. The normal operating voltage is set to $V0 = 4500$ V at normal pressure (1013 hPa at Hamburg). The gas system is operated at a constant overpressure with respect to the atmospheric pressure outside. Since the charge gain of streamer chambers depends on the pressure we regulate the high voltage according to the outside pressure. The gain variation amounts to $dQ/Q = -1.73\% dP/\mathrm{hPa}$, while the high voltage $V0$ is automatically adjusted by +2.75 V/hPa. As can be seen from Figure 6.4 this leads to a small overcompensation. In Hamburg we observe pressure changes of up to $\approx$ 6 hPa/h, and the total variation lies below 80 hPa. Other relevant parameters such as temperature are monitored and remain fairly constant over long periods. The currents of all channels within the HV mainframes are constantly monitored. If the current of a single channel exceeds 5 μA, the corresponding voltage is automatically reduced until this maximum current is no longer reached. Channels are switched off, if this limit is exceeded for more than one minute. As another precaution the high voltage is totally switched off if the fraction of isobutane deviates from the range between 8.5 % and 9.9 %.

6.1.4 Readout system

The readout system of the LST detector is split into two parts. The readout of the analog information is incorporated as part of the main calorimeter and is discussed in Section 5.4. Due to the high bunch-crossing frequency and the great number of channels, the development of a new readout system was necessary for the wire- and strip-readout. Each wire (strip) is connected to a comparator, a synchronisation circuit and a digital pipeline. In a first step the wire signal is digitized according to an exernally adjustable threshold. The output is then synchronized with the HERA bunch crossing frequency and fed into a digital pipeline every 96 nsec. These pipelines have a depth of 32 steps corresponding to a total storage time of $\approx$ 3.1 μsec.

In order to minimize the space required for the front-end electronics the complete logic, starting from the synchronisation stage, for eight data channels has been integrated in a gate array [130] as shown in Figure 6.5.

The leading edge of the input signal clocks the first flip-flop of a dead time-free synchronization circuit. The synchronized data patterns are buffered in a pipeline register. As soon as a trigger is accepted, the filling of pipelines is stopped. The data pattern correlated to the triggered event is kept in the known stage of the pipeline, and can be strobed to the last one by appropriate steering signals. By means of a remotely controlled signal (ENO) it can be decided whether the data pattern of one time slice, or the logical OR of two adjacent time slices is read out. This is necessary since the signal propagation within the chambers can extend to more than 100 ns. In addition the eightfold OR of the stored data pattern is clocked into a separate flip-flop of the readout chain, thus providing a reduced granularity for trigger purposes.

As a test facility a known data pattern can be fed into the circuit, and be strobed through the pipeline where it is then read out and compared to the original data pattern. With this possibility it is easy to do a complete test of the whole readout electronic chain. Specially during the installation period this feature allowed for easy identification of bad or wrong connections.

The electronics for 16 channels is housed on a readout card which is directly mounted onto the streamer chamber layers. This allows for early digitization and thus provides high noise resistance and a significant reduction in the number of cables needed. Multiple readout cards can be daisy chained. A whole layer of LST-chambers is thus read out serially. The readout chains of a maximum of 24 layers are connected to special VME-based readout controllers (ROC), which are responsible for the data transfer from the chambers to the ROC's and provide zero suppression, and data encoding. They also submit all relevant steering signals to the readout cards.

Upon arrival of the first level trigger (L1), the ROC's start to collect the data from the electronics. The absolute position of the data corresponding to the triggered event within the frontend pipelines depends on the decision time of the trigger and the distance between the central trigger logic and the respective chambers. Due to the physical dimensions of our detector, the latter delay is different for different areas.

One ROC serves up to 12300 digital channels corresponding to 24 chamber planes with 512 channels each. Since we operate 64 of these ROCs simultaneously less than 300 μs are needed to collect all data.

The architecture of the local DAQ environment is given in Figure 6.7. Due to the zero suppression and encoding performed in the ROCs, only the channel numbers of hit channels have to be collected by a processor. The VME crates are distributed in five clusters around the detector. The readout of these units starts after a second level trigger (L2). VME processors collect the data which are then first stored locally. Again pipe-lining is available on this level. The data of up to 20 events can be stored locally before they are delivered to the central H1 data acquisition system. The readout time of the LST detector depends on the total number of hit channels and is shown in Figure 6.6. For multiplicities observed in H1 we are able to collect data with a frequency of $\approx 300 - 500$ Hz with the present configuration. The mapping from an on-line to off-line numbering scheme is taken care of already in the local on-line system, as well as substantial monitoring tasks which provide an overview of the performance of the LST detector.

6.1.5 Track reconstruction

The track reconstruction uses all the information available in the LST system, i. e. 16 wire, 5 strip and 11 pad layers. The resolution for wire and strip hits is 3-4 mm and 10-15 mm respectively. Wires and strips planes are perpendicular to each other. The pads are defining coarse space points with a precision of about 10 cm.

With 16 layers the track resolving power is best for the wires. Therefore the pattern recognition starts with the wires. Track segments are parametrized by straight lines and must fulfill certain quality requirements. These are derived from the triplet residuals to account for the resolution and from the fraction of all penetrated layers showing a hit to account for the single layer efficiency of typically 80%. To get curved track candidates several segments are connected. Then the pattern recognition is looking for track segments in the strips. They must have at least one matching wire track candidate which has in all layers of the strip candidate at least one hit in the same physical LST chamber. These matching wires and strips are then combined to a three dimensional track. In case of ambiguities the pad information is used to resolve them. The combination which fits best to the pads in space and amplitude (analog pad charge divided by number of wires hit) is chosen. If there are no strips for some wire tracks the other coordinate is taken from the center of gravity of the pads belonging to the wires.

For a reconstructed track at least three wire layers, one of these inside the iron, are required. The magnetic field $\vec{B}(\vec{r})$ varies strongly inside the iron plates and in the gaps and the energy

loss in one plate is at least 80 MeV. The track fit uses an average magnetic field for each plate and gap and performs a least square fit simultaneously to wires and strips. The effect of the energy loss is accounted for by an iteration procedure. The result of the fit are the five track parameters and their errors at the innermost wire ($Q/p, \phi, \theta$, two space coordinates) and the list of wires, strips and pads used.

6.1.6 Performance

After installation into the iron all chamber planes had been tested again. Some profiles did have problems from the beginning, such that they could not be operated with high voltage. If the number of bad profiles in one plane was too high, the plane was dismounted again and repaired. Otherwise the profiles affected were grounded. About 60 profiles had to be disconnected (i.e. 0.65 % of all installed profiles) after the detector was moved into the beam position. A final technical run proved that the detector was working properly before the area interlock was set.

Calibration data have been taken during extensive cosmic runs. One result of such calibration runs is the efficiency of the chambers, which is given in Figure 6.8. It agrees well with the expected values for our operating condition, and the activity in the different modules reflects nicely the angular spectrum of the cosmic muons. The number of noisy channels amounts to a total of only 26 (6 single and two neighboring noisy strips, and two single noisy wires and a whole noisy profile of 16 channels). After HERA came into operation some very high activity was observed in the LST detector (and the others as well). Specially during injection periods in the very beginning when the safety precautions of reduced HV was not yet activated, the chambers tend to draw current and cause HV trips in the corresponding HV channels. Similar observations can be made when beams are accidentally lost during energy ramping and steering periods. Probably due to such occasions some additional 20 profiles had to be grounded during these times. Some of these disconnected profiles could be recovered after some increase of the gas flow. The time dependence is shown in Figure 6.9. However no changes in the efficiencies have been noticed since the beginning of the ep collisions, and also the number of noisy channels has not increased. Figure 6.10 shows the number of wires and strips per event for events triggered by the muon system. The wire data show a signal starting at a multiplicity of 13 which is roughly the mean number of wires expected for single penetrating muons with a plane efficiency of 80 %. Figure 6.11 finally shows the corresponding activity distribution within the detector. The high rate in the six modules in the forward area indicates that most of the hits in the LST system occur in the region close to the beam pipe in proton direction and are produced by proton remnants.

The two spikes (in the backward endcap and the forward barrel) are due to noisy wires. The distribution in the barrel structure reflects the fact, that some triggers originate from cosmic muons (the trigger rate from cosmic muons amounts to 2 Hz). The counting rate in the backward endcap is rather low. Most of the particles which pass the backward endcap are due to beam halo muons coming parallel to the proton beam, which are excluded from these distributions.

In the barrel region cosmic muons can be used to determine the reconstruction effiency extrapolating jet chamber tracks. Geometrical acceptance limits this efficiency to 89 % in the plateau region above the threshold of 2 GeV as shown in Figure 6.12.

6.2 Forward muon system

6.2.1 General description

The purpose of the forward muon spectrometer is to measure high energy muons in the range of polar angles $3° \leq \theta \leq 17°$. The detector consists of drift chamber planes mounted on either

side of a toroidal magnet. The design aim was to measure the momenta of muons in the range between 5 GeV/c and 200 GeV/c, the lower limit being given by the amount of material the muons have to penetrate and the influence on the momentum resolution of the multiple Coulomb scattering in the magnet iron. The upper limit is set by the magnetic field strength of the toroid together with the spatial resolution of the drift chambers. The expected momentum resolution at 5 GeV/c is 24% and deteriorates slowly to 36% at 200 GeV/c. Muon momenta below 5 GeV/c are be measured in the forward tracker.

Figure 6.13a shows schematically the detector arrangement and the toroid magnet. The latter is described in Section 3.4. The drift chamber planes, which increase in size from about 4 m diameter for the first detector plane to 6 m diameter for the last, are all divided into octants of individual drift cells mounted on Al-frames. The orientation of the drift cells is such that four of the planes essentially measure the polar angle (θ) and thereby provide the momentum of the traversing muon while the remaining two measure the azimuthal angle (ϕ). Each plane consists of a double layer of drift cells staggered by half a cell width (Figure 6.13b). This arrangement enables the resolution of left-right ambiguities and also the determination of t_0 as will be explained below. The total number of drift cells is 1520.

6.2.2 Chamber design

All drift cells have a rectangular cross section with a depth of 2 cm, a width of 12 cm and lengths between 40 cm and 240 cm. With a central sense wire the maximum drift distance is 6 cm. The cells have 50 μm thick Nichrome wires except for the inner short cells where the diameter is 40 μm. For cells longer than 1.5 m there is a wire support in the middle. As illustrated in Figure 6.14 each cell comprises two printed circuit board (PCB) planes, copper-coated on both sides, and 0.7 mm thick extruded Al-profiles between cells. The outer copper surface of the PCB is grounded to form a screened box together with the Al profiles. The inner surface has been machined to give 4 mm wide strips which are used as drift electrodes. They are connected to a 230 MΩ metal film resistor chain mounted on the end cap to obtain a uniform drift field. The end caps are made of moulded Noryl with high precision holes to locate the crimp pins for fixing the sense wires and the holes for the gas connections. One end contains the high voltage distribution resistor chain and the sense wire read-out connection isolated via a 1 nF ceramic disc capacitor. Sense wires of adjacent cells are linked together via a 330 Ω resistor at the other end forming the equivalent of a U-shaped cell which then is read out at both ends. This allows not only a determination of the track position transverse to the sense wire from the measurement of the drift time but also of a coordinate along the wire by charge division measurement and thereby giving information on which cell of a coupled pair was hit.

The chamber signals are amplified, digitized and read out using the same components as all other drift chambers within the H1 detector (see Section 4.4).

6.2.3 The chamber gas and high voltage system

The choice of gas for the drift chambers was determined by several requirements. One is the desire to work in a drift voltage range where the drift velocity is constant. Further the gas has to be fast enough for the pulse to arrive in time for the trigger and finally it should be non-inflammable for safety reasons. Currently the so called FMS-gas (forward muon spectrometer gas), which is a mixture of 92.5% argon, 5% CO_2 and 2.5% methane, has been chosen for the chambers. The gas is mixed and purified in a recirculator. The chambers have a total gas volume of 4 m^3, and with a small overpressure of about 0.2 hPa measured at the output, the return gas flow is typically 90% of the input and the oxygen content is of order 100 ppm. For the FMS-gas

the drift velocity as a function of the drift field voltage, corrected for atmospheric pressure, is shown in Figure 6.15. An average drift field of 480 V/cm gives the desired drift velocity of $\sim$5 cm/μs. The drift field is defined by an increasing positive potential from the grounded cathode to +2.88 kV on the center electrode at the position of the sense wire. The sense wire is kept typically at 4.21 kV for the 40 μm wires and at 4.26 kV for the 50 μm wires. The gas gain is controlled by the difference in voltage between the sense wire and the drift field close to the wire.

A 120-channel high voltage system [129] supplies distribution boxes on the detector with high voltage via 50 m long coaxial cables. One module (6 kV, 1 mA) supplies drift voltage to an entire octant, feeding 20-40 individual resistor chains.

Similarly another module (8 kV, 200 μA) supplies the sense voltage to all but the 12 innermost cells of a θ-octant. In case of bad beam conditions it is set to a lower voltage. For the ϕ-octants the central section which is close to the beam tube can be moved outwards mechanically by remote controls and thus there is no need for any special HV arrangement.

There is a continuous monitoring of the gas composition and flow rates as well as of the high voltage, communicated vía an Apple Macintosh II ci in the control room. From this work station it is also possible to control the high voltage of the detector and the toroid magnet.

6.2.4 The charge-time analysis

Only the rising edge and peak region of a pulse are used to get the time and charge information. A pulse is said to start when there are two successively rising digitisings above threshold (see also Section 4.4.7).

The end of a pulse is taken as the second successive digitising after the peak which is below threshold, or eight 9.6 ns time bins from the start of the pulse, whichever occurs first. The arrival time of the pulse is obtained by extrapolating a line fitted to the steepest part of the leading edge back to the intercept with the background level. With a test set up, looking at cosmic muons, this method gave a resolution of < 200 μm as illustrated in Figure 6.16. This result was obtained with a gas mixture of 90% argon and 10% propane providing a drift velocity of 4 cm/μs. However, to satisfy the gas requirements specified in Section 6.2.3 we have chosen the FMS-gas with a drift velocity of $\sim$5 cm/μs, resulting in an expected resolution of $\sim$250 μm. Pairs of pulses which originate from the same hit are associated by requiring the difference of their arrival times to be less than the full propagation time through the two sense wires the linking resistor.

The collected charge is found by integrating the digitisings of the pulses from the two wire ends over intervals of the same length, with subtraction of a constant background. A correction for fractional time bins was found to be important since the start times for the two pulses are subject to variable propagation delays. With cosmic muons in the test set up we found a charge-division versus distance characteristic linear to about 1%, which is well matched to the resolution.

6.2.5 Track reconstruction

The space points obtained from the charge-time analysis of the chamber hits are used in a three step procedure for track reconstruction which starts with the pairing of hits in each double layer followed by association of pairs into straight track segments and finally the linking of track segments through the toroid to form full tracks and thus provide a momentum measurement. Pair finding in the double layers is decisive due to the displacements of cells which results in the

sum of drift times being a constant (compare Figure 6.13b). A vertex pointing requirement is applied as selection criteria but also unpaired hits are kept to be considered in the track segment finding where we demand 3 out of 4 hits in the θ-layers. The measuring errors of the space points for a pair define a cone which is extrapolated to the other θ-layer on the same side of the toroid. In the area defined by the cone, hits are tried for segment fits and are selected by a χ^2−cut. In the future the information from the ϕ-layers will also be used.

For the linking procedure each pre-toroid segment is tracked through the magnetic field of the toroid, taking into account energy loss and multiple Coulomb scattering in the magnet iron. By doing this for a minimal reconstructible momentum of 2.5 GeV/c in the spectrometer and for either of the two muon charges possible, regions in the θ-layers after the toroid are defined inside which segment candidates for linking are considered. From the crossing angle of two linked segments an estimate of the momentum is made. Starting from the pre-toroid segment and the estimated momentum the tracking is repeated as the momentum is changed in small steps around the estimated value. Each post-toroid segment obtained from the tracking is compared to the actual segment found and a χ^2 is calculated. The minimum of the χ^2 variation with momentum defines the momentum corresponding to the best fit.

6.2.6 Drift velocity and t_0-determination

Beam halo muons are used to determine the drift velocity. From the uniform population of the total number of tracks (N) over the full drift distance (Δy), recorded in a run, a rectangular distribution is expected if the drift velocity is constant. However, due to field variations close to the sense wire, dependence on the angle of the track, the possibility of tracks traversing only the corner of a cell etc., the drift velocity will be altered and cause a smearing of the distribution (Figure 6.17). In spite of this smearing, the drift time (t_{mid}), corresponding to half the drift distance (3 cm), can be defined as the time which leaves equal number of tracks above and below. Taking an arbitrary time interval (Δt) symmetrically around t_{mid}, where the distribution is still flat, we can count the number of tracks (N_{mid}) in this interval and use it for a determination of the drift velocity using $v = (\Delta y \cdot N_{mid})/(\Delta t \cdot N)$. The result is $v = 4.926 \pm 0.039\ cm/\mu s$.

t_0 is determined from the specific geometry of the detector which makes one of the following check sums true for each track.

$$t_1 + t_2 + t_3 + t_4 = 4 \cdot t_{mid} \qquad t_1 + t_2 - t_3 - t_4 = 0$$

Here $t_i (i = 1, 4)$ are the drift times in the four θ-layers. The first check sum thus will provide an independent measurement of t_{mid}. t_0 can now be determined from: $t_0 = (3\ \text{cm})/v - t_{mid}$. The widths of the two check sum distributions can be used to find the spatial resolution of the chambers.

6.2.7 Chamber alignment

The drift chambers must be aligned with respect to each other and to the rest of the detector. The cells of a θ-layer are positioned on its supporting Al-frame to a precision of $\sim$50 μm along the drift direction and to $\sim$1 mm in the two other directions. This is better than the achievable resolution and therefore we only have to consider the alignment of the full octants.

Simulation studies and analysis of a small sample of real data have shown that beam halo tracks are suitable for providing the two translational and one rotational quantities which are needed to specify the position of the octant in the plane transverse to the beam direction. Further studies with angle tracks together with the survey will determine the relative positions of the octants along the direction of the beam.

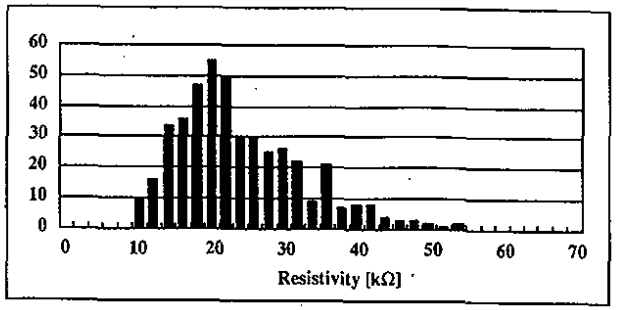

Figure 6.1: Uniformity of profile resistivity.

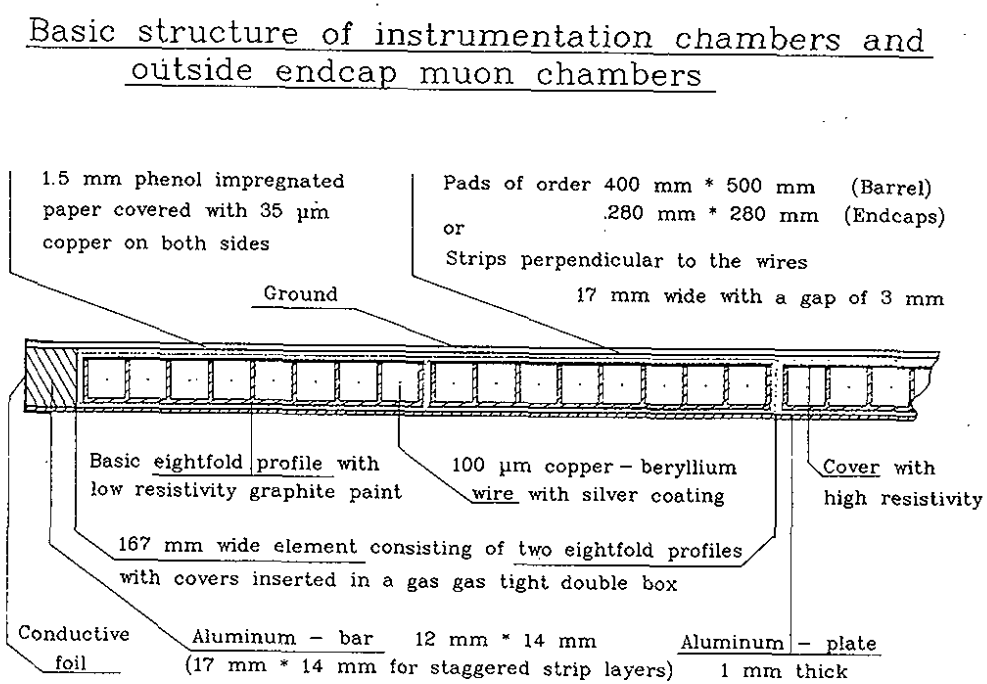

Figure 6.2: Structure of LST chambers.

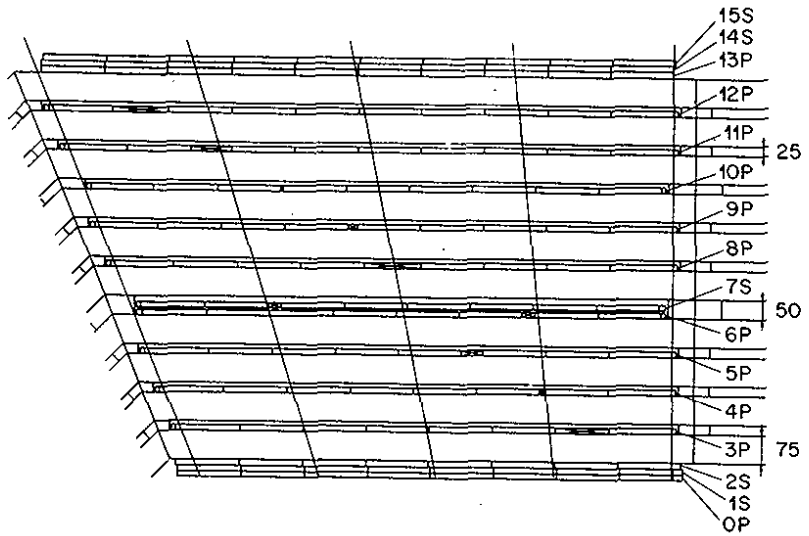

Figure 6.3: Iron instrumentation. The the pointing pad structure of the barrel region is depicted. The crossed elements represent the implementation of so called dummy modules. The available width of the iron slits increases as the radius increases. With the granularity of 16-fold profiles not all slits can be completely filled with active chambers. The dummies fill the remaining space in a defined way to ensure that the dead areas are not aligned for tracks from the vertex region.

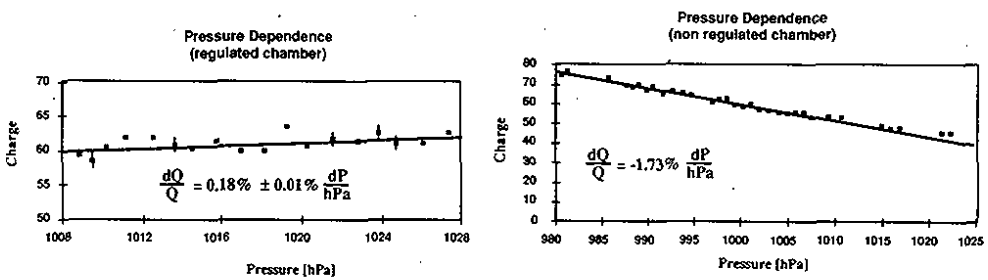

Figure 6.4: Pressure dependence of the gain.

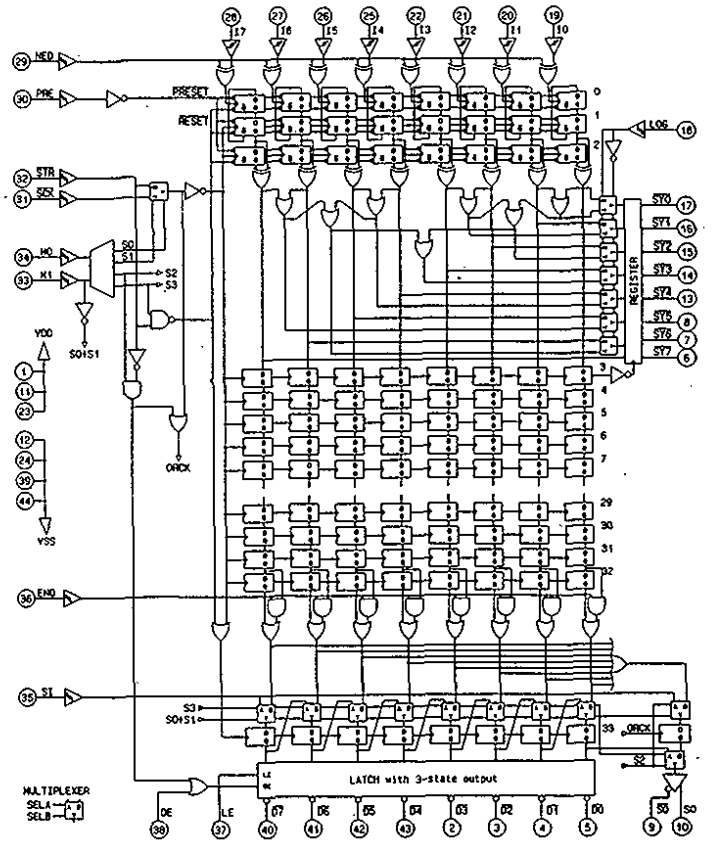

PIPELINE REGISTER
Gatearray Plessey CLA 53024

Figure 6.5: Schematics of the gate array.

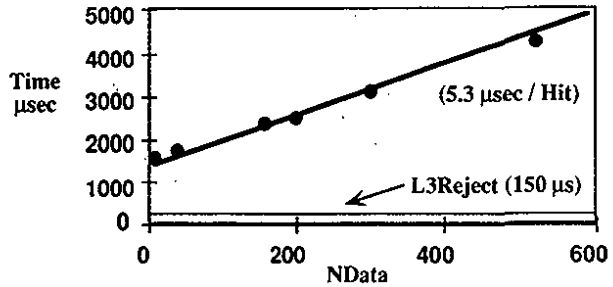

Figure 6.6: Time needed to collect the data from the ROC's in function of the number of hits.

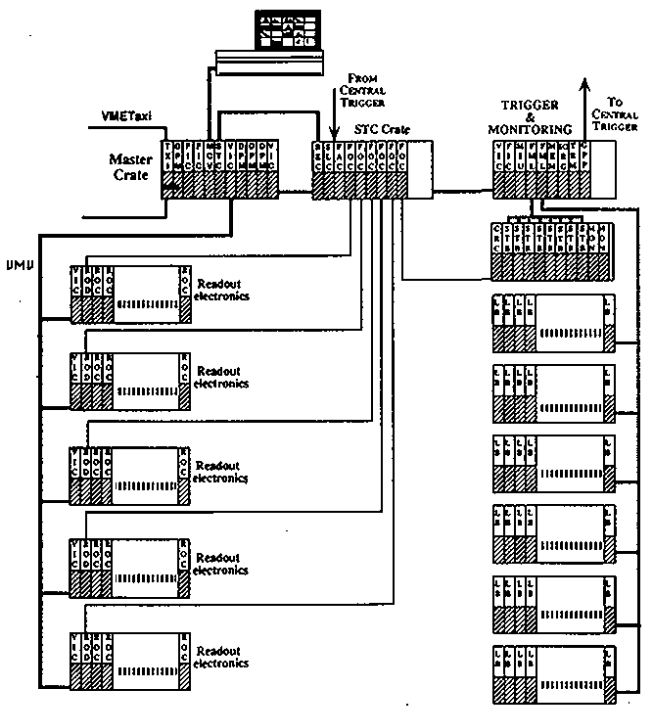

Figure 6.7: The local data acquisition system.

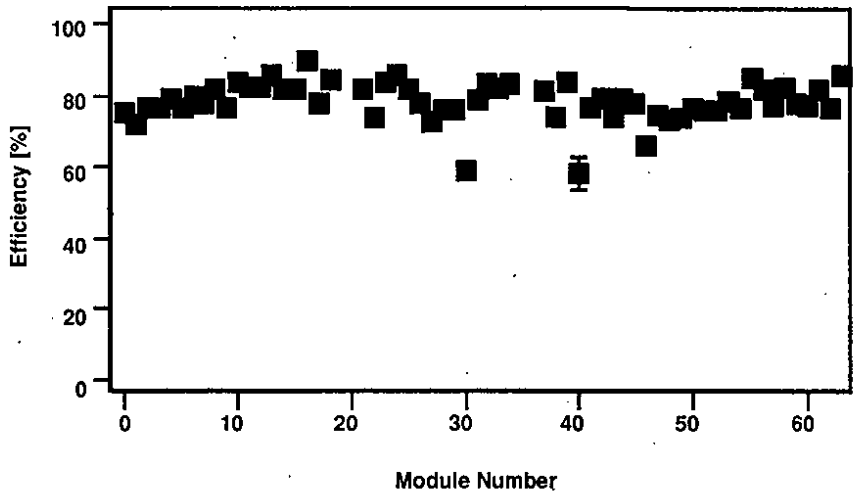

Figure 6.8: Efficiency of chamber planes. The following numbering scheme is used: 0 - 15 backward endcap (from bottom to top), 16 - 31 backward barrel, 32 - 47 forward barrel, 48 - 63 forward endcap (from bottom to top).

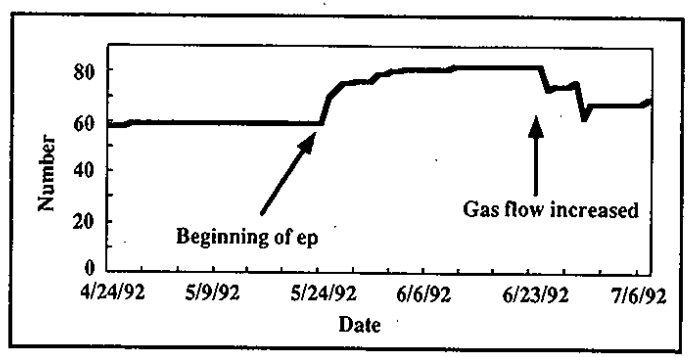

Figure 6.9: History of disconnected profiles.

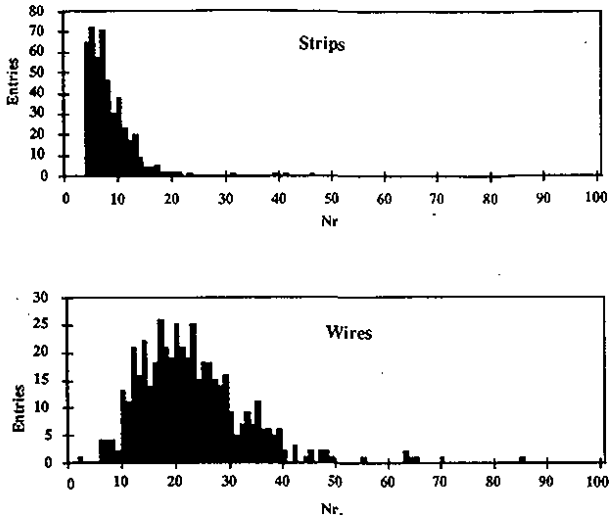

Figure 6.10: Wire and strip multiplicity per event.

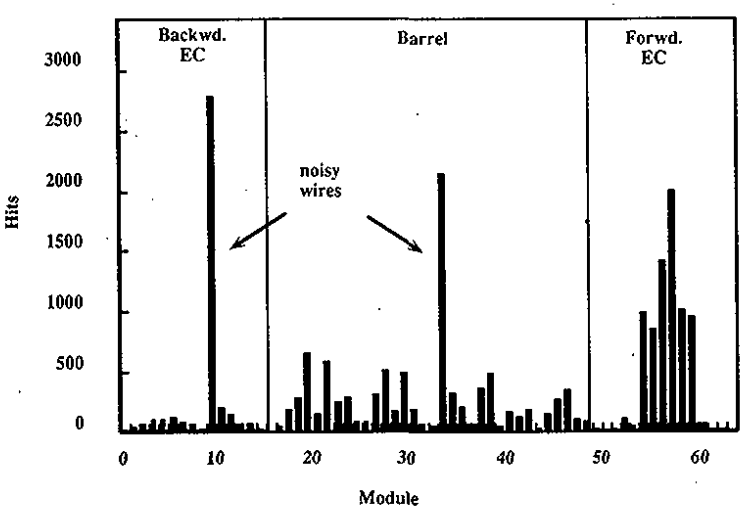

Figure 6.11: Activity profile.

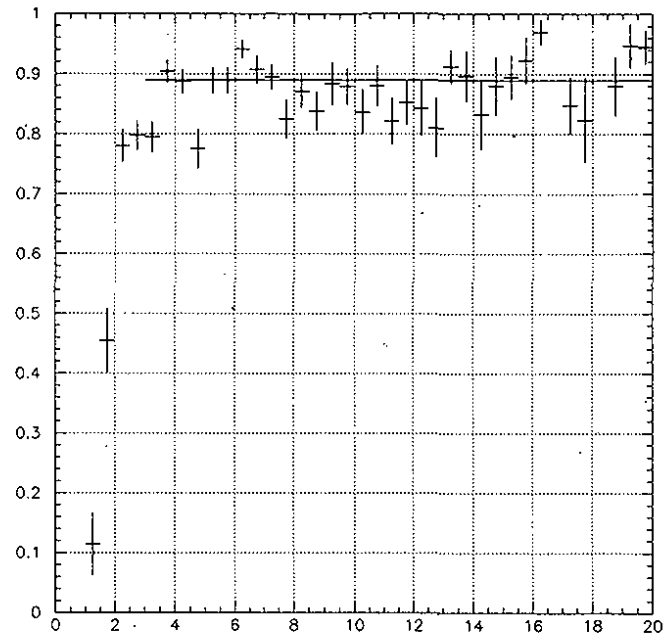

Figure 6.12: Muon reconstruction efficiency in the barrel region as function of the muon energy [GeV] determined from cosmic muons. The average efficiency in the plateau region is 89 % and is determined by geometrical acceptance.

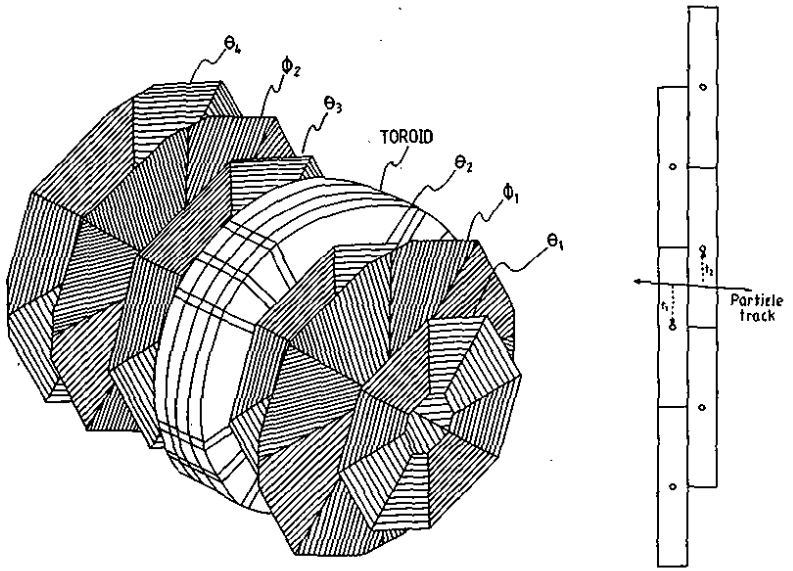

Figure 6.13: a) A schematic view of the forward muon spectrometer and b) the cell structure of a double layer.

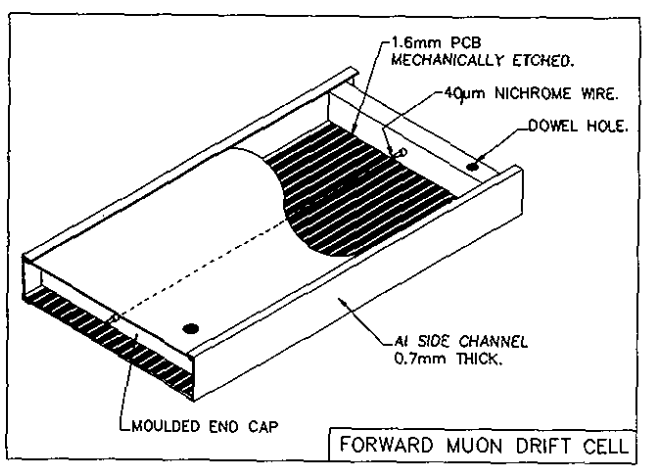

Figure 6.14: The construction of a drift cell.

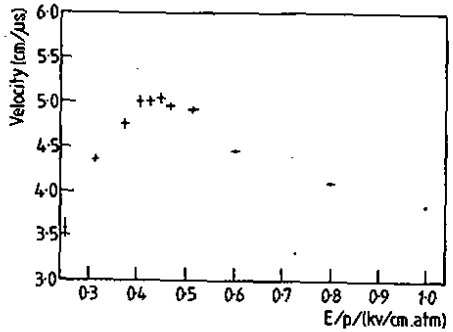

Figure 6.15: The drift velocity versus the drift voltage, corrected for atmospheric pressure, for the FMS-gas.

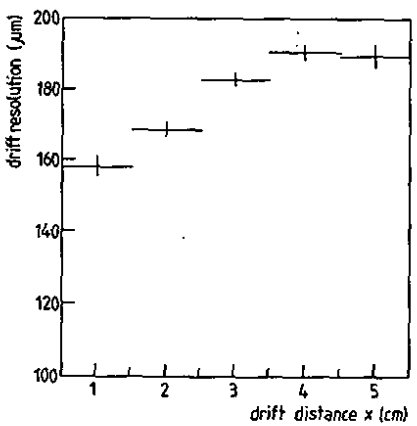

Figure 6.16: The space resolution of a drift cell as a function of drift distance for the gas mixture 90% argon and 10% propane (drift velocity 4 cm/μs).

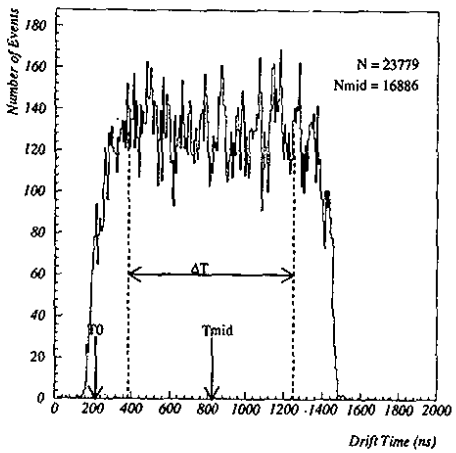

Figure 6.17: The drift time distribution for beam halo tracks used to extract t_0 with the FMS-gas.

7 Luminosity system and electron tagger

The luminosity system is designed as a multipurpose device. Its main task is a fast relative luminosity measurement with a statistical precision of $\sim$ 2% s^{-1} at nominal conditions. In addition it provides electron beam monitoring for the HERA machine, absolute luminosity measurement in the interaction region with an accuracy of $\sim$ 5%, tagging of the photoproduction events and energy measurement for small angle scattered electrons and radiative photons from initial state radiation.

7.1 System Overview

The luminosity is determined from the rate of the Bethe-Heitler events $ep \to ep\gamma$ having a large and precisely calculable cross section [131]. The main source of background is bremsstrahlung from the residual gas in the beam pipe, $eA \to eA\gamma$, with even a larger cross section and the same experimental signature. The rate of these events at design luminosity for the pressure in our beam pipe is expected to be at the level of 10 % of the $ep \to ep\gamma$ rate. This background is measured experimentally using electron pilot bunches. Then the luminosity is calculated as

$$L = \frac{R_{tot} - (I_{tot}/I_0)R_0}{\sigma_{vis}}$$

where R_{tot} is the total rate of the bremsstrahlung events, R_0 is the rate in the electron pilot bunches, I_{tot}, I_0 are the corresponding electron beam currents and σ_{vis} is a visible part of the $ep \to ep\gamma$ cross section, taking into account the acceptance and the trigger efficiency of the whole system.

The luminosity monitor detects scattered electrons and outgoing photons in coincidence. It contains therefore two arms: the electron tagger (ET) and the photon detector (PD). Since the angular distributions for both the electrons and photons are strongly peaked in the direction of the primary e-beam – at 30 GeV polar angles are of the order of $\theta \simeq O(m/E) \simeq 17$ μrad – the detectors should be placed close to the beamline and very far from the interaction region in order to cover these small angles.

The general view of the luminosity system is shown in Fig. 7.1. Scattered electrons are deflected by a set of warm low-beta quadrupoles and a bending magnet located in the region 5.8 m $< -z <$ 23.8 m, pass exit window at $-z$ = 27.3 m and hit ET at $-z$ = 33.4 m. The bremsstrahlung photons leave the proton beam pipe through the photon exit window at $-z$ = 92.3 m, where the proton beam pipe bends upward, and hit PD at $-z$ = 102.9 m. A Pb filter (2 X_0) followed by a water Čerenkov (1 X_0) counter, located in front of PD, protects the detector from the high synchrotron flux. From the p-beam side PD is shielded by an iron wall of 2m length against the proton halo. The water counter can be used as a veto (VC) to select only clean events where the bremsstrahlung photons pass through the filter without interacting. Both ET and PD are installed on remotely controlled movable platforms, and can be moved down from the working positions in the median plane of the e-beam during the beam injection. The time needed to return from the parking to the working position is 1 – 2 min, the accuracy of the platform position measurement is $\sim$ 10 μm.

The acceptance of the luminosity system for nominal electron beam conditions (E_e = 30 GeV, zero tilt) and the expected rates at the design luminosity of 1.5×10^{31} $cm^{-2}s^{-1}$ are given in the Table 7.1. One of the main contributions to the systematic error in the absolute luminosity comes from the dependence of the system acceptance on possible variations of the electron beam angle in the interaction region. This tilt (θ_x, θ_y), typically of the order of 100 μrad, is controlled by the position of the beam profile at PD with high precision, of the order of 10

	unit	ET	PD
Energy interval, $E_\gamma/E_e = 1 - E_{e'}/E_e$		0.2 – 0.8	0.004 – 1.0
Polar angle acceptance interval	mrad	0 – 5	0 – 0.45
Average acceptance for luminosity events	%	48	98
Average acceptance for photoproduction	%	36	–
Visible $ep \to ep\gamma$ cross section	mb	28	174
Luminosity rate for $E > E_{th}$, = 4 GeV	MHz	0.4	1.3
Photoproduction event rate	Hz	20 – 30	–

Table 7.1: Acceptance parameters of the luminosity system.

μrad. The corresponding corrections $C(\theta_x, \theta_y)$ to the σ_{vis} are taken into account already online: $\sigma_{vis}(\theta_x, \theta_y) = \sigma_{vis}(0,0)C(\theta_x, \theta_y)$, and can be further improved during the offline analysis.

Besides the luminosity measurement, the system is used to tag quasi-real photoproduction events with $Q^2 < 0.01$ GeV^2 in the energy interval $0.2 < E_{e'}/E_e < 0.8$. In this case the trigger requires only the energy in ET, while PD and VC act as a veto. The use of such eTAG trigger in coincidence with one of the main detector trigger elements allows to suppress proton induced background by approximately a factor of 200 and thus to enrich the photoproduction physics sample about 20 times [132]. This is especially important during the first stage of the data taking when the background conditions are usually very hard.

7.2 Detectors

In order to perform all their functions at HERA the luminosity detectors should possess high radiation resistance, provide good energy, coordinate and time resolution and be rather compact. This has been achieved using total absorption Čerenkov calorimeters, made of KRS-15 crystals, with a hodoscopic structure. The properties of these calorimeters are summarized in the Table 7.2. The values given for the resolution have been reached at HERA.

Parameter	unit	ET	PD
Aperture $x \times y$	mm^2	154 × 154	100 × 100
Lateral granularity		7 × 7	5 × 5
Chemical composition		TlCl(78%) + TlBr(22%)	
Radiation length, X_0	cm	0.93	
Moliere radius, R_m	cm	2.10	
Crystal length	cm	20	
Radiation hardness	Rad	$> 6 \cdot 10^7$	
Energy resolution, σ_E/E	%	$1 \oplus 10/\sqrt{E}$, (E in GeV)	
Position resolution, $\sigma_x = \sigma_y$	mm	0.3 – 1.2	
Time resolution, σ_τ	ns	< 3	

Table 7.2: *Properties of the luminosity detectors.*

Each cell of the calorimeters is read out by a separate photomultiplier FEU-147 [133] with a 20 mm diameter cathode coupled to the crystal over the gap with an optical contact.

The veto counter is viewed by two phototubes operating in different regimes. The PM running in a standard mode is included in a common spectrometric branch of the photon arm.

The second PM is operating with increased voltage and reacts with an efficiency of 100% to the charged particles with total range in VC exeeding 35 cm. Taking into account the material in front of VC, this corresponds to the 100% efficiency for the e.m. showers initiated by the photons with $E_\gamma > 1.5$ GeV. The veto signal used in the trigger branch is created as "OR" of the two VC channels.

The absolute calibration is an important problem for the luminosity detectors. They should be able to operate at extremely high rates, up to few MHz at design luminosity. In addition, these rates may vary within one beam filling by a factor of 3 to 10. Both calorimeters are being permanently calibrated during data taking, using the energy constraint for the luminosity events selected: $E_{ET} + E_{PD} = E_{e-beam}$. Although the calibration coefficients themselves are not stable enough and may change within 5 – 20% due to the changing conditions, this method allows to achieve high precision of the absolute calibration, better than 1%. Figure 7.2 illustrates the energy correlation between the e and γ arms for the luminosity events selected by the trigger: ET*PD*$\overline{\text{VC}}$.

7.3 Trigger and Data Acquisition

The system must allow to measure total and H1 gated luminosity without dead time, to trigger the photoproduction candidates and to provide information for the ep events triggered by the main detector. Consequently, this implies a special trigger concept, based on the two completely independent trigger and data acquisition branches.

The output signals from the photomultipliers of PD, VC and ET are read out into differential preamplifiers mounted close to the detectors and then driven via fast coaxial cable pairs, 170 m and 100 m long respectively, to a second set of preamplifiers, installed in a trigger electronics crate. This solution provides the relevant noise reduction and compensates the signal attenuation in the long cables. The second set of the preamplifiers, having a double fanout structure, is connected to two asynchronously running groups of FADC (2 × 80 channels).

The first FADC group operates in a standard mode, similar to all other subdetector trigger systems (see Section 8.3.4). The trigger electronics discriminates the analog energy sums against the individually set thresholds, producing a dead time free trigger bit stream, sampled by the HERA beam crossing frequency. The trigger elements, which can be used in a central trigger logic, are any combination built of the three basic trigger bits: ET – electron arm signal ($E_{ET} > E_{ET}^{thr}$), PD – photon arm signal ($E_{PD+VC} > E_{PD+VC}^{th}$), VC – veto counter signal ("OR" of the two VC channels). An additional set of more complicated ET and PD topological trigger elements is also formed. The main physical trigger element, used so far, was eTAG = ET*$\overline{\text{PD}}$*$\overline{\text{VC}}$, giving an e-tagged event sample for γp physics. The front end readout and the data transfer to the central data acquisition are done by a program running on the master processor FIC8230 [55].

The second FADC group is controlled by the local trigger controller of the luminosity branch and is completely decoupled from the H1 trigger system. Two basic triggers are used for the luminosity calculation: ET*PD and ET*PD*$\overline{\text{VC}}$. The latter is used as well for the online detector calibration. All combinations of any 5 trigger elements, chosen by the operator, are being permanently stored without dead time for each of the 220 bunches in a special fast histogramming memory of 32×220 channels. The content of this memory gives a complete information for all bunch related trigger statistics. This allows, for example, to monitor the level of the accidental coincidences, which is essential for the high rates expected at design luminosity. The online luminosity event processing, including the fast reconstruction, calibration, trigger verification and calculation of the current luminosity value, is performed by the second FIC8230 processor.

7.4 Performance

The luminosity subdetector is equipped with a set of special sensors and switches and is integrated to the central slow control system, which allows to monitor all critical parameters essential for a safe and reliable operation. The luminosity information is transmitted via the normal event stream to the central IBM, where it is stored in the H1 database. In addition, it is distributed to other users (H1 control room, HERA control room, TV screens). A typical example of the information provided by the luminosity system during *ep* collisions is shown in Fig. 7.3.

The system works successfully since April 1992. For safety reasons, the measurements at HERA in 1991 [134] in a stand alone e−beam mode and then during the first ep−collisions have been done using the alternative lead-scintillator calorimeters as ET and PD. In the early phase, when HERA operated at 1% of the design luminosity, the detectors have been permanently used even during the injection and ramping of the electron beam, which allowed machine crew to understand better the details of the beam dynamics and to achieve the collisions quickly.

The total integrated luminosity for the 1992, as measured by H1, is shown in Fig. 7.4. The present understanding of the systematic error is summarized in the Table 7.3. Due to the redundancy in the trigger, the systematic error can be further reduced in future by combining the present method with other possible triggers (e.g. with the total photon flux measurements [135] etc.).

The eTAG sample taken with the help of this system was so far the main source for the clean γp physics [136, 137].

Contibution	Design	Achieved
Corrections to σ Bethe-Heitler [138]	0.1	0.3
Acceptance calculation	3.5	5.5
Background subtraction	0.1-0.5	2.0
Trigger efficiency and purity	1.0	2.5
Absolute calibration	0.5	2.0
Total	≤ 4	≤ 7

Table 7.3: Systematic error for the absolute luminosity measurement (in %).

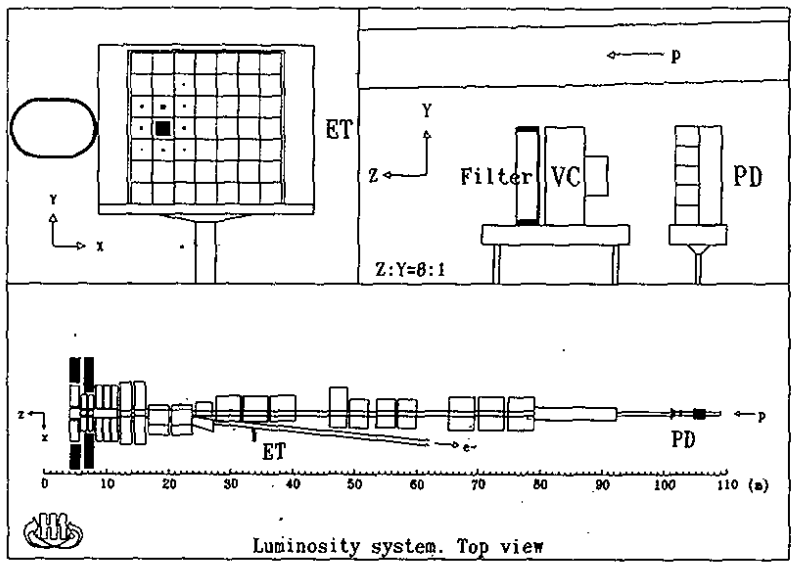

Figure 7.1: The layout of the luminosity system.

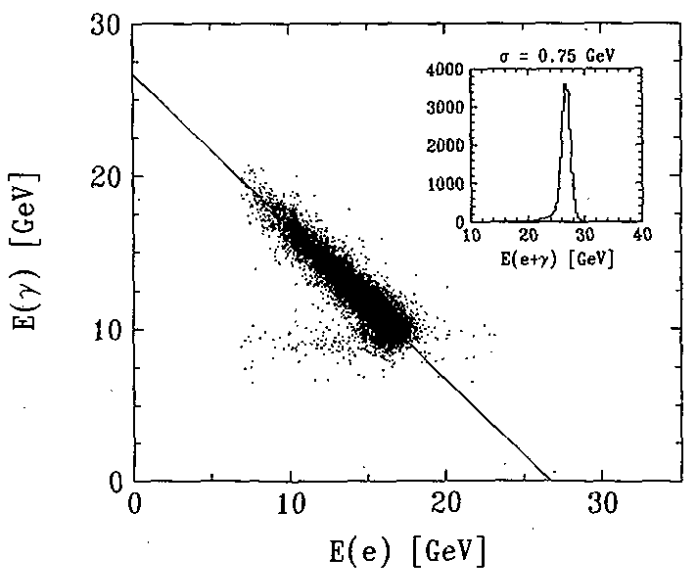

Figure 7.2: $e-\gamma$ energy correlation for bremsstrahlung events detected by the luminosity calorimeters. In the upper corner the total reconstructed energy is shown. Data from the summer 1992 HERA run at 26.7 × 820 GeV collision energy.

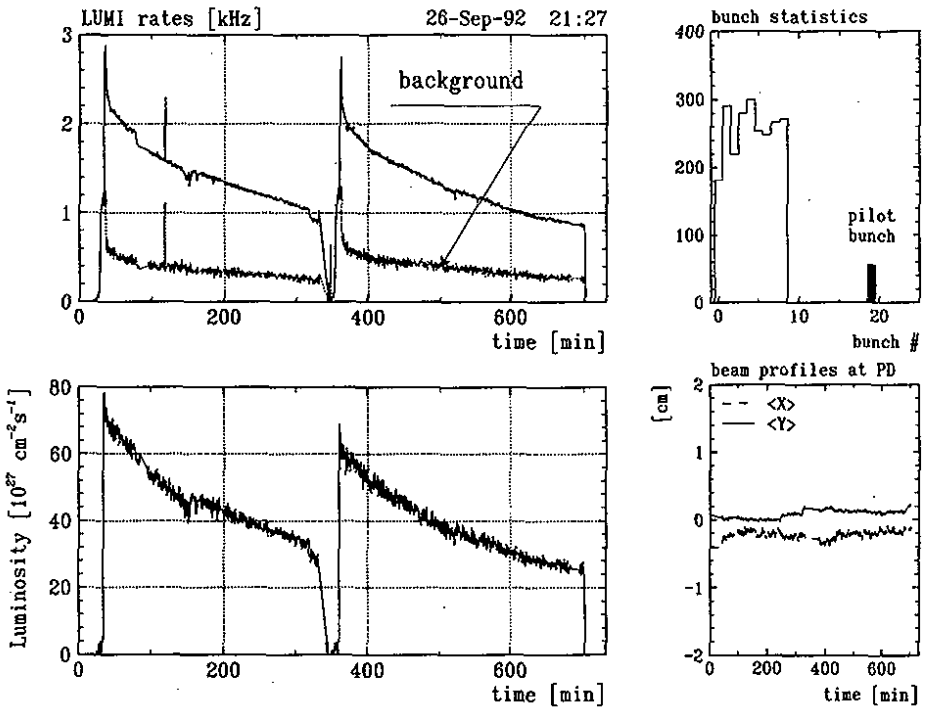

Figure 7.3: Data provided by the luminosity system during the *ep* collisions at HERA. Statistical fluctuations correspond to one measurement every 10 s.

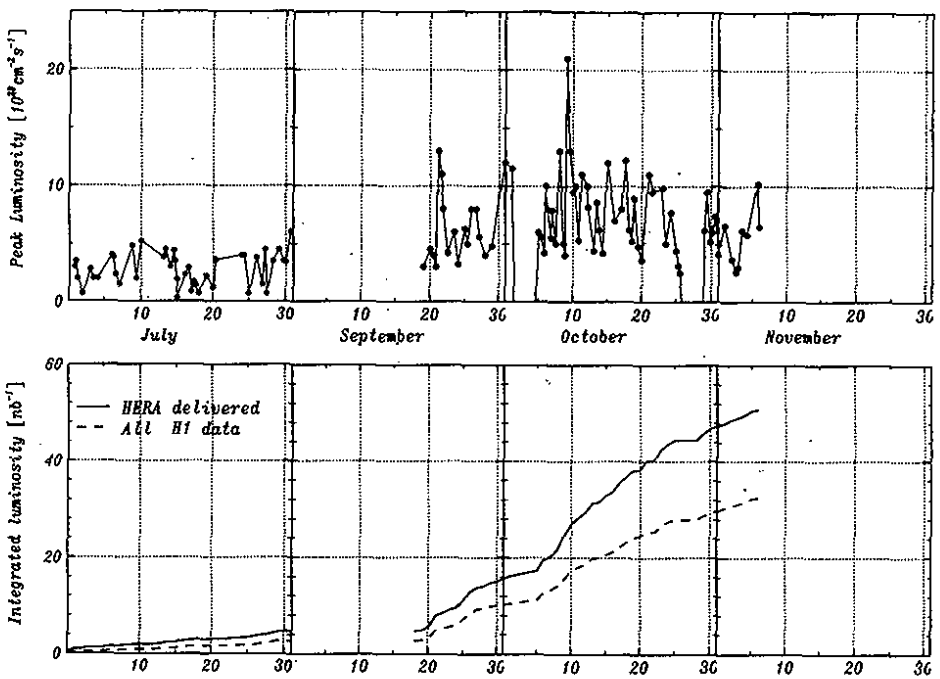

Figure 7.4: Luminosity measured by the fast monitor during data taking at HERA in 1992.

8 Trigger

8.1 Introduction and trigger requirements

The purpose of the trigger system is to select interesting *ep* collision events and to reject background events. To deal with the low *ep* physics cross section, large proton and electron accelerator beam currents are required, which is only possible by running in a multibunch mode. 210 p and e bunches circulate in HERA with total beam currents of $I_p = 160$ mA and $I_e = 60$ mA (design values). These give rise to the three basic types of background: synchrotron radiation from the electron beam, proton gas interaction in the beam pipe vacuum of about 10^{-9} mbar and stray protons, which produce particle showers by hitting the beam tube and other apertures around the accelerator.

This background situation, the short bunch time intervall of 96 ns and the request for low deadtime of the readout system result in a new challenge for a collider experiment: a centrally clocked fully pipelined front end system keeps the detector information stored, during all the time the first level trigger calculations take place, their result are transported to the central trigger decision logic and the global decision is distributed again to the subdetectors to stop the pipelines (see next paragraph for a more detailed discussion of pipelining). Of course also all trigger calculation and decision logic has to be built in a pipelined architecture such that there is a trigger decision for each bunch crossing separately. In such a system the first level trigger is completely deadtime free.

Most of the many subdetectors of H1 produce trigger information such that already the first level trigger decision is made according to the main basic physics quantities. However to allow decisions of increasing complexity, a multilevel trigger concept is being used: Following the deadtime free level 1 trigger there are two levels of synchronous trigger systems (level 2 and 3) which operate during the primary deadtime of the front end readout and one asynchronous event filter system (level 4) which consists of a fast processor farm which has access to the full event information and allows a complete event reconstruction online.

The only unique feature, which distinguishes the *ep* events from most of the background, is their origin from the nominal fiducial volume of the *ep* interaction region. Consequently we make use of the track origin information in several different ways: The time of flight wall gives us information whether there are tracks coming from upstream by comparing the arrival time with the accelerator clock phase. The central jet chamber measures the distance of closest approach (DCA) of single tracks in the plane perpendicular to the beam axis and allows a global fit to the event origin in this plane. The central and forward multiwire proportional chambers allow a fast estimation of the position of the vertex along the beam axis.

However there is still background originating from beam gas interaction in the nominal *ep* interaction region or from secondary interactions in the beam pipe and the inner detector regions faking an event origin inside the fiducial volume. Further requirements on the event selection are needed, depending on the event classes looked at.

First of all hard scattering events have higher total transverse energy. Therefore both the liquid argon calorimeter and the backward electromagnetic calorimeter deliver information about the observed energy deposition. The missing total transverse energy of the liquid argon signal is used to identify charged current deep inelastic events, while the requirement of some electromagnetic but no hadronic energy deposited in a given position of the liquid argon calorimeter, spots a scattered electron from a neutral current event.

There are two further event classes, for which we require special conditions: Events with an electron scattered under small angle into the electron tagger of the luminosity system (low Q^2

photoproduction) and events with muons detected in the instrumented iron or forward muon system indicating a heavy quark or exotic physics candidate. Since these events rather uniquely mark an *ep* event, the general requirements on the vertex determination and the calorimetric energy can be somewhat relaxed here.

All conditions mentioned so far are applied in the first level trigger already. However for photoproduction and heavy quark physics, where the scattered electron remains in the beam pipe and no muon is observed in the final state with sufficient energy, triggering becomes more difficult: Here we can make use of the event topology, since proton beam induced background has a more forward oriented kinematics compared to *ep* events. This was so far only done in the offline analysis.

8.2 Front end pipelining

The time intervall between two consecutive bunch crossings of 96 ns is used as the time unit (1 BC) in the following. The time needed to run trigger signals even through a few circuits performing simple logical calculations is usually longer than that. Moreover the large size of the experiment and the electronic trailor attached to it introduces cable delays of several BC. Finally certain detectors have a long detector response time which means that the information of these detectors is only available some BC after the event (liquid argon calorimeter 13 BC due to long integration time of the preamplifiers, central drift chamber 11 BC due to a longest drifttime of 1 μs). Of course such long response times can only be tolerated because due to a relatively low event rate (compared to a *pp* collider) the probability for an interaction per bunch crossing is small (of order 10^{-3}).

The final L1 trigger decision (called L1keep signal) is available centrally 24 BC after the real *ep* event time. Further time is needed to distribute this signal around to stop the various subdetector pipelines otherwise the information which belongs to the relevant BC would be lost. The total pipeline length varies between 27 and 35 BC (depending on the subdetector) and turned out to be in some cases just long enough to operate the system. For future system designs we would advise to increase this pipeline length to gain more flexibility in the timing of such a system or - even better - to perform signal processing and zero suppression before entering the pipelines and store the information dynamically.

The chosen concept of a pipelined front end system also avoids huge amount of analog cable delays and allows to reconstruct offline the history of the event over several BC for timing studies and to identify pile up.

H1 uses four different types of pipelines (For a more detailed description of the electronics see the chapters of the respective detectors):

- Fast random access memory (RAM) is used to store the digitised information of the drift chambers for readout only (central and forward tracker, forward muon system) as well as of the liquid argon calorimeter (LAr) for trigger purposes. The analog to digital converters operate at a frequency of 10.4 MHz for the LAr and 104 MHz for the driftchambers. This clock is synchronised to the HERA clock and is also used to increment the 8-bit address of the RAM, which operates therefore as circular buffer. At L1keep time the overwriting of the RAMs is stopped to save the information for the readout process. In addition RAM buffers are used to pipeline information in the drift chamber trigger and in the central trigger logic.

- *Digital shift registers are used to store the single bit information, generated by threshold* discriminators followed by a special HERA clock phase synchronisation circuit, in the instrumented iron system, the multiwire proportional chambers, the driftchamber trigger branch, the BEMC trigger branch and the two scintillator systems. A custom designed gate array contains the clock synchronisation circuit and a 8 channel 32 stage pipeline realized as D-Flipflops. See the chapter 6.14 for a description of this gate array.

- Analog delay lines are used to *store the pulseheight of the backward electromagnetic* calorimeter (BEMC). The L1keep signal is used to hold a sample and hold circuit from which the digitisation takes place only during the deadtime of the readout.

- Signal pulseshaping of the LAr and tailcatcher (instrumented iron analog readout of pads) is adjusted such, that the signal's maximum occurs at L1keep time. The same type of sample and hold and digitisation is used as in the BEMC case.

The timing of the synchronisation step and the analog to digital conversion clocks is critical. The information produced needs to be uniquely attached to the bunch crosssing the event originated from, such that the trigger calculations based on all channels within a subsystem and also systemwide are derived from the same bunchcrossing. The adjustement of the HERA clock phase, which defines this synchronisation time in each subsystem, is therefore a major setup task, which needed several iterations of delay curves combined with offline analysis and it turned out to be a much more complex operation than expected. Bunch and clock phase monitors have been added later to assure stable operation at the correct timing values.

8.3 Trigger level 1

The trigger level 1 system consists of nine different trigger systems each based on the information of a certain subdetector. The outputs of these systems are called trigger elements. These trigger elements are fed to a central trigger logic where they are combined to various so called *subtriggers. Each single subtrigger suffices to produce a L1keep signal to stop the pipelines and* prepare the event readout.

During the data taking in the first year of operation all the synchronous part of the triggering happened in level 1. Since the level 1 decision time is completely deadtime free, this is in fact the preferable situation.

In the following paragraphs these nine systems and the central trigger logic are described.

8.3.1 Vertex position oriented trigger *systems*

The geometrical origin of the event is the main handle to suppress background at a HERA experiment. Vertices which lie far outside the nominal ep interaction region identify uniquely background events. These trigger elements are therefore in one or the other way used for almost all subtriggers, with the exception of the higher threshold triggers of the calorimeters.

8.3.1.1 The backward time-of-flight system Beamwall and beamgas events originating from the protons upstream direction produce showers, which mostly run through both scintillator walls (see Section 4.7) behind the BEMC. A background (BG) and an interaction (IA) timing window (derived from the HERA clock signal) define for each scintillator of each wall whether the hits belong to particles originating from upstream or from the nominal interaction region. The signals from the single scintillator sheets of each wall are 'ORed' together to form a signal

for each plane, and the two planes are then put into coincidence forming the final $ToF - BG$ and $ToF - IA$ trigger elements.

The $ToF - BG$ trigger element is the simplest and most effective background rejection criterium and is therefore applied to most of the physics subtriggers as a veto condition. The logic is realised fully in conventional NIM electronics.

8.3.1.2 The $z-$vertex trigger The central and the first forward proportional chamber are used to estimate the event vertex position along the beam axis ($z-$axis) (for a more detailed description see [139]). A particle originating from the beam passes four layers of chambers (either the double layers of CIP and COP or CIP and first forward proportional chamber). The first step of the vertex estimator, the so called rayfinder, needs therefore to combine four cathode pad signals (see Section 4.5.2) which lie on a straight line into an object called ray. In the plane perpendicular to the beam a 16 fold segmentation (ϕ - sectors) is used, such that the rays of each segment are treated separately. A total of 34'400 different rays are examined for each bunch crossing simultanously.

A histogram with 16 bins along z with a bin width of 5.4 cm is filled according to the $z-$coordinate of the origin of each ray. The rays which were formed by the correct combinations of pads all enter in the same bin and form a significant peak above the background entries, which originate from rays from wrong combinations of pads and are therefore randomly distributed (see Figure 8.1(a)). Events which have their vertex far outside of the nominal interaction region do not develop significant peaks, in this case the histogram contains only the background from accidental rays.

From this histogram various trigger elements are derived. First of all the $zVTX - t0$ trigger element is activated, if there is at least one entry in the histogram. This information is used as an indication, that there is at least some activity in the central region of H1 and also for bunch crossing identification in combination with low threshold energy triggers of the calorimeters. Then peak significance analysis is performed and the trigger element $zVTX - sig1$ or $zVTX - sig2$ are activated, if the histogram peak exceeds a given significance threshold (two different threshold settings are available in parallel). For events with a few tracks only, a special trigger element indicates that there were only few entries in the histogram, but they were all clustered together. This histogram analysis is fully programmable, such that the meaning of the trigger elements can easily be changed.

The rayfinder is based on a custom designed gate array (1.5 μm CMOS technology), of which 2112 pieces were needed. It contains the logic to examine the signals of 45 cathode pads and form 30 rays (allowing also a flexible 3 out of 4 logic), the adder tree to count the active rays, the grouping of these rays into big rays (see below) and some pipeline structure for delays. For the final histogram bulding and the peak analysis programmable logic cell arrays (XILINX family 3000 [140]) and a 22 bit lookup table realised with 4 Mbyte of fast static RAM are being used (see Figure 8.1(b) for a block diagram).

8.3.1.3 The forward ray trigger The cathode pad signals of the FWPC and the CIP are fed into a logic, which finds rays originating from the nominal interaction region and pointing in the forward direction (for more detailed description see [141]). A ray here is a set of impacts on three or four chambers, compatible with a track coming from the interaction region in one $2\pi/16$ ϕ-sector. Among the six or eight chamber planes (2 planes per chamber) which should have seen the track, only one is allowed to miss. For each of the 16 ϕ-sectors there are 32 possible rays corresponding to radial bands for impacts on the second FWPC. The width of these bands increases in geometrical progression, the lower radius is 21 cm, and the largest one 75 cm, so the smallest angle for a detected track is 5.63°, and the largest one is 24.72°.

These rays are counted and a trigger element is activated if there is at least one road found. Other trigger elements indicate that there are active rays in adjacent ϕ-sectors (the $x-y$ plane is divided into 16 ϕ-sectors as in the $z-$vertex trigger above). Furthermore certain topology conditions in the 16 ϕ-sectors can be recognised, e.g. if the rays lay all in two back to back sectors a special trigger element is activated.

This system is realised by a total of 320 RAMs, which are used as hierachically organised lookup tables.

8.3.1.4 Other MWPC triggers Additional trigger elements are derived from the CIP for cosmics data taking. Furthermore a trigger element is activated if three out of the four planes of the backward MWPC have seen a hit.

If there are more than three sectors in the backward quarter of the CIP active, the trigger element CIP-backward might indicate an upstream p beamgas event. This is used as a veto for certain subtriggers which are derived from tracking information only.

8.3.1.5 Big rays The rays found by the forward ray trigger and the $z-$vertex trigger (in the latter case only the rays originating from the highest peak in the $z-$vertex histogram, see Figure 8.1(b)) are combined to 224 'regions of interest' called big rays, which have the same geometrical properties as the 'big towers' of the liquid argon calorimeter trigger (see below and Figure 8.4), and with which they are put into coincidence (see Figure 8.3).

8.3.1.6 The central jet chamber trigger This trigger finds tracks in the CJC, which have a distance of closest approach of less than 2 cm from the nominal beam axis and therefore suppresses beamwall events as well as synchrotron radiation background (For a more detailed description see [142]). To keep the logic reasonably small and without degrading the performance significantly only 10 out of 56 signal wire layers of the CJC are used in the trigger. See Figure 8.2 for the following description of the logic.

In a first step the signals from the CJC are digitised by a threshold comparator (independent of the normal readout branch) and synchronised to the HERA clock of 10.4 MHz. This way the drifttime information is kept with an accuracy of 96 ns or about 5 mm of position resolution in general, while for the innermost two driftcells this resolution is enhanced by doubling the clock frequency.

In a second step the hits are serially clocked into shiftregisters by the HERA clock. Track masks are defined according to their position in driftspace and their curvature in the magnetic field. A total of 10'000 different such masks are now applied to the parallel outputs of the shiftregisters to mark the active roads. Tracks with low or high transverse momentum can be distinguished as well as the sign of the low momentum tracks. The number of roads found in each of the 15 ϕ-segments and in the two momentum bins for each sign are counted seperately as 3 bit numbers.

In the final step these track counts are further processed to generate trigger elements. Two different thresholds on the total number of tracks can be used simultanously. In addition a topological analysis in the x-y plane is performed, for instance a track activity opposite in ϕ can be recognised.

Most of the digital logic is programmed into about 1200 programmable logic cell arrays (XILINX [140] family 3000).

8.3.1.7 The $z-$chamber trigger The $z-$chamber trigger uses the signals of the driftchambers CIZ and COZ in a similar way as the CJC-Trigger, utilizing the high spatial resolution obtained from the drift chambers (for details see reference [36]). Signals are synchronized with twice the HERA bunch frequency and stored in shift register pipelines. Their parallel outputs are fed into coincidence circuits used as lookup tables for all possible tracks coming either out of the interaction region of 50 cm length (vertex tracks), or from the proton beam region with $20° \leq \theta \leq 90°$ with respect to the beamline (background tracks).

In a first step tracks are found with a granularity of 2.4 mm within the individual CIZ and COZ systems. For the vertex tracks we combine in a second step the CIZ and COZ logic to enter inputs into a 96 bin vertex histogram by an analog technique. By gating the system with an OR of the central proportional chambers we search for a peak in this histogram as a minimum requirement for a physics event. A resolution of 5 mm for the vertex reconstruction is achieved. In addition to the vertex position also the driftcells including left-right information which are associated with valid vertex tracks are stored, giving a fast θ measurement of a track.

The background tracks are summed up per drift cell and form the "background histogram". In a neural net chip this background histogram is compared with the highest peak found in the vertex histogram and other histogram analysis is performed.

The shiftregisters and the lookup tables are configured in 1060 logic cell arrays (XILINX [140] family 3064 and 3090).

This trigger is still under development and was not used in the first periods of datataking.

8.3.2 Calorimetric triggers

The selection of deep inelastic ep reactions is based primarily on the calorimetric triggers. These events are characterized by large energy depositions originating from jets and eventually the primary scattered electron. New physics beyond the standard model is expected to lead to similar signatures. Correspondingly, the calorimeter triggers have to cope with a wide spectrum of trigger observables, from narrow, localized energy depositions (e. g. electrons) to global energy sums such as transverse or missing transverse energy.

8.3.2.1 The liquid argon calorimeter trigger The liquid argon trigger system is designed to calculate the energy deposited in various topological parts of the calorimeter as well as the total energy and other global energy sums which can be weighted by position-dependent weighting factors (for more detailed description see [143]).

The realisation of this system contains an analog and a digital part (compare Figure 8.3). In the analog part the signals from the calorimetric stacks are split from the readout chain at the preamplifier input already and are seperately amplified, shaped to a pulse width of about 600 ns FWHM and added to Trigger Towers (TT). The TT's are approximately pointing to the vertex and are segmented in 23 bins in θ and in ≤ 32 bins in ϕ. While the electromagnetic and hadronic signals are still separated in the TT's, the sum of the two is fed into an analog discriminator turning both signals off for later summing, if the level is below an adjustable threshold ("AGM threshold"), determined by the electronic noise. The same signal is used to determine the exact time (called t_0) of the signal by a constant fraction type method. The total number of all active t_0 signals is available as a trigger element.

Depending on the θ region, either one, two or four TT's are summed up to big towers (BT), providing finer granularity in the forward direction (see Figure 8.4). A total of 240 such BT's are formed from the 40000 LAr calorimeter cells, another 12 BT's are derived in a similar way from the signals of the BEMC and the plug calorimeter.

The electromagnetic and hadronic signals of each BT are then digitised seperately by analog to digital converters running at the speed of the HERA clock frequency of 10.4 MHz. The digital outputs are calibrated by a RAM lookup table and two threshold discriminators are used to look for a potential electron signature in each BT, which is defined by high electromagnetic and low hadronic energy in the respective sections of the tower. Another discriminator lookup table marks all BT's to be transferred to the higher trigger levels. The electromagnetic and hadronic parts of each BT are summed up and the total BT energies are then available for further processing. A threshold is set on the total BT signal put into coincidence with the Big Rays derived from the MWPC triggers (see Section 8.3.1.5), and the number of these towers is counted, discriminated and provided as a trigger element to the central trigger logic.

The total BT energy is next fed into a set of lookup tables producing the weighted energy of this big tower for the various global sums: For the total transverse energy a weight of $\sin\theta$ is used, the transverse components E_x and E_y are obtained by multiplication with $\sin\theta\sin\phi$ and $\sin\theta\cos\phi$, respectively, to build the missing energy. A further channel can be used for arbitrary purposes, e.g. for generating a trigger with uniformly distributed rates over the polar angle by weighting each BT with the inverse of the background rate of its angular region. A 'topological' channel allows to sum up separately the energies in five predefined topological regions (BEMC, central barrel (CB), forward barrel (FB), inner forward (IF), and plug). For these regions, the total energy as well as the energies in each of the contributing quadrants are calculated. Furthermore the total energies are calculated for the total barrel (CB+FB) and the forward (IF+Plug) and backward (FB+CB+BEMC) regions. For the summing of the weighted BT energies, custom specific gate arrays are used, all summing being done in 8 bit accuracy.

In the last step further RAM-based lookup tables are used to encode the various global and topological sums into two-bit threshold functions provided as trigger elements to the central trigger logic. One such lookup table also builds the missing energy from the two signed components E_x and E_y with subsequent discrimination and encoding into two bits.

8.3.2.2 The BEMC single electron trigger The purpose of the BEMC Single Electron trigger (BSET) (for more detailed description see [144]) is to identify scattered electrons from DIS processes in the angular acceptance of the BEMC. The basic concept of this trigger is to provide cluster recognition and to place energy thresholds on the sum of all energy clusters in the BEMC. The trigger is based on energies deposited in BEMC stacks. This granularity is well matched to the transverse spread of electromagnetic showers.

Analog signals from preamplifiers of single wavelength shifters are first added to form stack sums representing a high granularity trigger element. The summed analog stack signals are then adjusted in their gain and timing in order to provide an equal analog response to energy and to uniquely assign the energy depositions in all stacks to a single HERA bunch crossing. Two thresholds are applied to these signals. A low threshold just above noise level and a high threshold to be used as a cluster seed. Typical values are 1.3 GeV for the low threshold and 2.3 GeV for the high threshold. A cluster identification module then detects the cluster seeds and assigns neighbouring stacks to define clusters. Two trigger elements reflect the cluster multiplicity (one or more clusters, exactly one cluster). The energy of all clusters is then summed up and three possible thresholds can be placed on this sum, which activate the respective trigger elements. The total energy summed over all stacks exceeding the low threshold is also compared to a threshold and activates another trigger element. Finally the cluster energy and the total energy sum is digitised into an eight-bit number to be used for correlations with other quantities at the central trigger logic.

The trigger has been able to operate in coincidence with a timing veto from the time-of-flight system (see Section 8.3.1.1) and a cluster threshold of 2.5 GeV during the first data taking period. The threshold curve for the cluster energy is shown in Figure 8.5.

8.3.3 Muon triggers

Both the instrumented iron system and the forward muon spectrometer deliver level 1 trigger information, as described below.

8.3.3.1 The instrumented iron muon trigger The instrumented iron system is logically divided into 4 subdetectors (front end cap, forward barrel, backward barrel and backward end-cap) (for a detailed description see [145]). Each subdetector consists of 16 modules (see detector description for details). 5 of the 12 chambers (plane numbers 3, 4, 5, 8 and 12) of each module have their wire signals made available to the level 1 trigger: The pipeline gate arrays used in this system have this output available after the synchronisation step, but before the entry into the pipeline. The "OR" of 16 wires of these signals is called a profile and all profiles of one chamber are again ORed together to form a single plane signal. Any condition on the 5 plane signals of one module can be requested by means of RAM lookup tables (e.g. a 3 out of 5 condition of the chamber planes) for each module independently. An additional signal from the first plane detects, when there is more than one hit in the plane indicating the hits rather originating from a cluster tail of the calorimeter than a single muon.

The (maximum eight different) outputs of each of the 64 modules are then fed into a central muon trigger logic which is organised in RAM lookup tables again.

So far only a counting of the number of muons found in each subdetector has been loaded into the RAMs and two trigger elements per subdetector were used: exactly one muon candidate and more than one muon candidate.

8.3.3.2 The forward muon trigger The signals from the driftchambers of the forward muon spectrometer are discriminated and fed into an electronic system which extracts the appropriate t_0 and the coordinate within the drift space of chamber hits which correspond to tracks (detailed description in [146]). This is achieved by making use of the staggered arrangement of two adjacent drift cells as shown in Fig 8.6. For correct t_0 the sum of the drift times of the two cells is defined for any track coming from the collision point, while the difference of the two drift times gives the coordinate within the drift space. A field-programmable 32×32 coincidence array with serial-load shift register axes, built in a 1.5 μm CMOS custom specific chip is used to make the correlations between the two drift times and thus identify bunch number and track position.

A similar coincidence matrix with parallel-loaded axis is then used to define pairs of track segments which correspond to tracks in the chambers before the toroid and seperately in the chambers after the toroid. A variable width road may be applied to require the tracks point to the interaction vertex. In the third step of this trigger processor pre-toroid and post-toroid tracks are fed into a further coincidence matrix which finds pairs of tracks which have traversed the toroid. The momentum selection of the trigger is made by varying the widths of the roads.

The trigger deals with each octant of the forward muon chambers seperately. The track candidates found in each octant are allocated to eight regions at different polar angles to the beam. The 8-bit hit patterns from all eight octants are fed into a RAM based lookup table which counts the number of muon candidates and allows programmable topological correlations to be made . Eight bits of trigger information are then sent to the central trigger as trigger elements.

8.3.4 Triggers derived from the luminosity system

The luminosity system runs with an independent data acquisition and triggering system as described previously in chapter 7. However the trigger signals, derived from the three detectors this system consists of, are available also to the main trigger system: Independant thresholds can be set on the electron energy, the photon energy and the calibrated sum of the two. Together with the signals of the veto counter in front of the photon detector this information is fed into a lookup table to form logical combinations. The outputs are connected to the central trigger logic as trigger elements.

So far mainly the electron signal was used to tag photoproduction events.

8.3.5 Central trigger level 1 decision

The information generated by the subdetector triggersystems described above is represented in a total of 128 bits (16 groups of 8 trigger elements), which are connected to the central trigger logic (a detailed description can be found in [147]). Here all trigger elements are fed into a pipeline (realised as double ported RAM based circular buffers), which allows to adjust the delays of all incoming signals to the proper bunch crossing.

Furthermore the information stored in these trigger element pipelines is recorded at readout time, allowing to study the time evolution some bunchcrossings before and after the actual event took place.

The trigger elements are logically combined to generate a level 1 trigger signal. Up to 128 different subtriggers are formed by applying coincidence and threshold requirements. (Lookup tables are used to form 16 fold coincidences of arbitrary logic expressions from up to 11 predefined input bits). A trigger description language (TDL) has been developped to keep up with the ever changing demands for new subtriggers and to properly log the logic and the status of the triggers loaded.

The subtriggers are assigned to a given physics event class (physics trigger), to experimental data needed e.g. for measuring the efficiency of a given detector (monitor trigger) or to cosmic ray events for calibration purposes (cosmics trigger).

The rate of each subtrigger is counted separately and can be prescaled if needed. The final L1keep signal is then given by the logical OR of all subtriggers after prescaling and is distributed to the front end electronics of all subsystems to stop the pipelines. At this point the primary deadtime begins.

Of course all this logic works in a pipelined way as all the subdetector triggersystems described above, clocked by the HERA clock, and delivering a trigger decision every 96 ns.

8.4 Intermediate trigger levels

The two intermediate trigger levels 2 and 3 operate during primary deadtime of the readout and are therefore called synchronous. The calculations which are performed in these systems and the decision criterias applied depend on the subtrigger derived in the level 1 system, which acts in this way as a rough event classification.

As we have seen in the previous chapter, deadtime starts after the level 1 trigger system has given a positive decision. The Level 2 trigger system now can evaluate complex decisions based on more detailed information. After a fixed time of typically 20 μs the decision of the level 2 trigger defines whether a fast reject should happen or whether the event is to be treated further.

For the level 2 decision processsors various hardware solutions are under construction including a complex topological correlator [148] and a neural network approach to exploit the correlations between the trigger quantities from the various subsystems in a multidimensional space [149]. The massively parallel decision algorithm of these systems makes them ideally suited for fast trigger applications.

Only if the event is accepted by the level 2, the bigger readout operations like zero-suppressing of the drift chamber digital signals and the calorimeter analog to digital conversion and DSP processing are started. During this time the trigger level 3 system based on a AM 29000 RISC processor performs further calculations [150]. The level 3 decision is available after typically a few hundred μs, in case of a reject the readout operations are aborted and the experiment is alive again after a few μsec.

The calculations of both level 2 and level 3 triggers are based on the same information prepared by the trigger level 1 systems described in the previous section: MWPC (Big Rays, z–vertex histogram), central driftchamber (number of tracks found in each ϕ-sector by the level 1 trigger), BEMC (individual stack information, energy sums built in the trigger level 1 system), LAr calorimeter (individual big tower electromagnetic and hadronic energies and the global sums, as built in the trigger level 1 system) and intermediate information generated by the main and forward muon triggers. Topological and other complex correlations between these values are the main applications for these intermediate trigger systems.

The events which survive the level 2 and 3 triggers are then taken over by the central data acquisition system with a typical maximum rate of 50 Hz (see chapter 10 for upgrading state of this limit). Since this system works asynchronous to the primary trigger system, there is no further deadtime involved as long as the level 3 accept rate stays safely below these 50 Hz. The decision times of these systems (level 2: 20 μs, level 3: assume 100 μs average) and the total primary deadtime of about 1 ms for fully accepted events imply, that the level 1 (level 2) trigger accept rate must not exceed 1000 Hz (200Hz) to be able to run the experiment with an overall deadtime below 10 %.

During the first year of operation the level 2 and 3 processing systems were not in use yet, however all accept and reject control signals were available and the system was run just by forcing level 2 and level 3 accept decisions for each event. The level 1 accept rate had therefore to meet the central data acquisition limitation of 50 Hz, which was easily possible given the reduced background rate due to the actual HERA electron and proton currents of about 1% of their design values.

8.5 The level 4 filter farm

The level 4 filter farm is an asynchronous software trigger based on fast mips R3000 based processor boards[151]. It is integrated into the central data acquisition system and has the raw data of the full event available as a basis for its decision making algorithms. This allows for online trigger selections with the full intrinsic detector resolution. In 1992 fourteen processor boards ran in parallel. Each board processes one event completely until a decision is reached. The hardware layout is described in detail in chapter 10.

In order to reach a decision in the shortest possible time, the L4 algorithm is split into various logical modules, which are run only if a quantity calculated by the respective module is needed to reach this decision. The L4 modules use either fast algorithms designed specifically for the filter farm, or contain parts of the standard offline reconstruction program. The execution of the modules is controlled by a steering bank containing text in a steering language written explicitly for this purpose. The final decision is based on statements containing logical combinations of

numerical or logical values. The event is either accepted or rejected if the statement is true. A small fraction - typically 1 % - of all rejected events was kept for monitoring purposes. Execution of the statement is terminated and the next statement is executed as soon as a subcondition is false. It is possible to run any statement in test mode without influence on the actual decision. This allows the evaluation of the effect of new statements with high statistics prior to activation and the flagging of particularly interesting events, e.g. for the online event display. In most cases, the first condition in a statement is simply a mask of L1 trigger bits. This scheme allows for high flexibility without changes in the program code and facilitates book keeping as the steering bank is automatically stored in the H1 database.

In the 1992 runs the filter farm was mainly used to reject events with vertices outside of the nominal interaction region along the beam axis, which survived the relatively weak conditions set in the first level trigger. The largest reduction was achieved using charge division information from the trackers: In a first statement, a histogram of z–intercepts is evaluated. These are derived from the projection of straight lines defined by pairs of well separated wire hits in cells of the central jet chamber (CJC). If more than 50 % of all entries are below $z = -75$ cm, the event is rejected. This condition rejects upstream beam-gas and beam-wall interactions. A similar algorithm evaluates multiple hits on neighbouring CJC wires. If the ratio of hit pairs with an absolute angle of less than 10° vs. the beam direction to all hit pairs is greater 1/2, the event is rejected. Events with this topology are predominantly due to electron induced background originating from synchrotron radiation. These algorithms are very fast: both tests combined need an average of 8 ms on the processor boards and rejected 50-80 % of the events triggered by tracker triggers in 1992. The full track reconstruction in the CJC is run on events passing the above criteria. Events with only positive charged tracks or no tracks at all in the beam interaction region are rejected. Three or more well reconstructed tracks originating from $z < -1$ m also lead to rejection of the event.

The BSET trigger described in Section 8.3.2.2 has a large background due to particles directly hitting a single photodiode (mainly synchrotron radiation related). Events with a disproportionate fraction of the total stack energy in just one of the four photodiodes are rejected. In addition false BSET triggers from upstream proton beam background are rejected by the tracker cuts described previously. Muon triggers in the instrumented iron are verified by requiring a reconstructed track in the iron.

As can be seen in the above examples, the L4 filter farm has been rejecting background events based primarily on technical quantities. It has rejected an average of 70% of the input events. At higher luminosity rejection of beam-gas events in the nominal interaction region will become necessary. In addition, the increased number of filled bunches will necessitate the rejection of cosmic ray events.

The filter farm is not only used for event filtering purposes. As reconstructed data of the whole detector merges there for the first time, it is also well suited for monitoring and calibration. The reconstruction modules fill numerous monitor histograms which can be inspected online. Warning messages can also be sent to the central control console, informing the shift crew immediately of potential problems. Calibration data are sent to the data base for immediate use by the online reconstruction process.

8.6 Performance and outlook

With the above described system we reduced the high background rate at trigger level 1 to typically 26 Hz at the present luminosities delivered by HERA. 70 % of these events were rejected by the level 4 event filter, so we ended up with a tape recording rate of 8 Hz at a overall dead time of the system of 8 %.

The total rate of p background events into the experiment due to proton beam losses from upstream was expected to be of order 50 kHz. In fact we measured at a total proton beam current of 0.8 mA (0.5 % of the design value) an event rate of 225 Hz in the time of flight scintillator wall, which scales perfectly with this expectation.

A proton residual gas interaction rate of about 1 kHz/m can be calculated from the observed vaccum of 10^{-9} mbar and at design luminosity. This scales to 5 Hz within the interaction region (±25 cm) and at the reduced luminosity condition mentioned above. We effectively observed a rate of about 2 Hz of such beamgas events triggered with the central tracking triggers.

The rate of synchrotron radiation background turned out to be a bigger problem than expected. However by using the DC track trigger these events can easily be suppressed. For the low Q^2 deep inelastic neutral scattering events with the scattered electron observed in the BEMC this background is a more serious problem, only spatial correlation between BWPC and BEMC and relativ signal distributions in the BEMC photodiodes (see previous section) give a significant reduction of this type of background.

Offline studies based on the data taken during the first year of HERA operation show, that it is possible by setting more stringent coincidence requirements for the level 1 subtriggers to run the system in the same manner (only level 1 and level 4 triggers) at 10 times higher beam currents without cutting significantly into physics acceptance and with the same performance concerning rates and deadtimes. However at design luminosity (100 times higher than our first year experience) we will have to tighten the requirements on the events in level 2 and 3 trigger systems. But it looks still possible to trigger with high acceptance for physics events, perhaps with the exception of the heavy quark production of which a large fraction of events have not enough transverse energy for the calorimetric triggers and no or only low energy electrons or muons in the final state. Therefore they have to be triggered in the first level by central tracking information alone resulting in a high beam gas background from the nominal ep interaction region. We will have to use topological criterias in the level 4 or even in level 2 or 3 to recognize these events.

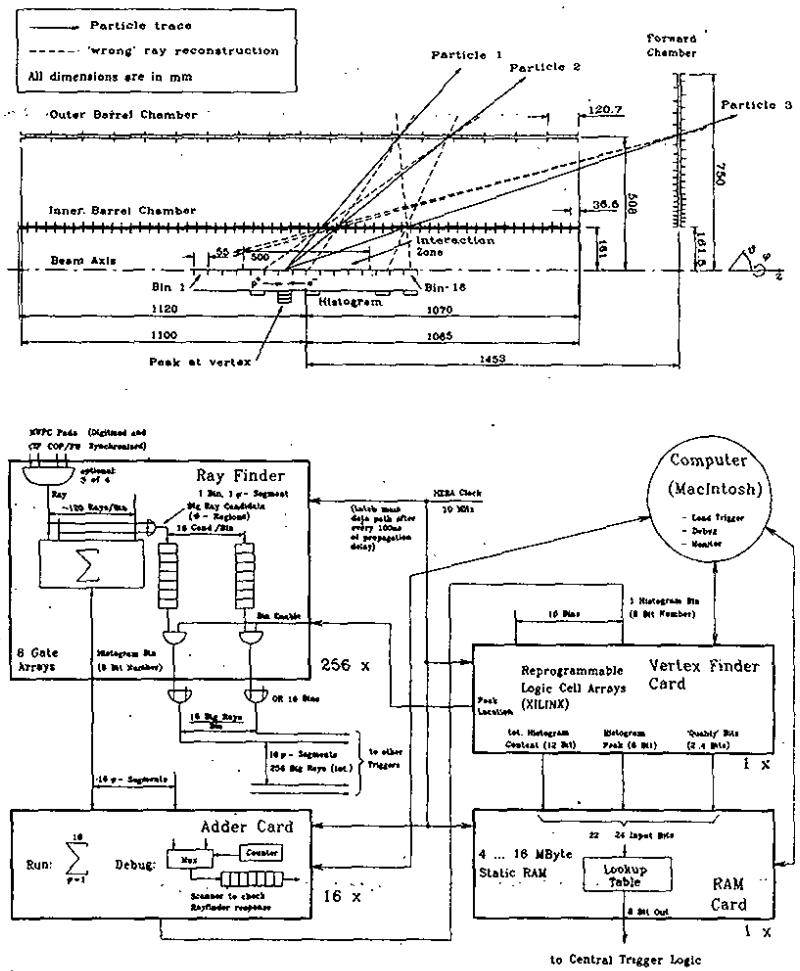

Figure 8.1: (a) z–vertex reconstruction by building a histogram, which displays a peak at the true vertex location. (b) Blockdiagram of the z–vertex trigger.

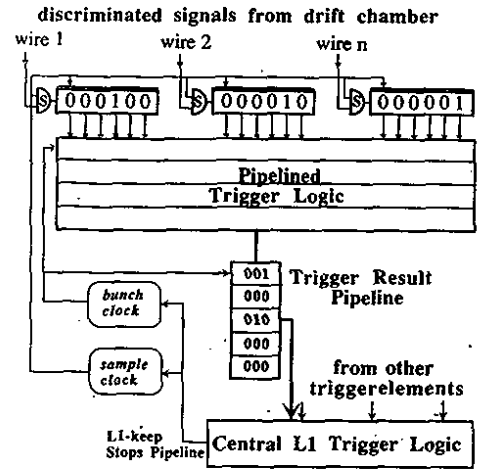

Figure 8.2: Blockdiagram of the driftchamber trigger.

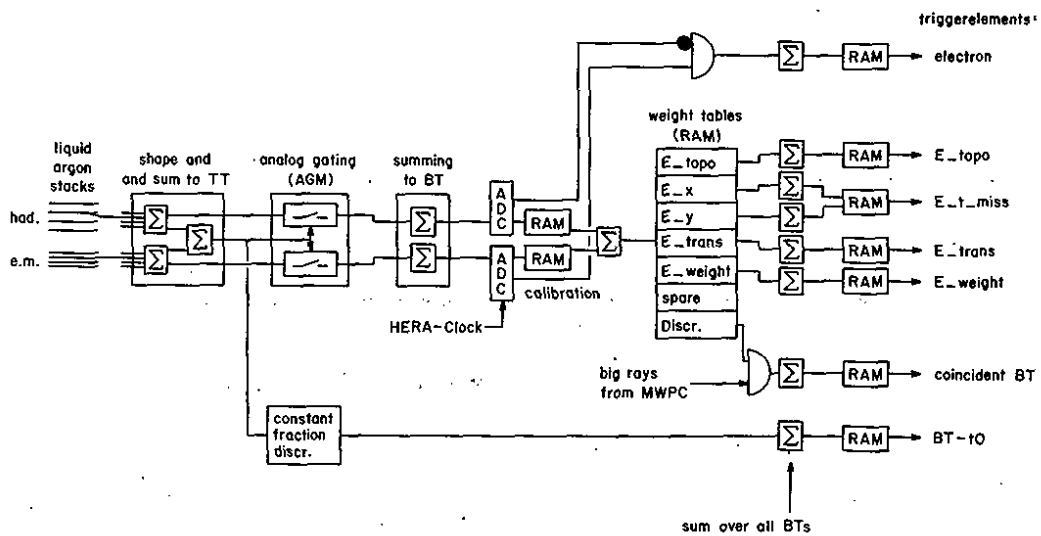

Figure 8.3: Blockdiagram of the liquid argon calorimeter trigger.

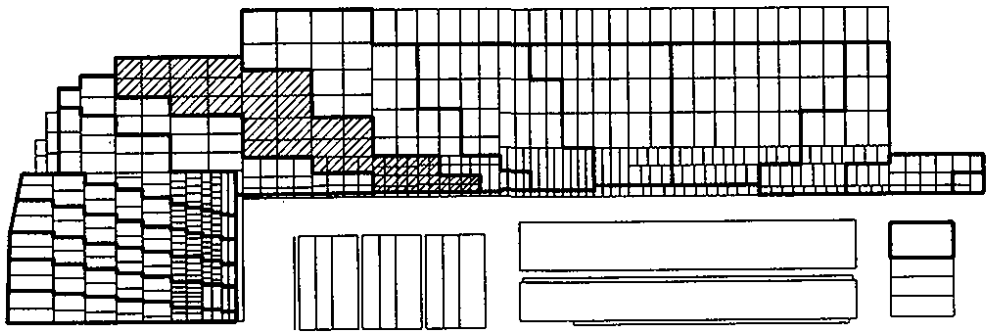

Figure 8.4: Cross section through the θ plane of the liquid argon calorimeter showing the pointing geometry of the trigger cells. The shaded area shows one example of the 240 big towers.

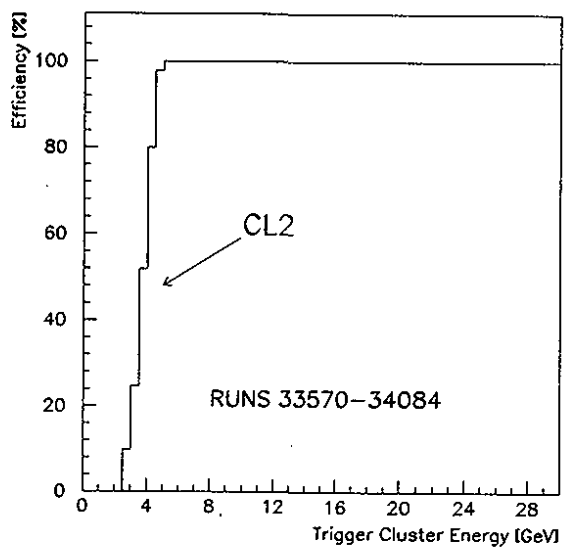

Figure 8.5: Acceptance of the BEMC single electron trigger as a function of cluster energy, with the settings used in the first running period.

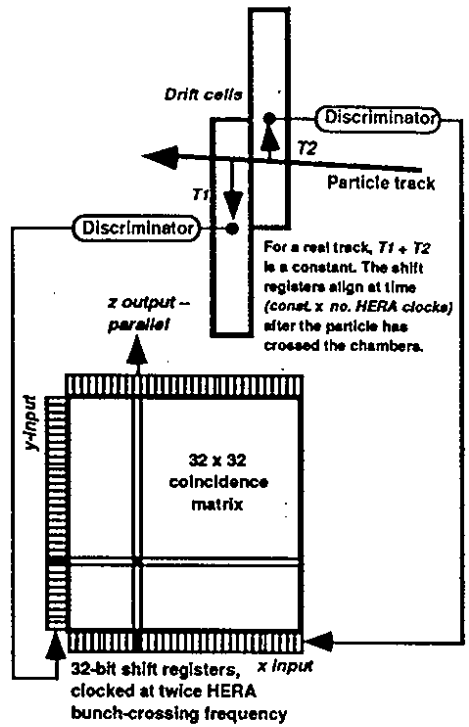

Figure 8.6: Principle of track recognition in the forward muon trigger.

9 Slow control

The slow control system of H1 is designed to take care of all parameters of the experiment which would be constant in an ideal world. Except for central control and monitoring of all VME crates, all subdetectors described above are equipped with a slow control system of their own. All systems use VME controlled by Macintosh or OS-9 computers and some of them use a VME-controlled multichannel slow control system developed at H1 [152]. The integration of subsystems is achieved in two ways, a simple hardware alarm system and a computer control network (CCN). A combined database is used for maintenance of static data and storage of measurements.

Throughout the slow control system we use the notions of slow channel (SC) and slow event (SE) [153]. A slow channel is a single measurable quantity of a single signal type of a single physical channel (e.g. a real setting of a high voltage power supply channel, or the value loaded into this channel). Each SC is uniquely identified by its code (ID). All slow channels are first initialized by their subsystem computer in agreement with the central database. A microevent occurs when a significantly new result is obtained from the measurement on a SC. In this sense the data are zero-suppressed. Microevents are accumulated in their slow event buffer until the status of some SC's changed, the time allowed for a SE accumulation has expired, the command to send a SE was received or the maximum number of microevents within a SE has been reached. As a result of any of the above conditions (SE triggers) a slow event is sent to the central slow control computer.

We use a relational database management system for the maintenance of slow control data. Central relational databases have been designed for the maintenance of setting data (used by software to load front-end hardware and initialize monitoring) and of maintenance of cabling description data (used by production software in the form of maps) and for automatic book-keeping of data produced by the data acquisition and other event-oriented processes (MC simulation, reconstruction, compression, analysis, etc.). We exploit considerably the potential of structured query language (ANSI SQL) for the purpose of data integrity, control of access and commitment, and, of course, for queries. The complete history of the databases is kept. All their maintenance is done without any need to manipulate redundant data interactively. Any set of reports from queries can be automatically formatted into H1 standard records suitable for production programs. Unlike the data above, slow events are stored in two standard files. The slow event archive file uses keyed access to SE's. The evolution n-tuple files contain the same data organized in time evolutions of all slow channels. Both of these history files are zero-suppressed in the sense of microevent definition. We have a good interactive access to slow control data stored on the mainframe IBM computer. A menu tree can be used to guide casual users. Remote access to all databases and history files is made transparent by a TCP/IP database server.

The control network consists of subsystem control computers (Macintosh and OS-9) attached to different detector parts (Figure 9.1). They are connected via Ethernet (TCP/IP). CCN is used to monitor all parameters of H1. All slow control computers produce slow events (SE) and transfer them to the central slow control (CSC) computer. the CSC computer provides data for the online display of the detector status [154] running on Macintosh computers. SE's are also injected into main data acquisition event data stream. On the mainframe IBM computer they are copied to the history files. The CSC computer itself monitors some 150 VME-crates and other devices not linked to a particular subdetector.

Hardware alarms do not depend on computers. Only hardwired combinatorial logic is involved to handle critical situations immediately (e.g. to switch off high voltage power supplies). The central logic [155] uses open/close switch signals. It is connected to the experiment via a routing array which makes it possible to receive input from or deliver output to any location

within H1. The central logic drives an alarm signalisation panel in the control room and provides status flags read out by the data acquisition and included into the event data.

In summary, the hardware alarm system presently monitors some 170 signals and is essentially completed. It works reliably and can readily accommodate new input or output anywhere within the whole experiment. The only change foreseen is automatic interaction with the accelerator. The computer control network has been successfully tested and implemented on a first few subsystems (some 3000 slow channels). Extension to the rest of H1 is in progress. Our experience with the use of relational databases is very positive. Both central slow control and integrated subsystems use them to the full extent.

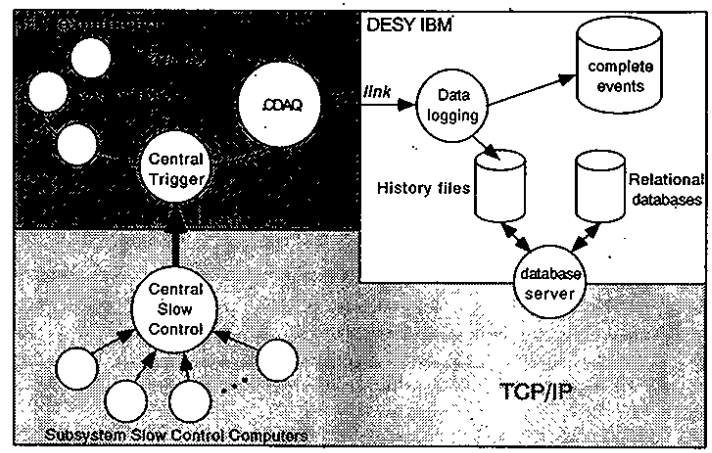

Figure 9.1: Flow of slow control data within H1. The data flow between the database server and slow control computers over TCP/IP has been omitted.

10 The data acquisition system

This section concentrates on the central part of the H1 data acquisition system, the front-end readout and triggering subsystems having been dealt with extensively in previous chapters.

From the real-time computational point of view, a total of over a quarter of a million analogue channels are read-out and digitised, resulting in some 3 Mbyte of raw digitised information for a triggered event. As the time between successive electron-proton bunch crossings is just 96 ns, various levels of hardware triggering, software filtering and digital compression are employed before reducing final data sizes to acceptable storage- media recording rates. For the data acquisition several hundred processing elements are embedded largely within the IEEE VMEbus standard [156]. Descriptions of the system also exist elsewhere [157, 158].

Figure 10.1 summarises the overall data acquisition system and the key rates at full HERA design luminosity. Information is digitised and read-out in parallel from many subdetector partitions before being finally merged. Four main levels of hardware triggering and software filtering can be enabled on all or part of the various detector partitions. In parallel data compression and formatting reduce the 3 Mbyte of raw data to event sizes of between 50 Kbyte and 100 Kbyte so that final data recording rates are restricted, at present, to a maximum 1.2 Mbyte/s. The first level (L1) pipelined triggering system selects initial candidates for data processing from the background. After a L1 accept the front-end pipelines are held. Dead-time then begins. A more refined hardwired L2 decision, based on combined information, can then be activated within 20 μs. Front-end electronics readout is not initiated until an early-level triggering decision is made whereupon each component has a maximum digitisation time of 800 μs before the pipelines are re-enabled; a large amount of the data compression also takes place during this phase. A third level of filtering can be enabled so that should readout commence the pipelines are immediately reactivated if a L3 reject occurs.

In logical structure the detector components are merged, in parallel, into individual subdetector VMEbus crates which each contain a readout controller and memory buffer plus a fibre optic link to a coordinating event management task. A parallel array of RISC processors provides the fourth level of software-coded filtering once all of the full-event information is combined over the fibre-optics [151]. At all stages workstation intervention provides for data monitoring and detector control. To avoid saturation on global VMEbusses, extensive use is made of the local VSB specification [56]. To minimise any further dead-time contributions, memory buffering is provided at the key data processing stages. Finally a local area network (Ethernet) caters for the relatively slow exchange of general operating conditions, files and even event-records between different subsystems. This also serves the external international community with current status and event information over wide-area networks.

10.1 System components

To provide a coherently managed system, between over 200 electronics crates, a baseline set of standards was established to ease maintenance and software development overheads.

10.1.1 Basic hardware components

For general-purpose real-time control within VMEbus, a common 68020/30/40 series processor card was selected [55]. On-board memory is dual-ported so that it can be accessed externally from the VMEbus (for communication) as well as internally from the processor itself. VSB local bus access can be extended to memory boards in adjacent crates but is never used as an

inter-crate connection. For even more calculation-intensive applications RISC processor-based modules are employed. The RAID 8235/8239 is a single-width VMEbus/VSB board based on the MIPS R3000 processor (25/40 MHz clock) and the R3010 Floating-Point Accelerator with up to 32 Mbyte of onboard DRAM [159]. To enhance memory bandwidths and reduce instruction access times, up to 128 Kbyte of independent data and instruction cache ensure that each board has an equivalent computing power of around 50 % of an IBM 3090 mainframe. The DPM 8242 is the basic memory module and can be equipped with up to 16 Mbyte of 70 ns static RAM, having equal priority in arbitration from the VME and VSB ports [160]. A broadcast mode selection allows any VMEbus master to write to several memories simultaneously. Both the VMEbus and VSB memory base addresses are software programmable via VME accessible registers, permitting a managing Event Coordinator task (see later) to switch units between different events. Due to their graphics-user-interface and open NuBus architecture, Macintosh computers are used extensively for the purpose of software development and operator control. Up to 24 VMEbus crates can be mapped directly onto each Macintosh via MacVEE and Micron, MacVEE interface card resident on NuBus [67]. No sophisticated protocol needs to be initialised, unlike other DMA-based connections.

10.1.2 VMEtaxi

In many of the front-end subsystems the standard VICbus is used to interconnect crates [53]. However for coordinating the fast data acquisition transmission protocol, between the different readout subsystems, VMEtaxi modules are employed [161]. These can connect VMEbus crates up to several kilometres with fibre-optics. Figure 10.2 illustrates the basic philosophy. All boards are interconnected with multimode optic fibres to form a ring, using AMD 7968/7969 TAXI-chip transmitter/receiver pairs. Because of this, there is theoretically no limit on the number of such devices which can be interconnected within a single ring; in practice one is limited by the software overhead in setting up transfers. Each single- width board has a cpu controller and single level VMEbus arbiter. The software protocol, discussed further in the following sections, is purpose-written and optimised for speed and efficiency in a data acquisition environment; no FDDI or similar networking protocol is adopted. In setting up transfers between any two crates, an initial description packet is sent around the ring; those modules not engaged in the subsequent activity can enable by-pass registers so as to establish a direct connection between the two VMEtaxis that are involved, analogous with SCI [162]. During the early stages of data-taking, a 25 MHz 68020-based board was used with 125 MHz taxi chips. Upgraded Mark-2 modules are now installed which exploit 50 MHz 68030 processors and either 175 MHz or 250 MHz taxi chips. By driving double-links in parallel there is the potential for 55 Mbyte/s point-to-point data transfers between crates up to distances of several km. The link reliability has been tested to a bit error rate of less than 1 in 10^{13}. Program memory is provided for by 128 Kbyte of on-board fast static RAM with an additional 2 Mbyte of on-board extension static RAM accessible over the VMEbus by external processors. On-board EPROM and EEPROM provide for firmware storage and configuration parameters. VME64 and VSB block transfer modes are realised on the Mark-2 modules with XILINX gate arrays.

10.1.3 Software

The architectural structure of the hardware, discussed in the following section, defines how the software is written and developed. Dedicated tasks run on dedicated processors throughout the VMEbus system with operator intervention provided for via graphics-orientated computers such as Macintosh. Different languages and approaches are used depending on the application being developed. Much of the online data acquisition systems code which executes on 68000 series microprocessors, within the VMEbus, is written in either C or Assembler. Final-level filtering

algorithms, which execute on the R3000 boards, have large code resources originating offline and written in Fortran [151]. Control programs which run on the Macintosh computers exploit the latest object- orientated and graphics-based packages currently on the market [163]. It can be seen that the Macintosh provides a convenient integral component in both software development and operator-control. In order to encompass the framework of VMEbus, extra tools have been developed to ease the integration into the VMEbus [164]. As a result, no formal operating system is required to run on the VMEbus boards; all basic functions can be controlled from a Macintosh via external directives through dual-ported mailbox memories. In order to enhance information exchange between control computers a dedicated package has been written based on international networking protocols [165]; this has the added advantage of enabling the complete system to be monitored from external laboratories and institutes.

10.2 System Integration

By convention the data acquisition system breaks down into three main categories for the purpose of central coordination and management. First there are the front-end "producers" of data; the end result of extensive electronics digitisation from the subdetectors or "branches". Second, the data are merged and distributed to several full-event "consumers"; subsystems which monitor and record the data onto permanent storage media. Third, the system is initiated and controlled via external processes for overall system supervision and operator intervention. Figure 10.3 shows the physical layout of the complete system, managed centrally through several layers of software protocol, purpose-written around the VMEtaxi fibre-optic ring [166]. Common, shared, memory blocks provide for the communication between all system processors and external computer stations. The master of the ring executes the "Event Coordinator" task, controlling the whole sequence of management processes. A separate object module provides a software library to interface the individual subsystem elements, with features ranging from full module testing and control through to basic buffer management and system coordination.

10.2.1 The architecture of the front-end producers

The readout system of each branch is autonomous up to and including a central subdetector VMEbus crate. Each central subdetector crate contains a dedicated supervisory readout controller, a multi-event buffer (MEB), a VMEtaxi and any input drivers necessary to access the data (Figure 10.4). Consequently the design allows a particular subdetector to be decoupled from the rest of the system, during installation and test phases, and does not exclude the use of other busses for front-end digitisation. Data are placed into the multi-event buffer over VMEbus and then extracted by the VMEtaxi either over VSB or locally, depending on wether the buffer uses a DPM or exploits the extension RAM of the VMEtaxi. The Event Coordinator management task runs on the master VMEtaxi of the ring and interacts with each readout controller via shared memory blocks. Before commencing data acquisition, the Event Coordinator is responsible for hardware recognition and initialisation of the various branches. During acquisition, when it is free for event building, it searches the subdetector multi-event buffers for the next event. When all branches are ready with the same event number, the separate banks are transferred via the optical ring into a full-event buffering system. On completion, each corresponding buffer is released. A subdetector crate may also contain additional processors for data reduction, an interface to a subdetector monitoring computer and a subsystem trigger controller (STC). All STCs are interfaced to a dedicated central trigger controller which, in turn, coordinates the sequence of all hardware triggering levels together with obtaining information from the HERA machine [52]. Each STC provides signal ports for the component electronics and communicates with the readout through VMEbus read-write cycles and interrupts. A consequence of this is that the Event Coordinator needs no hardwired connection with the central trigger controller

itself; all management sequences are handled by software, so providing a portable solution to any large multi-crate VMEbus system [166].

At the subdetector branch level, the software library provides multi-event-unit routines catering for initialisation, accessing status information, requesting buffers and signalling when event data are ready for merging. Readout error codes are normally indicated as standard parameters, but messages can be sent through the system in standard ASCII format to describe branch- specific anomalies. Figure 10.6 also shows how the protocol has been transparently mapped from a main branch through to a sub-branch structure by incorporating standard VIC links to merge smaller subsystem components.

10.2.2 The management of full-event consumers

As the Event Coordinator VMEtaxi builds full-event records it simultaneously broadcasts them along its VMEbus to dual-ported memories associated with parallel sets of "full-event units". Event tasks are performed by connecting the unit processors with their respective full- event buffer (FEB) memories via VSB in order to minimise any bandwidth overheads (Figure 10.5). Since the memory has read/write access from both the event task processors and the Event Coordinator, full-event units need not only be "consumers" of data. An event unit can also become a "producer" of data, "feeding-back" data into the system. Consumers are able to determine which data they wish to receive, ie directly built events from the front-end branches or data fed-back into the system from, for example, a parallel filter farm. All this is handled modularly by the software protocol and its associated library of routines.

Typical full-event tasks are data-logging, event display, data monitoring and histogramming. Final event records are sent to the central IBM facility at DESY, some 3 km distant, at rates of up to 7 Mbyte/s [167]; at present the disc writing rate limits the system to 1.2 Mbyte/s. The data logging task requests every event to be recorded and so there must always be a free buffer associated with it. In case of link failure a backup event task, that drives a storage device directly from VMEbus, can be enabled. A more sophisticated form of unit is the fourth level filter "farm" consisting of many R3000 processor "nodes" working in parallel. Each node executes the same algorithm independently on different events. This provides not only a final level of triggering but a further stage of data processing and online reconstruction, as the event display of Figure 10.6 demonstrates [168].

Event records are passed to the different nodes under control of a filter input controller, which communicates with the Event Coordinator as a normal consumer full-event task. When a node is free it signals this to the filter input task which searches for an event ready in its full-event buffer. The data are then extracted over the VSB and sent to the free node, releasing that particular buffer and enabling a further node to be serviced. When a node has finished processing an event it signals completion to a filter output controller (a "feedback" event task). The latter then decides whether to pass the event back into the central system managed by the Event Coordinator and free the node for further processing. As a full-event unit, the parallel filter can be easily enabled or disabled.

The software protocol of the Event Coordinator allows for several banks of filters to be implemented, each with their own input and output controllers. Currently the single Event Coordinator task can accommodate the handling of the filter-output due to the relatively low acceptance rates at Level-4; however, due to the modular architecture, additional processors can be readily introduced to share this task if required.

10.2.3 System supervision and operator-control

The H1 system is capable of running entirely in VMEbus; Figure 10.7 illustrates the composition of the central part where dedicated processors run dedicated tasks so that the net result is one of a conventional multi-tasking system. This leads to a natural division of tasks and processes. The primary tasks of data acquisition are performed by the subsystem readout controllers, event builders, filter control tasks and event units, all managed by the Event Coordinator. All fast processing and readout is done within VMEbus. An exhaustive software library caters for external control by providing a full set of routines for system configuration, testing, system-status and monitoring [166]. NuBus-based Macintosh computers take over the responsibility of program development and run- time operator-control. The System Supervisor Mac [169] initialises the readout and checks the status of all elements by initiating VMEbus tasks such as the Event Coordinator. To provide a central focus of monitoring it also communicates with event tasks and subsystems either through VMEbus or over Ethernet. Additionally it serves the network with status information for external monitoring. The graphics-based philosophy of the Mac ensures that the operator is presented with, arguably, one of the most human-interactive interfaces, available today, to a complex real-time system.

10.3 Observations and performance

The H1 data acquisition system was initially commissioned during cosmic-ray tests in Spring 1991 and then used to read out the complete detector during first HERA operation in Summer 1992. Its advanced preparation, and relatively stable operation, was in no small measure due to the choice of an open, industrial bus- standard and the incorporation of modern commercially-available hardware and software where suitable. Of particular note has been the extensive use of the networking facilities in addition to the main data flow. The ability to control and monitor the system externally, even from the latest generation of portable note-book computers, has been extensively capitalised upon.

From the master VMEtaxi the system can manage up to 32 branches and 16 full-event units, including the parallel filter farm, providing status information and accepting control command sequences from the System Supervisor Macintosh. Presently 100 Kbyte-sized events can be coordinated from 12 branches at rates of 200 Hz using the Mark-2 VMEtaxi modules. The primary sources of dead-time remain at the front-end, where future injections of greater processing and refined triggers are made more comfortable by working within an international bus standard.

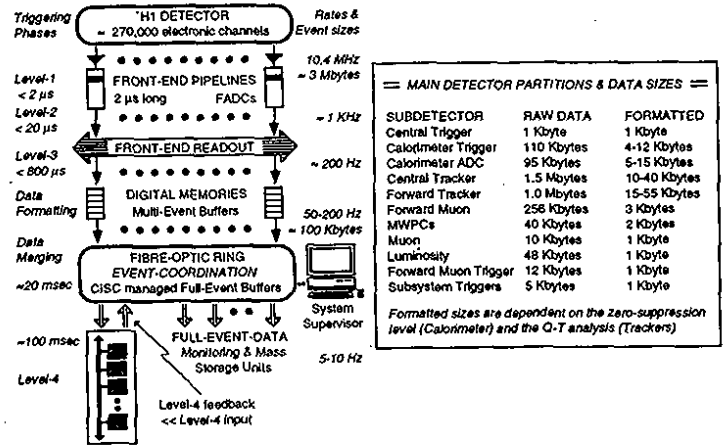

Figure 10.1: Overview of the H1 data acquisition system.

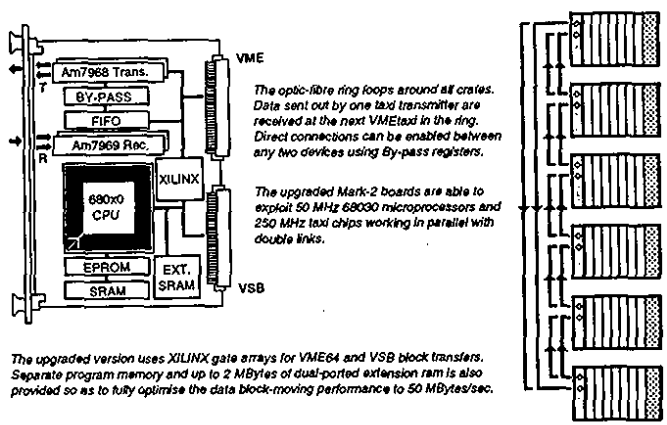

Figure 10.2: VMEtaxi fundamentals.

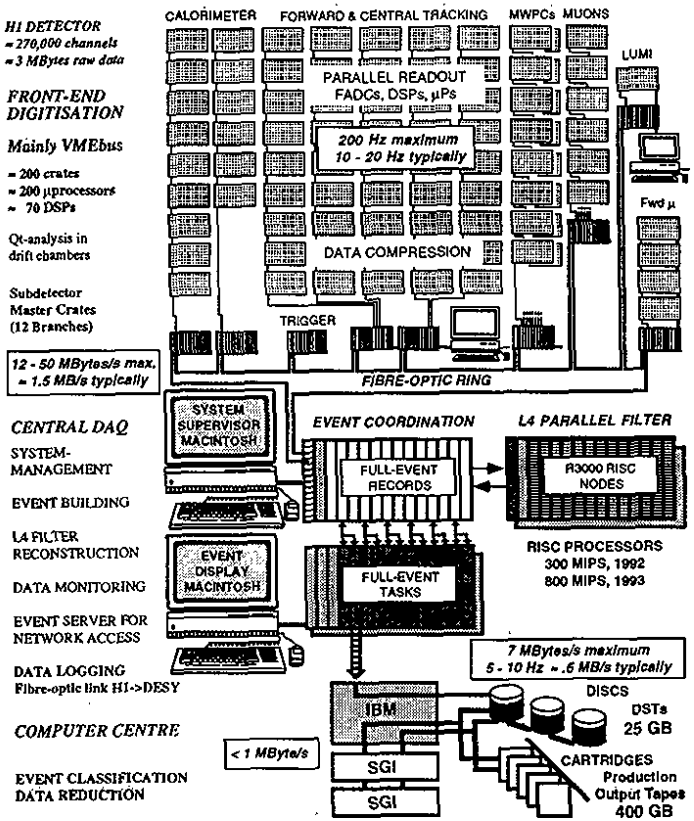

Figure 10.3: Physical layout of the key features of the H1 data acquisition system. See text for details.

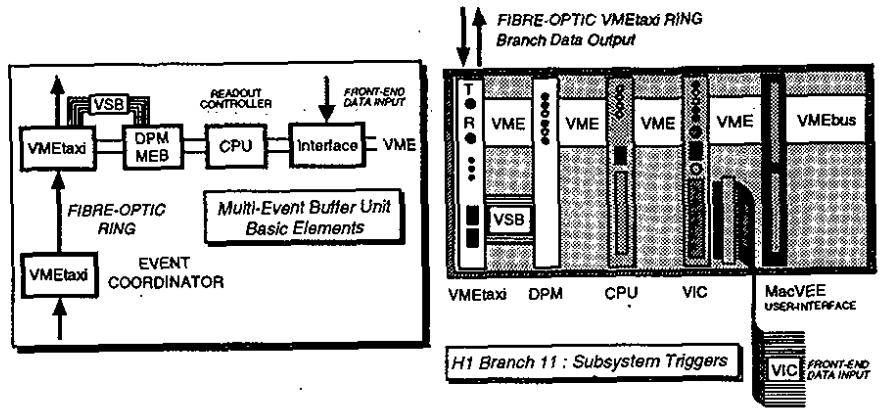

Figure 10.4: Multi-event buffer units.

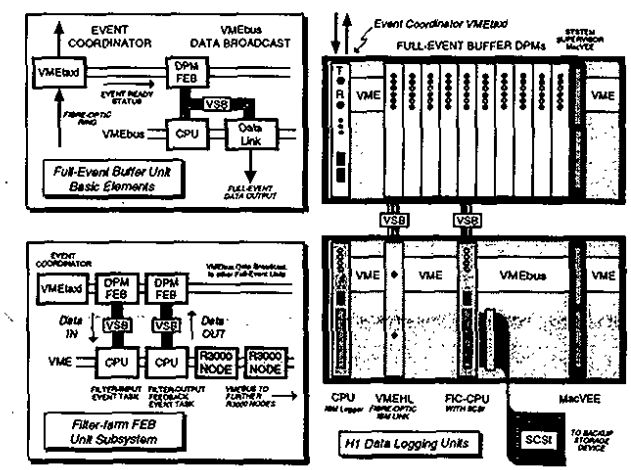

Figure 10.5: Full event buffer units.

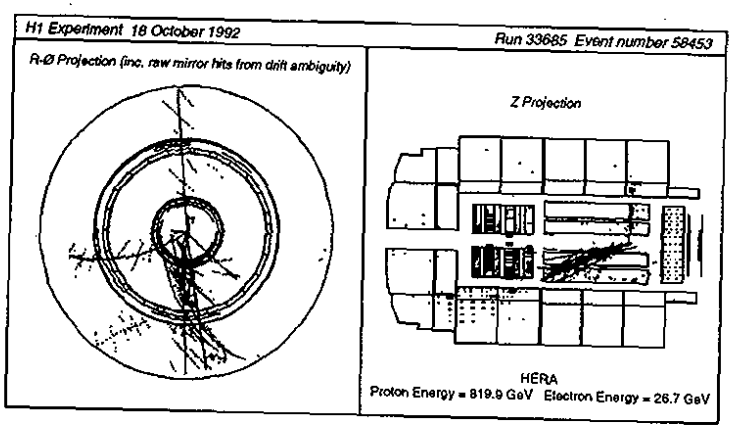

Figure 10.6: A deep inelastic event reconstructed online at H1.

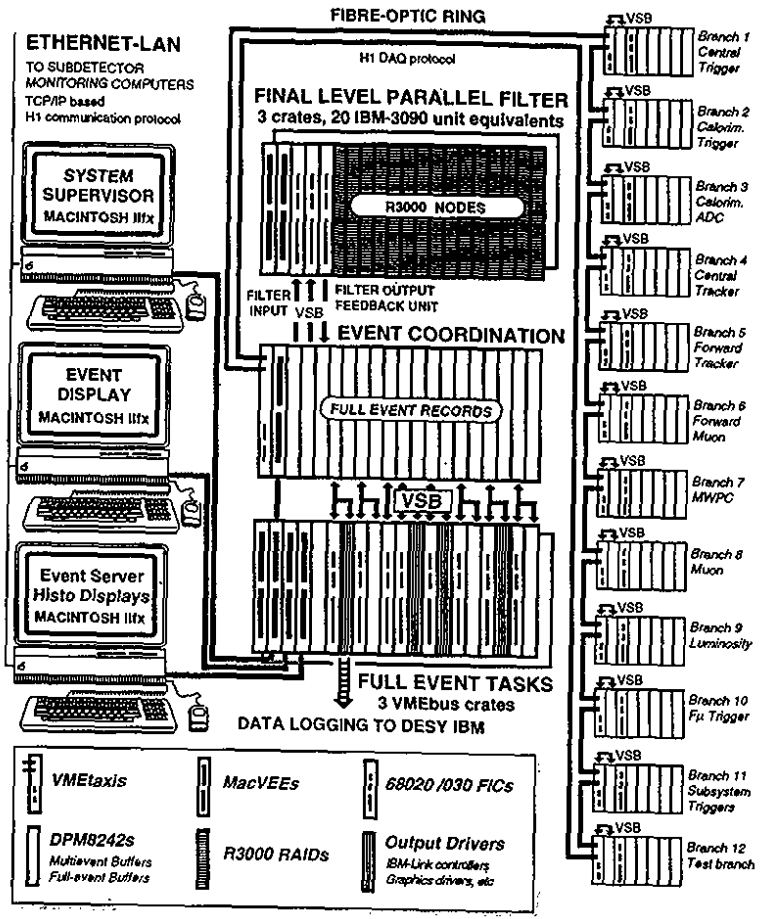

Figure 10.7: Physical composition of the central part of the H1 data acquisition system as during the initial running periods of 1992.

11 Off-line data handling and simulation

This section concentrates on the off-line data handling, quasi-online data reconstruction, event simulation and the H1 analysis environment.

11.1 Off-line computing

The data recorded by the H1 experiment are transfered to the IBM ES 9000/720 VF mainframe on the DESY site via a fast link at rates of up to 7 Mbyte/s (see Section 10.2.2). The IBM mainframe is utilized to store and manage all the data of the experiment: raw, simulated and reconstructed data and the data summary tapes (DST) for physics analysis. Export of data via IBM 3480 or Exabyte cartridges is also organized on the IBM. H1 further uses for number crunching tasks three Silicon Graphics (SGI) 4D/460 workstations with six processors each. These workstations are connected to the IBM via a fast UltraNet link, which can support a high bandwidth. A memory to memory transfer rate of 7.5 Mbyte/s has been measured. During data taking one of the SGI 4D/460 workstations is dedicated to the data reconstruction task. The analysis of data is performed on the IBM mainframe, on HP 425 and HP 730 workstations and on the SGI 4D/460 computers. These workstations are interconnected via Ethernet and Apollo token ring. Several external institutes have also installed RISC processor based workstations at DESY for analysis purposes, connected to the local network facilities.

An overview of the H1 off-line computing environment at DESY is given in Figure 11.1, showing the central role of the IBM, the SGI 4D/460 number crunchers, and analysis workstation cluster.

The raw, reconstructed and simulated data are stored on IBM 3480 cartridges in the STK 4400 ACS silos of the DESY computing centre. During normal HERA operation, the data taking proceeds with an average rate of about 500 Kbyte/s, leading to an expected yearly data volume of about 5 Tbyte. To ensure an efficient environment for physics analysis the DST's must be accessable by many users simultaneously and are therefore kept on fast disks both on the IBM and on the SGI 4D/460 workstations. In total 20 Gbyte and 50 Gbyte of disk space is reserved for DST files on the IBM mainframe and SGI 4D/460 workstations, respectively. Multi-user access posibilities to data on cartridge are also offered by the efficient staging mechanism on the IBM.

Care has been taken from the beginning that all offline processing of the data and simulation was portable between DESY and external institutes. Meanwhile many of these institutes have installed the complete offline program chain and participate in simulation and data analysis. More than half of the detailed detector simulated data was produced in external institutes. Furthermore, most institutes are connected to DESY via fast network links.

H1 uses the dynamic memory management package BOS [170] for its software. A general input/output package, FPACK [171], was written in order to have a simple and unique system for all data transfer in the experiment. It contains automatic wordformat conversions between different machine representations (IBM VAX DEC IEEE), includes record selection options and supports event directory based fast access to data. A data base package was developed and is used to store run dependent data and Monte Carlo information. Further, the code manager CMZ [172] is used for the H1 software packages. A set of simple but solid rules, complemented by the necessary subdivision of responsibilities and the imposing of discipline, has created a successful and efficient environment for code development in this large collaboration. Details on code management with CMZ in H1 can be found in [172].

An important aspect of the software is the concept of modularity [173]. Modules are self-contained sets of routines with clear I/O interfaces. They take care of their own initialisation

upon first call. Modules communicate to each other only via BOS banks. A larger program, such as the reconstruction program, consists of a simple series of module calls. Purpose written utility software performs automatic bookkeeping of used input and created output BOS banks and guarantees the internal consistency of the data after reprocessing of modules. The dynamic memory management package BOS includes modularity oriented functions to support this scheme.

H1 also uses an entity relationship model as a basis for data structures of all event data. A data management tool DATMAN [174] provides an easy and userfriendly access to the data.

11.2 Data reconstruction and reduction

The H1 data are reconstructed quasi-online [175]. The logged and dumped data are automatically copied from the IBM mainframe to a SGI 4D/460 workstation via UltraNet, and fed into a reconstruction task. This task runs in parallel six identical and independent processes, whereby a set of shared memory areas and semaphores is used to share data among the processes. The reconstructed data are sent back to the IBM and are stored on cartridges. The reconstruction of an event takes on average 1.25 CPU-s on a SGI 4D/460 processor. Thus the reconstruction task can keep up with the data logging rate of 5 Hz of the experiment. If needed a second SGI 4D/460 workstation can be included in parallel in order to deal with higher rates. In all, the reconstructed data become available to the users typically a few hours after the raw data are recorded by the experiment. The amount of recorded data by experiments at HERA is large. During the July '92 data taking period about 3×10^6 triggers were recorded. The total integrated luminosity in that period was about 3 nb^{-1}, leading us to expect that a few percent of these triggers are genuine ep collisions. Most recorded triggers are caused by proton and electron beam-wall and beam-gas interactions. Off-line event classification and background rejection filters, based on reconstructed energies and tracks, reduce this amount of background presently with a factor 20-30 during DST production. Background rejection filters include cosmic muon and muon-halo filters, recognition of coherent noise patterns and filters for beam-wall and beam-gas collisions originating from outside the detector. The latter reject events which have a prominent number of reconstructed tracks originating from outside the detector, or events with TOF scintillator signals detected in the background time window.

The dominant source of background events on DST after these selections are interactions of protons with the residual gas within the detector. These interactions produce mainly soft particles produced in central and forward region, and are an important background for soft ep processes such as VDM photoproduction and heavy flavour production. Large background reduction factors can be obtained by exploiting the difference in event kinematics and topology for background and genuine ep collisions. As an example the correlation between the energy flow $\sum p_z / \sum p$ and $y_h = \sum (E - p_z)/2E_e$ is shown in Figure 11.2. The summation is performed over tracks and calorimeter cells, where calorimeter cells behind tracks were masked to avoid double counting of energy. The energy flow of the background events is characterized by a value of $\sum p_z / \sum p$ near to 1, due to the large Lorentz boost, and a small value for y_h. Figure 11.2 shows the event distribution in the two variables for a background sample taken from events coming from the so called proton pilot bunch with no electron bunch partner compared to the VDM photoproduction events from Monte Carlo simulation. With the indicated cuts the proton beam-gas background is reduced by a factor 100, while very little of the signal is lost.

Moreover, these proton beam-gas background events are often accompanied by a number of protons which are identified by their energy loss in the central jet chamber, or contain considerably more positively charged than negatively charged tracks. Both these criteria can be exploited to reduce the background as well and are an important cross check for the efficiency of the kinematic selection criteria.

11.3 Event simulation

A complete detector simulation program has been assembled within the GEANT [111] framework. The geometry of the full detector and the beamline within ±100 m around the interaction region are implemented with two different levels of detail, called fine and coarse granularities. For the fine granularity the longitudinal structure of all calorimeter stacks is implemented layer by layer, whereas for the coarse geometry a calorimeter stack is implemented as a block of properly mixed homogeneous material with no longitudinal structure. For the tracking detectors seperate volumes are implemented for each active cell (wire) for the detailed geometry, whereas for the coarse geometry an entire gas volume is treated as one volume. For accurate detector response, particularly in the detailed geometry option, the tracking cutoff parameters for the kinetic energies have to be set as low as 1 MeV. This leads to simulation times of the order of 600 s for a typical low Q^2 deep inelastic event on a SGI 4D/460 processor. Three strategies were followed to tackle this large CPU time consumption for event simulation:

- The time consuming part of the actual tracking of particles through the geometry was strictly separated from the digitisation part of the detector response. Run dependent detector effects and the actually achieved resolutions can easily be adjusted by just reprocessing the digitisation part only, which use only a fraction of a second per event. A similar scheme was used for the simulation of the trigger response.
- A bookkeeping is made of all energy depositions in the detector, both for visible and invisible (nuclear breakup, neutrinos, slow neutrons) energies, and both in active and dead detector regions [176]. This allows to reconstruct the calorimeter response after simulation with simple response functions, which are basically sums over the smeared true energy depositions. The absolute energy scale can thus be reconstructed correctly, which gives an important handle for testing the reconstruction programs and also to understand the behaviour of a non-compensating calorimeter.
- A fast but accurate energy shower parametrization [106, 109] was developed. This so called H1FAST mode was included into the GEANT framework. The main idea is sketched in Figure 11.3. The time consuming part of the full shower development in the detailed geometry is replaced by a shower parametrization in the coarse geometry leading to reduction of the CPU time consumption by a factor 10. Showers which cross crack boundaries are simulated in detail, in order to keep accuracy.

Besides the detailed simulation program, H1 possesses of a fast parametrized detector simulation program: H1PSI. It contains a simplified pointing tower geometry and produces reconstructed quantities and trigger response. The event processing time is about 0.1 s/event on a 4D/460 processor. This program was heavily used for feasibility studies in the physics analysis preparation phase of the experiment.

11.4 Physics analysis

The visual aspect of the physics analysis is mainly handled by a purpose written general system for graphics applications, baptized LOOK [170]. The aim is to have one –and only one– graphics package for all graphical applications: event display, histograming, analysis, etc. LOOK can be considered as a layer between the user application and low level graphics functions, for which at present GKS functions are used. LOOK organizes the management of the display and e.g. hardcopy devices. It further contains a histogram package and a powerful command processor and is portable to many platforms. The H1 event display program, H1ED, is an application

based on LOOK. Figure 11.4 shows an example of an event display and histogram analysis combined in one session. LOOK can be used for interactive analysis, e.g. n-tuple analysis of data. PAW is also used for interactive analysis, due its presently more powerful possibilities for n-tuple manipulation.

The program H1PHAN is a tool to access event data and simplify physics analysis programs. The data are filled in internal event buffers called Q-vectors, which are accessible in simple Fortran DO-loops. Thus the user does not need to know the –sometimes complicated– underlying bank structure of the data. H1PHAN further contains tools for particle identification, secondary vertex fitting, jet finding and analysis, determining kinematical variables of deep inelastic event candidates, etc.

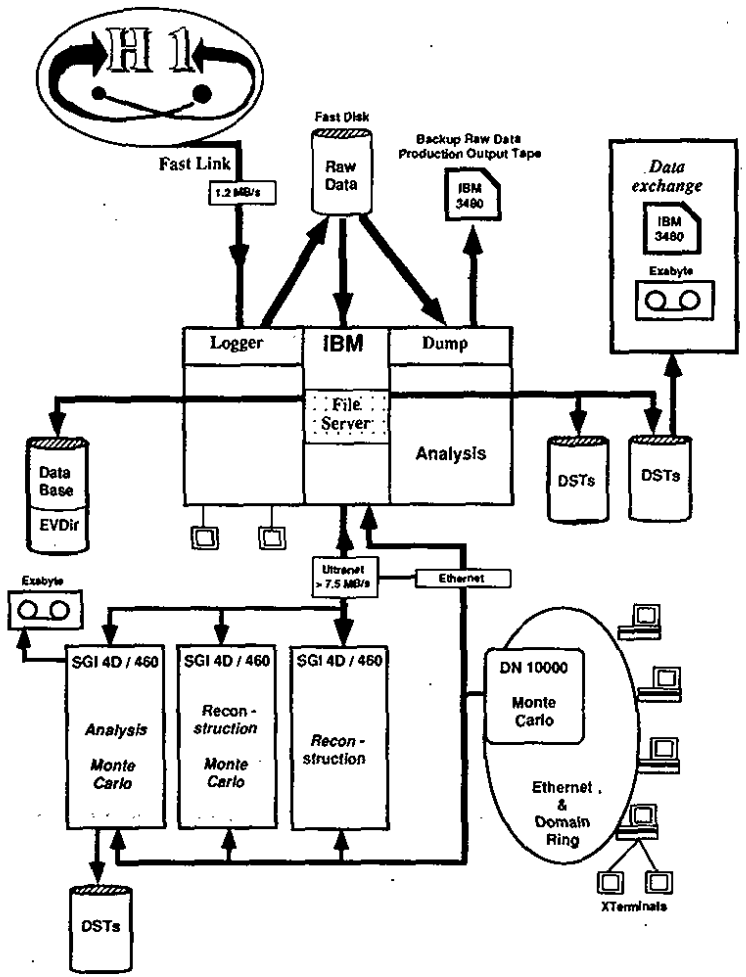

Figure 11.1: H1 off-line computing environment

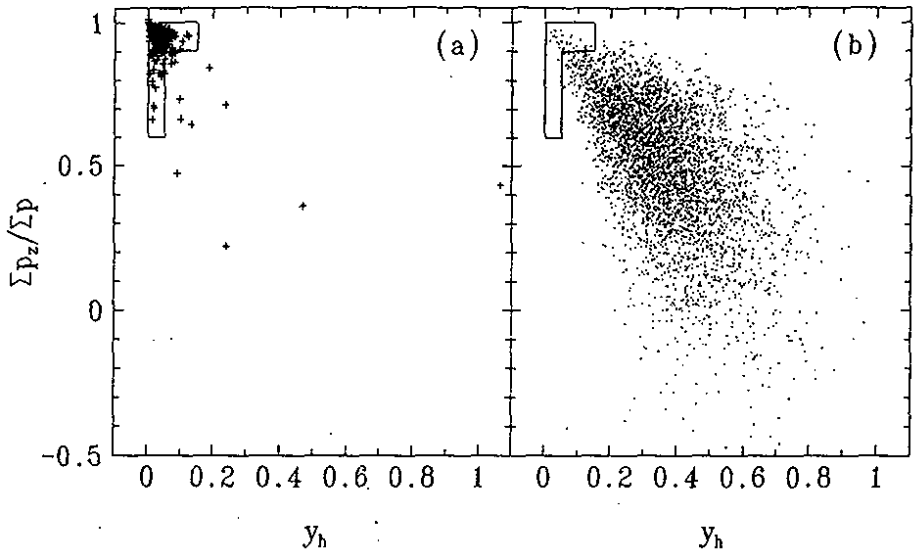

Figure 11.2: Distributions of $\sum p_z / \sum p$ versus y_h for the proton pilot bunch data (a) and for tagged γp MC events (b). The cuts applied for the proton–gas background rejection are indicated by the solid line.

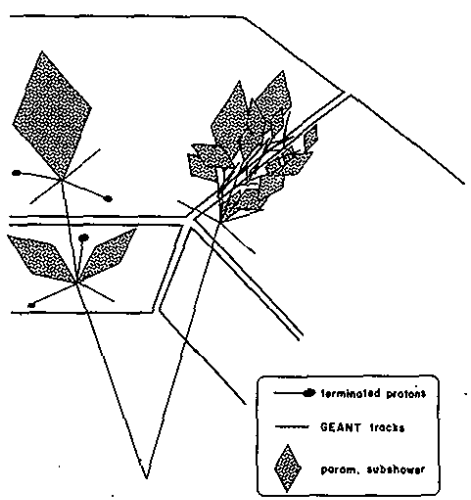

Figure 11.3: Schematic view of the parametrized shower simulation in a coarse geometry.

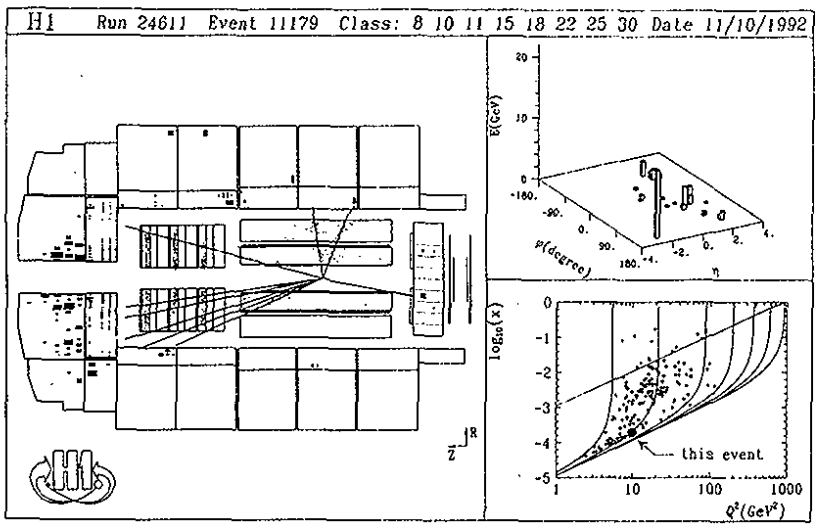

Figure 11.4: Physics analysis with LOOK

12 Summary of first operation at HERA

The successful operation of the H1-detector during the initial phase of HERA is evidenced by five publications [137, 177, 136, 178, 179] which resulted from it.

The measurement of the total photoproduction cross section [136] relied mainly on the luminosity monitor and electron tagger. It showed that the novel technique of monitoring luminosity via the $ep \to ep\gamma$ bremsstrahlung process combined with on-line background subtraction using electron pilot bunches can be used confidently. Potential improvements of the systematic errors are foreseeable, once beam tune shifts can be better controlled. The electron tagger signal alone provides a fairly clean trigger for all photoproduction physics in the very low Q^2 range. Supplemented with tracker and calorimeter information at the trigger and reconstruction level the prominent beam gas background can be removed completely, as demonstrated in the analysis for hard photon scattering [137]. Figures 12.1 and 12.2 show two events typical for these type of processes and the background. Often, but unfortunately normally not as dramatic as shown in Figure 12.1, beam gas events produce a large excess of positive tracks (usually protons). Most beam gas events are more likely not looking too different from the electron tagged two-jet event shown in Figure 12.2. However, as e. g. apparent from Figure 11.2, the comparison of the electron energy loss y measured from the hadron information and compared to the electron information allows a distinction of the two classes, because the background is characterized by $y_h \leq 0.1$ and $\sum p_z / \sum p \approx 1$ due to the large boost induced by the incoming proton.

The total cross section measurement with the electron tagger was crosschecked with data triggered only by the $z-$vertex trigger (see Section 8.3.1), which required a minimum number of tracks from a common vertex in the interaction region. Though photoproduction events from a different range of Q^2 and y are accepted by this trigger, a detailed understanding of this trigger and its dependence on chamber efficiency, noise, crosstalk and track transverse momentum p_t and energy loss is required, and lastly a subtraction of proton pilot bunch data is needed, the results nicely confirm the electron tagger analysis.

The above examples were cited to emphasize again one of the stronger points of the H1 detector, which has been explained in more detail in the trigger section above, namely the facility to trigger on the soft physics while not loosing the deep inelastic events or vice versa. The use of topological information rather than just thresholds on individual detectors, deadtime free through use of pipelines with the technical difficulties imposed by the short bunch crossing interval must be considered a major step forward and should ease dealing with the even harder conditions expected at future pp colliders. Of course the higher luminosities expected also for future running at HERA will require further fine tuning and more sophisticated application of this concept.

The first measurement of deep inelastic scattering in the new kinematical domain accessible to HERA required a rapid understanding of the energy response from the backward electromagnetic calorimeter (BEMC) and from the backward and cental parts of the LAr calorimeter. Figure 12.3 shows the spectrum of energy clusters in the BEMC. Without additional constraints the trigger rate amounts to a few Hz/GeV even at the low beam intensities achieved so far. The observed rate is totally dominated by proton induced background hitting the rear part of the calorimeter. The rate can be reduced by almost two orders of magnitude by a simple timing requirent in the time-of-flight detector. In the analysis simple event topology and track matching cuts produce an almost background free electron spectrum for energies exceeding 15 GeV. Below that value fake electron signatures from photoproduction hadronic final states become dominant. To reject those active electron identification tools (like shower shape analysis) are under development. However the kinematical peak, a feature discussed in our first publication on deep inelastic scattering at low x [178], and also in Section 5.2 in the context of the BEMC calibration, is clearly seen in this spectrum already.

The first closer look at the hadronic final state [177] deals with events of the type shown in Figure 12.4. This analysis put the software compensated liquid argon calorimeter to a first stringent test. The check of the balance in transverse momentum (see Figure 5.18 entails the understanding of both the hadronic as well as the electromanetic part of the liquid argon calorimeter, and the link between tracker and calorimeter information.

On the technical side, the high stability, reliability and small number of dead channels in the liquid argon calorimeter deserve to be singled out. The noise level was found to be low enough to extend its use down to quite low energies. Trigger thresholds in the stand alone mode need further improvement and elimination of coherent noise sources.

The spectroscopic tools available through the tracking system have not reached their ultimate resolution because of several reasons. The software packages to link the $z-$chamber information to the that from the CJC are still in a rudimentary stage, optimum gas mixtures have not been used yet, the forward tracker was not fully equipped with electronics in the early stage and the pattern recognition in this area is still being optimized. Some of the forward proportional chamber electronic proved faulty, which limited the trigger performance, and the linking between forward tracks, central tracks and muon system ist still not completely in hand. The resolution of the K^0_s peak in the $\pi^+\pi^-$ mass spectrum and of the $\Lambda(\bar{\Lambda})$ signal shown in Figure 12.5 can thus not be considered final, at least a factor of two in improvement is conceivable. Despite this limitation it may serve as evidence, that the isolation of J/Ψ, D^*-tagging etc. should be feasible, once sufficient statistics is available. The few $J/Psi \rightarrow \mu^+\mu^-$ candidates found prove, that the tracker muon link can be made, and also put the novel design of the muon system with emphasis on inherent safety to a first test for its use in future physics analysis.

On the software side the online filtering and reconstruction concepts have permitted a fast access to the data, and also their quick reduction and dissemination to the various analysis centers.

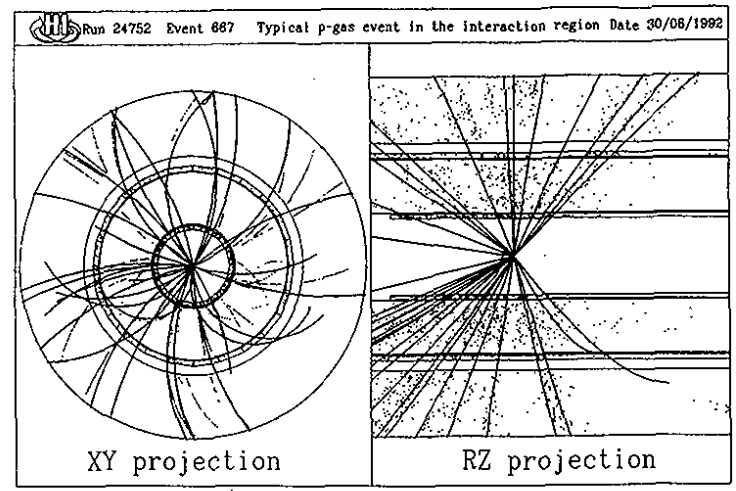

Figure 12.1: Typical beam gas event from the interaction region.

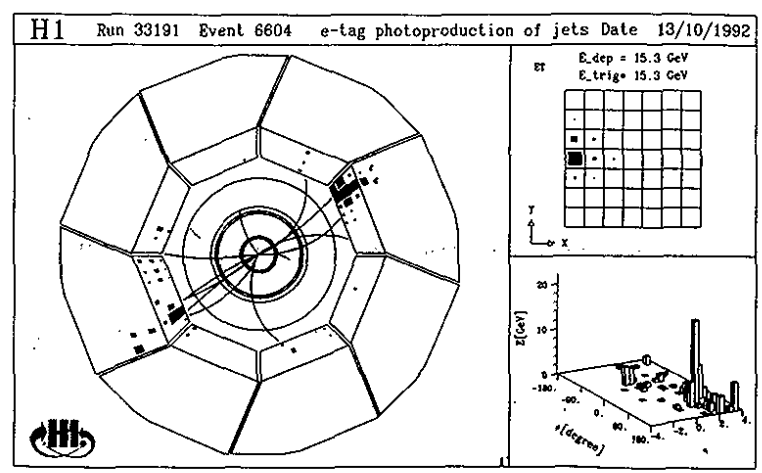

Figure 12.2: Typical two jet event from $\gamma - g$ fusion tagged by an electron in the tagger.

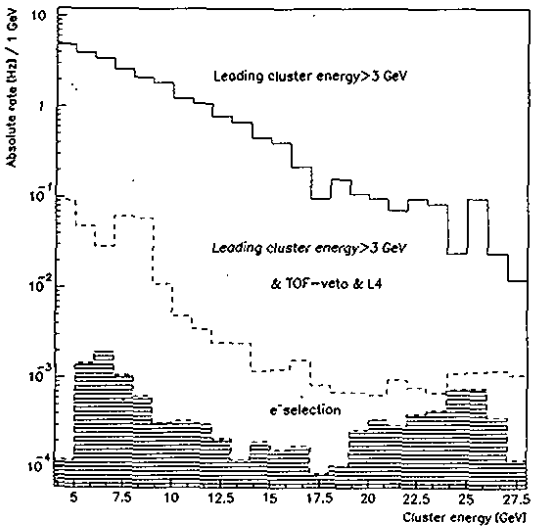

Figure 12.3: Absolute trigger rates recorded in the backward electromagnetic calorimeter in function of cluster energy at different trigger and reconstruction levels.

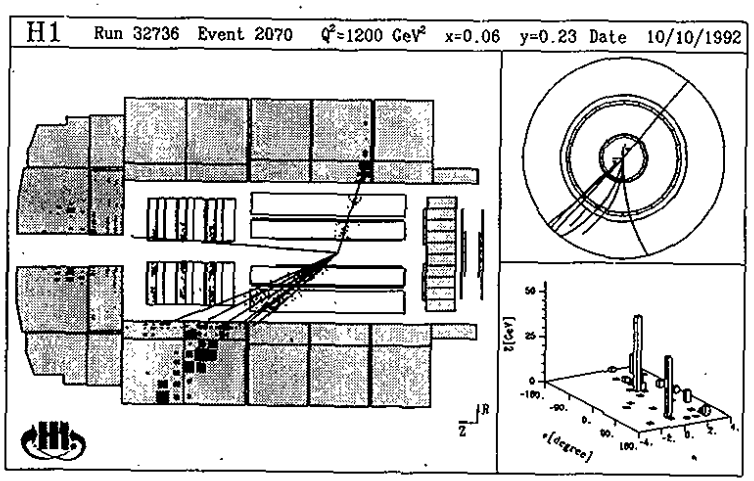

Figure 12.4: Typical high Q^2 event with both the scattered electron and the hadronic recoil jet observed in the liquid Ar calorimeter. Kinematical parameters: $Q^2 = 1200$ GeV^2, $x = 0.06$, $y = 0.23$.

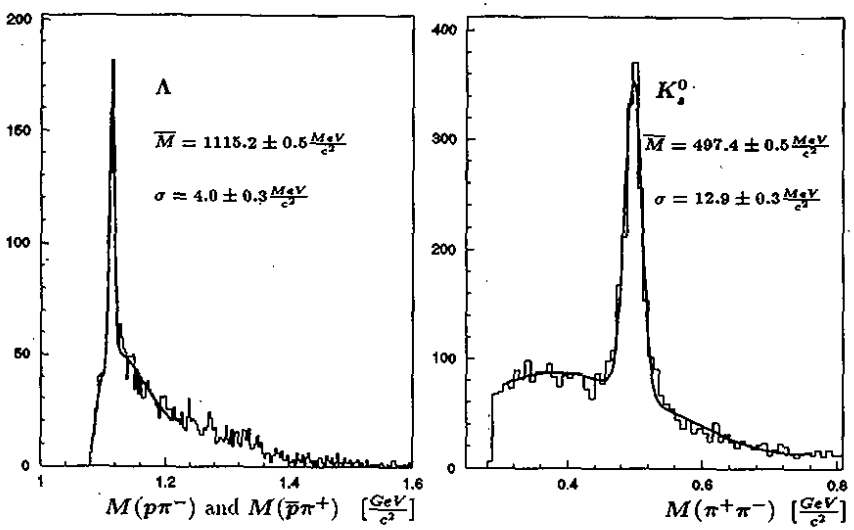

Figure 12.5: K^0_s and $\Lambda(\bar{\Lambda})$ signal observed in the central jet chamber.

References

[1] M. Breidenbach et al., Phys. Rev. Lett. **23** (1969), 935; 1990 Nobel prize lectures: R. Taylor, Rev. Mod. Phys. **63** (1991), 573; H. W. Kendall, ibid. p. 597; J. Friedman, ibid. p. 615.

[2] EMC: J. J. Aubert et al., Nucl. Phys. **259** (1985), 189, ibid. **293** (1987), 740; BCDMS: A. C. Benvenuti et al., Phys. Lett. **B223** (1989), 485, ibid. **B237** (1990), 592; NMC: P. Amaudruz et al., Phys. Lett. **B294** (1992), 120, ibid. **295**, 159.

[3] J. Bartels, Structure functions at small x: new physics at HERA, Particle World **2** (1991), 46.

[4] Proc. of the study for an *ep* facility for Europe (1979), U. Amaldi ed., DESY-report 79-48 (1979).

[5] Proc. of the HERA workshop, Hamburg (1987), R. D. Peccei ed., DESY, Hamburg (1988), vol. I, II.

[6] Proc. of the workshop on Physics at HERA, Hamburg (1991), W. Buchmüller and G. Ingelman eds., DESY, Hamburg (1992), vol. I, II, III.

[7] J. Feltesse, in ref. [5], vol. I, p. 33.

[8] A. Jacquet, and F. Blondel, in ref. [4], p. 391.

[9] S. Bentvelsen, J. Engelen, and P. Kooijman, in ref. [6], vol. I, p. 25.

[10] W. Bartel et al., Prospects for charm physics with the H1-Detector at HERA, pres. by F. Ould-Saada, Proc. 4^{th} Int. Symp. on Heavy Flavour Physics, Orsay, France (1991), eds. M. Davier, and G. Wormser (Editions Frontières, Gif-sur-Yvette 1992), p. 515; see also S. Egli et al., in ref. [6], vol. II, p. 770.

[11] G. Bernardi, W. Hildesheim, A detailed simulation of F_2 measurability at HERA, LPNHE-Paris report LPNHE-92-01 (1992); in ref. [6], vol. I, p. 79.

[12] G. Lopez et al., in ref. [180], p. 251.

[13] D. Pitzl et al., A silicon vertex detector for H1 at HERA, Proc. IEEE Nuclear Science Symp., Orlando, Florida (1992); Paul-Scherrer Institut report PSI-PR-92-35, Villigen (1992).

[14] H. Behrend et al., Technical proposal to build silicon tracking detectors for H1, H1-report 07/92-226, DESY, Hamburg (1992), unpublished.

[15] UA5-collaboration: G. J. Alner et al., Zeit. f. Phys. **C32** (1986) 153; ibid. **C33** (1986) 1; R. E. Ansorge et al., Zeit. f. Phys. **C33** (1986) 175; D. P. Johnson, Beam gas background at HERA, H1-report 07/87-65, DESY, Hamburg (1992), unpublished.

[16] B. H. Wiik, HERA status, in ref. [6], vol. I, p. 1.

[17] F. Willeke, in ref. [180], p. 28.

[18] D. Pitzl, Diploma thesis, University of Hamburg (1987), unpublished.

[19] D. Decamps et al., Nucl. Instr. and Meth. **A294** (1990) 121.

[20] P. Aarnio et al., Nucl. Instr. and Meth. **A303** (1991) 233.

[21] Vakuumschmelze, D-6450 Hanau.

[22] P. T. M. Clee, and D. E. Baynham, Towards the realisation of two 1.2 Tesla superconducting solenoids for particle physics experiments, Proc. 11^{th} Int. Conf. on Magnet Technology, Tsukuba (1989), T. Sekiguchi, and S. Shimamoto eds., Elsevier Applied Science (London, 1990), p. 206.

[23] D. Barber and J. Rossbach, Some analytical and numerical calculations of the effects of the H1 and ZEUS solenoids on the HERA optics, DESY report HERA 86-13, Hamburg (1986), unpublished.

[24] ASEA Brown Boveri, CH-8050 Zürich.

[25] W. Beckhusen et al., Field measurements of the compensating solenoids in the HERA e-p storage ring, Proc. 12^{th} Int. Conf. on Magnet Technology, Leningrad (1991), IEEE Trans. Magn. **28** (1992) 801.

[26] J. Bürger et al., Nucl. Inst. and Meth. **A279** (1989) 217.

[27] J. Bürger, Tracking at H1 in the environment of HERA, Proc. 4^{th} Topical Sem. on Exp. Apparatus in High Energy Particle Physics and Astrophysics, San Miniato, Italy (1990), eds. P. Giusti et al. (World Scientific, Singapore, 1991), p. 272.

[28] H. Drumm et al., Nucl. Instr. and Meth. **A176** (1980) 333.

[29] Glass fibre/epoxy: Stesalit AG, Zullwil, Switzerland; and Permali, F 54320 Marseille, France.

[30] V. Karimäki, Fast code to fit circular arcs, Helsinki University report HU-SEFT-1991-10 (1991), unpublished.

[31] C. Ley, Ph. D. thesis, RWTH Aachen (1993), in preparation.

[32] N. Sahlmann, Reconstruction of Λ and K^0_s with the H1 detector, H1-report 04/93-281, DESY, Hamburg (1993), unpublished.

[33] R. Luchsinger, and C. Grab, Comp. Phys. Comm. (1993), in print.

[34] M. W. Schulz, Untersuchung von Methoden zur Kalibrierung der H1-Jetkammer, Ph. D. thesis, University of Hamburg (1993), H1-report FH1T-93-01, DESY, Hamburg (1993), unpublished.

[35] S. Prell, Z-Kalibration und dE/dx−Kalibration der zentralen Spurkammer des H1 - Detektors, Diploma thesis, University of Hamburg (1992), H1-report FH1T-92-04, DESY, Hamburg (1992), unpublished.

[36] H. J. Behrend and W. Zimmermann, A hardwired trigger processor using logic cell arrays (XILINX), in ref. [181], p. 237.

[37] S. Egli et al., Nucl. Instr. and Meth. **A283** (1989) 487.

[38] P. Robmann et al., Nucl. Instr. and Meth. **A277** (1989) 368.

[39] H. Bärwolff et al., Nucl. Instr. and Meth. **A283** (1989) 467.

[40] H. Bärwolff et al., Proc. 4^{th} San Miniato Topical Seminar on Experimental Apparatus for High-Energy Physics and Astrophysics (1990), P. Giusti et al. eds., World Scientific 1990, p. 284.

[41] P. Robmann, The central inner z–chamber of the H1-experiment at HERA, Ph. D. thesis, University of Zürich (1993), in preparation.

[42] California Fine Wire Company, Grover City, Cal. 93433.

[43] Rohacell 51: Roehm GmbH, Darmstadt, Germany.

[44] K. Esslinger, and P. Robmann, A sensitive current monitor for drift chambers, Nucl. Instr. and Meth. (1993), in print.

[45] H. Bärwolff et al., Nucl. Instr. and Meth. **A294** (1990) 117.

[46] NOMEX: Eurocomposites, L 6401 Echternach, Luxembourg.

[47] G. A. Beck et al., Nucl. Inst. and Meth. **A283** (1989) 471.

[48] H. Graessler et al., Nucl. Inst. and Meth. **A283** (1989) 622.

[49] H. Graessler et al., Nucl. Inst. and Meth. **A310** (1991) 535.

[50] J. M. Bailey et al., Nucl. Inst. and Meth. **A323** (1992) 184.

[51] H. Graessler et al., Nucl. Inst. and Meth. **A323** (1992) 401.

[52] H. Krehbiel, H1 trigger control system, H1-report 12/88-101, DESY, Hamburg (1988), unpublished.

[53] VICbus, VME Inter-Crate Bus, ISO/IEC JTC 1/SC26.

[54] W. Zimmermann et al., A 16 channel VME flash ADC system (F1001-FADC), H1 internal report, DESY, Hamburg (1989), unpublished; manufacturer: Struck, Tangstedt/Hamburg.

[55] Creative Electronics Systems SA, Fast intelligent controller FIC 8230/8232, Geneva, CH, 1987/1992.

[56] The VME Subsystem Bus (VSB) specification, IEEE standard 1096.

[57] M. de Palma et al., Nucl. Instr. and Meth. **216** (1983) 393.

[58] J. Boucrot et al., Nucl. Instr. and Meth. **176** (1980) 291.

[59] DAG and Electrodag graphite solutions: Acheson Colloiden, Scheemda, Netherlands; Deutsche Acheson Colloids, Ulm, Germany.

[60] K. Müller et al., Nucl. Instr. and Meth. **A457** (1992) 457.

[61] Araldit: epoxy glue manufactured by CIBA-Geigy AG, Basel, Switzerland.

[62] J. A. Kadyk, Nucl. Instr. and Meth. **A300** (1991) 436.

[63] R–4825 Johnson Mathey, Conductive Adhesives and Coatings.

[64] G. Bertrand-Coremans et al., Nucl. Phys. B (Proc. Suppl.) **16** (1990) 518.

[65] G. Bertrand-Coremans et al., IIHE–Bruxelles Report (1992), to be published.

[66] VMEbus repeater link, VME Microsystems Int. Corp. (1992).

[67] B. G. Taylor, MICRON: VMEbus and CAMAC access from Macintosh, Conf. VMEbus in Research, Zürich, CH (1988).

[68] P. Huet, The H1 MWPC data acquisition, Ph. D. thesis, Bruxelles (1993),unpublished.

[69] J. Moreels et al., The H1 MWPC data acquisition system, to be published.

[70] BASF AG, Ludwigshafen, Germany.

[71] G. Kemmerling, Untersuchungen zur Beimischung von Alkoholdampf in geschlossene Gaskreisläufe für den Betrieb von Drift- und Proportionalkammern, Diploma thesis, RWTH Aachen (1990), unpublished.

[72] S. Masson, Ph. D. thesis, RWTH Aachen (1993), unpublished.

[73] R. Etienne, Diploma thesis, RWTH Aachen (1993), unpublished.

[74] Messer Griessheim AG, Griessheim, Germany.

[75] BAYER AG, Leverkusen (Vertrieb Hamburg), Germany.

[76] H. B. Dreis, Bau einer automatisierten Gaschromatographie Messtation für den H1 - Detektor, Diploma thesis, RWTH Aachen (1991), unpublished.

[77] W. A. Dietz, Response factors for gas chromatography, Esso Res. and Eng. Co., Analytical Res. Div., Linden, New Jersey, 68 (1967).

[78] V. Commichau, RWTH Aachen III. Physik. Inst. Lehrstuhl B, internal report, unpublished.

[79] P. Göttlicher, Entwicklung und Bau eines rechnergesteuerten Gassystems für eine Präzisionsdriftkammer, Ph. D. thesis, RWTH Aachen (1993), unpublished.

[80] C. Leverenz, Aufbau und Test eines Szintillationszählersystems zur Bestimmung des Strahluntergrundès am H1 Experiment sowie erste Strahlstudien an HERA, Diploma thesis, University of Hamburg (1991), unpublished.

[81] V. Korbel, Erste HERA - Strahluntergrundstudien in der H1 Wechselwirkungszone im November 1991, DESY-report HERA 92-07, Hamburg (1992), unpublished.

[82] K. Flamm, Messungen von Strahluntergrund bei HERA für den Betrieb von H1, H1-report FH1K-92-03, DESY, Hamburg (1992), unpublished.

[83] H1 collaboration, C. Berger et al., Technical proposal for the H1 detector, DESY-report PRC 86-02, Hamburg (1986), unpublished.

[84] H1 calorimeter group, B. Andrieu et al., The H1 liquid argon calorimeter system, DESY-report 93-078, Hamburg (1993), submitted to Nucl. Instr. and Meth.

[85] J. Stier, Kalibration des H1 Flüssig-Argon Kalorimeters mit kosmischen Myonen, DESY FH1K-92-04, Diploma thesis, University of Hamburg (1992), unpublished.

[86] R.Bernier et al., Pedestal drift and cable pickup problems in multiplexed analog signal transmission, NS Symposium 34, San Francisco, IEEE. Transactions on Nuclear Science **34** (1988) 131.

[87] K. Djidi, DSP readout of ADCs for the H1 calorimeter, Proc. 2nd Int. Conf. on Advanced Technology and Particle Physics, Como (1990), E. Borchi et al. eds., Nucl. Phys. B (Proc. Suppl.) **23A** (1991) 186.

[88] N. Huot, Estimation et Réjection de l'Empilement pour la Mesure des Fonctions de Structure par les Calorimètres de H1, Ph. D. thesis, University of Paris 7 (1992),unpublished.

[89] H1 calorimeter group, Electron identification in liquid argon calorimeters, Proc. 3rd Int. Conf. on Advanced Technology and Particle Physics, Como, Italy (1992), E. Borchi et al. eds., Nucl. Phys. B (Proc. Suppl.) **32** (1993) 97.

[90] H. Abramowicz et al., Nucl. Instr. and Meth. **180** (1981) 429.

[91] H1 collaboration, W. Braunschweig et al., Nucl. Instr. and Meth. **A265** (1988) 419.

[92] H1 collaboration, W. Braunschweig et al., Nucl. Instr. and Meth. **A275** (1989) 246.

[93] H. Greif, Untersuchung zur kalorimetrischen Messung von Jeteigenschaften in hochenergetischen Elektron - Proton Speicherring - Experimenten, Ph. D. thesis, Technical University of München (1990), unpublished.

[94] H1 calorimeter group, H. Oberlack, Study of software compensation for single particles and jets in the H1 calorimeter, Contr. paper # 417, XXV. Int. Conf. on High Energy Physics, Singapore, 1990.

[95] P. Loch, Kalibration des H1 Flüssig-Argon Kalorimeters unter Berücksichtigung der Gewichtungsmethode für Teilchen-Jets, H1-report FH1K-92-02, DESY, Hamburg (1992); Ph. D. thesis, University of Hamburg (1992), unpublished.

[96] H1 calorimeter group, B. Andrieu et al., Results from pion calibration runs for the H1 liquid argon calorimeter and comparisons with simulations, DESY-report 93-047, Hamburg (1993), submitted to Nucl. Instr. and Meth.

[97] H1 calorimeter group, B. Andrieu et al., Test beam results and calibration of the H1 liquid argon calorimeter for electrons, to be submitted to Nucl. Instr. and Meth.

[98] W. Braunschweig et al., Results from a test of a Pb-Fe liquid argon calorimeter, DESY-report 89-022, Hamburg (1989).

[99] H1 collaboration, W. Braunschweig et al., Nucl. Instr. and Meth. **A270** (1988) 334.

[100] R. Haydar, Test et Calibration du Calorimètre Hadronique de l'Expérience H1 à HERA, Ph. D. thesis, University of Paris-Sud (1991), unpublished.

[101] R. Grässler, Kalibration eines elektromagnetischen Kalorimetermoduls für den H1-Detektor, Diploma thesis, RWTH Aachen (1991), unpublished.

[102] J.-F. Laporte, Diffusion Profondément Inélastique à HERA et Calibration Absolue de la Mesure en Energie d'un Electron dans le Calorimètre à Argon Liquide de l'Expérience H1, Ph. D. thesis, University of Paris-Sud (1991), unpublished.

[103] K. Borras, Aufbau und Kalibration eines Flüssig-Argon Kalorimeters im H1 Detektor, Ph. D. thesis, University of Dortmund (1992), unpublished.

[104] M. Flieser, Untersuchungen zur Energieauflösung eines Flüssig-Argon-Kalorimeters für Elektronen und Pionen im Energiebereich von 3.7 - 170 GeV, MPI-Phe/92-08, H1-report 07/92-231, DESY, Hamburg (1992), unpublished; Diploma thesis, Technical University of München (1992), unpublished.

[105] P. Hartz, Kalibration eines Blei-Flüssigargon Kalorimeters mit Elektronen für das H1-Experiment, Ph. D. thesis, University of Dortmund (1993), unpublished.

[106] S. Peters, Die parametrisierte Simulation elektromagnetischer Schauer, MPI-PhE/92-13, Ph. D. thesis, University of Hamburg (1992), unpublished.

[107] J. Gayler, Proc. Workshop on Detector and Event Simulation, K. Bos and B. van Eijk eds., NIKHEF-H-report, Amsterdam (1991), p. 312.

[108] B. Delcourt et al., Comparison of pion calorimeter test data with simulation for CB2/CB3 period, H1-report 04/92-220, DESY, Hamburg (1992), unpublished.

[109] M. Rudowicz, Hadronische Schauersimulation fuer den H1 Detektor, MPI-PhE/92-14, Ph. D. thesis, University of Hamburg (1992), unpublished.

[110] H. Fesefeldt, Nucl. Instr. and Meth. **A263** (1988) 114.

[111] R. Brun et al. GEANT long write-up, CERN Program Library, W5103, 1989.

[112] H. Bergstein, Eichung des H1 Tail Catchers als stand-alone Kalorimeter und in der Kombination mit dem H1 Flüssig Argon Kalorimeter, Ph. D. thesis, RWTH Aachen (1993), unpublished.

[113] Kyowa Gas Chemical ind. Co. Ltd., Nihonbashi, 3-8-2, Chuo-ku, Tokyo 103, Japan.

[114] HAMAMATSU Photonics K.K., Ichino-cho, Hamamatsu City, Japan.

[115] Floeth Electronic , Landsberg a. Lech, Germany.

[116] E. Fretwurst et al., Nucl.Instr. and Meth. **A288** (1990) 1.

[117] M. Eberle et al., Electromagnetic MC-simulations with EGS4 and GEANT – How to make them work for thin detectors, H1-report 05/89-113, DESY report 89-104, Hamburg (1989).

[118] M. Eberle et al., Test Experiment und Monte-Carlo-Simulationen für Silizium-Instrumentierte Kalorimeter, Annual report 1990/1991, I. Inst. Phys., University of Hamburg (1991), unpublished; M.Eberle, Ph. D. thesis, University of Hamburg, in preparation.

[119] I. Fedder, Untersuchungen an Silizium-instrumentierten Test-Kalorimeter für elektromagnetische und hadronische Schauer, Ph. D. thesis, University of Hamburg (1991), unpublished.

[120] M. Ruffer, Implementierung des siliziuminstrumentierten PLUG-Kalorimeters in den H1-Detektor, Ph. D. thesis, University of Hamburg (1992), unpublished.

[121] R. Wunstorf, Systematische Untersuchungen zur Strahlenresistenz von Silizium-Detektoren für die Verwendung in Hochenergiephysik-Experimenten, Ph. D. thesis, University of, Hamburg (1992), unpublished; H1-report FH1K-92-01, DESY, Hamburg (1992), unpublished.

[122] F. Niebergall, Calibration and data correction for the TC calorimeter, H1-report 02/91-163, DESY, Hamburg (1991), unpublished.

[123] H. Bergstein et al., Beam calibration of the H1 tail catcher at CERN, H1-report 10/91-197, DESY, Hamburg (1991), unpublished.

[124] L. Büngener, Interkalibration der Türme des H1 Tailcatchers, Diploma thesis, University of Hamburg (1992), unpublished.

[125] G. Battistoni et al., Nucl. Instr. and Meth. **A152** (1978) 423; ibid. **A176** (1980) 297.

[126] Luranyl: BASF, Ludwigshafen, Germany.

[127] F. Ferrarotto, R. Kotthaus, and B. Stella, Study of alternative materials for streamer tubes, H1-report TR-406, DESY, Hamburg (1987), unpublished.

[128] V. Masbender, and R. Felst, Resistivity measurements of sprayed and painted Luranyl profiles at Aachen, H1-report H1LSTEC 90-4, DESY, Hamburg (1990), unpublished.

[129] CAEN High Voltage System SY 127, Costruzioni Apparechiature Elettroniche Nucleari S.p.A., I-55049 Viareggio.

[130] K. Geske, H. Riege, and R. van Staa, The digital electronics of the H1 streamer tube detector, H1-report H1LSTEC 90-8, DESY, Hamburg (1990), unpublished.

[131] H. Bethe, and W. Heitler, Proc. Roy. Soc. **A146** (1934) 83.

[132] S. Levonian, in ref. [6], vol. I, p. 499.

[133] FEU-147, MELZ, Moscow, Russia.

[134] S. Levonian, DESY report HERA 92-07, Hamburg (1992) 247.

[135] C. Bini et al., Nucl. Instr. and Meth., **A306** (1991) 467.

[136] T. Ahmed et al., H1-collaboration, Phys. Lett. **B299** (1993), 374.

[137] T. Ahmed et al., H1-collaboration, Phys. Lett. **B297** (1992), 205.

[138] G. L. Kotkin, S. I. Polityko, A. Schiller, and V. G. Serbo, Zeit. f. Phys. **C39** (1988) 61.

[139] S. Eichenberger et al., Nucl. Instr. and Meth. **A323** (1992) 532; see also ref. [182].

[140] XILINX, The Programmable Gate Array Company, 2100 Logic Drive, San Jose, CA 95124, USA.

[141] R. Eichler et al., The first level MWPC trigger for the H1 detector, H1-report 04/87-61, DESY, Hamburg (1987), unpublished.

[142] T. Wolff et al., Nucl. Instr. and Meth. **A323** (1992), 537.

[143] H. Brettel et al., Calorimeter event t_0 and trigger elements for CTL and DSP, MPI-Munich report H1-MPI-140, Munich (1990), unpublished.

[144] J. Ban et al., The BEMC single electron trigger, H1-report 07/92-235, DESY, Hamburg (1992), unpublished.

[145] J. Tutas, A level 1 trigger from the limited streamer tube system, H1-report 07/91-185, DESY, Hamburg (1991), unpublished.

[146] T. Ahmed et al., A pipelined first level forward muon drift chamber trigger for H1, in ref. [182]; H1-report 10/92-251, DESY, Hamburg (1992), unpublished.

[147] H. Krehbiel, The H1 trigger decider: from trigger elements to L1-keep, H1-report 09/92-239, DESY, Hamburg (1992), unpublished.

[148] J.C. Bizot et al., Hardware study for a topological level 2 trigger, H1-report 09/92-240, DESY, Hamburg (1992); J.C. Bizot et al., Status of simulation for a topological level 2 trigger, H1-report 09/92-212, DESY, Hamburg (1992), unpublished.

[149] J. Fent et al., A level 2 calorimeter trigger using neural networks, H1-report 04/91-172, DESY, Hamburg (1991), unpublished.

[150] E. Barrelet et al., The hardware implementation of L3 triggers in H1, H1-report 12/88-100, DESY, Hamburg (1988), unpublished.

[151] A. Campbell, A RISC multiprocessor event trigger for the data acquisition system of the H1 experiment at HERA, Int. Conf. Real Time '91, Jülich, FRG (1991).

[152] R. van Staa, A slow control system for the H1 streamer tube detector, University of Hamburg II. Inst. of Physics internal report (1990), unpublished.

[153] J. Strachota, S. Guenther, and P. Skvaril, A model of minimal traffic monitoring, to be published.

[154] J. M. Le Goff et al., ARGUS: a graphic user interface package to monitor the slowly changing parameters of a physics experiment on a Macintosh II, CERN-report ECP 91-31, Geneva (1991).

[155] J. Pothier, BBL3, CERN-report EF/L3, Geneva (1989); and private communication.

[156] The VMEbus specification, IEEE standard 1014.

[157] W. J. Haynes, Bus-based architectures in the H1 data acquisition system, VITA Int. Conf. Open Bus Systems '92 in Research and Industry, Zürich, Switzerland, (1992),ISBN 90-72577-11-6 (1992) 27; *Rutherford Appleton Laboratory report RAL 92-048 (1992).*

[158] W. J. Haynes, Experiences at HERA with the H1 data acquisition system, in ref. [182]; DESY report 92-129, Hamburg (1992), ISSN 0418-9833.

[159] *Creative Electronics Systems SA, RAID 8235, R3000 VMEbus controller, Geneva, CH,* 1990.

[160] Creative Electronics Systems SA, VME/VSB Dual ported memory DPM 8242, Geneva, CH, 1989.

[161] E. Pietarinen, VMEbus cross interface processor module with high speed fibre-optic links: *VMExi, Univ. of Helsinki Report HU-SEFT-1991-14, Helsinki, Finland (1991).*

[162] *The scalable coherent interface (SCI), IEEE standard 1596.*

[163] J. Coughlan, D. Düllmann, M. Savitski, M. Zimmer, Object orientated programming for online systems at *H1*, in ref. [182].

[164] W. J. Haynes, *VME_TOOLS, VMEbus interaction from the MPW shell, DESY, Version* 3.0, February 1992.

[165] E. Deffur, P. Fuhrmann, M. Zimmer, Communication on the *H1* local area network, *H1* internal report, DESY, Hamburg (1991), unpublished.

[166] W. J. Haynes, VMEXI_SSP : VMEtaxi system software package, DESY, Version 3.9, June 1992.

[167] G. Hochweller et al, VME-HSSL VMEbus High Speed Serial Link, Int. Conf. Open Bus Systems '92, Zürich (1992).

[168] *P. Hill,* MacEvLook *Online* version of *H1* event display, *DESY* internal report (*1991*), unpublished.

[169] M. Zimmer, Graphics-orientated operator interfaces at H1, in ref. [181], p. 269.

[170] V. Blobel, BOS and related packages, Proc. 14. Workshop of the *INFN* Eloisatron Project: Data Structures for Particle Physics Experiments: Evolution or Revolution, Erice, Sicily, Italy (1990), R. Brun, P. Kunz and P. Palazzi eds., World Scientific (Singapore, 1991), p. 1.

[171] V. Blobel, The F-package for input-output, in ref. [182].

[172] M. Brun, R. Brun and A. A. Rademakers, CMZ - a source code management system, Proc. Int. Conf. on Computing in High Energy Physics, Oxford (1989), R. C. E. Devenish, T. Daniels eds., Comp. Phys. Comm. 57 (1989) 235.

[173] S. Egli, BOS modules in H1 software - A set of rules and recommendations H1-software note 12, DESY, Hamburg (1990), unpublished.

[174] U. Berthon et al. A data management tool package for H1 reconstruction and analysis, H1-software note 8, DESY, Hamburg (1990), unpublished.

[175] R. Gerhards and Z. Szkutnik, First experience with online reconstruction in H1, in ref. [182].

[176] M. Kuhlen, The fast H1 detector Monte Carlo, in ref. [183].

[177] T. Ahmed et al., H1-collaboration, Phys. Lett. **B298** (1993), 469.

[178] T. Ahmed et al., H1-collaboration, Phys. Lett. **B299** (1993), 385.

[179] I. Abt et al., H1-collaboration, Nucl. Phys. **B396** (1993), 3.

[180] Proc. XVth Int. Conf. on High-Energy Accelerators, Hamburg (1992), J. Rossbach ed., Int. J. Mod. Phys. A (Proc. Suppl.) 2A (1993).

[181] Proc. Int. Conf. Computing in High Energy Physics, Tsukuba, Japan (1991), Universal Academy Press, ISBN 4-946443-09-6 (1991).

[182] Proc. Int. Conf. on Computing in High Energy Physics, Annecy, France (1992).

[183] Proc. 26th Int. Conf. on High Energy Physics, Dallas, Texas, (1992).